

RESONANT ULTRASOUND INVESTIGATIONS OF CORRELATED ELECTRON SYSTEMS

A Dissertation

Presented to the Faculty of the Graduate School

of Cornell University

in Partial Fulfillment of the Requirements for the Degree of

Doctor of Philosophy

by

Sayak Ghosh

August 2022

© 2022 Sayak Ghosh
ALL RIGHTS RESERVED

RESONANT ULTRASOUND INVESTIGATIONS OF CORRELATED ELECTRON SYSTEMS

Sayak Ghosh, Ph.D.

Cornell University 2022

This thesis presents elastic moduli measurements in two materials, the heavy-fermion material URu_2Si_2 and the unconventional superconductor Sr_2RuO_4 . Both of these materials have phase transitions where, in spite of extensive experimental efforts, the exact broken symmetries have remained unknown. Our measurements place strong thermodynamic constraints on the order parameter (OP) symmetry at these transitions. I start by explaining how measurements of elastic moduli discontinuities at a second order transition can help constrain or identify the symmetries of the OP that condenses. Then I describe in details the experimental technique used to measure these moduli discontinuities, resonant ultrasound spectroscopy (RUS). The first material I studied, URu_2Si_2 , has a “hidden order” transition at $T_{\text{HO}} = 17.5$ K, with multiple proposals for the OP. The results, published in *Science Advances*, 6(10), 2020 [1], rules out theories of hidden order that are based on two-component OPs. The second material, Sr_2RuO_4 , becomes a superconductor at $T_c = 1.45$ K. The measurements in Sr_2RuO_4 provide evidence for a two-component OP, and narrows down the possibilities to two specific order parameter candidates. These were published in *Nature Physics*, 17(2):199–204, Feb 2021 [2]. Further, ultrasound attenuation in Sr_2RuO_4 is seen to immensely increase below T_c , thereby signifying highly anomalous dynamics. Formation of superconducting domains is found to best explain this striking observation, as detailed in this arXiv preprint [3].

BIOGRAPHICAL SKETCH

Sayak Ghosh was born in 1994 in the city of Kolkata, India. He went to school at Salt Lake School. In middle school, he loved solving math problems but got more attracted to the wide-range of applicability of physics in high school. He went on to study physics at the Indian Institute of Science, Bangalore, supported by a KVPY fellowship. While working as an undergraduate researcher, he discovered his love for building an experiment from scratch to study and learn about unexplored physics. He completed his Bachelor of Science degree from IISc in 2016.

He then moved halfway across the world to start his PhD in Physics at Cornell University, not heeding to dire warnings about the weather in Ithaca. He joined the research group of Brad Ramshaw as one of its first members in 2017. He worked primarily on low-temperature ultrasound experiments during his PhD, while also delving into quantum transport measurements towards the end of his PhD. While at Ithaca, he enjoyed hiking in the gorges and visiting the various state parks in the area while also learning how to survive the upstate NY winters. When not thinking about physics, he enjoys cooking, going on road trips and gets overly excited about watching soccer.

ACKNOWLEDGEMENTS

I have received a lot of support and encouragement during my six-year long journey as a graduate student at Cornell. It's impossible to list everyone here, but I will try my best.

First and foremost, I want to thank Brad for his wonderful mentorship. The things I have learnt from him in the last five years range from hands-on skills required to build experiments to writing scientific papers for reporting the results, including most of the intermediate steps. Brad's enthusiasm made the learning process an immensely enjoyable experience. He has been a constant source of encouragement from day one, and I wish to emulate his clarity of thinking in my own scientific thought process one day.

I am grateful for the enlightening conversations with my committee members, Eun-Ah Kim and Katja Nowack, which widened my knowledge of physics and helped me place my work within the broader field of quantum materials research. One of the projects reported in this thesis, on URu_2Si_2 , was in fact undertaken in collaboration with Eun-Ah's group.

I thank the rest of the Ramshaw group, Yawen, Patrick, Florian, Avi and Gael, for being an amazing group of people to work with. Performing experiments in the lab often requires the assistance of an extra pair of hands, and they were always willing to help me out. It was a pleasure sharing an office with all of you, and you made the basement of Clark Hall a less depressing place.

A large part of this work would not have been possible without the technical expertise of Jeevak Parpia and Eric Smith, and their willingness to share their invaluable knowledge regarding low-temperature physics. Every time I was unsure about a piece of cryogenic equipment in the lab, I could show up in Eric's office and count on his expertise to guide me in the right direction.

I am extremely grateful to Robert Page and the rest of the LASSP machine shop staff for always being accommodating with my machining requirements. I have lost count of the number of times I showed up Rob's office with a slightly different design for the same part, and he would make time in his busy schedule for me. Special thanks to Nate Ellis, I hope to remember the machining skills he taught me and apply them again in the future.

I had the privilege of having scientific collaborations and discussions with people both within and outside of Cornell during my PhD. For their contributions towards making this thesis possible, I am thankful to Andrew Mackenzie (and his group at MPI Dresden), Steve Kivelson, Arkady Shekhter, Daniel Agterberg, Joerg Schmalian, Kimberly Modic, Michael Matty and Thomas Kiely. I feel fortunate to have attended the courses taught by Dan Ralph, Jim Sethna and Debdeep Jena at Cornell, which were important for strengthening my fundamentals as well as helping me appreciate the diversity of research problems within solid state physics.

During my time as a graduate student, I had an extremely supportive group of friends who made going through graduate school a whole lot easier. They listened to me vent, kept me sane through the COVID lockdown and always stayed in touch. To Amlan, Debaditya, Kishalay, Mayukh, Sandip, Subhendu, Tamoghna, Indrayudh, Mitrajyoti, Samriddha, Rohan, Ritwik, Vishakha, Sayanti, Diptarka, Diptarup, Anik, Sayan, Moni, Samarpan, Minakshi, Debyeet, Anusha, Somdatta and last but not at all the least, Renata, I am awfully lucky to know all of you. I could not have done this without you.

I want to finally thank my parents for everything they have done for me. My father was my first physics teacher back in middle school, and was instrumental in making me appreciate physics in the first place. As parents, they have always encouraged me to improve, and I don't have the words to thank them enough.

TABLE OF CONTENTS

Biographical Sketch	iii
Acknowledgements	iv
Table of Contents	vi
List of Tables	viii
List of Figures	ix
1 Introduction	1
2 Second Order Phase Transitions	7
2.1 Order Parameters and Group Theory	9
2.2 Elastic Properties Near Second Order Transitions	12
2.2.1 Static Elastic Constants	12
2.2.2 Dynamical Effects	14
2.3 Landau Theory and Strain-Order Parameter Coupling	17
2.3.1 Landau Theory for a Ferromagnetic Transition	21
2.3.2 Linear in Order Parameter Coupling to Strain	22
2.3.3 Quadratic in Order Parameter Coupling to Strain	24
2.4 Multi-Component Order Parameters	27
2.4.1 Symmetry-enforced Degeneracy	28
2.4.2 Accidental Degeneracy	33
2.5 Ehrenfest Relations	37
2.5.1 Ehrenfest Relations for Compressional Strains	37
2.5.2 Ehrenfest Relations for Shear Strains	38
2.6 Fluctuations and Ginzburg Criterion	42
3 Resonant Ultrasound Spectroscopy	45
3.1 Experimental Setup	45
3.2 Sample Preparation	51
3.3 RUS at Low Temperatures	53
3.3.1 Low Temperature Setup	54
3.3.2 Thermal Homogeneity Considerations	55
3.4 Temperature Evolution of Resonances	59
3.4.1 Fitting Lorentzian	59
3.4.2 Phase-Locked Loop (PLL)	61
3.5 Data Analysis	65
4 Hidden Order Transition in URu₂Si₂	68
4.1 Electronic phases of URu ₂ Si ₂	68
4.2 Strain-Order Parameter Coupling	71
4.3 Sample Details	73
4.4 Data Analysis	74
4.4.1 Traditional Analysis	76
4.4.2 Machine Learning-based Analysis	79

4.5	Additional Experimental Considerations	85
4.5.1	Resolving the Origin of Jumps	85
4.5.2	Compositions of Resonances	86
4.5.3	Possible Effects from Parasitic AFM	88
4.6	Discussion and Outlook	89
5	Superconductivity of Sr_2RuO_4	91
5.1	Experimental evidences in Sr_2RuO_4	92
5.2	Strain-Order Parameter Coupling	95
5.3	Sample Details	97
5.4	High Temperature Elastic Moduli	98
5.4.1	Anomalous $(c_{11} - c_{12})/2$ Softening	99
5.5	Elastic Moduli Across T_c	106
5.5.1	Jump in c_{66}	106
5.5.2	Uncertainty Analysis	109
5.5.3	Ehrenfest Relations	111
5.5.4	Possible Two-component OPs	113
5.6	Sound Attenuation in Sr_2RuO_4	116
5.6.1	Sound Attenuation in Superconductors	117
5.6.2	Attenuation Measurement in RUS	118
5.6.3	Increase in Compressional Viscosities	120
5.6.4	Understanding the Increase in Viscosity	124
5.6.5	Comparison to Pulse-echo Measurements	131
5.6.6	Background Attenuation in RUS and Pulse-echo	133
5.6.7	Constraints on the Order Parameter	135
5.7	Large B_{1g} Viscosity in Normal State	137
5.7.1	Fermi Liquid Model	138
5.7.2	Deformation Potential	141
6	Conclusions and Outlook	147
A	Converting between α coefficients	150
B	Resonance Linewidth and Attenuation Coefficient	151
C	Rotations of moduli	153
D	Bulk Modulus and Young's Moduli	157
E	Table of Frequencies	160
	Bibliography	173

LIST OF TABLES

2.1	Different equilibrium two-component OPs in D_{4h}. Order parameters that minimize the free energy Equation 2.39 and the discontinuities they produce in various elastic moduli. The negative sign for Δc_m s show that moduli decrease through the transition. In parentheses, we note fluctuation of which OP mode couples to ultrasound. Note that the consistency relation Equation 2.38 holds for all of these order parameters, as expected.	31
4.1	Order parameters in URu_2Si_2. Proposed order parameters of the HO state in URu_2Si_2 , classified by their dimensionality and their point-group representation. Note that designations such as “hexadecapole” order are only applicable in free space—crystalline electric fields break these large multipoles into the representations listed in this table.	71
4.2	Elastic moduli of URu_2Si_2. The six independent elastic moduli in URu_2Si_2 measured with RUS, at room temperature (300 K) and at 20 K.	76
5.1	Elastic moduli of Sr_2RuO_4 measured with RUS.	99
5.2	Experimental uncertainties in moduli jumps in Sr_2RuO_4. The two sources of uncertainty—from width of superconducting transition and from sample dimensions—are added in quadrature to get the total uncertainty in the jump in the six moduli. This leads to the error bars plotted in Figure 5.10.	111
5.3	Some superconducting order parameters in D_{4h}. For the odd-parity spin-triplet order parameters, \hat{x} , \hat{y} and \hat{z} represent the pair wavefunction in spin space in the \mathbf{d} -vector notation [4]. Two-component order parameters $\{\eta_x, \eta_y\}$ can order as η_x , η_y , $\eta_x \pm \eta_y$, or $\eta_x \pm i\eta_y$, depending on microscopic details. It is this latter combination that forms the time-reversal symmetry breaking state (e.g. $(p_x + ip_y)\hat{z}$, or $d_{xz} + id_{yz}$). The “Ultrasound” column indicates whether an order parameter is consistent with a jump in c_{66} at T_c , the “NMR” column indicates whether it is consistent with the suppression of the Knight shift at T_c . Note that the $B_{1g} \oplus A_{2g}$ state does not belong to a single irrep of D_{4h} , and thus transition temperatures of the d and g components must be “fine-tuned” if they are to coincide.	114
E.1	Fit for RUS frequencies of URu_2Si_2 at ~ 300 K.	160
E.2	Fit for RUS frequencies of URu_2Si_2 at 20 K.	162
E.3	Fit for RUS frequencies of Sr_2RuO_4 at ~ 300 K.	165
E.4	Fit for RUS frequencies of Sr_2RuO_4 at 4 K.	169

LIST OF FIGURES

2.1	Landau theory of second order transitions. (a) The Landau free energy \mathcal{F} near a second order phase transition, above and below the transition temperature T_0 . Above T_0 , there is no order parameter ($\Psi = 0$), while below T_0 , two equivalent minima appear at non-zero Ψ . (b) Order parameter that minimizes the free energy as a function of temperature. Below T_0 , Ψ grows as $\sqrt{T_0 - T}$	17
2.2	Specific heat from Landau theory. The specific heat of a system undergoing a second order transition shows a discontinuity at the transition temperature T_0	20
2.3	Linear and quadratic strain-order parameter coupling. (a) Linear-in-OP, linear-in-strain coupling causes softening of the associated elastic constant c_m towards the transition (see Equation 2.29). The transition occurs when c_m softens to zero. (b) Quadratic-in-OP, linear-in-strain coupling leads to a discontinuity in the associated elastic constant at T_0 (see Equation 2.36). This jump can be related to the jump in specific heat through Ehrenfest relations (see Section 2.5).	25
2.4	Frequency dependence of moduli jumps. The jump in an elastic moduli gets broader as the experimental frequency gets closer to the timescale of OP relaxation. Near T_c , we model $\tau \sim \tau_0/ T/T_c - 1 $ and ω is the experimental frequency.	33
2.5	Phase diagram showing multiple superconducting states. The superconducting phase diagram as a function of electron concentration n , with V , W and U certain parameters of an extended Hubbard model as considered in Raghu et al. [5]. Multiple stable states are seen: xy and $x^2 - y^2$ are d -wave states, 1 is s-wave, and $xy(x^2 - y^2)$ is g -wave. An accidental degeneracy can occur if a system is close to one of the phase boundaries. Figure reproduced from Ref. [5].	34
2.6	Strain-induced splitting of the transition temperature $T_{c,0}$. Under B_{1g} shear strain, the two components Ψ_y and Ψ_x condense at different temperatures, T_c and T_{TRSB} , respectively. Above T_c , both the components are zero, and the sample is not superconducting. At T_c , the Meissner effect sets in, and finally, below T_{TRSB} , the system becomes a chiral superconductor. Qualitatively similar behavior is expected for B_{2g} shear strain.	40

3.1	Resonant ultrasound spectroscopy (RUS) apparatus. (a) Schematic of the RUS apparatus, where the sample (not shown) is held between the freely pivoting arm and the bottom plug. The height of the bottom plug can be continuously changed. (b) Photograph of the machined apparatus, with transducers and a sample in between. The black Stycast block on the top arm provides some extra weight which improves the experimental signal-to-noise while measuring resonances.	47
3.2	RUS measurement electronics. (a) The various electronic components required for a RUS measurement assembled within an instrument box. The red board is a commercially available FPGA, Red Pitaya, that outputs experimental frequencies in the range 0.4–5 MHz and performs lock-in measurement at these frequencies. The charge amplifier used on the return signal (“IN”) is the green board, the output of which is the input to Red Pitaya. We communicate to the Pitaya through ethernet connection. (b) Schematic showing the connections between components of (a).	48
3.3	RUS frequency sweep. Measured RUS spectra of a single crystal sample of Sr_2RuO_4 at room temperature, showing the in-phase ($X(\omega)$) and out-of-phase ($Y(\omega)$) responses. The peaks in the spectrum correspond to natural resonances of the sample.	49
3.4	Schematics of resonances. (a) A subset of the scan shown in Figure 3.3, where the amplitude $ Z(\omega) $ is plotted. See Equation 3.10 for definition of $ Z(\omega) $. (b)-(e) show schematically the standing wave patterns for the resonances marked in (a). These were simulated in COMSOL using the elastic constants, density and dimensions of the sample.	52
3.5	Low temperature RUS setup. (a) False color schematic of custom-built low temperature RUS experimental setup, consisting of an outer brass chamber and an inner copper chamber. These two are connected through steel half-tubes, one of which is shown in transparent green. An indium seal is formed between the copper chamber and the stainless steel (SS) ring shown in yellow. Gas flow to the inner chamber occurs through a SS tube that is welded to the grey piece which sits inside the indium seal. Gas flow to the outer chamber occurs through a SS tube directly soldered to the brass part. The RUS sample holder, shown in light red, is attached to the copper part. The inner and outer chambers are sealed with a copper can and a brass can, respectively, which are not shown here. (b) Photograph of the setup with measurement wiring and thermometer.	56

3.6	Measured signal at a resonance. The recorded signal via lock-in techniques at a particular resonance, showing both the in-phase ($X(\omega)$) and out-of-phase ($Y(\omega)$) signals. Note the higher density of points near the center of the resonance compared to the tails. This produces data that uniformly spans the circle in complex plane, shown in Figure 3.7. The amplitude $ Z(\omega) = \sqrt{X(\omega)^2 + Y(\omega)^2}$ is also plotted.	61
3.7	Resonance in complex plane. (a) The resonance shown in Figure 3.6 plotted in the complex plane. The ends of the resonance map on to the cyan point z_0 . The data is fit to a circle to determine the center z_c . The angle θ , as shown in the figure, is related to the resonance frequency ω_0 and the linewidth Γ as $\tan \theta = (\omega - \omega_0)/(\Gamma/2)$. The fit to this expression is shown in (b), which yields $\omega_0 = 2.34504$ MHz and $\Gamma = 0.13$ kHz.	62
3.8	Phase of resonance for PLL. The phase θ of the resonance shown in Figure 3.6. To follow this with PLL, the phase setpoint should be set somewhere close to $\theta = 0^\circ$. Note that for resonances that lie on a big background, the total phase change can be smaller and not centered around zero, in which case the phase setpoint should be chosen accordingly near the center of the resonance.	63
3.9	Improved data acquisition with phase-locked loop. Comparison between the lock-in technique that fits a Lorentzian and phase-locked loop (PLL) for the same resonance frequency of a URu ₂ Si ₂ sample that is cooled through the hidden order transition ($T_{\text{HO}} = 17.25$ K). Data taken with PLL has lower fluctuations and a much higher density of frequency points.	64
4.1	Phase diagram of URu₂Si₂. Pressure-temperature phase diagram of URu ₂ Si ₂ in zero magnetic field. The metallic (heavy Fermi liquid) phase at high temperatures gives way to hidden order (HO) at small pressures, while it evolves into an antiferromagnet (AF) at higher pressures. Superconductivity (SC) is seen to condense from the HO phase at lower temperatures. Figure reproduced from Ref. [6].	69
4.2	Irreducible strains in URu₂Si₂. The tetragonal unit cell of URu ₂ Si ₂ , along with its deformations corresponding to the irreducible representations of strain. There are two compressional (A_{1g}) strains and three shear strains, belonging to B_{1g} , B_{2g} and E_g representations of D_{4h} . There is an elastic modulus corresponding to each of these strains, and a sixth modulus c_{13} which arises from the coupling of the two A_{1g} strains.	73
4.3	Two samples of URu₂Si₂. Photographs of the two URu ₂ Si ₂ samples, S1 and S2, studied using RUS.	74

4.4	Resistance vs temperature for S2. Resistance of sample S2 measured from 300K down to 2K. Inset shows the feature at hidden order transition, from which we determine $T_{\text{HO}} = 17.52$ K for this sample. We find $\text{RRR} \sim 17$ for the sample.	75
4.5	Resonance frequencies of URu₂Si₂ through T_{HO}. Seven representative frequencies of URu ₂ Si ₂ measured through the hidden order transition—plots are shifted vertically for clarity. Three resonances (672, 713 and 1564 kHz) show jumps at T_{HO} (inset shows what is meant by jump), while the others do not, signifying contributions from different symmetry channels.	77
4.6	Temperature evolution of elastic moduli in URu₂Si₂. (a) Compressional and (b) shear moduli of URu ₂ Si ₂ measured with RUS between 275 K and 10 K. The HO transition occurs around 17.25 K, shown in more details in Figure 4.7. We plot the moduli as fractional changes $\frac{\delta c(T)}{c} = \frac{c(T)}{c(275 \text{ K})} - 1$	78
4.7	Elastic moduli of URu₂Si₂ through T_{HO}. (a) Compressional (shown in orange) and (b) shear (shown in blue) moduli of URu ₂ Si ₂ measured through the hidden order transition. Dashed guides to the eye show the temperature dependence extrapolated from below and above T_{HO} , and $\frac{\Delta c}{c}$ shows how we define the jump at T_{HO}	80
4.8	Discontinuities in elastic moduli of URu₂Si₂. Magnitudes of the jumps ($\frac{\Delta c}{c}$) at T_{HO} , along with their experimental uncertainties. Non-zero jumps are seen only in two of the compressional (A_{1g}) moduli, and in none of the shear moduli.	81
4.9	Schematic of the algorithm used to generate training data. Values for elastic moduli and dimensions are chosen randomly from a range that bounds our experimental uncertainties. One-component OPs give jumps only in A_{1g} moduli, whereas two-component OPs also give jumps in B_{1g} and B_{2g} moduli. Separate output files are generated corresponding to one-component and two-component OPs, each containing n jumps, where n is the number of frequencies whose temperature evolution could be experimentally measured. The output value is the network's judgment on the likelihood of whether the jumps come from one-component or two-component OP.	81

4.10	Results of the ANN analysis for two samples of URu_2Si_2.	
	Upper blue curves show the averaged, sorted, simulated frequency shift (“jump”) data plotted against its index in the sorted list for a two-component OP for (a) sample S1 and (b) sample S2. The data are normalized to range from 0 to 1. Lower, red curves shows the same for a one-component OP. Grey dots show experimental data for critical temperature assignment (a) $T_{\text{HO}} = 17.26$ K and (b) $T_{\text{HO}} = 17.505$ K, which visually aligns more closely with the average one-component simulated data than the two-component simulations. Insets: percent confidence of the one-component output neuron for various assignments of T_{HO} averaged over 10 trained networks. A maximum confidence of (a) 83.2% occurs for $T_{\text{HO}} = 17.26$ K and (b) 89.7% for $T_{\text{HO}} = 17.505$ K.	84
4.11	Three frequencies and their attenuation through T_{HO}.	
	A clear discontinuity can be seen in all three resonances and a small peak-like feature can be seen in the attenuation at T_{HO} . The lack of any large temperature-dependent feature in the attenuation rules out anomalous order parameter dynamics interfering with our results.	86
4.12	Elastic moduli with contribution above T_{HO} subtracted.	
	Background subtraction above T_{HO} isolates the effect of the order parameter on the elastic moduli. Plots are vertically shifted for visual clarity. It can be clearly seen that $(c_{11} + c_{12})/2$ and c_{13} show a drop at T_{HO} before starting to stiffen in the HO phase, while all other moduli only show increased stiffening/softening through T_{HO} .	87
4.13	Estimating compositions of resonances.	
	Temperature dependence of two representative resonances (blue and green) between ~ 25 K to 145 K. The fit estimates that the blue curve is composed of mostly E_g and some A_{1g} symmetry vibrations, whereas the green curve is dominated by vibrations in B_{1g} channel.	87
5.1	Fermi surface of Sr_2RuO_4.	
	The Fermi surface of Sr_2RuO_4 at $k_z = 0$, showing the α , β and γ bands.	93
5.2	Strain-order parameter coupling in Sr_2RuO_4.	
	The tetragonal crystal structure of Sr_2RuO_4 and unit cell deformations that illustrate the irreducible representations of strain. There is an elastic modulus that corresponds to each of these strains, and a sixth modulus, c_{13} , arises from coupling between the two A_{1g} strains. Green check marks denote the allowed linear-order couplings to strain for superconducting order parameter bilinears, and red crosses denote that such coupling is forbidden. These couplings lead to discontinuities in the elastic moduli at T_c . A list of relevant possible order parameters in Sr_2RuO_4 is given in Table 5.3.	96

5.3	Laue images of Sr_2RuO_4 sample. Laue X-ray diffraction on the Sr_2RuO_4 RUS sample after aligning and polishing. Images obtained with X-rays incident on the (a) [001] plane and (b) [110] plane, with 110 mm distance between the X-ray source and the sample. The patterns show that the sample is extremely well-aligned with the crystal axes.	97
5.4	Characterization of the Sr_2RuO_4 rod. (a) Specific heat and (b) susceptibility measurements of the upper critical field, measured on different parts of the same rod from which the sample for RUS was obtained. T_c varies by ~ 200 mK between different parts of the rod.	98
5.5	High-temperature elastic moduli in Sr_2RuO_4. (a) The three in-plane elastic moduli of Sr_2RuO_4 , between room temperature and 25 K. (b) The B_{1g} modulus is fit to a Curie-Weiss form ($\sim (T - T_0)^{-1}$), yielding $T_0 \approx -128$ K. Good agreement is found over most of the temperature range, before the data is seen to deviate from the fit around 50 K. We plot the moduli as fractional changes $\frac{\delta c(T)}{c} = \frac{c(T)}{c(293 \text{ K})} - 1$	101
5.6	Calculated elastic moduli in Sr_2RuO_4. The in-plane A_{1g} and B_{1g} elastic moduli of Sr_2RuO_4 calculated within a simple non-interacting picture of a single band close to a van Hove singularity. A large softening is seen in the B_{1g} modulus.	102
5.7	Temperature evolution of elastic moduli in Sr_2RuO_4. (a) Compressional and (b) shear moduli of Sr_2RuO_4 measured with RUS between 60 K and 2 K. We plot the moduli as fractional changes $\frac{\delta c(T)}{c} = \frac{c(T)}{c(60 \text{ K})} - 1$	105
5.8	Resonance frequencies of Sr_2RuO_4 through T_c. Temperature evolution of 18 resonance frequencies of Sr_2RuO_4 through T_c , with panels (a) and (b) each showing 9 frequencies. These were used to calculate the six independent moduli in Sr_2RuO_4 . Plots are vertically shifted for visual clarity.	107
5.9	Elastic moduli of Sr_2RuO_4 through T_c. (a) Compressional and (b) shear moduli of Sr_2RuO_4 measured through the superconducting transition ($T_c \approx 1.42$ K).	108
5.10	Discontinuities in elastic moduli of Sr_2RuO_4. Magnitudes of the jumps ($\frac{\Delta c}{c}$) at T_c , along with their experimental uncertainties. Non-zero jumps are seen only in all the compressional (A_{1g}) moduli, and in the shear modulus c_{66}	109

5.11	Extracting the jumps in moduli and their uncertainties. We extrapolate fits to data (red lines) from above and below T_c at temperature points within the transition (highlighted in yellow). The average between the minimum and maximum jump is taken to be the jump magnitude; the difference is the uncertainty. This procedure is illustrated for c_{66} in panel (a), and c_{44} in panel (b). Note the significantly reduced vertical scale in (b) as compared to (a).	110
5.12	Resonance linewidths of Sr_2RuO_4 through T_c. Temperature evolution of normalized resonance linewidth of 18 resonances of Sr_2RuO_4 through T_c , with panels (a) and (b) each showing 9 resonances. These 18 resonances were used to calculate the six independent components of the viscosity tensor through T_c	120
5.13	Symmetry-resolved viscosities in Sr_2RuO_4 through T_c. (a) Compressional and (b) shear viscosity of Sr_2RuO_4 measured through the superconducting transition ($T_c \approx 1.42$ K).	122
5.14	Relation between L100 and irreducible strains. The Sr_2RuO_4 unit cell under a deformation corresponding to the longitudinal strain ϵ_{xx} , which is excited in L100 mode in pulse-echo. This mode is a superposition of pure compression $\epsilon_{xx} + \epsilon_{yy}$ and pure shear $\epsilon_{xx} - \epsilon_{yy}$	123
5.15	Sound attenuation due to coherence factors. (a) Normalized viscosity ($\eta(T)/\eta(T_c)$) for an isotropic s -wave gap and a $d_{x^2-y^2}$ gap, calculated within the BCS framework. (b) $\eta(T)/\eta(T_c)$ for a time reversal symmetry breaking gap below T_c . A peak is seen at high enough frequencies ($\sim \text{THz}$) but not at our experimental frequencies ($\sim \text{MHz}$). These calculations were done by Thomas G. Kiely.	126
5.16	Sound attenuation due to Cooper pair breaking. Attenuation peak at different frequencies due to pair-breaking effects in a $d_{x^2-y^2}$ gap. The inset shows the plot at our experimental frequency in detail—a tiny peak is seen about 0.01 nK below T_c ($\delta\eta(T) = \eta(T) - \eta(T_c)$ and $\delta T = T - T_c$). These calculations were done by Thomas G. Kiely.	126
5.17	Sound attenuation due to domain wall motion. Normalized viscosity in the A_{1g} channels of Sr_2RuO_4 through T_c , fit to the viscosity expected from domain wall motion below T_c	128
5.18	Viscosity from domains in the RUS frequency range. Viscosity from domains plotted at the lowest and highest frequencies used in the RUS experiment. We take 2.5 MHz as the experimental frequency to extract the domain wall frequency. The shift in the position of the peak is only $\sim 0.01T_c$ from 1.7 MHz to 3.2 MHz. . .	130

5.19	Sound attenuation from order parameter modes. Normalized $(\eta_{11} + \eta_{12})/2$ in Sr_2RuO_4 fit to two different models of increased sound attenuation below T_c . The green curve is a fit to Equation 5.21, which models sound attenuation due to OP collective modes. The red curve is a fit to Equation 5.18, which models the sound attenuation arising from domain wall motion. Near T_c , the red curve clearly fits the experimental data better than the green one.	131
5.20	Comparison to pulse-echo measurements of viscosity. Normalized (a) $(\eta_{11} - \eta_{12})/2$ and (b) η_{11} measured by RUS and pulse-echo techniques. The agreement is good except right below T_c in η_{11} . Pulse-echo data reproduced from Ref. [7].	132
5.21	Viscosity from domains at high frequencies. (a) Normalized $(\eta_{11} + \eta_{12})/2$ from domains plotted at various frequencies. (b) The normalized η_{11} from Ref. [7] (green points), plus calculated including the contribution of domains and compared to pulse-echo measurements. The contribution from domains has a strong frequency dependence, so we choose the pulse-echo frequency (83 MHz) for calculating its contribution to η_{11} . Pulse-echo data reproduced from Ref. [7].	132
5.22	Shear (B_{1g}) viscosity above T_c in Sr_2RuO_4. (a) The in-plane shear viscosity $(\eta_{11} - \eta_{12})/2$ of Sr_2RuO_4 between 2 K and 14 K. It is fit to a combination of background (η_b) and Fermi liquid contribution ($A+BT^2$). The fit gives $\eta_b = 0.19 \text{ Pa.s}$, $A = 1.21 \text{ Pa}^{-1}.\text{s}^{-1}$ and $B = 0.12 \text{ Pa}^{-1}.\text{s}^{-1}.\text{K}^{-2}$. (b) Inverse of background subtracted $(\eta_{11} - \eta_{12})/2$ along with the fit is shown. The fit is seen to deviate from the data above $\sim 12 \text{ K}$	139
5.23	Calculations of viscosity from deformation potentials. Polar plot of $\tilde{\eta}_{ijkl}$ (defined in text) on the γ -band for in-plane (a) A_{1g} , (b) B_{1g} and (c) B_{2g} viscosities. They are plotted in arbitrary units. (d) The plots in (a), (b) and (c) are plotted together. It can be seen that the B_{1g} viscosity is much larger than the B_{2g} viscosity.	145

CHAPTER 1

INTRODUCTION

Phase transitions are ubiquitous in nature. They mark the boundaries between different states of matter, such as liquid to solid, or paramagnet to ferromagnet. They occur when the equilibrium state of a material changes, as a function of temperature, pressure, magnetic field, etc. What is particularly intriguing is that even though the states on two sides of a phase transition are in the same system with the same constituents, the system ends up choosing a completely different equilibrium state as it goes through the phase transition. For example, when iron becomes a ferromagnet below 770°C , or 1043 K , it still has the same atoms it had in the paramagnetic state at higher temperatures. But in contrast to the paramagnetic state, the electron's spins in the ferromagnetic state choose to order in a particular direction. This is what gives iron its magnetism.

The above example illustrates a general fact about phase transitions, they are associated with the “ordering” of something in the system. This formation of order naturally breaks a symmetry which was originally present in the system. For the example of iron, this broken symmetry is the spin rotation symmetry. When the spins point randomly in all directions in the paramagnetic phase, spin rotation is a symmetry of the system. As the spins choose a single direction in the ferromagnetic phase, this symmetry is clearly broken. For a liquid to solid transition (water to ice, for example), the corresponding broken symmetry is translational symmetry—liquids are translationally invariant whereas solids are translationally invariant only up to a lattice spacing. Phase transitions, and therefore states of matter, can be classified in terms of their broken symmetries. We note here that in the last thirty years, states of matter have also been discovered which differ not in their symmetry

properties, but in their topological properties [8]. We will, however, exclusively talk about symmetry-breaking phase transitions in this thesis.

In solid state systems, all of which are ultimately lattices of atomic nuclei and their electrons (which maybe itinerant or localized), an enormous variety of phases have been discovered. Examples include various forms of magnetism (ferro/antiferromagnetism), superconductors, charge density waves, spin density waves, electronic nematicity, and so on. Broadly speaking, a phase transition occurs when the interaction energy that favors ordering can out-compete the thermal energy $k_B T$, which prevents ordering. The above-mentioned phases generally condense at temperatures $\lesssim 100$ K, which corresponds to an energy scale $\lesssim 8$ meV. In a solid, the energy scales corresponding to the nuclei and the core electrons are much higher, which leaves the correlations among the outer electrons as the primary interactions that are important at the meV energies. An important goal of condensed matter physics is to understand the microscopic electronic interactions that lead to this great diversity of phases.

To construct a theoretical model for a phase of matter, we first need to know the broken symmetries of that phase. While identifying the presence of a phase transition is relatively simple, pinning down the broken symmetries is not always straightforward. Some of the outstanding examples in this regard are the pseudogap phase of the cuprate high temperature superconductors [9] and the “hidden order” phase in the heavy-fermion superconductor URu₂Si₂ [10]. In spite of extensive efforts to identify the broken symmetries in these phases (described in Refs. [9, 10]), the broken symmetries have remained unknown. It is therefore of utmost importance to develop experimental tools that can probe the broken symmetries for a wide range of phases of matter.

One way to probe symmetry properties is through “gently” perturbing the system from its equilibrium state, and measuring the response to that perturbation. The trick is to find a perturbing field that couples to the broken symmetry, so that the response is different in the ordered (broken symmetry) phase compared to the disordered phase. For iron, this is an external magnetic field: ferromagnetic iron, after experiencing an external magnetic field, remains a magnet when the external field is removed, while paramagnetic iron loses its magnetism once the field is removed. To constrain or identify the exact broken symmetries, it is desirable to have a perturbation that can couple to many different kinds of broken symmetries.

Strain in solids has many independent components that have unique symmetry properties. These properties, for long-wavelength strains, depend solely on the specific crystal structure, or more correctly, the point group symmetries of the crystal. Applying a strain field in a solid may thus allow unique couplings between the broken symmetry(ies) and the strain components, thereby showing a different response for each component of strain. The simplest response that can be measured are the elastic moduli of the solid as it goes through the phase transition. In the elastic deformation (small strains) limit, stress σ in a solid is related to strain ϵ through the elastic moduli tensor,

$$\sigma_{ij} = c_{ijkl}\epsilon_{kl}. \quad (1.1)$$

The elements of c_{ijkl} are thermodynamic quantities which are indicative of the equilibrium properties of the solid, and thus their behavior can allow identifying or placing strong constraints on the symmetries broken at a phase transition.

In addition to the thermodynamic response, strains can also investigate the dynamics in a solid near a phase transition. Under a time-varying strain, the

above relationship becomes,

$$\sigma_{ij} = c_{ijkl}\epsilon_{kl} - \eta_{ijkl}\frac{\partial\epsilon_{kl}}{\partial t}. \quad (1.2)$$

The viscosity tensor η_{ijkl} has the same symmetry properties as the elastic tensor c_{ijkl} , and describes how energy is dissipated in the presence of time-varying strain. The behavior of its elements can therefore indicate anomalous dynamics in one or more symmetry channels near the transition possibly arising from low energy excitations in the new phase. We note that this viscosity is related to the hydrodynamic flow of the electron-phonon fluid, in contrast to the usual hydrodynamic limit of electron transport.

Ultrasound-based techniques are generally employed to measure the elastic response in solids. Historically, pulse-echo ultrasound, which measures sound velocities in a solid, has been primarily used for this purpose. Using different combinations of sound propagation direction and polarization with respect to the crystal axes, pulse-echo can measure various combinations of elastic moduli and viscosity, from which the independent components of both these tensors can be obtained [7]. We use a relatively less-employed experimental technique, resonant ultrasound spectroscopy (RUS) [11, 12], to study the materials investigated in this thesis. As will be discussed later in the thesis, the resonance frequencies of a piece of solid are related to its elastic moduli, while the linewidths of these resonances carry information about sound attenuation, which is directly related to the viscosity. RUS thus yields the entire elastic and viscosity tensors in a single measurement.

We now mention some physics discoveries that were made possible by ultrasound measurements. The measurement of sound attenuation below T_c provided one of the early verifications of the Bardeen-Cooper-Schrieffer (BCS) theory of superconductivity in elemental superconductors [13]. BCS theory predicted an ex-

ponential decay of sound attenuation in the superconducting state, which could be verified experimentally. From the exponential decay, it was possible to calculate the magnitude of the superconducting gap Δ_0 in these superconductors. Consequently, the BCS prediction for the relation between Δ_0 and T_c could also be verified. In the heavy-fermion superconductor UPt₃, ultrasound measurements revealed additional phase transitions below the superconducting transition [14]. This established the existence of multiple phases in the magnetic field-temperature phase diagram of UPt₃. More recently, RUS measurements have shown evidence for electronic nematicity in the Fe-based superconductors [15], and have demonstrated that there is a thermodynamic phase transition at the onset of the pseudogap phase in cuprates [11].

Beyond ultrasound techniques, which work at the zero strain limit, experimental methods that use an externally applied strain as a tuning parameter have received a lot of traction in the last ten years. This has been largely driven by the development of strain devices that work at cryogenic temperatures [16, 17]. In particular, such experiments have measured how transition temperatures may change as a function of strain [18], or whether one transition may be split into two using appropriate uniaxial strains [19]. Similar to the elastic tensor, there is an elastoresistivity tensor in metals that relate the change in components of resistivity (both longitudinal and Hall) to an applied strain. Elastoresistivity measurements, for specific kinds of transitions, can reveal the broken symmetry in a straightforward way [20, 21]. Very recently, the elastocaloric effect has been employed to study the strain dependence of phase transitions [22, 23]. The idea here is to measure temperature fluctuations under an applied AC strain. This reveals the dependence of transition temperature on particular strains with high precision, which have implications for the broken symmetries rooted in thermodynamics. Knowledge of

the elastic moduli of the material being studied is extremely important for these strain-based techniques, since that determines the amount of strain being applied to the material. Since RUS measures the entire elastic tensor in a single experiment, it allows one to easily compute the particular combinations of elastic moduli that might be relevant for uniaxial strain experiments.

The thesis is organized as follows. In [Chapter 2](#), we detail how the measurement of elastic moduli can reveal important symmetry information at phase transitions, specifically, second order transitions. We then describe the experimental technique of RUS in [Chapter 3](#), along with details of our custom-built apparatus and the data analysis. The next two chapters show how using RUS, we investigated particular systems where the broken symmetries have been remained unknown over more than 25 years. The transitions we studied were the hidden order (HO) transition in URu_2Si_2 ([Chapter 4](#)) and the superconducting transition in Sr_2RuO_4 ([Chapter 5](#)). Finally, specific improvements for the RUS technique, as well as possible next experiments in URu_2Si_2 and Sr_2RuO_4 are mentioned in [Chapter 6](#).

CHAPTER 2

SECOND ORDER PHASE TRANSITIONS

Imagine bringing a kettle of water to a boil. If we are heating it at a constant rate, the temperature will increase linearly with time. This happens till the temperature of water becomes $100\text{ }^{\circ}\text{C}$, or 373 K . At this stage, the temperature of water stays at $100\text{ }^{\circ}\text{C}$ till all the water has boiled off into steam. Clearly, the heat absorbed by water at $100\text{ }^{\circ}\text{C}$ does not go into raising its temperature. Instead, the heat is required to increase the entropy of water, since water and steam (per unit volume) have vastly different entropies. The heat required to convert water at $100\text{ }^{\circ}\text{C}$ to steam at $100\text{ }^{\circ}\text{C}$ is called the latent heat of vaporization of water.

Latent heat at a transition implies a discontinuity in the entropy of the system. Entropy is the first derivative of free energy with respect to temperature, which was the rationale behind Ehrenfest’s classification of phase transitions [24] as first order and second order. At a second order transition, the second derivative of free energy with respect to temperature—the specific heat—has a discontinuity. The entropy stays continuous through such a transition, and hence there is no latent heat. However, not all second order transitions may show a finite discontinuity in specific heat, but instead show some sort of divergence (see, for example, the λ -point transition in ^4He [25]), which has led to the modern classification of transitions as “first order” and “continuous”. Here, we will use the terms second order and continuous interchangeably, referring to the same class of transitions. Microscopically, a system undergoing a first order transition is usually correlated over finite distances, leading to the coexistence of two phases in the mixed-phase regime. In contrast, the correlation length at a second order transition diverges, thereby driving the entire system through the phase transition at once.

At a continuous transition, the system’s energy landscape develops two (or more) minima. The degeneracy of these minima is the hallmark of a continuous transition, and at the transition, the system chooses to condense into one of these minima. More formally, this is known as spontaneous symmetry breaking—the system spontaneously chooses a minimum and in the process, breaks a symmetry that it had to begin with. This choice, in principle, is random, such that the same system cooled through the same transition multiple times may not choose the same degenerate minimum each time. Relatively well-known examples of continuous transitions are ferromagnetic/antiferromagnetic transitions, superconducting and superfluid transitions, electronic nematic transitions, etc.

We have been intentionally abstract about what these minima are, or, in other words, what is the space in which the energy is minimum. The general answer, at least in solids, is some space which includes the positions, charges, spins, etc. of the electrons and ions constituting the solid. However, that is not a particularly helpful answer since it involves a lot of variables. Landau revolutionized the study of phase transitions in condensed matter when he introduced the idea of an order parameter “turning on” at the phase transition [26]. Above the transition, zero order parameter minimizes the energy whereas below the transition, the energy is minimum at a non-zero value of order parameter. Quite helpfully, it turns that most properties of a system near a transition can be understood in terms of these order parameters which describe the broken symmetries of the system in a succinct way. We discuss order parameters in details in [Section 2.1](#). We then talk about how elastic properties of a solid may change close to a second order transition, due to interactions between strain and the order parameter. The next few sections in this chapter are dedicated to developing a simple formalism (Landau theory) to understand these interactions in materials with particular crystalline symmetries.

We will end the chapter by showing that the way we employ Landau theories in the context of transitions only work under particular circumstances—which is called the Ginzburg criterion. A lot of this chapter has been incorporated from statistical mechanics textbooks, in particular, Refs. [27–29].

2.1 Order Parameters and Group Theory

It is instructive to look at examples of order parameters (OPs) to start understanding them. At a ferromagnetic transition, for example, the OP is the total magnetization \vec{M} of the system. The spins in a ferromagnetic material can point in any direction above the transition but below the transition, all of them choose a specific direction to point in. Thus, a ferromagnet (FM) breaks spin rotation symmetry. The net magnetization \vec{M} of a ferromagnet is a measure of the local spin magnetic moment, and hence it points in the same direction as majority of the spins point toward locally. The term “locally” will be clarified in [Section 2.3](#). Note that \vec{M} encodes the symmetry properties of the FM—it is zero above the transition, and is only non-zero below the transition. We can essentially forget about the individual spins and just think in terms of \vec{M} for the FM phase. With this background, we can now define an order parameter as a mathematical object that encodes the symmetry properties of a phase, allowing us to distinguish between different phases of matter. Further examples of OPs can be found in Chapter 9 of Ref. [27].

We will always talk about OPs in the context of crystalline solids in the thesis, and crystals already break the symmetries that exist in free space, such as translation and rotation. In a crystal, we have to respect point group symmetries, which describe operations that leave the crystal unchanged. The symmetry properties of

crystals break the degeneracies that exist in free space. As an illustrative example, we consider the five d orbitals— $d_{x^2-y^2}$, d_{z^2} , d_{xy} , d_{yz} and d_{xz} —that are degenerate in a free space atom. In a cubic crystal (point group O_h), where x , y and z directions are equivalent but are not equivalent to the face diagonals, the five-fold degeneracy is broken into two sets which are separately degenerate: $\{d_{xy}, d_{yz}, d_{xz}\}$ and $\{d_{x^2-y^2}, d_{z^2}\}$. Lowering the symmetry from a cubic to a tetragonal crystal (point group D_{4h}), which has x and y directions equivalent and different than z , the degeneracy is further broken, giving four sets: $d_{x^2-y^2}$, d_{z^2} , d_{xy} and $\{d_{yz}, d_{xz}\}$. Further symmetry lowering to an orthorhombic crystal (point group D_{2h}), where x , y and z are all different, makes all the five d orbitals non-degenerate.

The crystalline point group also places non-negotiable constraints on possible order parameters that may exist in a particular material (see, for example, Sec. II.B in Ref. [30]). Possible OPs have to respect these properties, since an OP that does not satisfy even one of the crystal's symmetries cannot exist in that environment. In other words, if at a transition, an OP condenses that breaks one of the crystal's symmetries, that transition should lead to a lowering of the crystalline symmetry. Thus order parameters have to belong to one of the irreducible representations (irreps) of the point group, which are the minimal symmetry objects that transform correctly under specific point group operations. The irreps can be thought of as forming a basis set for a particular point group. For example, in a tetragonal crystal, any OP has to belong to one (or a combination) of the ten irreps of D_{4h} : $A_{1g/u}$, $A_{2g/u}$, $B_{1g/u}$, $B_{2g/u}$ and $E_{g/u}$. Here, the subscript g or u stand for gerade and ungerade, respectively, which signify if an irrep is even or odd under inversion. This classification works for any order parameter, based solely on symmetry properties of the crystal and independent of the microscopic mechanism leading to the transition.

It is useful to highlight that while we based the above discussion primarily on OPs, externally applied fields, such as an electric field, magnetic field or a strain field also can be expressed in terms of irreps of the crystal's point group. Group multiplication tables determine which products between these fields and a possible order parameter are allowed in a crystalline environment, and provide strong symmetry constraints on which fields “see” which OPs. Strain in solids, being a second rank tensor quantity, can couple to possible OPs in ways that lower rank quantities, such as temperature and electric field, cannot. This, in short, will be the basis for using ultrasound experiments to probe OP symmetry at phase transitions in correlated materials.

We end this section by mentioning some examples of various symmetry OPs in different materials, a larger list maybe found in Rehwald [31]. The BCS superconductors (SCs) have an *s*-wave superconducting OP, which, being isotropic, always belongs to the identity representation (A_{1g} in D_{4h} or D_{6h} point groups, for example). The cuprate SC LSCO has a superconducting OP that, in the D_{4h} point group of the material, belongs to a B_{1g} irrep [32]. Both of these are one-component OPs, that is, they belong to singly degenerate irreps. A two-component OP is possibly realized in the heavy-fermion SC UPt₃, which is a hexagonal material with D_{6h} point group. The OP belongs to the E_{2u} irrep [33], which is a two-component representation in D_{6h} . The structural transition of SrTiO₃, from cubic (O_h) to tetragonal structure, has a three-component OP, which belongs to the T_{1g} irrep of O_h [31]. In particular, the OP at this transition chooses one of the three components to become non-zero while the other two remain zero. This breaks the degeneracy of the three components and leads to a symmetry lowering at the transition.

2.2 Elastic Properties Near Second Order Transitions

We review the thermodynamics of a second order transition in the presence of small strains in this section, which forms the basis for understanding how strain-order parameter coupling can lead to modified elastic constants near a transition. We first analyze the static limit, i.e., where elastic constants are calculated in the zero-frequency limit. We then analyze how finite frequency may lead to dynamical effects.

2.2.1 Static Elastic Constants

We start by writing the free energy \mathbb{F} of a system near a second order transition in terms of temperature T , order parameter Ψ and strains ϵ_m ,

$$d\mathbb{F} = -SdT + \Phi d\Psi + \sigma_m d\epsilon_m. \quad (2.1)$$

Here, S is the entropy and σ_m are elastic stresses. Φ is the thermodynamic conjugate to the OP Ψ —it can be thought of as a restoring force bringing Ψ back to equilibrium. Physically, Φ can be thought of as the stiffness of the system to deformations of the order parameter [27]. Since the system chooses an order parameter that minimizes its free energy below the transition, deforming this order parameter costs energy, which is given by $\Phi d\Psi$. For example, ferromagnets, which prefer to have all their spins pointing in the same direction, resist any change in the orientation of their magnetization.

We want to calculate how elastic constants change as the system goes through the transition. From [Equation 2.1](#), elastic constants are defined as $c_{mn} = d\sigma_m/d\epsilon_n$. In particular, we focus on elastic constants under isothermal ($dT = 0$) conditions,

since experiments probing thermodynamic properties use small enough perturbations which do not cause large temperature fluctuations in the material, and are performed slowly enough such that any such temperature fluctuations die out on the time scale of the experiment. Far above the transition, the equilibrium state has $\Psi = 0$ and fluctuations in the order parameter, if they arise, die out extremely quickly to restore equilibrium. Thus, in this state, the OP stays constant ($d\Psi = 0$). Near or below the transition, strain-OP interactions can strongly modify the order parameter away from the equilibrium order parameter and hold it at this value. Thus, this state requires a fixed restoring force Φ which tries to restore the OP to its equilibrium value, i.e., $d\Phi = 0$. This leads to elastic constants getting modified near or across a second order transition due to coupling between strains and the order parameter.

We now calculate $c_{mn}^{T,\Phi}$ (fixed Φ) and relate it to $c_{mn}^{T,\Psi}$ (fixed Ψ) using the above free energy expression. Following [Equation 2.1](#), we can write

$$d\Phi = \frac{\partial\Phi}{\partial T}dT + \frac{\partial\Phi}{\partial\Psi}d\Psi + \frac{\partial\Phi}{\partial\epsilon_m}d\epsilon_m, \quad (2.2)$$

and

$$d\sigma_m = \frac{\partial\sigma_m}{\partial T}dT + \frac{\partial\sigma_m}{\partial\Psi}d\Psi + \frac{\partial\sigma_m}{\partial\epsilon_n}d\epsilon_n = \frac{\partial\sigma_m}{\partial T}dT + \frac{\partial\sigma_m}{\partial\Psi}d\Psi + c_{mn}^{T,\Psi}d\epsilon_n. \quad (2.3)$$

Here we have identified $c_{mn}^{T,\Psi} = d\sigma_m/d\epsilon_n$ under constant T and Ψ . Setting $d\Phi = 0$ and $dT = 0$ in [Equation 2.2](#) gives

$$\frac{\partial\Phi}{\partial\Psi}d\Psi + \frac{\partial\Phi}{\partial\epsilon_n}d\epsilon_n = 0 \implies \frac{d\Psi}{d\epsilon_n} = -\frac{\partial\Phi/\partial\epsilon_n}{\partial\Phi/\partial\Psi}. \quad (2.4)$$

Using [Equation 2.4](#) in [Equation 2.3](#) and setting $dT = 0$, we get

$$d\sigma_m = -\frac{\partial\sigma_m}{\partial\Psi} \frac{\partial\Phi/\partial\epsilon_n}{\partial\Phi/\partial\Psi}d\epsilon_n + c_{mn}^{T,\Psi}d\epsilon_n \implies c_{mn}^{T,\Phi} = c_{mn}^{T,\Psi} - \frac{\partial\sigma_m}{\partial\Psi} \frac{\partial\Phi/\partial\epsilon_n}{\partial\Phi/\partial\Psi}. \quad (2.5)$$

Written in terms of free energy derivatives, [Equation 2.5](#) becomes

$$c_{mn}^{T,\Phi} = c_{mn}^{T,\Psi} - \frac{\frac{\partial^2 \mathbb{F}}{\partial \Psi \partial \epsilon_m} \frac{\partial^2 \mathbb{F}}{\partial \Psi \partial \epsilon_n}}{\frac{\partial^2 \mathbb{F}}{\partial \Psi^2}} \equiv c_{mn}^{T,\Psi} - \frac{Z_m Z_n}{Y} \implies \Delta c_{mn} = -\frac{Z_m Z_n}{Y}, \quad (2.6)$$

where $Z_m \equiv \frac{\partial^2 \mathbb{F}}{\partial \Psi \partial \epsilon_m}$ and $Y \equiv \frac{\partial^2 \mathbb{F}}{\partial \Psi^2}$.

It is immediately clear that a particular elastic constant c_{mn} gets modified near the transition if both Z_m and Z_n are non-zero. These coefficients, being mixed derivatives, will only be non-zero if the free energy includes terms that couple particular strains ϵ_m and ϵ_n to the order parameter. We explore the allowed couplings between strain and order parameter in more details in the section on Landau theory. We further show how [Equation 2.6](#) proves particularly useful to calculate elastic constants starting from a Landau theory description of a transition. It is important to note, however, that [Equation 2.6](#) is valid in general, even for transitions which are not described by a mean-field Landau theory.

2.2.2 Dynamical Effects

Order parameter fluctuations near a transition have a timescale associated with them, and therefore if experiments probing the transition have a frequency comparable to this intrinsic frequency, dynamical effects may be observable. For example, if the external strain is applied at such a frequency, the measured elastic constants may not be the equilibrium elastic constants but have a frequency dependence to them. OP fluctuations can also absorb energy out of the applied strain wave, thereby attenuating it strongly near the transition. The standard, and possibly the simplest, way to model OP fluctuations is through the Landau-Khalatnikov (LK) formulation of overdamped dynamics (see, for example, Miyake and Varma [\[34\]](#) and references within). Specific microscopic considerations may motivate more com-

plicated formulation of the fluctuations, which we will not delve into here. Within the LK formalism, the dynamics of an OP fluctuation $\delta\Psi$ away from equilibrium are described by the equation

$$\frac{\partial(\delta\Psi)}{\partial t} = -\xi \frac{\partial\mathbb{F}}{\partial\Psi} = -\xi\Phi, \quad (2.7)$$

where ξ is a constant characterizing how quickly the fluctuations die out. As written, this relation can be thought of as Newton's law $a = \frac{1}{m}F$ for the fluctuation $\delta\Psi$.

When the order parameter is at equilibrium, $\delta\Psi = 0$ and thus $\Phi = 0$, since there is no restoring force required to bring the OP back to equilibrium. For small external strains $\delta\epsilon_m$ (which cause small fluctuations $\delta\Psi$), and under isothermal conditions ($dT = 0$), we can write (following [Equation 2.2](#)),

$$\delta\Phi = \frac{\partial\Phi}{\partial\Psi}\delta\Psi + \frac{\partial\Phi}{\partial\epsilon_m}\delta\epsilon_m = Y\delta\Psi + Z_m\delta\epsilon_m. \quad (2.8)$$

Assuming linear response of the OP fluctuations to external strain, when strain is modulated at frequency ω ($\delta\epsilon_m \sim \delta\epsilon_m^0 e^{-i\omega t}$), [Equation 2.7](#) becomes

$$-i\omega\delta\Psi(\omega) = -\xi\left(Y\delta\Psi(\omega) + Z_m\delta\epsilon_m\right) = -\tau^{-1}\delta\Psi(\omega) - \xi Z_m\delta\epsilon_m, \quad (2.9)$$

where we have used [Equation 2.8](#) to replace $\delta\Phi$ and defined $\tau^{-1} = \xi Y$ as the relaxation time for the fluctuations. Rearranging the above equation gives the order parameter fluctuations in terms of the external strains,

$$\delta\Psi(\omega) = \frac{Z_m\delta\epsilon_m}{Y} \frac{1}{i\omega\tau - 1}. \quad (2.10)$$

The frequency dependence above is, in fact, just the Fourier transform of an exponential decay in time domain (with time constant τ), multiplied to a step function to preserve causality.

We can now calculate the frequency-dependent elastic constant from [Equation 2.5](#),

$$\begin{aligned} c_{mn}(\omega) &= c_{mn}^{T,\Psi} - \frac{Z_m Z_n}{Y} \frac{1}{1 - i\omega\tau} \\ \implies c_{mn}(\omega) &= c_{mn}(\omega = 0) + \frac{Z_m Z_n}{Y} \frac{\omega^2 \tau^2}{1 + \omega^2 \tau^2} + i \frac{Z_m Z_n}{Y} \frac{\omega \tau}{1 + \omega^2 \tau^2}. \end{aligned} \quad (2.11)$$

It is easy to check that as $\omega \rightarrow 0$, we recover the result in the static limit ([Equation 2.6](#)), i.e., $c_{mn}(\omega = 0) = c_{mn}^{T,\Phi}$. As the frequency is increased, the measured elastic constants differ from the static limit and eventually when $\omega\tau \gg 1$, no modifications in the elastic constants are measured. Thus, low frequency measurements are desirable to probe the “true” thermodynamic response.

A closer inspection of [Equation 2.10](#) shows that the OP fluctuations are not completely in phase with the the strain modulations at finite frequencies. This leads to an imaginary part in [Equation 2.11](#), which describes the system absorbing energy out of the strain wave and attenuating it. The imaginary part of the elastic constant—viscosity η —relates stress to time-varying strain. It is defined as

$$\eta = \frac{d\sigma_m}{d\dot{\epsilon}_m}, \quad (2.12)$$

where $\dot{\epsilon}_m$ is the time derivative of strain. For strain modulated at frequency ω ,

$$\eta = \frac{1}{\omega} \Im \left(\frac{d\sigma_m}{d\epsilon_m} \right). \quad (2.13)$$

From [Equation 2.11](#), viscosity becomes

$$\eta(\omega) = \frac{Z_m Z_n}{Y} \frac{\tau}{1 + \omega^2 \tau^2}, \quad (2.14)$$

which provides a non-resonant absorption mechanism near the transition. Thus, at frequencies $\omega \sim 1/\tau$, OP relaxation dynamics can lead to an increase in viscosity, which may be observable experimentally.

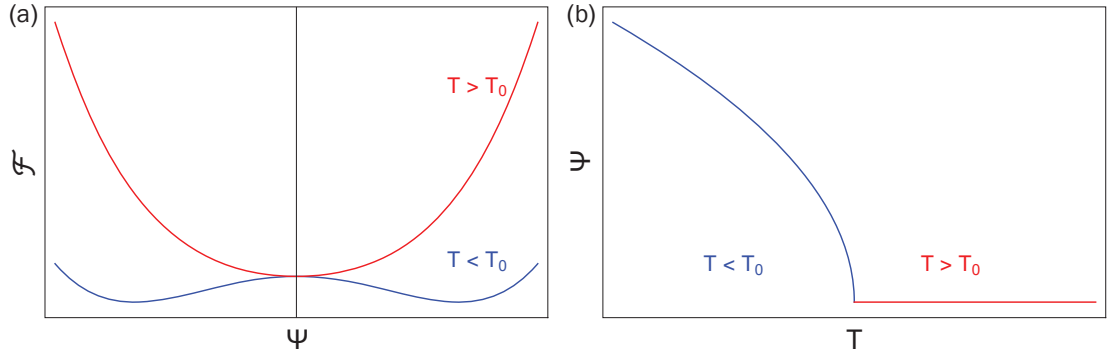


Figure 2.1: **Landau theory of second order transitions.** (a) The Landau free energy \mathcal{F} near a second order phase transition, above and below the transition temperature T_0 . Above T_0 , there is no order parameter ($\Psi = 0$), while below T_0 , two equivalent minima appear at non-zero Ψ . (b) Order parameter that minimizes the free energy as a function of temperature. Below T_0 , Ψ grows as $\sqrt{T_0 - T}$.

2.3 Landau Theory and Strain-Order Parameter Coupling

As we mentioned early in this chapter, the correlation length in a system near a continuous transition diverges, that is, atoms far apart from each other appear to behave in sync. Under these conditions, physics at the scale of lattice spacings becomes unimportant and it is sufficient to think only at mesoscopic scales (coarse-graining). These are length scales much greater than the lattice spacing but smaller than the sample size. Note that the coarse-graining process averages over lattice spacing scale physics, and only allows us to look at long wavelength, low frequency physics. The order parameter field, as we discussed in [Section 2.1](#), is in fact defined over this mesoscopic length scale. Thus, the “local” magnetization in a ferromagnet can be thought as the averaged magnetization over spins within a length scale δx , where $\delta x \gg a$ (a is the lattice spacing).

As early as 1937, Landau was trying to explain the onset of superfluidity in helium, which is a continuous phase transition. To this end, he made a series of assumptions to approximate the free energy of a system near a continuous tran-

sition which still captured the non-analytic behaviors that occur at continuous transitions. He argued that to capture the important degrees of freedom, it should be sufficient to expand the free energy in the powers of the order parameter. What is additionally important, however, is to have the free energy respect all the symmetries of the system, such as translational invariance, rotational symmetry, etc. This, in particular, is where most of the important physics happens in Landau free energies, which will become increasingly clear as we talk about strain-order parameter coupling in later parts of this chapter. In this simple phenomenological description, the non-analytic behavior is mainly captured by the sudden onset of the order parameter at the transition temperature. We will always focus on mean-field-like Landau theories, which are good descriptions for the transitions studied in this thesis. These transitions have relatively long correlation lengths. Many transitions where local interactions are strong, such as certain magnetic transitions, can be non-mean-field [35], which we will not discuss here.

We can now write down the Landau theory for a second order transition. In the absence of external fields such as strain or magnetic field, only even powers of the order parameter are allowed when the OP breaks one of the symmetries present in the system. We will also be looking at bulk properties, like specific heat and magnetization, so we ignore the spatial variations of the OP field. Then, the free energy \mathcal{F}_{op} for a second order transition reads

$$\mathcal{F}_{op} = a_0(T - T_0)\Psi^2 + \frac{1}{2}b\Psi^4, \quad (2.15)$$

where Ψ is the order parameter, $a_0 > 0$ and $b > 0$ are constants assumed to be temperature-independent near $T = T_0$, which is the transition temperature. We note that $b > 0$ is required to ensure the free energy goes to infinity as $\Psi \rightarrow \infty$. As shown in [Figure 2.1](#), the free energy is minimum at $\Psi = 0$ above T_0 , and develops two degenerate minima at non-zero Ψ below T_0 . Hence, above the transition,

system's ground state is unordered ($\Psi = 0$) while below the transition, the system orders by spontaneously choosing one of the degenerate minima ($\Psi \neq 0$).

From this free energy \mathcal{F}_{op} , we can calculate the specific heat discontinuity at the transition, which is present in any second order transition. Above $T = T_0$, the system's ground state has $\mathcal{F}_{op} = 0$, and thus the specific heat above T_0 ,

$$C_{>} = -T \frac{\partial^2 \mathcal{F}_{op}}{\partial T^2} = 0. \quad (2.16)$$

To calculate the specific heat below T_0 , we have to first find the Ψ that minimizes the free energy by setting $\partial \mathcal{F}_{op} / \partial \Psi = 0$. This gives

$$\Psi = \pm \sqrt{\frac{a_0(T_0 - T)}{b}}. \quad (2.17)$$

Replacing this Ψ in [Equation 2.15](#) gives

$$\mathcal{F}_{op} = -\frac{a_0^2(T_0 - T)^2}{2b}. \quad (2.18)$$

Specific heat below the transition then becomes

$$C_{<} = -T \frac{\partial^2 \mathcal{F}_{op}}{\partial T^2} = T \frac{a_0^2}{b}. \quad (2.19)$$

This gives the specific heat discontinuity at the transition (see [Figure 2.2](#))

$$\frac{\Delta C}{T} = \frac{1}{T}(C_{<} - C_{>}) = \frac{a_0^2}{b}. \quad (2.20)$$

Of course, the specific heat of a material undergoing a second order transition is not zero above T_0 . The presence of electrons and phonons, among others, gives the material a finite specific heat. However, the Landau free energy only includes physics arising from the order parameter, which is expected to be the dominating effect near a transition. This makes it a powerful tool to capture the “essential” physics at the transition, such as the specific heat discontinuity, without worrying about everything present in the material. For a real transition, higher order terms

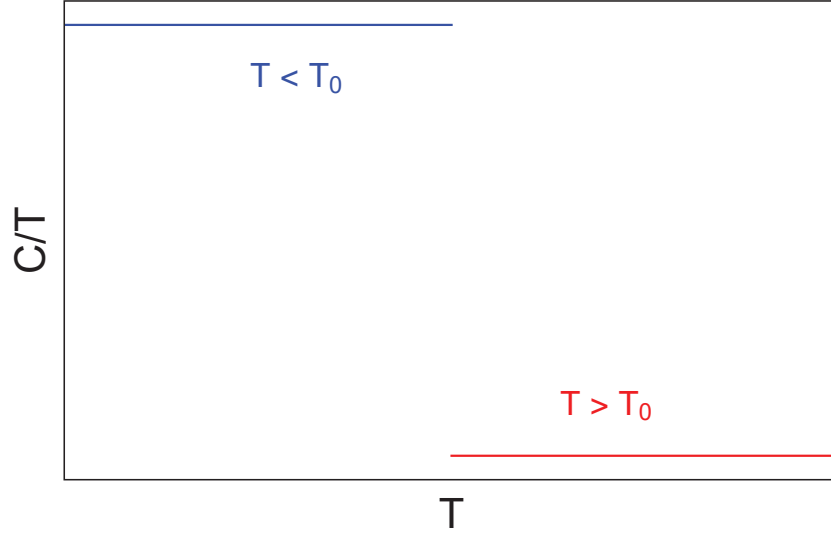


Figure 2.2: **Specific heat from Landau theory.** The specific heat of a system undergoing a second order transition shows a discontinuity at the transition temperature T_0 .

modify [Figure 2.2](#) but the discontinuity remains since that is the dominant behavior near T_0 .

We show in the following subsections how external fields, such as magnetic field or strain, can be introduced in this framework to calculate the susceptibility of a system to these external fields near a transition. We first show this for a ferromagnetic transition in the presence of a weak magnetic field, which gives the Curie-Weiss law for the susceptibility of a ferromagnet. We then focus on transitions in the presence of strain, which allows us to predict the behavior of different elastic constants (see Ref. [\[31\]](#) for an early review of elastic properties near transitions).

2.3.1 Landau Theory for a Ferromagnetic Transition

We talk about a simple example—a metal to ferromagnet transition in a weak magnetic field. We will consider Heisenberg spins that can point in any direction in space. The ferromagnetic OP is the net magnetization of the material \vec{M} . \vec{M} is zero above the transition, with all spins pointing randomly, and acquires a non-zero value below the transition, when the spins point along a favored direction. The presence of an external magnetic field \vec{H} adds a coupling term to the free energy,

$$\mathcal{F}_{coup} = -\vec{M} \cdot \vec{H}. \quad (2.21)$$

Clearly, this term breaks the rotational symmetry of the underlying spins and wants to make the magnetization point towards \vec{H} . Thus, with the direction of \vec{M} fixed by the external field \vec{H} , we can drop the vector symbols and write the total free energy as

$$\mathcal{F} = \mathcal{F}_{op} + \mathcal{F}_{coup} = a_0(T - T_0)M^2 + \frac{1}{2}bM^4 - MH. \quad (2.22)$$

Strictly speaking, the introduction of a term linear in M makes the transition first order. However, provided the magnetic field is small enough (as is ensured in magnetic susceptibility measurements), the transition will be very weakly first order and effects characteristic to a second order transition will still be observable. For a small external field H , we expect the magnetization to be slightly modified from its equilibrium value M_0 , such that $M = M_0 + \delta M$. Following the discussion leading to [Equation 2.17](#), $M_0 = 0$ above T_0 and $M_0 = \pm\sqrt{a_0(T_0 - T)/b}$ below T_0 , when $H = 0$. To calculate δM , we minimize \mathcal{F} ([Equation 2.22](#)) with respect to M by setting $\partial\mathcal{F}/\partial M = 0$, replace $M \rightarrow M_0 + \delta M$ and expand upto linear order in

δM . This gives

$$\begin{aligned}
\frac{\partial \mathcal{F}}{\partial M} &= 2a_0(T - T_0)M + 2bM^3 - H = 0 \\
\implies 2a_0(T - T_0)(M_0 + \delta M) + 2b(M_0^3 + 3M_0^2\delta M) - H &= 0 \\
\implies \delta M &= \frac{H}{2a_0(T - T_0) + 6bM_0^2}.
\end{aligned} \tag{2.23}$$

As expected for weak fields, the magnetization induced by the external magnetic field is found to be linear in the field, $\delta M \propto H$. Additionally, above the transition where $M_0 = 0$,

$$M = M_0 + \delta M = \frac{H}{2a_0(T - T_0)} \implies \chi_M = \frac{\partial M}{\partial H} \propto \frac{1}{T - T_0}. \tag{2.24}$$

This is the well-known Curie-Weiss law for the magnetic susceptibility χ_M of a ferromagnet above its transition temperature.

2.3.2 Linear in Order Parameter Coupling to Strain

The presence of external strains adds an elastic energy contribution to the free energy, given by

$$\mathcal{F}_{el} = \frac{1}{2} \sum_i c_i^0 \epsilon_i^2, \tag{2.25}$$

where c_i are the “bare” elastic constants corresponding to the independent strains ϵ_i . These are the elastic constants one would measure in the absence of any strain-order parameter coupling. In the spirit of Landau theory, the lowest strain-order parameter coupling term that is introduced in the free energy is linear in both strain ϵ_m and OP Ψ ,

$$\mathcal{F}_{coup} = -g\Psi\epsilon_m, \tag{2.26}$$

where g is a coupling constant. Such a term, however, is only allowed when both strain and order parameter have the same symmetry. The simplest example of a

transition where this is allowed is a structural transition, where the order parameter has the same symmetry as one of the strains in the material. For such a transition, the total free energy reads,

$$\mathcal{F} = a_0(T - T_0)\Psi^2 + \frac{1}{2}b\Psi^4 + \frac{1}{2}\sum_i c_i^0 \epsilon_i^2 - g\Psi\epsilon_m. \quad (2.27)$$

Note that this looks quite similar to the free energy in [Equation 2.22](#), with an additional elastic energy term. We can, in principle, solve for the elastic constants by following similar algebraic steps that led to [Equation 2.24](#). Instead, we are going to use [Equation 2.6](#), which allows us to directly calculate the elastic constant c_m corresponding to the coupling strain ϵ_m in terms of partial derivatives of the free energy \mathcal{F} . This eliminates the need to minimize \mathcal{F} in the presence of strains. We find the modified elastic constant to be

$$c_m = c_m^0 - \frac{Z_m^2}{Y} = c_m^0 - \frac{g^2}{2a_0(T - T_0) + 6b\Psi^2}. \quad (2.28)$$

Expressed as a fractional change, and with $\Psi = 0$ above T_0 ,

$$\frac{\Delta c_m}{c_m^0} = \frac{c_m - c_m^0}{c_m^0} = -\frac{g^2}{2a_0 c_m^0} \frac{1}{(T - T_0)}, \quad (2.29)$$

which looks similar to [Equation 2.24](#). Similar to how the magnetic susceptibility of a ferromagnet diverges towards the Curie temperature, the elastic constant in a system with a $\vec{Q} = 0$ structural transition diverges (but with a negative sign) above the transition temperature. This can be understood as the material showing a large strain response for a small applied stress as we get closer to the transition, analogous to how a ferromagnet has a large magnetic response for a small external field when near the Curie temperature. Experimentally, this shows up as a softening of the elastic constant towards zero, and since an elastic constant cannot become negative, the transition occurs when $c_m = 0$ (see [Figure 2.3\(a\)](#)).

We can calculate the modified transition temperature T_S as,

$$c_m^0 = \frac{g^2}{2a_0(T_S - T_0)} \implies T_S = T_0 + \frac{g^2}{2a_0 c_m^0}. \quad (2.30)$$

If the bare elastic constant c_m^0 was infinite, the transition would occur at $T = T_0$. However, in any real material, c_m^0 is finite and hence the transition already occurs at $T_S > T_0$.

A well-known example of the above kind of strain-OP coupling occurs in the electronic-nematic transition in BaFe_2As_2 , which is the parent compound for a family of iron-based superconductors (see Ref. [36] for a recent review). BaFe_2As_2 has a tetragonal crystal structure above the transition, and undergoes a nematic transition which leads to a structural distortion from tetragonal to orthorhombic structure. In the tetragonal structure (point group D_{4h}), there are five independent strains—two compressive strains transforming as the A_{1g} representation, and three shear strains, transforming as B_{1g} , B_{2g} and E_g representations. The nematic order parameter is known to be of B_{2g} symmetry, and hence can couple linearly to B_{2g} strain. Following Equation 2.29, the B_{2g} elastic constant, c_{66} , is expected to soften near the transition,

$$\frac{\Delta c_{66}}{c_{66}^0} = -\frac{g^2}{2a_0 c_{66}^0} \frac{1}{(T - T_0)}. \quad (2.31)$$

The other strains cannot couple to the B_{2g} OP in linear order, and therefore, their associated elastic constants show no anomalous behavior above the transition. Experimentally, c_{66} has been seen to go to zero near $T_S = 130$ K [15, 37], where BaFe_2As_2 undergoes the transition.

2.3.3 Quadratic in Order Parameter Coupling to Strain

While linear-in-order-parameter, linear-in-strain is the lowest order coupling term, not all order parameters can couple at linear order to strain. Notably, superconducting OPs or OPs that break translational symmetry of the lattice (such as

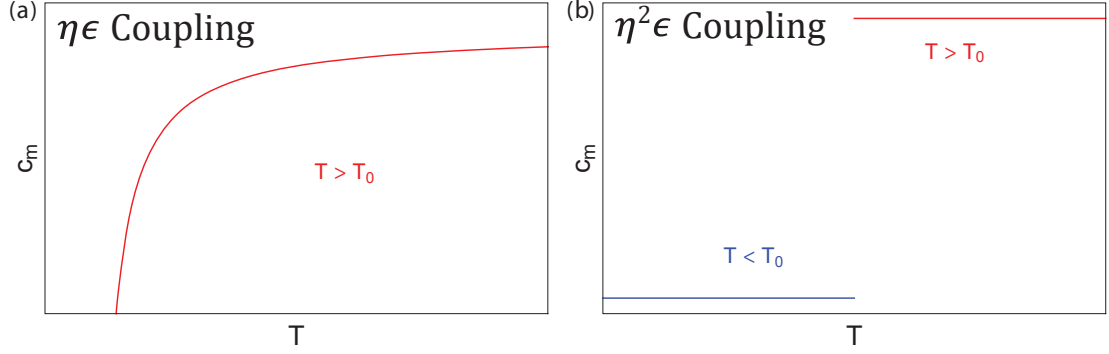


Figure 2.3: **Linear and quadratic strain-order parameter coupling.** (a) Linear-in-OP, linear-in-strain coupling causes softening of the associated elastic constant c_m towards the transition (see Equation 2.29). The transition occurs when c_m softens to zero. (b) Quadratic-in-OP, linear-in-strain coupling leads to a discontinuity in the associated elastic constant at T_0 (see Equation 2.36). This jump can be related to the jump in specific heat through Ehrenfest relations (see Section 2.5).

antiferromagnetism or charge-density waves) can only couple at quadratic order with strain. For example, for a superconducting OP $\Psi_{SC} = |\Psi_{SC}|e^{i\gamma}$, the product $\Psi_{SC} \cdot \epsilon$ breaks gauge symmetry and hence is not allowed in the free energy. The term $|\Psi_{SC}|^2$, however, does not break gauge symmetry and can couple to strains. We now examine the behavior of elastic constants in the presence of quadratic-in-order-parameter, linear-in-strain coupling,

$$\mathcal{F}_{coup} = -g|\Psi|^2\epsilon_m, \quad (2.32)$$

where g is a coupling constant. Such a coupling term is allowed for only those strains which have the the same symmetry as $|\Psi|^2$. Similar to Equation 2.27 but with a quadratic coupling term, the total free energy reads,

$$\begin{aligned} \mathcal{F} &= a_0(T - T_0)|\Psi|^2 + \frac{1}{2}b|\Psi|^4 + \frac{1}{2}\sum_i c_i^0 \epsilon_i^2 - g|\Psi|^2\epsilon_m \\ \implies \mathcal{F} &= (a_0(T - T_0) - g\epsilon_m)|\Psi|^2 + \frac{1}{2}b|\Psi|^4 + \frac{1}{2}\sum_i c_i^0 \epsilon_i^2. \end{aligned} \quad (2.33)$$

The transition occurs when the coefficient of $|\Psi|^2$ term goes to zero. Thus, when a quadratic coupling term is allowed, the presence of finite strain can add a linear-

in-strain term to the transition temperature T' ,

$$T' = T_0 + \frac{g\epsilon_m}{a_0}. \quad (2.34)$$

Note that g can be positive or negative, so the transition can occur above or below T_0 , unlike the case of linear coupling where the transition always occurs above T_0 .

We calculate the modified elastic constant c_m using [Equation 2.6](#),

$$c_m = c_m^0 - \frac{Z_m^2}{Y} = c_m^0 - \frac{4g|\Psi|^2}{2a_0(T - T_0) + 6b|\Psi|^2}, \quad (2.35)$$

where we have set $\epsilon_m \rightarrow 0$, since elastic constants are defined in the limit of zero strain. Above T_0 , $|\Psi|^2 = 0$ and hence, there is no change in the elastic constants above the transition. Below T_0 , $|\Psi|^2 = a_0(T_0 - T)/b$ (see [Equation 2.17](#)), which gives the modified elastic constant at T_0 ,

$$c_m = c_m^0 - \frac{g^2}{b} \implies \Delta c_m = c_m - c_m^0 = -\frac{g^2}{b}. \quad (2.36)$$

Thus, quadratic-in-order-parameter coupling leads to a discontinuity (or a “jump”) in elastic constants at the transition, as shown in [Figure 2.3\(b\)](#).

[Equation 2.6](#) also gives us a consistency check on various elastic constant discontinuities that maybe observed in a transition. If there is an elastic constant that couples two unique strains (say, ϵ_p and ϵ_q) having the same symmetry, then the jump in that constant $\Delta c_{pq} = \frac{\partial^2 \mathbb{F}}{\partial \epsilon_p \partial \epsilon_q}$ will be,

$$\Delta c_{pq} = -\frac{Z_p Z_q}{Y} \implies \Delta c_{pq}^2 = \left(\frac{Z_p Z_q}{Y} \right)^2 = \Delta c_p \Delta c_q, \quad (2.37)$$

where $c_{p(q)} = \frac{\partial^2 \mathbb{F}}{\partial \epsilon_{p(q)}^2}$. For example, in a tetragonal system (point group D_{4h}), the elastic constant c_{13} couples the compressional (A_{1g}) strains $\epsilon_{xx} + \epsilon_{yy}$ and ϵ_{zz} , associated with the elastic constants $(c_{11} + c_{12})/2$ and c_{33} , respectively. Thus, in a tetragonal system,

$$(\Delta c_{13})^2 = \Delta \left(\frac{c_{11} + c_{12}}{2} \right) \times \Delta c_{33}. \quad (2.38)$$

This relation also holds for a hexagonal system (point group D_{6h}), and similar relations can be found for elastic constant discontinuities in other point groups.

Elastic moduli discontinuities arising from quadratic-in-OP coupling to strain have been measured, for example, in the cuprate superconductor LSCO. LSCO has a tetragonal structure (point group D_{4h}), and has a $d_{x^2-y^2}$ superconducting order parameter [32] which belongs to the B_{1g} representation of D_{4h} . Since it is a superconducting OP, this can only couple to strain at quadratic order. The square of this OP transforms as A_{1g} , and can couple only to A_{1g} strains. Following Equation 2.36, this leads to discontinuities in the A_{1g} elastic moduli at T_c . Experimentally, a jump in the A_{1g} modulus c_{33} has been measured by Nyhus et al. [38]. They further show that an externally applied magnetic field that suppresses superconductivity removes the jump, implying the jump arises due to coupling to the superconducting OP.

2.4 Multi-Component Order Parameters

We can now look into order parameters that have more than one component, that is, OPs that cannot be described by a single number. They have multiple degrees of freedom that can show interesting dynamics. For example, a two-component OP can be thought of as vectors that can spin or wind in non-trivial ways and give rise to topological properties [39, 40]. Multi-component OPs can have unique quadratic-in-order-parameter, linear-in-strain couplings, leading to elastic modulus discontinuities that can never arise from one-component OPs. Thus ultrasound measurements are powerful tools to look for states of matter which may harbor such OPs, such as a topological superconductor.

It is natural to ask what guarantees the degeneracy of the multiple components of these OPs. The degeneracy is usually protected by a point group symmetry, leading to a unique transition temperature for all the components. We call this a symmetry-enforced degeneracy. In contrast to the symmetry-enforced case, the components may also happen to be degenerate even without any symmetry protecting them. There is still a unique transition in this case, which we call an accidental degeneracy. A well-known example is the cubic-to-tetragonal structural transition in SrTiO_3 . This transition has a multi-component symmetry-protected order parameter that produces discontinuities in both compressive and shear elastic moduli at the transition, see Refs. [41, 42] for extensive ultrasound studies on SrTiO_3 .

2.4.1 Symmetry-enforced Degeneracy

A symmetry-enforced degeneracy requires an OP that is a multi-component irreducible representation (irrep) of the point group, such as $E_{1g/u}$ or $E_{2g/u}$ irreps in a hexagonal system (point group D_{6h}), or $E_{g/u}$ irreps in a tetragonal system (point group D_{4h}). We consider an E_g , which is a two-component irrep, superconducting OP $\Psi = (\Psi_x, \Psi_y)$ in a tetragonal system in the following calculations. A superconducting OP breaks gauge symmetry and can therefore couple only at quadratic order to strains. Detailed calculations for some other multi-component superconducting OPs may be found in Ref. [30].

The square of an E_g OP gives rise to the bilinears $|\Psi_x|^2 + |\Psi_y|^2$ ($= |\Psi|^2$), $|\Psi_x|^2 - |\Psi_y|^2$ and $\Psi_x^* \Psi_y + \Psi_x \Psi_y^*$, which belong to the A_{1g} , B_{1g} and B_{2g} irreps of

D_{4h} respectively. The order parameter free energy expansion for this OP reads

$$\mathcal{F}_{op}(\Psi) = a|\Psi|^2 + \frac{b_1}{2}|\Psi|^4 + \frac{b_2}{2}(|\Psi_x|^2 - |\Psi_y|^2)^2 + \frac{b_3}{2}(\Psi_x^*\Psi_y + \Psi_x\Psi_y^*)^2 \quad (2.39)$$

where $a = a_0(T - T_{c,0})$, with $a_0 > 0$, and b_i are phenomenological constants. The extra quartic terms, compared to Equation 2.15, come from the square of B_{1g} and B_{2g} bilinears. These are allowed since the square of the B_i irreps transform as A_{1g} . In a tetragonal crystal, the elastic free energy density is given by

$$\begin{aligned} \mathcal{F}_{el} &= \frac{1}{2} \left(c_{11}(\epsilon_{xx}^2 + \epsilon_{yy}^2) + 2c_{12}\epsilon_{xx}\epsilon_{yy} + c_{33}\epsilon_{zz}^2 + 2c_{13}(\epsilon_{xx} + \epsilon_{yy})\epsilon_{zz} + 4c_{44}(\epsilon_{xz}^2 + \epsilon_{yz}^2) \right. \\ &\quad \left. + 4c_{66}\epsilon_{xy}^2 \right) \\ &= \frac{1}{2} \left(\frac{c_{11} + c_{12}}{2}(\epsilon_{xx} + \epsilon_{yy})^2 + c_{33}\epsilon_{zz}^2 + 2c_{13}(\epsilon_{xx} + \epsilon_{yy})\epsilon_{zz} + \frac{c_{11} - c_{12}}{2}(\epsilon_{xx} - \epsilon_{yy})^2 \right. \\ &\quad \left. + 4c_{44}(\epsilon_{xz}^2 + \epsilon_{yz}^2) + 4c_{66}\epsilon_{xy}^2 \right) \\ &= \frac{1}{2} \left(c_{A_{1g},1}^0 \epsilon_{A_{1g},1}^2 + c_{A_{1g},2}^0 \epsilon_{A_{1g},2}^2 + 2c_{A_{1g},3}^0 \epsilon_{A_{1g},1} \epsilon_{A_{1g},2} + c_{B_{1g}}^0 \epsilon_{B_{1g}}^2 + c_{E_g}^0 |\epsilon_{E_g}|^2 \right. \\ &\quad \left. + c_{B_{2g}}^0 \epsilon_{B_{2g}}^2 \right), \end{aligned} \quad (2.40)$$

where the strains are written as the irreducible representations of D_{4h} , $(\epsilon_{xx} + \epsilon_{yy}) \rightarrow \epsilon_{A_{1g},1}$, $\epsilon_{zz} \rightarrow \epsilon_{A_{1g},2}$, $(\epsilon_{xx} - \epsilon_{yy}) \rightarrow \epsilon_{B_{1g}}$, $2\epsilon_{xy} \rightarrow \epsilon_{B_{2g}}$ and $(2\epsilon_{xz}, 2\epsilon_{yz}) \rightarrow \epsilon_{E_g}$.

A multi-component OP can give rise to unique strain-OP couplings that are not possible for one-component OPs. The lowest order quadratic-in-order-parameter, linear-in-strain coupling terms gives rise to additional contributions to the free energy

$$\mathcal{F}_{coup} = (g_1\epsilon_{A_{1g},1} + g_2\epsilon_{A_{1g},2})|\Psi|^2 + g_4\epsilon_{B_{1g}}(|\Psi_x|^2 - |\Psi_y|^2) + g_5\epsilon_{B_{2g}}(\Psi_x^*\Psi_y + \Psi_x\Psi_y^*), \quad (2.41)$$

where g_i are coupling constants. In D_{4h} , coupling between OP and B_{1g} , B_{2g} strains are only allowed for two-component OPs; one-component OPs can only couple to compressive (A_{1g}) strains. Hence jumps in B_{1g} , B_{2g} shear moduli can only occur

if the OP is two-component. Since no superconducting OP in D_{4h} can couple to an E_g strain, c_{44} should not show a jump at T_c .

To get the explicit expressions for the moduli discontinuities, it is easier to parameterize Ψ in terms of amplitude, orientation and relative phase of the OP. Following Sigrist [43], we use the parameterization $\Psi = (\Psi_x, \Psi_y) = \Psi(\cos \theta, e^{i\gamma} \sin \theta)$. Here, θ describes the orientation of the OP while γ is the superconducting phase difference between the components. Depending on the relative magnitudes of b_1, b_2, b_3 , the system can have different equilibrium OPs [44], characterized by different equilibrium values of $(\theta, \gamma) = (\theta_0, \gamma_0)$: $(\pi/4, \pm\pi/2)$ for the chiral state, $(\pi/4, 0)$ for the diagonal nematic state and $(0, 0)$ for the horizontal nematic state. These states also have different equilibrium values of $\Psi = \Psi_0$, which can be calculated from $\partial\mathcal{F}_{op}/\partial\Psi|_{(\theta,\gamma)\rightarrow(\theta_0,\gamma_0)} = 0$. Fluctuations of the order parameter amplitude Ψ , orientation θ or relative phase γ can couple to different strains, leading to the jump in corresponding modulus.

For a multi-component OP Ψ , Equation 2.6 gets modified to

$$c_{mn} = c_{mn}^0 - \mathbf{Z}_m^T \mathbf{Y}^{-1} \mathbf{Z}_n \implies \Delta c_{mn} = -\mathbf{Z}_m^T \mathbf{Y}^{-1} \mathbf{Z}_n \quad (2.42)$$

where $\mathbf{Z}_i = \partial^2\mathcal{F}_{coup}/\partial\Psi\partial\epsilon_i$ are now vectors and $\mathbf{Y} = \partial^2\mathcal{F}_{op}/\partial\Psi^2$ are matrices. For the above parameterization of the OP, each \mathbf{Z}_i has three components, which are derivatives with respect to Ψ , θ and γ , respectively. The components of \mathbf{Y} are double (or mixed) derivatives with respect to these parameters, making it a 3×3 matrix. Thus, $Y_{11} = \partial^2\mathcal{F}_{op}/\partial\Psi^2$, $Y_{12} = \partial^2\mathcal{F}_{op}/\partial\Psi\partial\theta$, $Y_{13} = \partial^2\mathcal{F}_{op}/\partial\Psi\partial\gamma$ and so on.

We now evaluate \mathbf{Y} and \mathbf{Z}_i s using the equilibrium Ψ_0 , θ_0 and γ_0 for the chiral

OP	Chiral	Diagonal Nematic	Horizontal Nematic
(θ_0, γ_0)	$(\pi/4, \pm\pi/2)$	$(\pi/4, 0)$	$(0, 0)$
Ψ_0	$\sqrt{\frac{-a}{b_1}}$	$\sqrt{\frac{-a}{b_1+b_3}}$	$\sqrt{\frac{-a}{b_1+b_2}}$
\mathcal{F}_{min}	$-\frac{a_0^2(T-T_c)^2}{2b_1}$	$-\frac{a_0^2(T-T_c)^2}{2(b_1+b_3)}$	$-\frac{a_0^2(T-T_c)^2}{2(b_1+b_2)}$
$\Delta C/T$	$\frac{a_0^2}{b_1}$	$\frac{a_0^2}{b_1+b_3}$	$\frac{a_0^2}{b_1+b_2}$
$\Delta c_{A_{1g},1}$	$-\frac{g_1^2}{b_1} (\Psi)$	$-\frac{g_1^2}{b_1+b_3} (\Psi)$	$-\frac{g_1^2}{b_1+b_2} (\Psi)$
$\Delta c_{A_{1g},2}$	$-\frac{g_2^2}{b_1} (\Psi)$	$-\frac{g_2^2}{b_1+b_3} (\Psi)$	$-\frac{g_2^2}{b_1+b_2} (\Psi)$
$\Delta c_{A_{1g},3}$	$-\frac{g_1 g_2}{b_1} (\Psi)$	$-\frac{g_1 g_2}{b_1+b_3} (\Psi)$	$-\frac{g_1 g_2}{b_1+b_2} (\Psi)$
$\Delta c_{B_{1g}}$	$-\frac{g_4^2}{b_2} (\theta)$	$-\frac{g_4^2}{b_2-b_3} (\theta)$	$-\frac{g_4^2}{b_1+b_2} (\Psi)$
$\Delta c_{B_{2g}}$	$-\frac{g_5^2}{b_3} (\gamma)$	$-\frac{g_5^2}{b_1+b_3} (\Psi)$	$-\frac{g_5^2}{b_3-b_2} (\theta)$

Table 2.1: **Different equilibrium two-component OPs in D_{4h} .** Order parameters that minimize the free energy [Equation 2.39](#) and the discontinuities they produce in various elastic moduli. The negative sign for Δc_m s show that moduli decrease through the transition. In parentheses, we note fluctuation of which OP mode couples to ultrasound. Note that the consistency relation [Equation 2.38](#) holds for all of these order parameters, as expected.

OP (listed in [Table 2.1](#)). This gives

$$Y = \begin{pmatrix} -4a & 0 & 0 \\ 0 & \frac{4a^2 b_2}{b_1^2} & 0 \\ 0 & 0 & \frac{a^2 b_3}{b_1^2} \end{pmatrix} \quad (2.43)$$

$$Z_{A_{1g},1(2)} = \begin{pmatrix} 2g_{1(2)}\sqrt{\frac{-a}{b_1}} \\ 0 \\ 0 \end{pmatrix}; Z_{B_{1g}} = \begin{pmatrix} 0 \\ 2g_4\frac{a}{b_1} \\ 0 \end{pmatrix}; Z_{B_{2g}} = \begin{pmatrix} 0 \\ 0 \\ g_5\frac{a}{b_1} \end{pmatrix}. \quad (2.44)$$

Within this formalism, one can find which OP fluctuation mode couples to a particular strain by looking at the \mathbf{Z}_i for that strain. The above shows that for the chiral OP, Ψ fluctuations couple to the A_{1g} strains, θ fluctuations couple to B_{1g} strain and γ fluctuations couple to B_{2g} strain, consistent with the conclusions of Ref. [\[43\]](#). The elastic moduli discontinuities for the various OPs is summarized in [Table 2.1](#).

Having established the static elastic response for multi-component OPs, we can now incorporate dynamical effects which may become important near a phase transition. In particular, we want to write Equation 2.11 for a multi-component OP. We start from Equation 2.9 and modify it to account for multiple components in the order parameter,

$$-i\omega\delta\tilde{\Psi}(\omega) = -\xi \left(\mathbf{Y}\delta\tilde{\Psi} + \sum_m \mathbf{Z}_m\delta\epsilon_m \right) = -\boldsymbol{\tau}^{-1}\delta\tilde{\Psi}(\omega) + \xi \sum_m \mathbf{Z}_m\delta\epsilon_m. \quad (2.45)$$

Here, $\delta\tilde{\Psi}$ are the fluctuations of OP components about equilibrium, and $-\xi\mathbf{Y}$ provides the restoring force towards equilibrium. We have also defined $\boldsymbol{\tau}^{-1} = \xi\mathbf{Y}$ as the matrix of relaxation times for independent OP modes.

Using the same parameterization as before ($\Psi = \Psi(\cos\theta, e^{i\gamma}\sin\theta)$) for a two-component OP in D_{4h} ,

$$\boldsymbol{\tau} = \begin{pmatrix} \tau_\Psi & 0 & 0 \\ 0 & \tau_\theta & 0 \\ 0 & 0 & \tau_\gamma \end{pmatrix} \implies (i\omega\boldsymbol{\tau} - \mathbb{I})^{-1} = \begin{pmatrix} (i\omega\tau_\Psi - 1)^{-1} & 0 & 0 \\ 0 & (i\omega\tau_\theta - 1)^{-1} & 0 \\ 0 & 0 & (i\omega\tau_\gamma - 1)^{-1} \end{pmatrix} \quad (2.46)$$

Using Equation 2.5 and replacing $\delta\tilde{\Psi}(\omega)$ from Equation 2.45, we calculate the dynamic elastic constant as,

$$c_{mn}(\omega) = c_{mn}^{T,\Psi} + \frac{\partial^2 \mathcal{F}_{coup}}{\partial \Psi \partial \epsilon_m} \frac{\partial \tilde{\Psi}}{\partial \epsilon_n} \implies \Delta c_{mn}(\omega) = \mathbf{Z}_m^T (i\omega\boldsymbol{\tau} - \mathbb{I})^{-1} \mathbf{Y}^{-1} \mathbf{Z}_n \quad (2.47)$$

Elastic moduli jumps come from the real part of Equation 2.47. Depending on which OP mode a particular symmetry strain couples to, the corresponding modulus dispersion $c_{mn}(\omega)$ picks up a contribution from the corresponding relaxation time. For example, for the chiral OP,

$$\Delta c_{A_{1g},1(2)} = \frac{-g_{1(2)}^2}{b_1} \frac{1}{1 + \omega^2 \tau_\Psi^2}; \Delta c_{B_{1g}} = \frac{-g_4^2}{b_2} \frac{1}{1 + \omega^2 \tau_\theta^2}; \Delta c_{B_{2g}} = \frac{-g_5^2}{b_3} \frac{1}{1 + \omega^2 \tau_\gamma^2}. \quad (2.48)$$

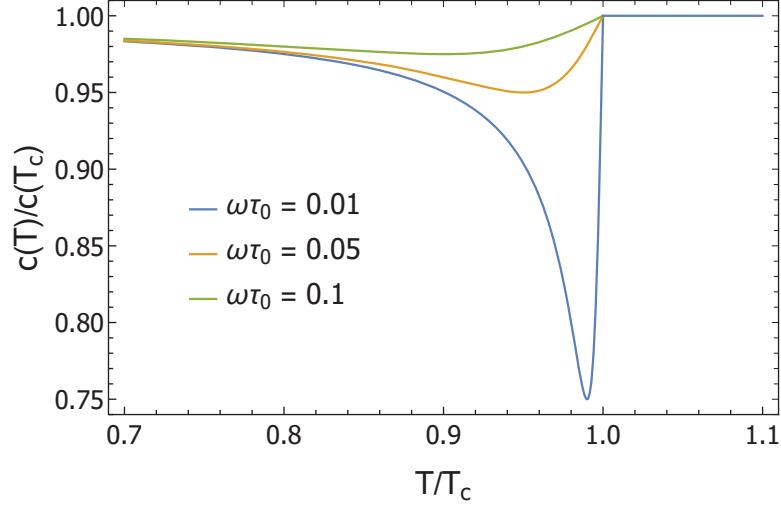


Figure 2.4: **Frequency dependence of moduli jumps.** The jump in an elastic moduli gets broader as the experimental frequency gets closer to the timescale of OP relaxation. Near T_c , we model $\tau \sim \tau_0/|T/T_c - 1|$ and ω is the experimental frequency.

The viscosities (see Equation 2.13) for the various symmetry channels come from the imaginary part of Equation 2.47. For the chiral OP, we have

$$\eta_{A_{1g},1(2)} = \frac{g_{1(2)}^2}{b_1} \frac{\tau_\Psi}{1 + \omega^2 \tau_\Psi^2}; \eta_{B_{1g}} = \frac{g_4^2}{b_2} \frac{\tau_\theta}{1 + \omega^2 \tau_\theta^2}; \eta_{B_{2g}} = \frac{g_5^2}{b_3} \frac{\tau_\gamma}{1 + \omega^2 \tau_\gamma^2}. \quad (2.49)$$

Thus OP relaxation effects can broaden out the elastic moduli jumps, if particular relaxation times are long compared to the experimental frequencies (see Figure 2.4). This has been observed experimentally, for example, in the cuprate superconductor LSCO [38]—higher frequencies reduce the magnitude of jump measured. At such high frequencies, a non-resonant absorption peak may also show up in the measured viscosity below the transition temperature.

2.4.2 Accidental Degeneracy

An accidentally degenerate two-component order parameter has components which together do not belong to a single irreducible representation, and thus their degen-

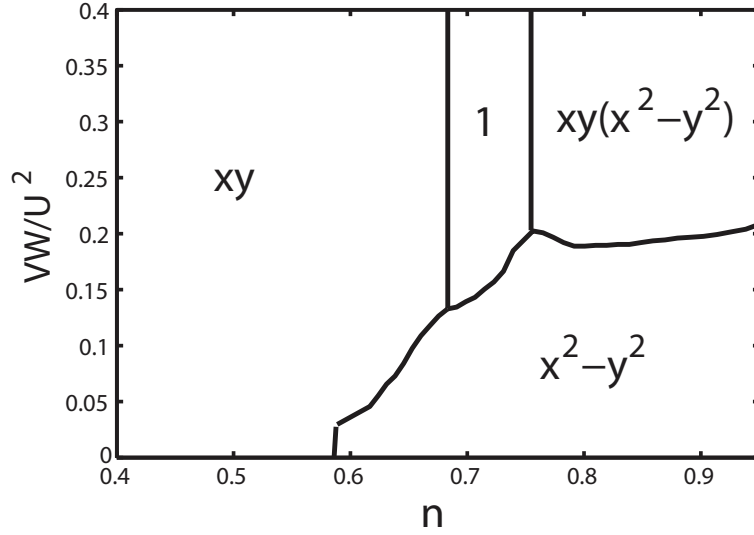


Figure 2.5: **Phase diagram showing multiple superconducting states.** The superconducting phase diagram as a function of electron concentration n , with V , W and U certain parameters of an extended Hubbard model as considered in Raghu et al. [5]. Multiple stable states are seen: xy and $x^2 - y^2$ are d -wave states, 1 is s -wave, and $xy(x^2 - y^2)$ is g -wave. An accidental degeneracy can occur if a system is close to one of the phase boundaries. Figure reproduced from Ref. [5].

eracy is not enforced by any of the point group symmetries. In principle, these two components could condense at different temperatures, leading to two transitions. A single transition temperature for the two components requires “fine-tuning”, which makes an accidental degeneracy less natural than a symmetry-enforced one. Nevertheless, we explore the idea here since it is possibly relevant for Sr_2RuO_4 , which has been studied in detail in this thesis. An accidental degeneracy can arise if a material is close enough, in some parameter space, to the boundary between two regimes where the two components are individually dominant (see Figure 2.5). Then, even though the second component is sub-dominant, it can show up around local defects and dislocations in the material, allowing it to realize an accidentally degenerate order parameter [45–47].

To write down the Landau theory for an accidentally two-component superconducting OP (Ψ_1, Ψ_2) in a tetragonal system, we assume a specific example— Ψ_1

is $d_{x^2-y^2}$ (belongs to B_{1g} irrep) and Ψ_2 is $g_{xy(x^2-y^2)}$ (belongs to A_{2g} irrep). This leads to a non-trivial jump in the B_{2g} shear modulus, since the bilinear $B_{1g} \otimes A_{2g}$ transforms as B_{2g} , and thus it can couple to B_{2g} strain. Motivated by experimental observation of time-reversal symmetry (TRS) breaking in Sr_2RuO_4 , we will also assume a chiral, TRS-breaking OP. The free energy \mathcal{F}_{op} is written as

$$\begin{aligned} \mathcal{F}_{op} = & a_1(T - T_1) (|\Psi_1|^2 + |\Psi_2|^2) + a_2(T - T_2) (|\Psi_1|^2 - |\Psi_2|^2) \\ & + \frac{b_1}{2} (|\Psi_1|^2 + |\Psi_2|^2)^2 + \frac{b_2}{2} (|\Psi_1|^2 - |\Psi_2|^2)^2 + \frac{b_3}{2} (\Psi_1^* \Psi_2 + \Psi_1 \Psi_2^*)^2, \end{aligned} \quad (2.50)$$

similar to how we wrote [Equation 2.39](#). From this, it can be seen that Ψ_1 condenses first at $T = T_c$, when

$$a_1(T_c - T_1) + a_2(T_c - T_2) = 0 \implies T_c = \frac{a_1 T_1 + a_2 T_2}{a_1 + a_2}. \quad (2.51)$$

The magnitude of Ψ_1 can be obtained by minimizing \mathcal{F}_{op} ([Equation 2.50](#)), with $\Psi_2 = 0$. This gives, for $T < T_c$,

$$|\Psi_1|^2 = \frac{a_1(T_1 - T) + a_2(T_2 - T)}{b_1 + b_2}. \quad (2.52)$$

The second component condenses at $T = T_{trsb}$, with $\Psi_2 = i|\Psi_2|$. This is calculated by setting the coefficient of $|\Psi_2|^2$ to zero, where Ψ_1 is given as above.

$$\begin{aligned} a_1(T_{trsb} - T_1) - a_2(T_{trsb} - T_2) + (b_1 - b_2)|\Psi_1|^2 &= 0 \\ \implies T_{trsb} &= \frac{a_1 b_2 T_1 - a_2 b_1 T_2}{a_1 b_2 - a_2 b_1} \end{aligned} \quad (2.53)$$

For the accidental degeneracy to produce a single transition, we require $T_1 = T_2 = T_0$, which is the ‘‘accident’’ that needs to happen. Inserting this in [Equation 2.51](#) and [Equation 2.53](#), the single transition temperature is $T_c = T_{trsb} = T_0$. Below T_0 , the amplitudes of Ψ_1 and Ψ_2 can be obtained by minimizing \mathcal{F}_{op} with respect to Ψ_1 and Ψ_2 , with $\Psi_2 = i|\Psi_2|$. This gives

$$\begin{aligned} |\Psi_1|^2 &= \left(\frac{a_1}{2b_1} + \frac{a_2}{2b_2} \right) (T_0 - T) \\ |\Psi_2|^2 &= \left(\frac{a_1}{2b_1} - \frac{a_2}{2b_2} \right) (T_0 - T), \end{aligned} \quad (2.54)$$

and the minimum free energy is

$$\mathcal{F}_{op,min} = -\frac{1}{2} \left(\frac{a_1^2}{b_1} + \frac{a_2^2}{b_2} \right) (T - T_0)^2. \quad (2.55)$$

The specific heat jump becomes,

$$\frac{\Delta C}{T} = \frac{a_1^2}{b_1} + \frac{a_2^2}{b_2}. \quad (2.56)$$

We can now introduce strain-OP couplings through \mathcal{F}_{coup} , and we only consider one A_{1g} strain to keep the algebra simple.

$$\mathcal{F}_{coup} = g_1 \epsilon_{A_{1g,1}} |\Psi_1|^2 + h_1 \epsilon_{A_{1g,1}} |\Psi_2|^2 + g_5 \epsilon_{B_{2g}} (\Psi_1^* \Psi_2 + \Psi_1 \Psi_2^*), \quad (2.57)$$

where the two OPs couple to A_{1g} strain through different coefficients because they belong to different irreps. In other words, the A_{1g} strain derivatives of T_1 and T_2 can be different. However, only one coupling to $\epsilon_{B_{2g}}$ is allowed, since that term requires a product of the two OPs. Considering only the couplings to A_{1g} strain (or, by setting $g_5 = 0$) and minimizing the free energy $\mathcal{F}_{op} + \mathcal{F}_{coup}$ gives

$$\begin{aligned} |\Psi_1|^2 &= \left(\frac{a_1}{2b_1} + \frac{a_2}{2b_2} \right) (T_0 - T) - \left(\frac{g_1 - h_1}{4b_2} + \frac{g_1 + h_1}{4b_1} \right) \epsilon_{A_{1g,1}} \\ |\Psi_2|^2 &= \left(\frac{a_1}{2b_1} - \frac{a_2}{2b_2} \right) (T_0 - T) + \left(\frac{g_1 - h_1}{4b_2} - \frac{g_1 + h_1}{4b_1} \right) \epsilon_{A_{1g,1}}. \end{aligned} \quad (2.58)$$

Note that although the two components $|\Psi_1|$ and $|\Psi_2|$ condense at the same temperature at zero strain, the strain dependence of their transition temperatures are different. Generally, since A_{1g} strains do not break any of the symmetries of the point group, an A_{1g} strain is not expected to split the transition. However, in the case of an accidental degeneracy, the transition can be split even by an A_{1g} strain.

To get the jump in $A_{1g,1}$ modulus, we replace Equation 2.58 in $\mathcal{F}_{op} + \mathcal{F}_{coup}$ (with $g_5 = 0$) to get

$$\Delta c_{A_{1g,1}} = \frac{\partial^2 (\mathcal{F}_{op} + \mathcal{F}_{coup})}{\partial \epsilon_{A_{1g,1}}^2} = -\frac{(g_1 - h_1)^2}{4b_2} - \frac{(g_1 + h_1)^2}{4b_1}. \quad (2.59)$$

The B_{1g} modulus jump is zero, since there is no coupling to $\epsilon_{B_{1g}}$. The B_{2g} modulus jump arises from relative phase fluctuations between Ψ_1 and Ψ_2 , and stays the same as in [Table 2.1](#) for a chiral OP,

$$\Delta c_{B_{2g}} = \frac{g_5^2}{b_3}. \quad (2.60)$$

2.5 Ehrenfest Relations

The discontinuities in various elastic moduli can be related to the specific heat jump at the transition through the so-called Ehrenfest relations [\[24\]](#). These relations arise from general thermodynamics arguments at a second order transition, such as the continuity of first derivatives of the free energy (for example, entropy). Therefore they hold for any second order transition [\[48, 49\]](#). We show how they may be expressed for compressional and shear strains in a tetragonal system in this section.

2.5.1 Ehrenfest Relations for Compressional Strains

For the various superconducting states discussed in [Table 2.1](#), the A_{1g} moduli jumps can be related to the specific heat jump ($\Delta C/T$) through

$$\Delta c_{A_{1g},1(2)} = -\frac{\Delta C}{T} \left(\frac{dT_c}{d\epsilon_{A_{1g},1(2)}} \right)^2; \Delta c_{A_{1g},3} = -\frac{\Delta C}{T} \left| \frac{dT_c}{d\epsilon_{A_{1g},1}} \right| \left| \frac{dT_c}{d\epsilon_{A_{1g},2}} \right|. \quad (2.61)$$

This relation, however, does not require a multi-component OP. A one-component OP in D_{4h} that couples at quadratic order to strain would lead to jumps in all three A_{1g} moduli, and [Equation 2.61](#) would hold for them. In a tetragonal system, the bulk modulus B is related to the three A_{1g} moduli as (see [Appendix D](#) for a

derivation)

$$B = \frac{c_{A_{1g},1}c_{A_{1g},2} - c_{A_{1g},3}^2}{c_{A_{1g},1} + c_{A_{1g},2} - 2c_{A_{1g},3}}. \quad (2.62)$$

A hydrostatic pressure P_{hyd} induces $\epsilon_{A_{1g},1} = (\epsilon_{xx} + \epsilon_{yy}) = \frac{c_{A_{1g},2} - c_{A_{1g},3}}{c_{A_{1g},1}c_{A_{1g},2} - c_{A_{1g},3}^2}P_{hyd}$, $\epsilon_{A_{1g},2} = \epsilon_{zz} = \frac{c_{A_{1g},1} - c_{A_{1g},3}}{c_{A_{1g},1}c_{A_{1g},2} - c_{A_{1g},3}^2}P_{hyd}$, and no shear strains. Using these expressions gives the dependence of T_c on hydrostatic pressure,

$$\begin{aligned} T_c &= T_{c,0} + \frac{g_1}{a_0}\epsilon_{A_{1g},1} + \frac{g_2}{a_0}\epsilon_{A_{1g},2} \\ \implies \frac{dT_c}{dP_{hyd}} &= \frac{g_1}{a_0} \frac{c_{A_{1g},2} - c_{A_{1g},3}}{c_{A_{1g},1}c_{A_{1g},2} - c_{A_{1g},3}^2} + \frac{g_2}{a_0} \frac{c_{A_{1g},1} - c_{A_{1g},3}}{c_{A_{1g},1}c_{A_{1g},2} - c_{A_{1g},3}^2}, \end{aligned} \quad (2.63)$$

similar to how we derived [Equation 2.34](#). Using [Equations 2.61](#), [2.62](#) and [2.63](#), the discontinuity in the bulk modulus $\Delta B/B$ at T_c can be related to $\Delta C/T$ through the Ehrenfest relation

$$\frac{\Delta B}{B^2} = -\frac{\Delta C}{T} \left(\frac{dT_c}{dP_{hyd}} \right)^2. \quad (2.64)$$

The negative sign shows that the jumps in the two quantities are in opposite directions—specific heat increases discontinuously at the transition while bulk modulus decreases at the transition. It's important to highlight that although we alluded to a specific point group to derive this relation, [Equation 2.64](#) is generally true at any second order phase transition.

2.5.2 Ehrenfest Relations for Shear Strains

Unlike A_{1g} strains, shear strains (B_{1g} and B_{2g}) in a tetragonal system are expected to split the transition if the OP is a symmetry-protected multi-component order parameter [\[18\]](#). This happens because shear strains break the tetragonal symmetry of the lattice, and hence the degenerate OP components of the unstrained crystal now have different condensation energies (and temperatures). Within weak coupling, a crystal under shear strain should therefore show two specific heat jumps [\[50\]](#),

and, for a chiral OP, time-reversal symmetry breaking (TRSB) should set in at a different temperature than Meissner effect [19]. We show that the shear modulus jump can be related to $\Delta C/T$ (at zero strain) through the strain derivatives of these two transition temperatures, T_c and T_{TRSB} ,

$$\Delta c_s = -\frac{\Delta C}{T} \left| \frac{dT_1}{d\epsilon_s} \right| \left| \frac{dT_2}{d\epsilon_s} \right|, \quad (2.65)$$

where s is either B_{1g} or B_{2g} , $T_1 = T_c$, and $T_2 = T_{TRSB}$.

We start from the free energy expressions \mathcal{F}_{op} and \mathcal{F}_c , and consider the case of a chiral OP. Further, we keep only the coupling to $\epsilon_{B_{1g}}$ to simplify the subsequent algebra. Then, with the phase between Ψ_x and Ψ_y set to $\pi/2$, \mathcal{F}_{op} and \mathcal{F}_{coup} are

$$\begin{aligned} \mathcal{F}_{op} &= a_0(T - T_{c,0})(\Psi_x^2 + \Psi_y^2) + \frac{b_1}{2}(\Psi_x^2 + \Psi_y^2)^2 + \frac{b_2}{2}(\Psi_x^2 - \Psi_y^2)^2 \\ \mathcal{F}_{coup} &= g_4 \epsilon_{B_{1g}}(\Psi_x^2 - \Psi_y^2), \end{aligned} \quad (2.66)$$

where $T_{c,0}$ is the unstrained T_c . Clearly, $\epsilon_{B_{1g}}$ breaks the $\eta_x \leftrightarrow \eta_y$ symmetry of the quadratic terms in free energy, thereby making the two components condense at different temperatures.

We assume $g_4 \epsilon_{B_{1g}} > 0$, which favors Ψ_y condensing before Ψ_x . The higher transition temperature $T_1 = T_c$ is determined by when the coefficient of Ψ_y^2 goes to zero (with $\Psi_x = 0$), that is, $a_0(T_1 - T_{c,0}) - g_4 \epsilon_{B_{1g}} = 0$. This gives

$$T_1 = T_{c,0} + \frac{g_4}{a_0} \epsilon_{B_{1g}}. \quad (2.67)$$

Then, the Ψ_y that minimizes $(\mathcal{F}_{op} + \mathcal{F}_{coup})$ is

$$\Psi_y^2 = \frac{a_0(T_{c,0} - T) + g_4 \epsilon_{B_{1g}}}{b_1 + b_2} = \frac{a_0(T_1 - T)}{b_1 + b_2}. \quad (2.68)$$

Further, the specific heat jump at this transition, calculated by using the above Ψ_y^2 , is

$$\left(\frac{\Delta C}{T} \right)_1 = \frac{a_0^2}{b_1 + b_2}. \quad (2.69)$$

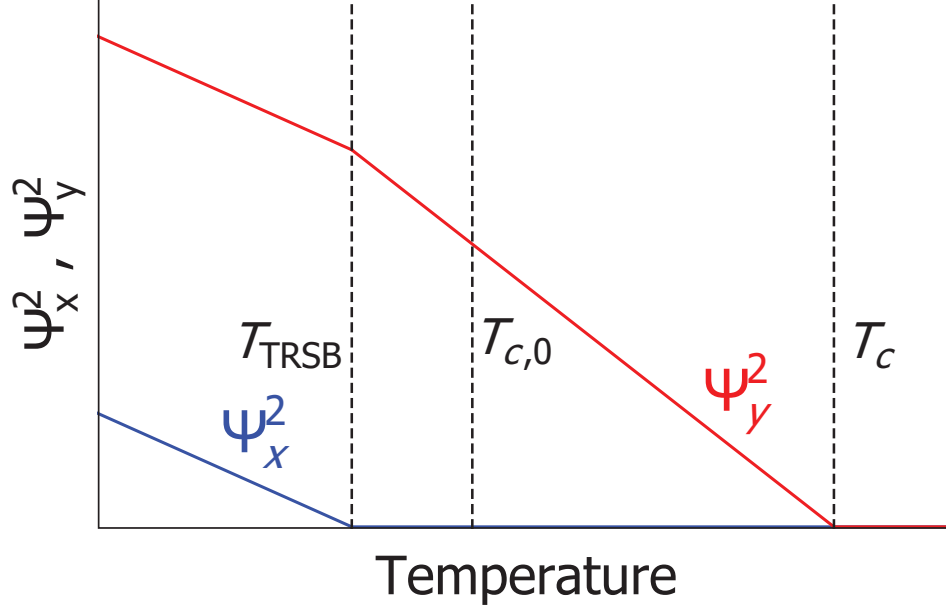


Figure 2.6: **Strain-induced splitting of the transition temperature $T_{c,0}$.** Under B_{1g} shear strain, the two components Ψ_y and Ψ_x condense at different temperatures, T_c and T_{TRSB} , respectively. Above T_c , both the components are zero, and the sample is not superconducting. At T_c , the Meissner effect sets in, and finally, below T_{TRSB} , the system becomes a chiral superconductor. Qualitatively similar behavior is expected for B_{2g} shear strain.

Below T_1 , the system undergoes TRSB transition when Ψ_x condenses. Naively, one might expect this to occur at $T_{c,0} - g_4 \epsilon_{B_{1g}} / a_0$, found by setting the quadratic coefficient of Ψ_x to zero. The condensation of Ψ_y prevents this, however, through the $\Psi_x^2 \Psi_y^2$ terms in \mathcal{F}_{op} . If the coefficient of this term is zero ($b_1 - b_2 = 0$), then there is no competition between Ψ_x and Ψ_y , in which case the second transition does occur at $T_{TRSB} = T_{c,0} - g_4 \epsilon_{B_{1g}} / a_0$.

For the more general case, when $b_1 \neq b_2$, $T_2 = T_{TRSB}$ is calculated by setting the coefficient of Ψ_x^2 to zero in the total free energy, with Ψ_y given by [Equation 2.68](#). This gives

$$\begin{aligned}
 a_0(T_2 - T_{c,0}) + (b_1 - b_2)\Psi_y^2 + g_4 \epsilon_{B_{1g}} &= 0 \\
 \implies T_2 = T_{c,0} - \frac{g_4}{a_0} \left(\frac{b_1}{b_2} \right) \epsilon_{B_{1g}}.
 \end{aligned} \tag{2.70}$$

Clearly, $T_2 = T_{c,0} - g_4 \epsilon_{B_{1g}} / a_0$ for $b_1 = b_2$. The specific heat jump at this transition can be calculated by subtracting the jump in first transition $(\Delta C/T)_1$ from the total jump $\Delta C/T$ in the unstrained case,

$$\left(\frac{\Delta C}{T}\right)_2 = \frac{a_0^2}{b_1} - \frac{a_0^2}{b_1 + b_2} = \frac{a_0^2}{(b_1 + b_2)} \frac{b_2}{b_1}. \quad (2.71)$$

The ratio of the two specific heat jumps can then be related by

$$\left(\frac{\Delta C}{T}\right)_1 \bigg/ \left(\frac{\Delta C}{T}\right)_2 = \frac{b_1}{b_2} = \left| \frac{dT_2}{d\epsilon_{B_{1g}}} \right| \bigg/ \left| \frac{dT_1}{d\epsilon_{B_{1g}}} \right|. \quad (2.72)$$

Below T_2 , the order parameter (Ψ_x, Ψ_y) can be calculated by minimizing $(\mathcal{F}_{op} + \mathcal{F}_{coup})$ with respect to both Ψ_x and Ψ_y . This gives

$$\begin{aligned} \Psi_x^2 &= \frac{a_0(T_2 - T)}{2b_1} \\ \Psi_y^2 &= \frac{a_0}{b_1 + b_2} \left((T_1 - T) - \frac{b_1 - b_2}{2b_1} (T_2 - T) \right) \end{aligned} \quad (2.73)$$

It is interesting to note that the condensation of Ψ_x at T_2 decreases the rate at which Ψ_y was growing below T_1 , demonstrating the competition between the two components (see [Figure 2.6](#)).

The jump in the B_{1g} shear modulus for chiral OP can now be expressed as,

$$\Delta c_{B_{1g}} = \frac{g_4^2}{b_2} = \frac{a_0^2}{b_1} \cdot \frac{g_4}{a_0} \cdot \frac{g_4}{a_0} \left(\frac{b_1}{b_2} \right) = -\frac{\Delta C}{T} \left| \frac{dT_1}{d\epsilon_{B_{1g}}} \right| \left| \frac{dT_2}{d\epsilon_{B_{1g}}} \right|. \quad (2.74)$$

A similar derivation can be carried out for B_{2g} strain. This can be performed simply by re-defining the order parameter variables as $\tilde{\Psi}_x = (\Psi_x + \Psi_y)/\sqrt{2}$ and $\tilde{\Psi}_y = (\Psi_x - \Psi_y)/\sqrt{2}$ and carrying out the same calculation as the B_{1g} case.

We finally mention two specific assumptions that go into the above derivation. First, we assume that the spontaneous strains generated in the crystal below the first transition are small, such that the quartic coefficients in Landau theory are not

strongly renormalized below T_1 . A second assumption is that the TRS-breaking transition under finite strain is a second order phase transition. The extent to which these assumptions hold depends on the specifics of the particular system, which we will not delve into here.

2.6 Fluctuations and Ginzburg Criterion

We end this chapter by mentioning why mean-field theories, of the kind we have been considering till now, may fail to describe the behavior of observables at certain transitions. The short answer is the presence of fluctuations in the system, which are extremely important for phase transitions but are ignored in a mean-field calculation. The fluctuations we considered before in this chapter are only small corrections to mean-field, whereas in general, they can be large enough to completely mask mean-field behavior. In fact, it can be shown that corrections to the free energy due to fluctuations become more and more important as the correlation length diverges. Within mean-field, the correlation length ξ diverges as $\xi_0/\sqrt{1 - T/T_0}$, where T_0 is the transition temperature. Since the correlation length always diverges at a transition, this would imply that fluctuations always destroy mean-field behavior.

From experimental evidence, we know that is not the case. Most superconductors show a specific heat discontinuity of the sort predicted by mean-field, whereas a superfluid transition usually shows a diverging behavior in specific heat (and not a step discontinuity). The difference lies in the numbers. Superconductors have Cooper pairs, which have correlation lengths $\approx 1000\text{\AA}$ because the electrons in the pair repel each other due to Coulomb forces. Superfluids, on the other hand,

have correlation lengths of the order of thermal wavelength $\lambda(T) = h/\sqrt{2\pi mk_B T}$. Putting in the mass m for helium, and $T = 2$ K, we get λ , and hence the correlation length to be $\lesssim 10\text{\AA}$. This is in fact comparable to atomic spacings, and hence it is probably not surprising that mean-field does not work for the superfluid transition. Recall that we averaged over the microscopic length scales and only considered spatial fluctuations over mesoscopic length scales much larger than atomic spacings to motivate Landau’s mean-field free energy.

From the above discussion, it appears that mean-field works as long as correlation lengths are large enough. To know what is “large enough”, we need to actually calculate the specific heat at the transition by including the effect of fluctuations. We only quote the result here from Ref. [28], which says that fluctuations are important when

$$\xi_0^{-d} t^{\frac{4-d}{2}} \gg \Delta C_{mf} \implies |t| \ll t_G \simeq (\xi_0^d \cdot \Delta C_{mf})^{\frac{2}{d-4}}. \quad (2.75)$$

Here, ΔC_{mf} is the mean-field specific heat discontinuity and d is the dimensionality of the system. The above relation is called the Ginzburg criterion, with t_G the reduced Ginzburg temperature. Equation 2.75 shows that fluctuation effects can always be measured if our experiment had enough temperature resolution, that is, we could measure arbitrarily close to T_0 . Note that in $d = 3$ (which is the case of most interest to us), $t_G \propto \xi_0^{-6}$, which implies that for a large ξ_0 , one has to get extremely close to T_0 to see fluctuation effects. This explains why superconducting transitions, with their large correlation lengths, are mostly mean-field like. In real samples, even if one could measure arbitrarily close to T_0 , disorder or system size always provides a cutoff which may obscure the fluctuation effects for certain systems.

We finally remark on the dimensionality d in Equation 2.75. For $d > 4$, the

effect of fluctuations can always be ignored and transitions will show mean-field behavior. This is known as the upper critical dimension. For $d \leq 2$, fluctuations generally destroy long-range order. This is related to the Mermin-Wagner theorem, which, in fact, was developed at Cornell [51]. At $d = 3$, which is most of the crystal systems surrounding us, fluctuations can modify the mean-field results but do not destroy long-range order—giving rise to a rich variety of critical phenomena.

CHAPTER 3

RESONANT ULTRASOUND SPECTROSCOPY

The main experimental technique used for the studies reported in this thesis is resonant ultrasound spectroscopy (RUS). RUS provides a way to measure the natural mechanical resonances of a solid. Similar to how a stretched string resonates at different frequencies that are determined by the tension and the mass per unit length of the string, a solid material has resonance frequencies defined by the elastic constants (or moduli) of the solid, its shape and its density. A three dimensional solid generally has multiple independent elastic constants determined by its symmetry [52], for example, an isotropic material (like steel) has two independent elastic moduli whereas a tetragonal single crystal (like Sr_2RuO_4) has six moduli. Using RUS, all these independent moduli can be measured in a single measurement by measuring sufficiently many (about the first 50) resonances—this makes RUS a particularly powerful technique. In this chapter, we describe the details of our experimental technique, which forms the basis for how all the data for the next two chapters were acquired and analyzed.

3.1 Experimental Setup

In an RUS experiment, a sample is placed on its corners between two piezoelectric transducers to provide nearly-free elastic boundary conditions [11, 12]. We use two compressional-mode lithium niobate transducers mounted in a mixture of Loctite Stycast 2850FT and tungsten powder to damp the transducer resonances. The bottom transducer is fixed to the apparatus while the top transducer is mounted on a freely-pivoting arm to allow for weak mechanical contact between the transducers and the sample. We also place two small wear plates (made of alumina) on the

two transducers with an indent in them to better hold the sample, and prevent the wearing out of LiNbO_3 over time. Our apparatus (see [Figure 3.1](#)) is made out of PLAVIS Polyimide, a commercially available material which is easy to machine, is acoustically unresponsive and has relatively good dimensional stability for a plastic. The second property is particularly important for RUS experiments, since we need the transducer vibrations that enter the apparatus instead of the sample to die out quickly, and not reach the second transducer. This removes cross-talk between the transducers, reducing the background signal and prevents any natural resonances of the apparatus itself from showing up in the data. This material is also electrically insulating and shows extremely low outgassing, which becomes important for low temperature experiments in vacuum spaces.

To measure the resonances, one transducer is driven at a fixed frequency and the response generated at the other transducer is detected using a custom-built charge amplifier (see [Figure 3.2](#) for picture of the electronics). More details of the measurement electronics and the custom amplifier can be found in Balakirev et al. [53]. Using digital lock-in, we detect both the in-phase (X) and out-of-phase (Y) response at each frequency. An RUS sample is typically of the order 1 mm^3 , and given sound velocities in solids are $\sim 1000 \text{ m/s}$, the lowest resonance frequencies are $\lesssim 1 \text{ MHz}$. We sweep the drive frequency in the range of 0.4 to 5 MHz to measure the lowest resonances of the sample. When the excitation frequency matches a mechanical resonance of the sample, maximum transmission between the drive and receive transducers is achieved and shows up as a peak in the recorded response (see [Figure 3.3](#)).

Calculating the natural resonances for a sample of given dimensions and density along with known elastic moduli is straightforward. The natural resonances are

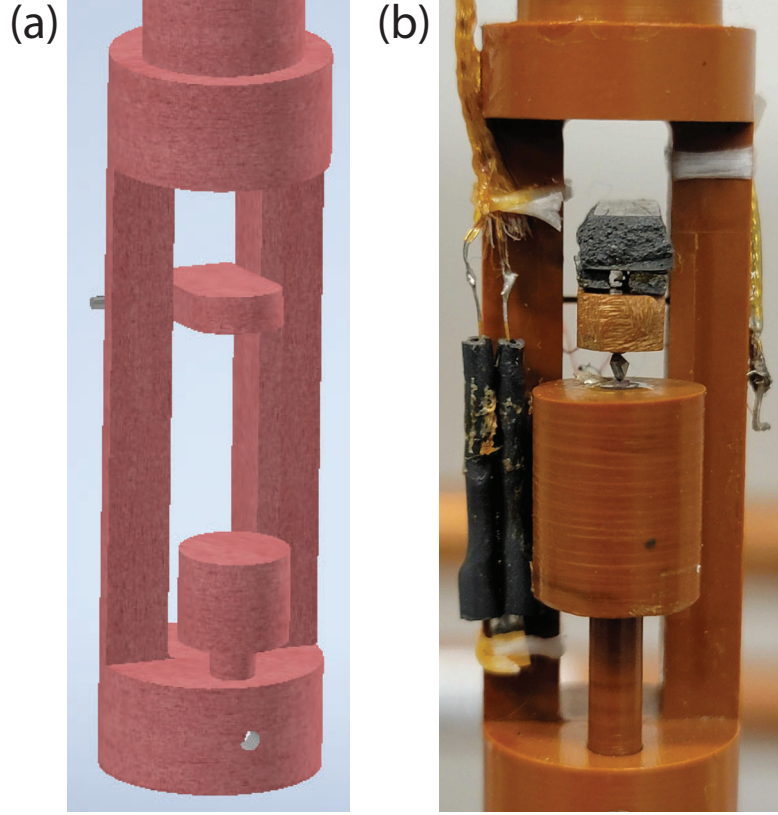


Figure 3.1: **Resonant ultrasound spectroscopy (RUS) apparatus.** (a) Schematic of the RUS apparatus, where the sample (not shown) is held between the freely pivoting arm and the bottom plug. The height of the bottom plug can be continuously changed. (b) Photograph of the machined apparatus, with transducers and a sample in between. The black Styrofoam block on the top arm provides some extra weight which improves the experimental signal-to-noise while measuring resonances.

the solutions ω of the elastic wave equation [54]

$$\rho\omega^2 u_i + c_{ijkl} \frac{\partial^2 u_k}{\partial x_l \partial x_j} = 0, \quad (3.1)$$

where ρ is the density, c_{ijkl} is the elastic tensor and x_i are spatial coordinates. Summation over repeated indices is implied. This can be written as an eigenvalue problem by choosing appropriate basis functions to expand the displacements u_i , as explained in Ref. [54]. Then the problem reduces to finding the eigenvalues, which are the resonance frequencies. To convert from resonance frequencies to the moduli, however, we need to solve the inverse problem, which is much harder. For

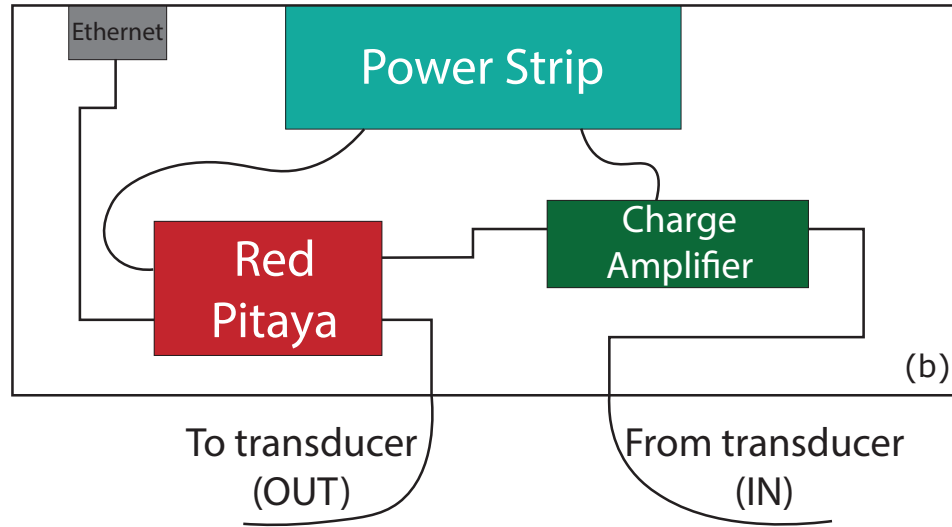
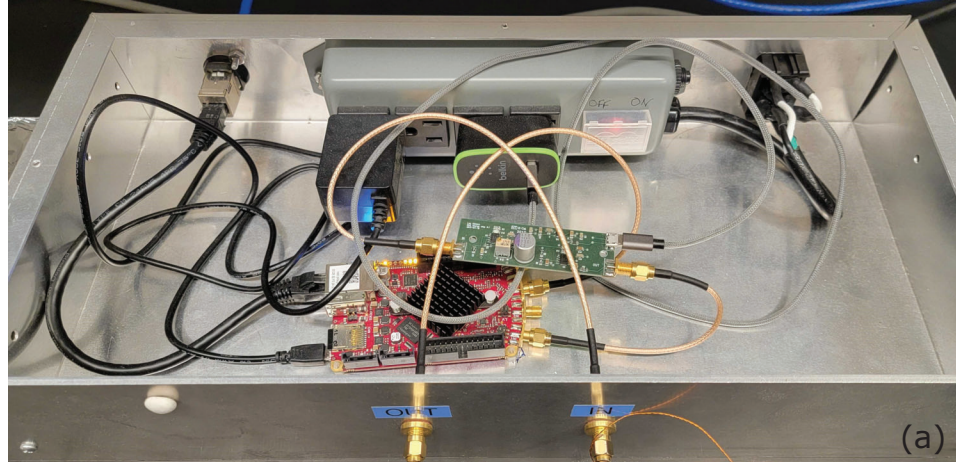


Figure 3.2: **RUS measurement electronics.** (a) The various electronic components required for a RUS measurement assembled within an instrument box. The red board is a commercially available FPGA, Red Pitaya, that outputs experimental frequencies in the range $0.4 - 5$ MHz and performs lock-in measurement at these frequencies. The charge amplifier used on the return signal (“IN”) is the green board, the output of which is the input to Red Pitaya. We communicate to the Pitaya through ethernet connection. (b) Schematic showing the connections between components of (a).

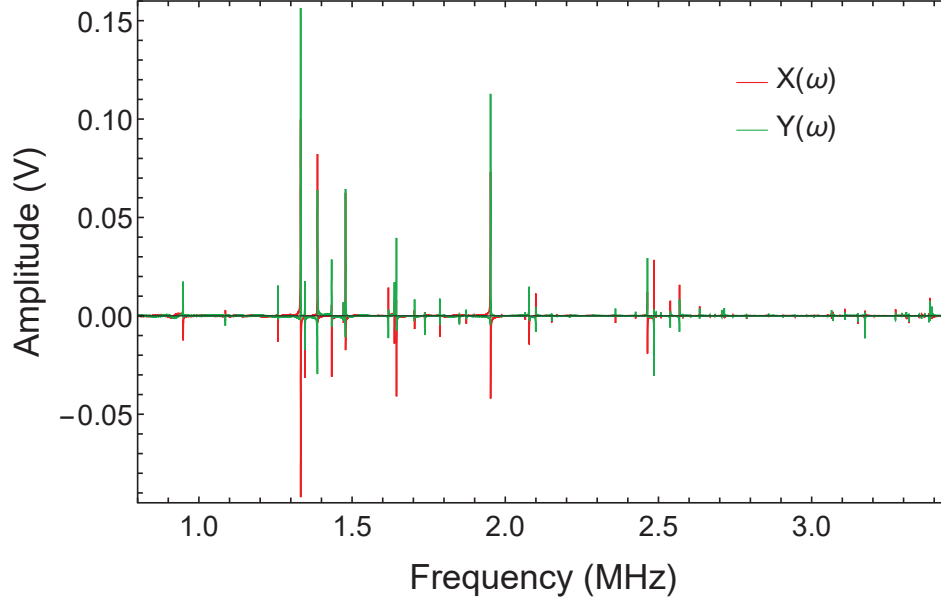


Figure 3.3: **RUS frequency sweep.** Measured RUS spectra of a single crystal sample of Sr_2RuO_4 at room temperature, showing the in-phase ($X(\omega)$) and out-of-phase ($Y(\omega)$) responses. The peaks in the spectrum correspond to natural resonances of the sample.

this reason, we need to shape RUS samples into a rectangular cuboid such that the dimensions are well-known. Figure 3.4 shows a few representative resonances for a rectangular cuboid of Sr_2RuO_4 . To inverse-solve the elastic wave equation to calculate all the moduli, we use a genetic algorithm-based program, the details of which can be found in [12]. The program starts with multiple sets of elastic constants within some user-defined range for the given sample dimensions and density and creates new sets by combining between the original sets. For each original (called “parent”) and new (called “child”) sets of elastic constants, the frequencies are calculated and the one that matches closer to the experimental data is kept. In the next generation, these sets are used as the parent sets and the same procedure is repeated till the difference (residual of the fit) between predicted and experimental frequencies is below some specified tolerance. In this way, we fit the measured resonances to get the entire elastic tensor.

A useful feature of this code is that it works even if a few resonances are “missing”. Experimentally, some resonances are harder to measure because of how the sample is mounted or what strain pattern the resonance excites in the sample. This leads to missing resonances in the spectrum and can prevent the fit from converging since it tries to match predicted and measured resonances sequentially and one-to-one. To incorporate these missing resonances, the code computes the residual by placing a missing resonance between each pair of resonances and keeps the missed resonance at a place that minimizes the residual. Computationally, this works well for 2 - 3 missing resonances but not with much more missing resonances, as then there are way too many combinations to take care of. For this reason, a suitable strategy is to start with a small set of resonances (~ 15) and try a fit with 2 - 3 missing resonances. It is important to scan slowly near these predicted missing resonances to see if they can be measured. If they do show up on a slower scan, that shows the fit is converging towards the right region of elastic constants. Once that works, it is better to add more experimental resonances and repeat the fit in order to get stronger bounds on the moduli. We define the root-mean-square error of the fit as

$$\text{Error} = \frac{1}{\sqrt{N-1}} \sqrt{\sum_{i=1}^N \frac{|f_i(\text{exp}) - f_i(\text{calc})|^2}{f_i^2(\text{calc})}} \times 100\%, \quad (3.2)$$

where N is the number of measured resonances. The missing resonances are ignored in this error calculation.

Once we have a good fit (error $\leq 1\%$) for all the measured frequencies giving us reasonable elastic moduli for the sample, it is important to know the compositions of the resonances, that is, which resonances are primarily compression and which are primarily shear. Mathematically, this is defined in terms of the α coefficients of the resonances, discussed in details in [Section 3.5](#). These parameters are known

from using the so-called RPR (rectangular parallelepiped resonator) code, details of which maybe found in Ref. [53]. This program finds a global minimum in the space of elastic moduli using gradient minimization, which is a useful check on the moduli obtained from the genetic algorithm. Further, this code gives us the α coefficients for all the resonances. We highlight that it is always advisable to first ensure there are no missing resonances using the genetic algorithm before using the RPR code. Even a single missing resonance can lead to the RPR reaching a completely different global minimum, yielding a wrong set of elastic constants.

3.2 Sample Preparation

The calculation of elastic constants reliably from the measured resonance frequencies of a single crystal sample requires the physical axes of the sample to be aligned almost perfectly along its crystallographic axes. RUS thus requires relatively large ($\sim 1 \text{ mm}^3$) single crystals of a material to start with, which has to be shaped into a cuboid aligned along crystal axes. The first step is to find a relatively flat face that is close to a crystallographic plane (say, (001)) and then to align it with the [001] crystal direction using Laue diffraction. If the starting crystal has no flat faces, it is important to dice it with a wire saw to create flat faces. Once one face is aligned, it is hand polished down with diamond lapping paper to create a smooth flat face. Then that flat face is turned over and the opposite face is polished down to create a pair of parallel faces that are aligned along a crystallographic direction. This procedure is then repeated for the other two pairs of faces, eventually leading to a single crystal sample with six polished faces.

The grit size of the lapping paper chosen for polishing depends on a number

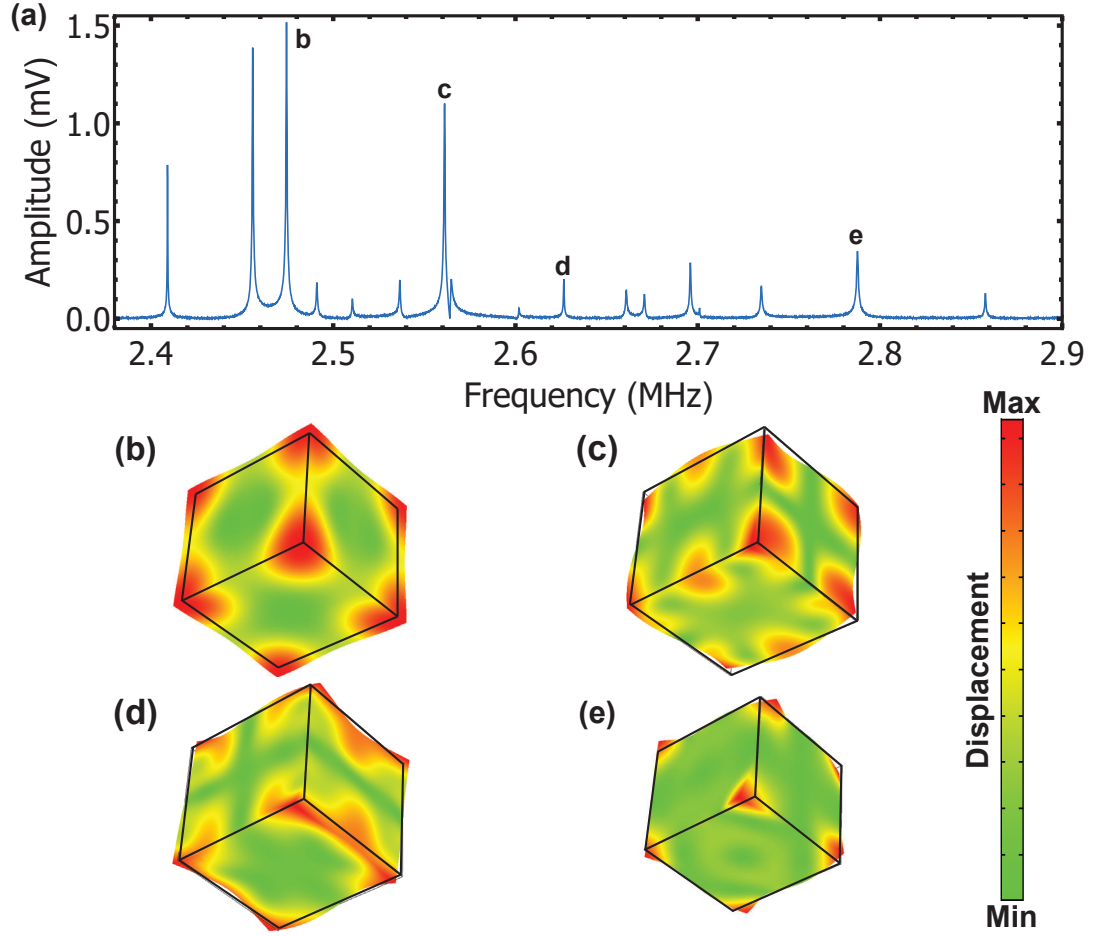


Figure 3.4: **Schematics of resonances.** (a) A subset of the scan shown in [Figure 3.3](#), where the amplitude $|Z(\omega)|$ is plotted. See [Equation 3.10](#) for definition of $|Z(\omega)|$. (b)-(e) show schematically the standing wave patterns for the resonances marked in (a). These were simulated in COMSOL using the elastic constants, density and dimensions of the sample.

of factors, including how brittle the sample is, how big the inclusions are and how much we want to polish down on a face. For highly brittle samples, one has to polish down extremely slowly in order to prevent the sample from breaking. Typically, it is sufficient to finish polishing on a $3\text{ }\mu\text{m}$ grit paper, since surface roughness does not have a big impact on the measured resonances, which primarily depend on the bulk composition of the sample. Thus, having holes or inclusions, such as metallic Ru in Sr_2RuO_4 or Ir in CeIrIn_5 , in the bulk of the material is particularly

undesirable. Such inclusions can usually be removed by polishing if they are visible on the sample surfaces. Polishing down a RUS sample is quite time consuming but is extremely important to get accurate elastic constants.

While preparing the sample, it is crucial to ensure that the final shape is far from becoming a cube, that is, its three dimensions are at least 5% different from each other. Having a final shape close to a perfect cube can cause the resonances to overlap, which makes it difficult to be sure of the compositions of the resonances. It is also important to ensure that the sample is not too thin along certain directions compared to other directions, that is, it does not become rod-like or plate-like. In such samples, the low frequencies will be dominated by bending-like modes and compressional modes along the thin direction will be difficult to excite. In that case, extracting the compressional modulus along the thin direction may become impossible from the sample. It is also generally useful to try a fit to the resonance spectrum with a relatively big sample first, and if the fit does not work well, that indicates the presence of inclusions or holes in the sample that need to be removed by polishing down. We typically stop polishing once a good fit for the measured spectrum is obtained, with reasonable elastic moduli values.

3.3 RUS at Low Temperatures

Resonant ultrasound samples, as mentioned above, are typically large ($\sim 1 \text{ mm}^3$) and are held in weak mechanical contact between transducers to ensure almost-free boundary conditions. Hence the thermal contact between the sample and its surroundings is weak. This means we always require exchange gas (typically helium) in the sample space to ensure uniform cooling of the sample. Otherwise,

when cooling down, the corners of the sample where it is held probably gets cold first and the cold front slowly propagates towards the center of the sample. This leads to broadening of the sharp discontinuities in elastic moduli expected, for example, at a superconducting transition. One of the materials studied in this thesis, Sr_2RuO_4 , has a superconducting $T_c = 1.4$ K, much lower than the boiling point of liquid helium. To cool down a Sr_2RuO_4 sample uniformly through its T_c , we thus needed to design a novel RUS setup.

3.3.1 Low Temperature Setup

In principle, to cool below 4.2 K, liquid helium could be introduced into the sample space and the space pumped directly. As RUS is extremely sensitive to vibrations, however, this introduces artifacts into the data and does not provide a particularly homogeneous thermal environment. To solve these problems, the RUS probe (shown in [Figure 3.1\(b\)](#)) was sealed inside a copper can with a small amount of exchange gas, which provided good thermal equilibration between the sample, thermometer, and the rest of the apparatus. This inner copper can was separated by a weak thermal link (thin-walled stainless steel) from an outer brass vacuum can, which provided isolation between the walls of the sample can and the bath. The temperature was regulated by pumping on the external helium bath, and the vacuum isolation of the sample chamber from the bath then allowed the sample space to cool very slowly once the bath was pumped to base temperature. We also used braided stainless steel coaxial cables to carry electronic signals to and from the transducers to reduce heat conduction from the top of the probe which is at room temperature (300 K). A heater made of manganin wire was attached to a copper thermal post that was affixed to the copper block on which the RUS

probe was attached, to have the option of heating the sample space if needed. The lowest temperature reached was approximately 1.25 K, as read by a CX-1030 thermometer (Lake Shore) affixed to the RUS probe. We found that the transition temperature and transition width observed by RUS are in extremely good agreement with those determined from independent susceptibility measurements, which suggests that our Sr_2RuO_4 sample was thermalized uniformly during the experiment.

3.3.2 Thermal Homogeneity Considerations

While the presence of exchange gas in the sample space ensures that all sample surfaces are at a uniform temperature (which is the same temperature read by the thermometer), we rely on good thermal conduction for the sample interior to equilibrate with the surfaces. Here we present an example calculation for Sr_2RuO_4 to show how to check for thermal homogeneity theoretically.

Sr_2RuO_4 in its normal state is a good metal which conducts heat well, and thus the entire volume of the sample should be in thermal equilibrium with surroundings. Below T_c , however, temperature gradients may be enhanced due to the loss of heat carriers, as Cooper pairs do not carry heat. Nominally, we do not expect this to be an issue since Sr_2RuO_4 is a nodal superconductor [4], which means that there are always normal quasiparticles that carry heat, and the lowest temperature we reach is $\sim 0.8T_c$, which means that the superconducting gap has only partially opened.

To confirm that the thermal gradients in our sample are always small, we

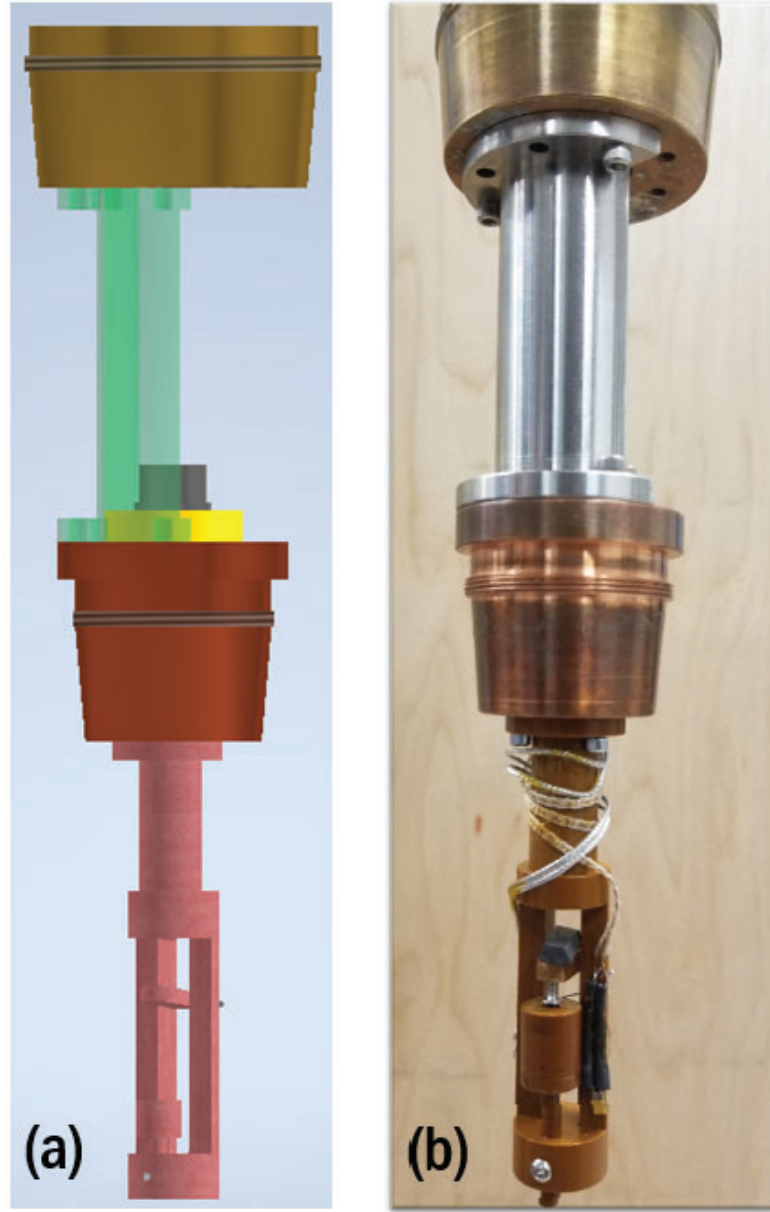


Figure 3.5: **Low temperature RUS setup.** (a) False color schematic of custom-built low temperature RUS experimental setup, consisting of an outer brass chamber and an inner copper chamber. These two are connected through steel half-tubes, one of which is shown in transparent green. An indium seal is formed between the copper chamber and the stainless steel (SS) ring shown in yellow. Gas flow to the inner chamber occurs through a SS tube that is welded to the grey piece which sits inside the indium seal. Gas flow to the outer chamber occurs through a SS tube directly soldered to the brass part. The RUS sample holder, shown in light red, is attached to the copper part. The inner and outer chambers are sealed with a copper can and a brass can, respectively, which are not shown here. (b) Photograph of the setup with measurement wiring and thermometer.

perform a simple calculation starting from the 3-dimensional heat flow equation,

$$\frac{\partial T}{\partial t} = \alpha \nabla^2 T, \quad (3.3)$$

where $T(x, y, z, t)$ denotes the temperature profile within the sample, and α is the thermal diffusivity. For tetragonal Sr_2RuO_4 , this takes the form

$$\frac{\partial T}{\partial t} = \alpha_a \left(\frac{\partial^2 T}{\partial x^2} + \frac{\partial^2 T}{\partial y^2} \right) + \alpha_c \frac{\partial^2 T}{\partial z^2}. \quad (3.4)$$

The thermal diffusivity α is related to the thermal conductivity κ as $\alpha = \kappa/\rho C$, where ρ is the density of Sr_2RuO_4 and C is the specific heat. For Sr_2RuO_4 below T_c , we have $C = 87 \text{ mJmol}^{-1}\text{K}^{-1}$, $\kappa_a = 13.05 \text{ Wm}^{-1}\text{K}^{-1}$ and $\kappa_c = 0.07 \text{ Wm}^{-1}\text{K}^{-1}$, giving $\alpha_a = 8.61 \times 10^{-3} \text{ m}^2/\text{s}$ and $\alpha_c = 0.05 \times 10^{-3} \text{ m}^2/\text{s}$.

We first consider the effects of a step-change in the exchange-gas temperature as a worst-case scenario. With the boundary condition that all sample surfaces are at T_0 , the solution of [Equation 3.4](#) is

$$\begin{aligned} T(x, y, z, t) = T_0 + \sum_{m,n,p=1}^{\infty} A_{mnp} \sin\left(\frac{m\pi x}{L_x}\right) \sin\left(\frac{n\pi y}{L_y}\right) \sin\left(\frac{p\pi z}{L_z}\right) \\ \cdot \exp\left(-\pi^2 \left(\frac{\alpha_a m^2}{L_x^2} + \frac{\alpha_a n^2}{L_y^2} + \frac{\alpha_c p^2}{L_z^2} \right) t\right), \end{aligned} \quad (3.5)$$

where m, n, p are integers, L_x, L_y, L_z are the sample dimensions, and the coefficients A_{mnp} depend on the initial temperature profile $T(x, y, z, t=0)$ within the sample. Thus, temperature variations from T_0 within the sample die out exponentially fast and, in the $t \rightarrow \infty$ limit, $T(x, y, z) \rightarrow T_0$. In particular, the slowest equilibration occurs when $A_{111} \neq 0$ and all other $A_{mnp} = 0$, since higher harmonic components have a faster exponential decay. In this case, [Equation 3.5](#) simplifies to

$$T(x, y, z, t) = T_0 + A_{111} \sin\left(\frac{\pi x}{L_x}\right) \sin\left(\frac{\pi y}{L_y}\right) \sin\left(\frac{\pi z}{L_z}\right) \cdot \exp\left(-\pi^2 \left(\frac{\alpha_a}{L_x^2} + \frac{\alpha_a}{L_y^2} + \frac{\alpha_c}{L_z^2} \right) t\right). \quad (3.6)$$

The temperature in the middle of the sample ($T_{mid}(t) = T(L_x/2, L_y/2, L_z/2, t)$) differs most from T_0 at $t = 0$, hence we can just look at T_{mid} to get an upper bound on how long it takes for the entire sample to come to T_0 .

$$T_{mid}(t) - T_0 = \Delta T \exp \left(-\pi^2 \left(\frac{\alpha_a}{L_x^2} + \frac{\alpha_a}{L_y^2} + \frac{\alpha_c}{L_z^2} \right) t \right) = \Delta T \exp \left(-\frac{t}{14 \mu s} \right), \quad (3.7)$$

where we have used the dimensions of the sample ($1.50\text{mm} \times 1.60\text{mm} \times 1.44\text{mm}$), and we have used the worst-case diffusivity taken below T_c from the thermal conductivity data reported in Ref. [55] and the specific heat measured on the same rod our sample came from. Equation 3.7 shows that if a temperature difference ΔT appears within the sample, it reduces by a factor of 1000 in less than 10^{-4} s. For comparison, we cool the sample at ≈ 0.3 mK/s, and acquire a data point roughly ever 10 mK. Thus the equilibration time is much faster than time scale over which we do our measurements.

Another consideration is the total temperature offset in the center of the sample as we sweep the temperature, which is not captured by Equation 3.7. The steady-state solution of Equation 3.4 for a constant cooling rate results in a parabolic temperature profile inside the sample. The steady state profile T_{eq} is given by,

$$T_{eq}(x, y, z) = T_0 + 64 \frac{x(L_x - x)y(L_y - y)z(L_z - z)}{L_x^2 L_y^2 L_z^2} \delta T \quad (3.8)$$

Clearly, $T_{eq} = T_0$ at the sample surfaces, and the middle of sample is at $T_0 + \delta T$. The offset δT can be calculated by evaluating Equation 3.3 at $(x = L_x/2, y = L_y/2, z = L_z/2)$ and using the cooling rate ($\partial T/\partial t = 0.3$ mK/s),

$$\delta T = \frac{\partial T/\partial t}{8 \left(\frac{\alpha_a}{L_x^2} + \frac{\alpha_a}{L_y^2} + \frac{\alpha_c}{L_z^2} \right)} \approx 6 \text{ nK}. \quad (3.9)$$

Immediately below T_c , the heat capacity increases by approximately 50%. Over our full temperature range, the thermal conductivity κ_a drops by about 10% [55].

The thermal diffusivity therefore drops by $\approx 50\%$ below T_c . Even with this relatively large change in diffusivity, our results above demonstrate that the sample is very homogeneous in temperature during the course of the RUS experiment—both above and below T_c .

3.4 Temperature Evolution of Resonances

To study the behavior of elastic moduli near a phase transition, we need to measure how the different resonance frequencies change with temperature. As explained above, measuring the first ~ 50 resonances is generally enough to get the entire elastic tensor. However, measuring the full resonance spectrum at each temperature is time-consuming and as we show in a later section, not necessary to get the temperature evolution of all the moduli. In fact, following a small number of resonances, usually 3 times the number of independent elastic moduli, is sufficient to extract the temperature dependence of the moduli. We use either of two methods to follow the resonances as we sweep temperature in a continuous fashion—a standard lock-in technique that requires fitting a Lorentzian or a phase-locked loop (PLL).

3.4.1 Fitting Lorentzian

To follow the positions of multiple resonances with temperature, we use the same lock-in technique that we use to scan the spectrum but focus on a few resonances. At each temperature, we scan in a small frequency range around each of the resonance frequencies we want to track. Each resonance can be modeled as the response

$Z(\omega)$ of a damped harmonic oscillator driven at frequency ω (see [Figure 3.6](#)),

$$Z(\omega) = X(\omega) + iY(\omega) = \frac{Ae^{i\phi}}{(\omega - \omega_0) + i\Gamma/2}, \quad (3.10)$$

which describes a Lorentzian lineshape. X and Y are the real and imaginary parts of the response, and A , Γ , and ϕ are the amplitude, linewidth, and phase, respectively. The real and imaginary parts of the response form a circle in the complex plane (shown in [Figure 3.7](#)). Knowing the resonance frequency ω_0 and linewidth Γ at one temperature, the response is measured at a set of frequencies that sample data points evenly around the circle at the next temperature. Then an efficient center-finding algorithm is used to precisely determine ω_0 and Γ at the new temperature. Since Lorentzian line shapes have so-called long tails, fitting the circle provides a better way to determine these parameters in a finite time compared to fitting a Lorentzian to recorded $|Z(\omega)|$ directly (see Ref. [\[11\]](#) for details of the fitting procedure). Note that Γ defined in this fashion is the full width of the resonance at $1/\sqrt{2}$ of the maximum amplitude.

In certain scenarios, such as when a frequency has a strong temperature dependence, this procedure can fail to track the frequency as the temperature is swept. This happens when the frequency moves by a large amount between consecutive temperatures such that it goes out of the scan range. While scanning uniformly on the circle, the scan range is fixed by the Γ and thus we cannot increase the range manually to ensure the resonance is tracked. One solution is to sweep the temperature slower so that the resonance does not get out of the narrow scan range as temperature changes. However to maintain reasonable sweeping rates, we scan uniformly in frequency in a user-defined range around a resonance, such as $\omega_0 - n\Gamma$ to $\omega_0 + n\Gamma$, where n (typically 10) can be chosen appropriately to ensure the resonance stays in the scan range. Although this method gives slightly noisier data, it allows tracking multiple resonances reliably over larger temperature ranges.

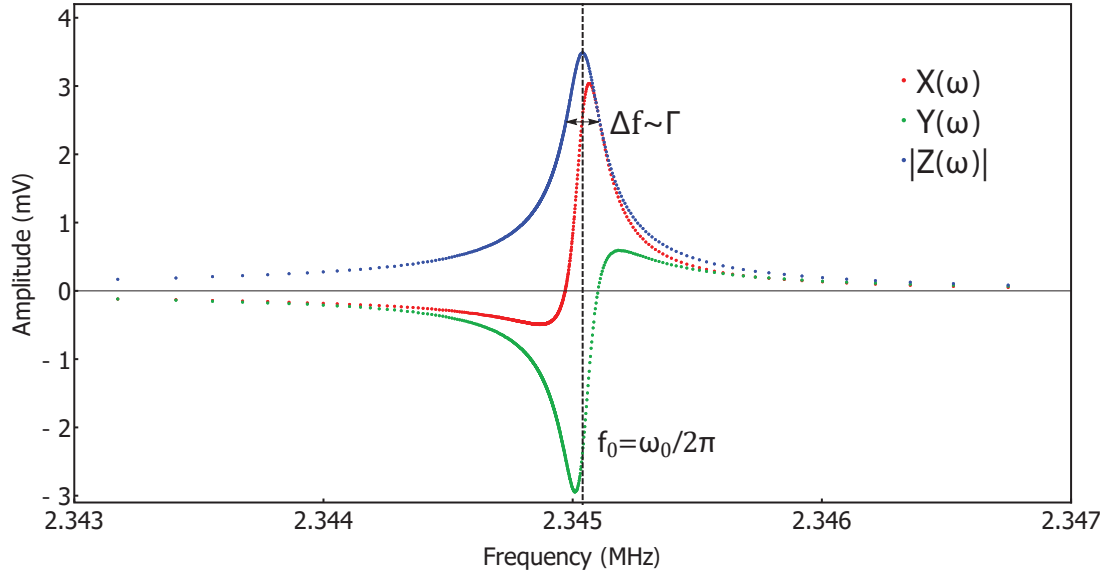


Figure 3.6: **Measured signal at a resonance.** The recorded signal via lock-in techniques at a particular resonance, showing both the in-phase ($X(\omega)$) and out-of-phase ($Y(\omega)$) signals. Note the higher density of points near the center of the resonance compared to the tails. This produces data that uniformly spans the circle in complex plane, shown in Figure 3.7. The amplitude $|Z(\omega)| = \sqrt{X(\omega)^2 + Y(\omega)^2}$ is also plotted.

3.4.2 Phase-Locked Loop (PLL)

The above procedure can fail to track a resonance correctly if the resonance moves too fast in the time difference between successive frequency scans. In such cases, we employ a phase locked loop (PLL), which provides a second method to track resonances with temperature. While in the lock-in technique, we have to measure the spectra in a small frequency range around the resonance at every temperature and fit a Lorentzian, using a PLL to track resonance frequencies eliminates the need to scan over a frequency range at every temperature. PLL comprises of a lock-in amplifier coupled to a PID controller. Lock-in measures amplitude $|Z(\omega)|$ and phase θ ($= \tan^{-1}(Y(\omega)/X(\omega))$) of the response at the drive frequency ω , and the PID controller adjusts drive frequency so as to maintain the phase at a setpoint. We typically choose the phase setpoint to coincide with the peak of the resonance since

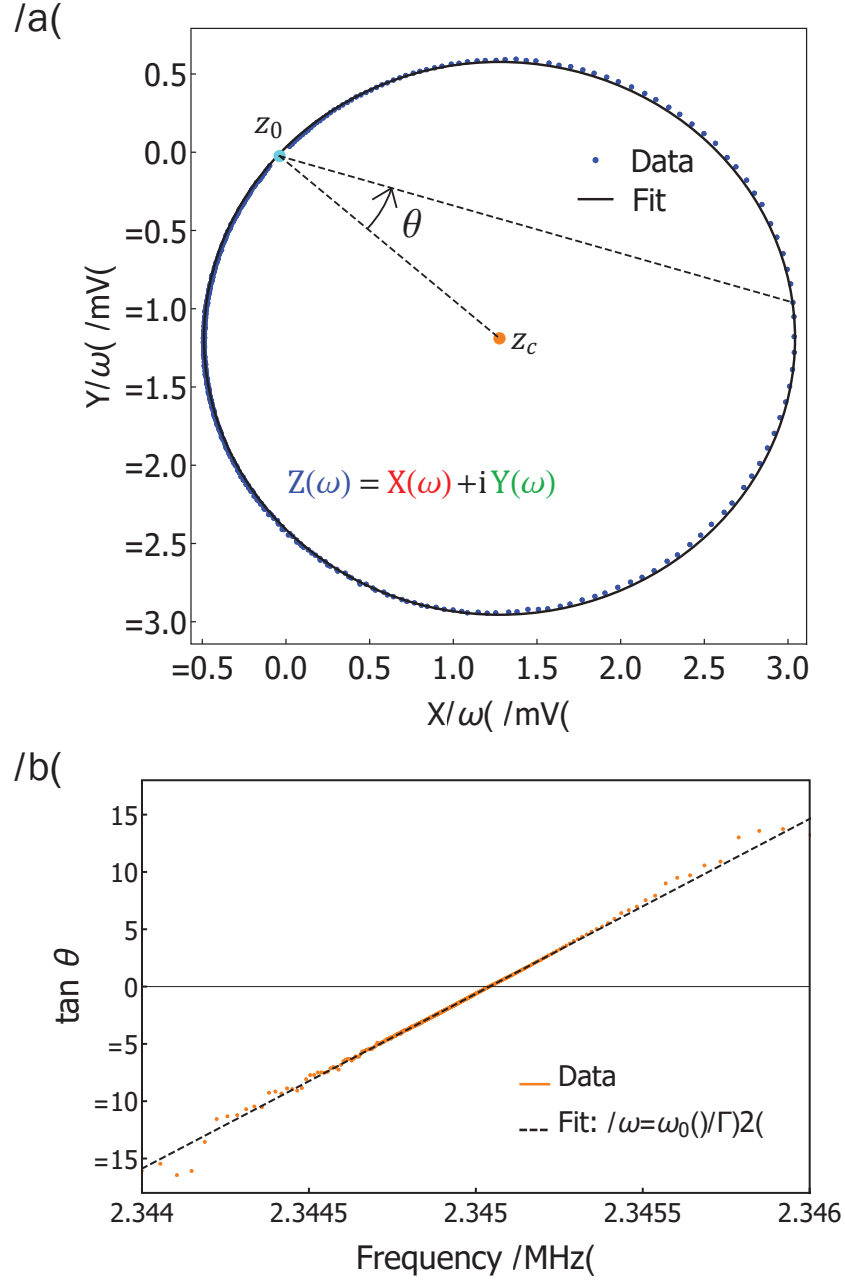


Figure 3.7: **Resonance in complex plane.** (a) The resonance shown in Figure 3.6 plotted in the complex plane. The ends of the resonance map on to the cyan point z_0 . The data is fit to a circle to determine the center z_c . The angle θ , as shown in the figure, is related to the resonance frequency ω_0 and the linewidth Γ as $\tan \theta = (\omega - \omega_0)/(\Gamma/2)$. The fit to this expression is shown in (b), which yields $\omega_0 = 2.34504$ MHz and $\Gamma = 0.13$ kHz.

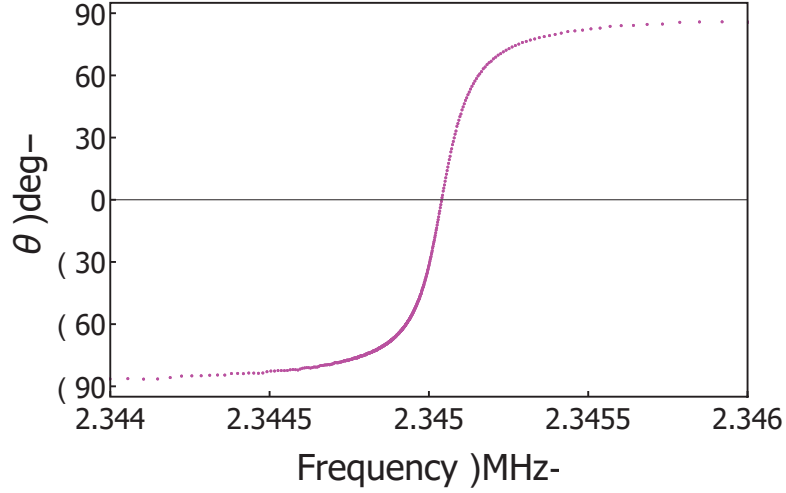


Figure 3.8: **Phase of resonance for PLL.** The phase θ of the resonance shown in Figure 3.6. To follow this with PLL, the phase setpoint should be set somewhere close to $\theta = 0^\circ$. Note that for resonances that lie on a big background, the total phase change can be smaller and not centered around zero, in which case the phase setpoint should be chosen accordingly near the center of the resonance.

the phase changes most rapidly with frequency there (see Figure 3.8). Then, as the temperature is swept and the resonance moves, the drive frequency is adjusted by the PLL, therefore tracking the resonance accurately. We find that compared to traditional RUS, PLL tracks resonances with higher sensitivity and the standard error is lower by a factor of 30 (see Figure 3.9). As there is no need to do a frequency scan and perform a fit at every temperature, this is also a faster measurement yielding 1000 times more points per unit temperature.

There are, however, situations where PLL does not work well. For example, if the phase at the peak of the resonance changes with temperature, the PLL's drive frequency will start moving from the peak of the resonance. This creates artificial changes in the temperature-dependence of frequencies. This can arise, among other things, from the electronic components used to perform the experiment, which may add background phase to the signal. Over large temperature ranges, the shape of a resonance usually changes leading to spurious phase changes, and using a PLL

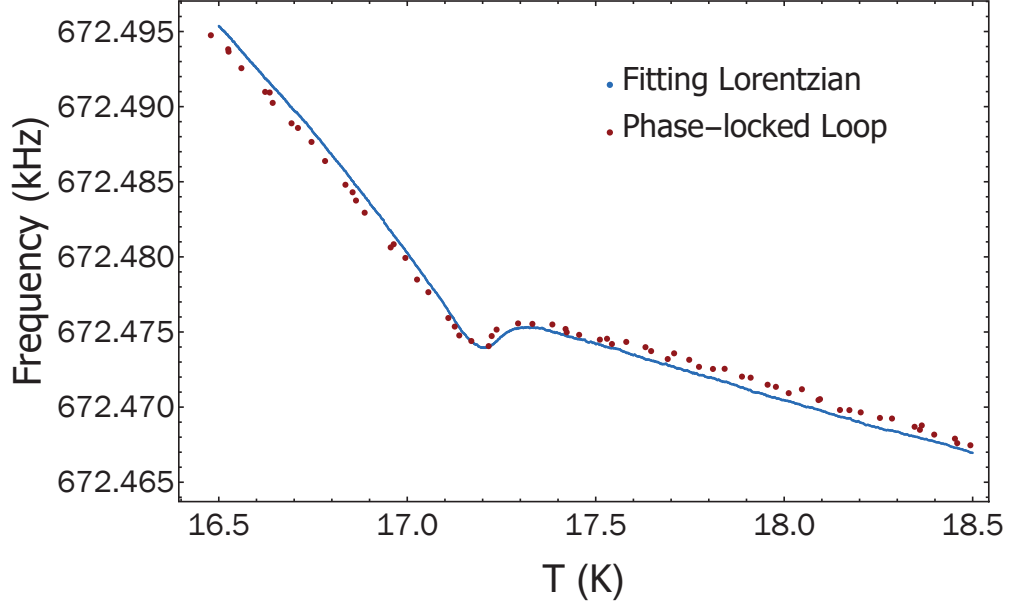


Figure 3.9: **Improved data acquisition with phase-locked loop.** Comparison between the lock-in technique that fits a Lorentzian and phase-locked loop (PLL) for the same resonance frequency of a URu_2Si_2 sample that is cooled through the hidden order transition ($T_{\text{HO}} = 17.25$ K). Data taken with PLL has lower fluctuations and a much higher density of frequency points.

becomes unreliable. Additionally, PLL can only follow one resonance frequency at a time since the lock-in is always set to output a drive frequency near the resonance being tracked. Hence, it is useful to employ PLL when we want to measure subtle changes in frequencies over small temperature ranges, such as through a transition, but to get data over large temperature ranges, it is generally better to scan in a small frequency range around the resonances at each temperature.

We used the PLL feature in a Zurich Instruments MFLI to experimentally measure resonances. We first stabilize at a temperature and take a long frequency scan to identify the resonances. We then set up the PLL in “Resonator Frequency” mode, which requires the resonance frequency ω_0 and its quality factor Q ($\sim \omega_0/\Gamma$). The PLL also needs a phase setpoint and a target bandwidth (BW), which is typically the precision to which we want to follow the resonance. For example, if

we expect few ppm changes in a 1 MHz resonance, the target BW should be set to about 1 Hz. Higher bandwidths make the PLL respond faster but gives noisy data, whereas at lower bandwidths, the PLL responds slowly but tracks the resonance with more closely. Knowing ω_0 , Q and the BW, the PLL internally calculates its PID constants and uses them to modify the drive frequency as the temperature is swept. To track multiple frequencies, the above procedure has to be repeated for each frequency in the temperature range of interest, thereby requiring multiple temperature sweeps in the same range.

3.5 Data Analysis

We now explain how to extract elastic moduli as a function of temperature from the temperature evolution of the resonance frequencies. Our fit to the resonance spectrum at a fixed temperature gives us the elastic moduli at that temperature and also the compositions of the resonances in terms of the α coefficients. For each resonance frequency ω_i , we define

$$\alpha_{i\mu} = \frac{\partial \ln \omega_i^2}{\partial \ln c_\mu} \implies \alpha_{i\mu} = 2 \frac{\partial \omega_i}{\partial c_\mu} \times \frac{c_\mu}{\omega_i}, \quad (3.11)$$

where c_μ are the independent elastic constants of the material. For example, for a tetragonal material with six independent moduli, there will be $\alpha_{i1}, \dots, \alpha_{i6}$ coefficients for each resonance frequency ω_i . These coefficients are essentially geometric factors that encode how much of the different strains are induced when a particular resonance is excited in the material. Thus the $\alpha_{i\mu}$ s are fairly temperature-independent, and this allows us to use the α coefficients known at a particular temperature to calculate the temperature evolution of all the elastic constants.

We denote the resonances and elastic moduli at some known temperature T_0

as $\omega_{i,0}$ and $c_{\mu,0}$. In an experiment, for example, T_0 could be room temperature. Then we measure the temperature evolution of frequencies $\omega_i(T)$ as we sweep the temperature. From [Equation 3.11](#), temperature-induced changes $\Delta c_\mu(T) = c_\mu(T) - c_{\mu,0}$ leads to changes $\Delta\omega_i(T) = \omega_i(T) - \omega_{i,0}$ in the frequencies as,

$$2 \frac{\Delta\omega_i(T)}{\omega_{i,0}} = \sum_{\mu} \alpha_{i\mu} \frac{\Delta c_\mu(T)}{c_{\mu,0}}. \quad (3.12)$$

This relates the fractional changes in the frequencies, which we measure, to fractional changes in the elastic moduli, which we want to calculate. We can calculate the moduli by measuring $\frac{\Delta\omega_i(T)}{\omega_{i,0}}$ for sufficiently many resonance frequencies, usually 3 times the number of independent moduli. This is required to reliably invert [Equation 3.12](#) to get the elastic moduli in terms of the temperature evolution of the frequencies. Expressed as a matrix equation, [Equation 3.12](#) at $T = T_1$ reads

$$2 \begin{pmatrix} \frac{\Delta\omega_1(T_1)}{\omega_{1,0}} \\ \vdots \\ \frac{\Delta\omega_N(T_1)}{\omega_{N,0}} \end{pmatrix} = \begin{pmatrix} \alpha_{11} & \alpha_{12} & \cdots & \cdots & \alpha_{1\lambda} \\ \vdots & & \ddots & & \vdots \\ \alpha_{N1} & \alpha_{N2} & \cdots & \cdots & \alpha_{N\lambda} \end{pmatrix} \begin{pmatrix} \frac{\Delta c_1(T_1)}{c_{1,0}} \\ \vdots \\ \frac{\Delta c_\lambda(T_1)}{c_{\lambda,0}} \end{pmatrix} \quad (3.13)$$

forming an overdetermined system of equations for the c_μ s. It is well-known that such a system usually has no unique solution [\[56\]](#), especially when dealing with real experimental data which always has noise and extraneous effects. Framed as a matrix equation $y = Mx$ (where M is a rectangular matrix), the “optimal” solution that minimizes the least square error $\|Mx - y\|$ is given by $x = (M^T M)^{-1} M^T y$. Thus, from [Equation 3.13](#), we calculate the elastic moduli as,

$$\begin{pmatrix} \frac{\Delta c_1(T_1)}{c_{1,0}} \\ \vdots \\ \frac{\Delta c_\lambda(T_1)}{c_{\lambda,0}} \end{pmatrix} = 2(M^T M)^{-1} M^T \begin{pmatrix} \frac{\Delta\omega_1(T_1)}{\omega_{1,0}} \\ \vdots \\ \frac{\Delta\omega_N(T_1)}{\omega_{N,0}} \end{pmatrix}, \quad (3.14)$$

where M is the matrix of $\alpha_{i\mu}$ s. Calculating this at every temperature gives the temperature dependence of the elastic constants $c_\mu(T)$ for all $\mu = 1, \dots, \lambda$.

The above procedure requires that the experimentally measured set of frequencies includes all the independent elastic constants. For example, if a particular elastic constant c_ν is only weakly present in the measured resonances ($|\alpha_{i\nu}| \lesssim 0.1$ for all measured ω_i), the calculation becomes unconstrained for that modulus and the result we get in $c_\nu(T)$ is primarily noise. On the other hand, having at least a couple of resonances that have more than 50% of a particular modulus is usually enough to well-constrain the temperature evolution of that modulus. A mathematical way to check whether the measured resonances constrains the elastic moduli well is to calculate the condition number C of the matrix M . It is defined as the ratio of the largest eigenvalue of a matrix to its lowest eigenvalue. The value of C is a measure of how much $\|Mx\|$, where x is a vector, changes for small changes in x . For an identity matrix, which is the ideal case, $C = 1$, while a large C signifies that $\|Mx\|$ is strongly affected by errors in x . Since our M will always be rectangular, the condition number is calculated as the ratio of the largest singular value to the lowest singular value in the singular value decomposition of M . A small C value ($\lesssim 20$) signifies that M is well-conditioned, and then the procedure outlined in [Equation 3.14](#) can be carried out reliably. On the other hand, $C > 100$ indicates that M is ill-conditioned and more resonances need to be measured to calculate all the independent moduli. In general, adding more rows to M does not increase C dramatically, since the system gets better constrained with more data. Removing a row, however, may sometimes increase C by a factor of 5-10, showing the importance of that resonance for constraining the calculation.

CHAPTER 4

HIDDEN ORDER TRANSITION IN URu₂Si₂

URu₂Si₂ is an archetypal example of a material with an ordered phase whose broken symmetries remain unknown. In spite of being studied for over 30 years, the order parameter (OP) characterizing this phase remains unknown, which has led to the name “hidden order” (HO) for this phase of matter. We describe in this chapter how using resonant ultrasound spectroscopy (RUS), we can rule out a whole class of order parameters for the HO phase. Most of this chapter has been adapted from a *Science Advances* paper [1] with Michael Matty, Ryan Baumbach, Eric D. Bauer, K. A. Modic, Arkady Shekhter, J. A. Mydosh, Eun-Ah Kim, and B. J. Ramshaw.

4.1 Electronic phases of URu₂Si₂

The 5*f* electron wave functions of uranium in URu₂Si₂, being on the border between localized and itinerant, give rise to a variety of phases that can be tuned with hydrostatic pressure, magnetic field and chemical doping. Detailed reviews of the various phases of URu₂Si₂, as well as experimental and theoretical proposals for the HO, can be found in Refs. [10, 57, 58]. Here we highlight the primary features in its pressure-temperature phase diagram, shown in Figure 4.1. At ambient pressures, URu₂Si₂ goes through the HO transition at $T_{\text{HO}} \approx 17.5$ K in the best crystals, and becomes a superconductor at even lower temperatures ($T_c \approx 1.5$ K). The HO phase was initially attributed to some form of magnetic order when the material was first grown around 1985 [59–61], although subsequent neutron scattering measurements ruled out any long-range magnetism in the HO phase [62, 63]. Under modest hydrostatic pressures of ~ 0.7 GPa, however, HO gives way to an

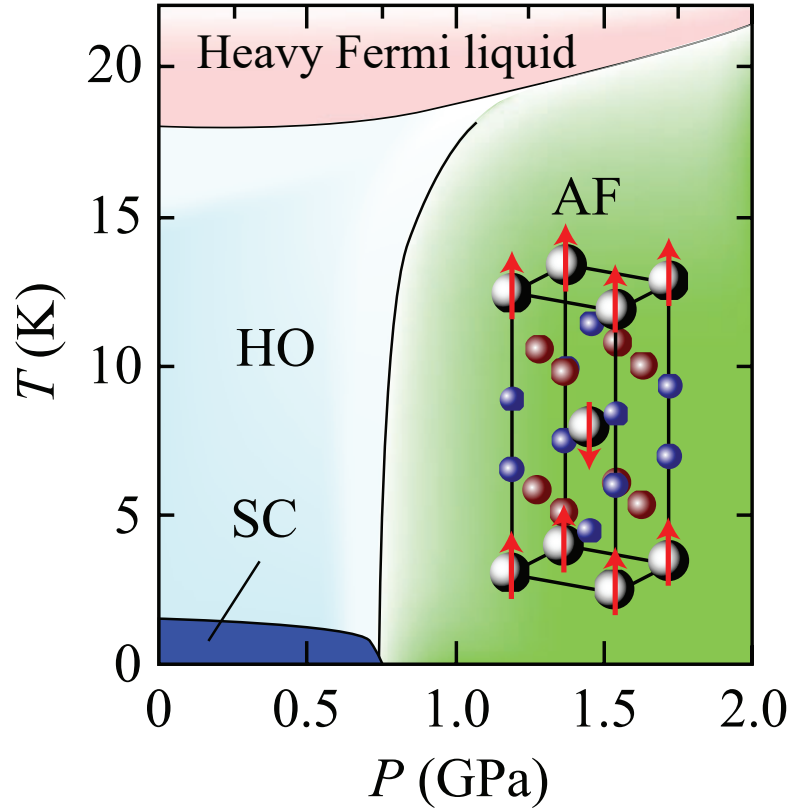


Figure 4.1: **Phase diagram of URu_2Si_2 .** Pressure-temperature phase diagram of URu_2Si_2 in zero magnetic field. The metallic (heavy Fermi liquid) phase at high temperatures gives way to hidden order (HO) at small pressures, while it evolves into an antiferromagnet (AF) at higher pressures. Superconductivity (SC) is seen to condense from the HO phase at lower temperatures. Figure reproduced from Ref. [6].

antiferromagnetic (AFM) phase. Interestingly, at about the same pressures that AFM is induced, superconductivity is suppressed, showing that SC emerges within HO but not in the AFM phase. Understanding the HO phase is thus critical for studying the superconductivity (SC), since the HO constrains the nature of the fluctuations from which unconventional superconductivity emerges.

Several possibilities have been put forth for the symmetry of the OP in the hidden order (HO) state of URu_2Si_2 (Table 4.1), but most of these rely on specific microscopic mechanisms that are difficult to verify experimentally. While the

broken symmetries of HO are unknown, most theories assume some form of ‘multipolar order’, whereby localized $5f$ electrons on the uranium site occupy orbitals that order below $T_{\text{HO}} = 17.5$ K. However, direct experimental evidence for localized $5f$ electrons—such as crystalline electric field level splitting—does not exist [10], leaving room for theories of HO based on itinerant $5f$ electrons. Many possible OPs remain in contention, but, whether itinerant or localized, all theories of HO can be classified based on the dimensionality of their point group representation: one-component [64–73] or two-component [74–80] (see Table 4.1). Theories of two-component OPs are motivated largely by the experiments of Okazaki et al. [81] and Tonegawa et al. [82], which detect a small C_4 symmetry breaking at T_{HO} . Recent X-ray experiments have cast doubt on these results [83], leaving the dimensionality of the OP in URu_2Si_2 an open question.

Establishing the dimensionality of the HO state not only allows us to rigorously exclude a large number of possible OPs, it also provides a starting place for understanding the unusual superconductivity that emerges at lower temperature in URu_2Si_2 . Given that the HO transition is a second order transition with a large mean-field-like specific heat discontinuity, it is expected to be appropriate for ultrasound measurements to look for jumps or discontinuities in elastic moduli at T_{HO} . Previous ultrasound studies in URu_2Si_2 did not measure any jumps, possibly due to insufficient experimental resolution [84–88]. Our high-resolution RUS experiment allows us to measure these discontinuities, and helps place strong constraints on the HO symmetry. In particular, as we explain in Section 4.2, RUS allows us to distinguish between one-component and two-component HO OPs independent of the microscopic mechanism, and therefore establishes the OP dimensionality.

Dimensionality	Symmetry	Reference
One-component	A_{1g}	Harrison and Jaime [89]
	A_{1u}	Kambe <i>et al.</i> [73]
	A_{2g}	Haule and Kotliar [68] Kusunose and Harima [70] Kung <i>et al.</i> [71]
	A_{2u}	Cricchio <i>et al.</i> [67]
	B_{1g}	Ohkawa and Shimizu [65] Santini and Amoretti [64]
	B_{1u}	Kiss and Fazekas [66]
	B_{2g}	Ohkawa and Shimizu [65] Santini and Amoretti [64] Harima <i>et al.</i> [69]
	B_{2u}	Kiss and Fazekas [66]
Two-component	E_g	Thalmeier and Takimoto [75] Tonegawa <i>et al.</i> [77] Rau and Kee [76] Riggs <i>et al.</i> [80]
	E_u	Hoshino <i>et al.</i> [79] Ikeda <i>et al.</i> [78] Riggs <i>et al.</i> [80]
	$E_{3/2,g}$	Chandra <i>et al.</i> [90]

Table 4.1: **Order parameters in URu₂Si₂.** Proposed order parameters of the HO state in URu₂Si₂, classified by their dimensionality and their point-group representation. Note that designations such as “hexadecapole” order are only applicable in free space—crystalline electric fields break these large multipoles into the representations listed in this table.

4.2 Strain-Order Parameter Coupling

In the tetragonal crystal structure of URu₂Si₂ (point group D_{4h}), elastic strain breaks into five irreducible representations (Figure 4.2): two compressive strains transforming as the identity A_{1g} representation, and three shear strains transforming as the B_{1g} , B_{2g} and E_g representations. The HO OP is thought to break at least translational symmetry. Experimentally, we induce long-wavelength strains in RUS which are in the $\vec{Q} = 0$ limit. Thus linear coupling between strain and OP is not allowed as this product would break translational symmetry. The lowest-

order terms in free energy allowed by both one-component and two-component OPs are linear in the A_{1g} strains and quadratic in OP: $\mathcal{F} = \epsilon_{A_{1g}} \cdot \eta^2$. Quadratic-in-order-parameter, linear-in-strain coupling produces a discontinuity in the associated elastic modulus at the phase transition [11, 91]. For OPs with one-component representations (any of the A_i or B_i representations of D_{4h}), only the A_{1g} compressional strains can couple in this manner. In contrast, shear strains couple as $\mathcal{F} = \epsilon_\mu^2 \cdot \eta^2$, and shear moduli show at most a change in slope at T_{HO} [12]. Thus $(c_{11} + c_{12})/2$, c_{33} and c_{13} may exhibit jumps at phase transitions corresponding to one-component HO order parameters, while $(c_{11} - c_{12})/2$, c_{66} , and c_{44} cannot.

Two-component OPs $\{\eta_x, \eta_y\}$ (of the E_i representations), on the other hand, have the bilinear forms $\eta_x^2 + \eta_y^2$, $\eta_x^2 - \eta_y^2$, and $\eta_x \eta_y$; transforming as A_{1g} , B_{1g} , and B_{2g} representations, respectively. Then, we have the coupling terms $\epsilon_{A_{1g}} \cdot (\eta_x^2 + \eta_y^2)$, $\epsilon_{B_{1g}} \cdot (\eta_x^2 - \eta_y^2)$ and $\epsilon_{B_{2g}} \cdot \eta_x \eta_y$. A second order phase transition characterized by a two-component OP therefore exhibits discontinuities in the B_{1g} and B_{2g} shear elastic moduli ($(c_{11} - c_{12})/2$ and c_{66} , respectively), in addition to jumps in the compressional A_{1g} moduli.

D_{4h} also contains half-integer representations, such as $E_{3/2,g}$ which is the representation of the slave boson responsible for the “hastatic” order parameter proposed by Chandra et al. [90] ($E_{3/2,g}$ is also known as Γ_7^+). $E_{3/2,g}$ forms bilinears of the A_{2g} and E_g representations (see Altmann et al. [92] table 33.8): this predicts no jump in either c_{66} or $(c_{11} - c_{12})/2$, but does predict a jump in c_{44} . If, however, the hastatic order only forms bilinears at finite \vec{Q} , then it will predict no jumps in any of the elastic moduli [92].

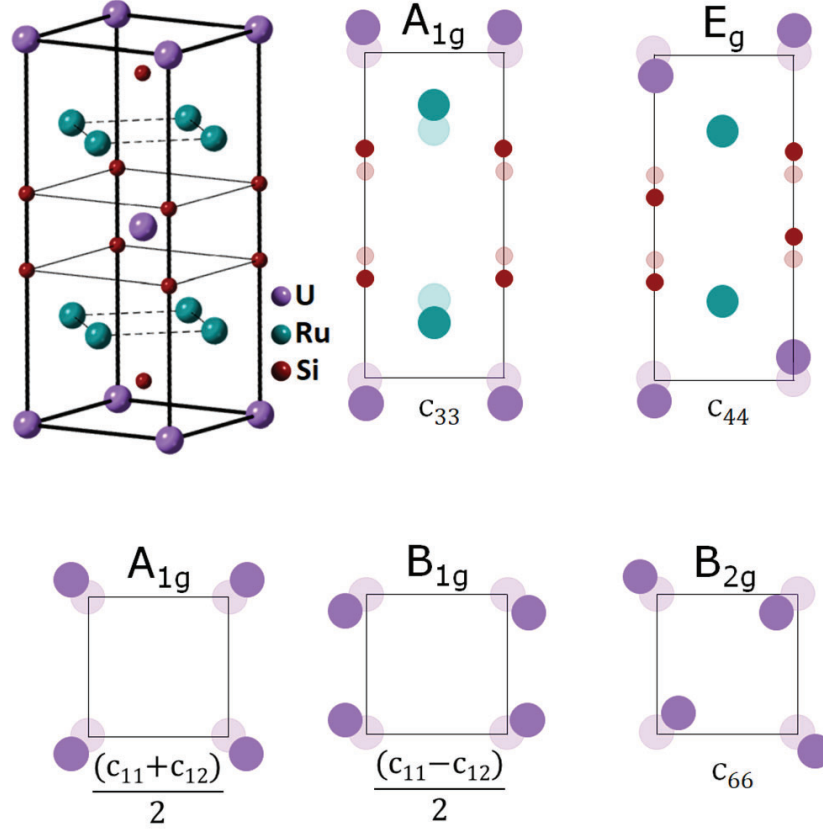


Figure 4.2: **Irreducible strains in URu_2Si_2 .** The tetragonal unit cell of URu_2Si_2 , along with its deformations corresponding to the irreducible representations of strain. There are two compressional (A_{1g}) strains and three shear strains, belonging to B_{1g} , B_{2g} and E_g representations of D_{4h} . There is an elastic modulus corresponding to each of these strains, and a sixth modulus c_{13} which arises from the coupling of the two A_{1g} strains.

4.3 Sample Details

Sample S1 was grown by the Czochralski method. A single crystal oriented along the crystallographic axes was polished to dimensions $3.0 \text{ mm} \times 2.8 \text{ mm} \times 2.6 \text{ mm}$, with 2.6 mm along the tetragonal long axis. S1 has the HO transition at $T_{\text{HO}} = 17.25 \text{ K}$, slightly lower than the 17.5 K reported in best samples.

Sample S2 was grown was grown by the Czochralski method and then processed by solid-state electrorefinement. Typical residual resistivity ratio (RRR) values for

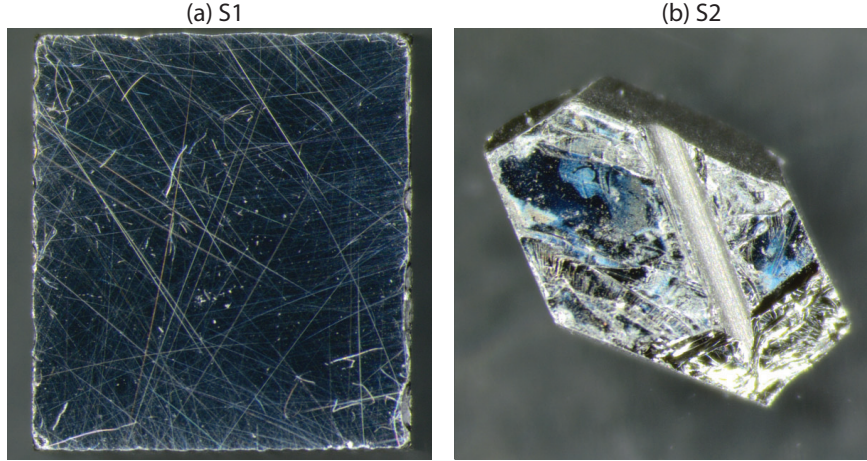


Figure 4.3: **Two samples of URu_2Si_2 .** Photographs of the two URu_2Si_2 samples, S1 and S2, studied using RUS.

ab-plane flakes of URu_2Si_2 taken from a large piece range from 100-500. The RRR values measured directly on larger pieces (see Figure 4.3) are between 10-20. A comparison of different growth methods for URu_2Si_2 can be found in Gallagher et al. [93]. To check the quality of sample S2, we measured its resistance from 300 K down to 2 K, as shown in Figure 4.4. The Kondo crossover is seen around 75 K and the resistance shows a sudden increase at the HO transition, consistent with previous reports. We use the feature near the hidden order transition to determine $T_{\text{HO}} = 17.52$ K for this sample. This value of T_{HO} [93, 94] confirms the higher quality of S2 compared to S1.

4.4 Data Analysis

We performed RUS measurements on two URu_2Si_2 samples, which are described above. All the frequency versus temperature data shown here was acquired using a phase-locked loop (details in Subsection 3.4.2). For S1, we can analyze the data in the traditional way to calculate elastic moduli from the frequencies (listed

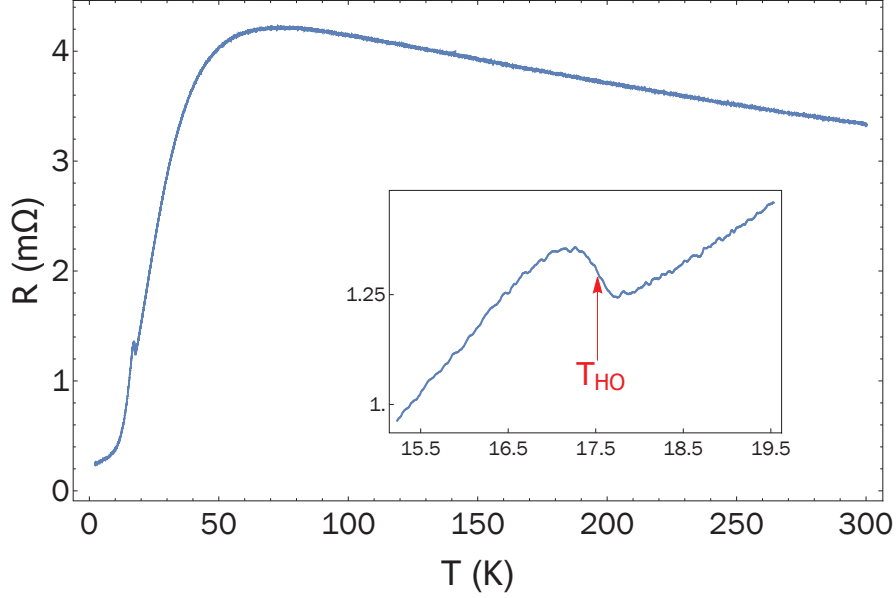


Figure 4.4: **Resistance vs temperature for S2.** Resistance of sample S2 measured from 300K down to 2K. Inset shows the feature at hidden order transition, from which we determine $T_{\text{HO}} = 17.52$ K for this sample. We find $\text{RRR} \sim 17$ for the sample.

in Table 4.2). In principle this traditional analysis is sufficient to determine the order-parameter dimensionality in URu_2Si_2 . The process of solving for the elastic moduli, however, incorporates systematic errors arising from sample alignment, parallelism, and dimensional uncertainty. Even more detrimental is the possibility that the measured spectrum is missing a resonance, rendering the entire analysis incorrect. While we are confident in our analysis for the particularly large and well-oriented sample S1, large samples of URu_2Si_2 are known to be of slightly lower quality [94]. Smaller, higher-quality crystals of URu_2Si_2 do not lend themselves well to RUS studies, being hard to align and polish to high precision. Smaller samples also produce weaker RUS signals, making it easier to miss a resonance.

We have developed a new method for extracting symmetry information directly from the resonance spectrum, without needing to first extract the elastic moduli themselves, even if the spectrum is incomplete. We take advantage of the fact that

Temperature (K)	$\frac{c_{11}+c_{12}}{2}$ (GPa)	c_{33} (GPa)	c_{13} (GPa)	$\frac{c_{11}-c_{12}}{2}$ (GPa)	c_{66} (GPa)	c_{44} (GPa)
300	216.3	299.9	112.8	65.3	136.8	98.2
20	218.0	307.4	112.8	65.2	140.6	101.8

Table 4.2: **Elastic moduli of URu₂Si₂**. The six independent elastic moduli in URu₂Si₂ measured with RUS, at room temperature (300 K) and at 20 K.

artificial neural networks can be trained to recognize features in complex data sets and classify the state of matter that produce such data [95–100]. We validate this approach by analyzing RUS data from a sample that we are confident can also be analyzed using traditional methods (data from sample S1 with a well-defined geometry). We then analyze data from the higher quality URu₂Si₂ sample S2 that has an ill-defined geometry—a task that is impossible for the traditional analysis method, but which is easily performed by our neural network.

4.4.1 Traditional Analysis

We first perform a traditional RUS analysis from the data on sample S1, extracting the temperature dependence of the six elastic moduli from 29 measured resonances (see Figure 4.5 for a few representative resonances), following the procedure outlined in Section 3.5. The temperature evolution of the six moduli down to 10 K is shown in Figure 4.6. Most of them show the usual stiffening behavior expected from an anharmonic lattice [101, 102]. The softening in the B_{1g} modulus $(c_{11} - c_{12})/2$ is anomalous, and points towards a B_{1g} nematic tendency in URu₂Si₂. A detailed theoretical treatment of the HO phase as a staggered B_{1g} nematic can be found in Ref. [103].

Focusing on the evolution of the elastic moduli across T_{HO} , we find jumps in two of the A_{1g} elastic moduli, whereas the B_{1g} and B_{2g} shear moduli show only

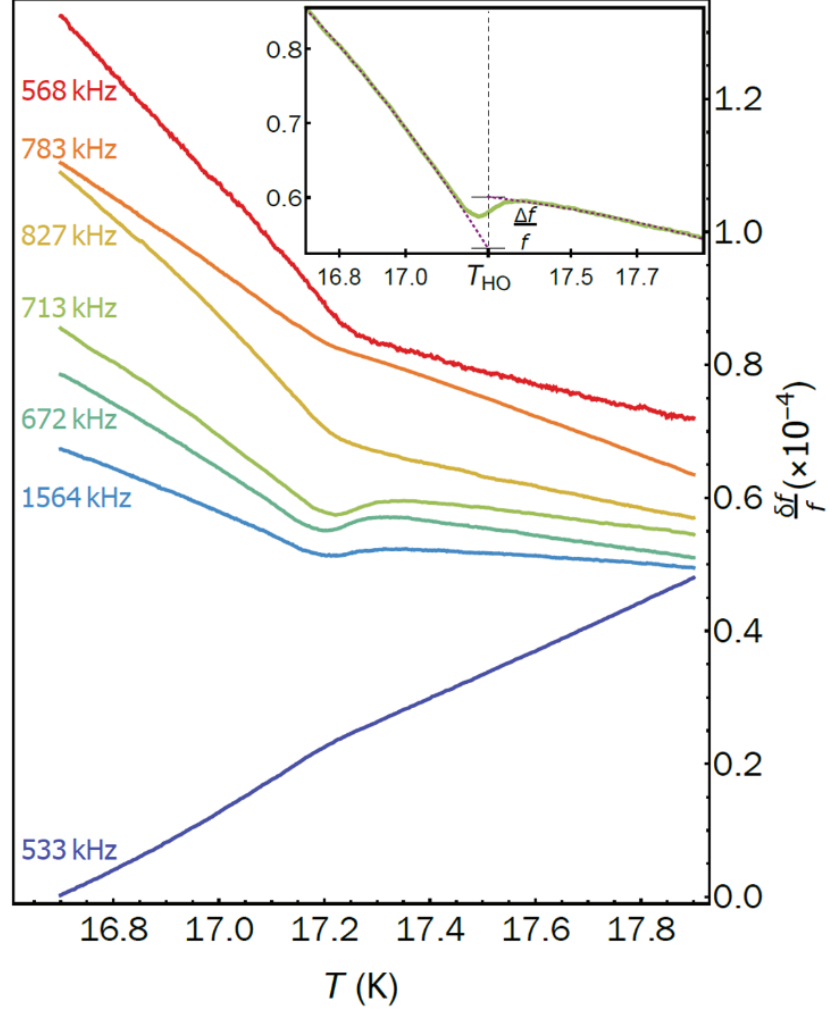


Figure 4.5: **Resonance frequencies of URu_2Si_2 through T_{HO} .** Seven representative frequencies of URu_2Si_2 measured through the hidden order transition—plots are shifted vertically for clarity. Three resonances (672, 713 and 1564 kHz) show jumps at T_{HO} (inset shows what is meant by jump), while the others do not, signifying contributions from different symmetry channels.

a break in slope at T_{HO} to within our experimental uncertainty (see Figure 4.7). Jumps in the shear moduli would be expected for any order parameter of the two-component E_i representations [74–80]—the fact that we do not resolve any shear jumps constrains the OP of the HO phase to belong to a one-component representation of D_{4h} . The fact that we do not resolve a jump in c_{33} is consistent with the magnitudes of the jumps in $(c_{11} + c_{12})/2$ and c_{13} , as we show below. The

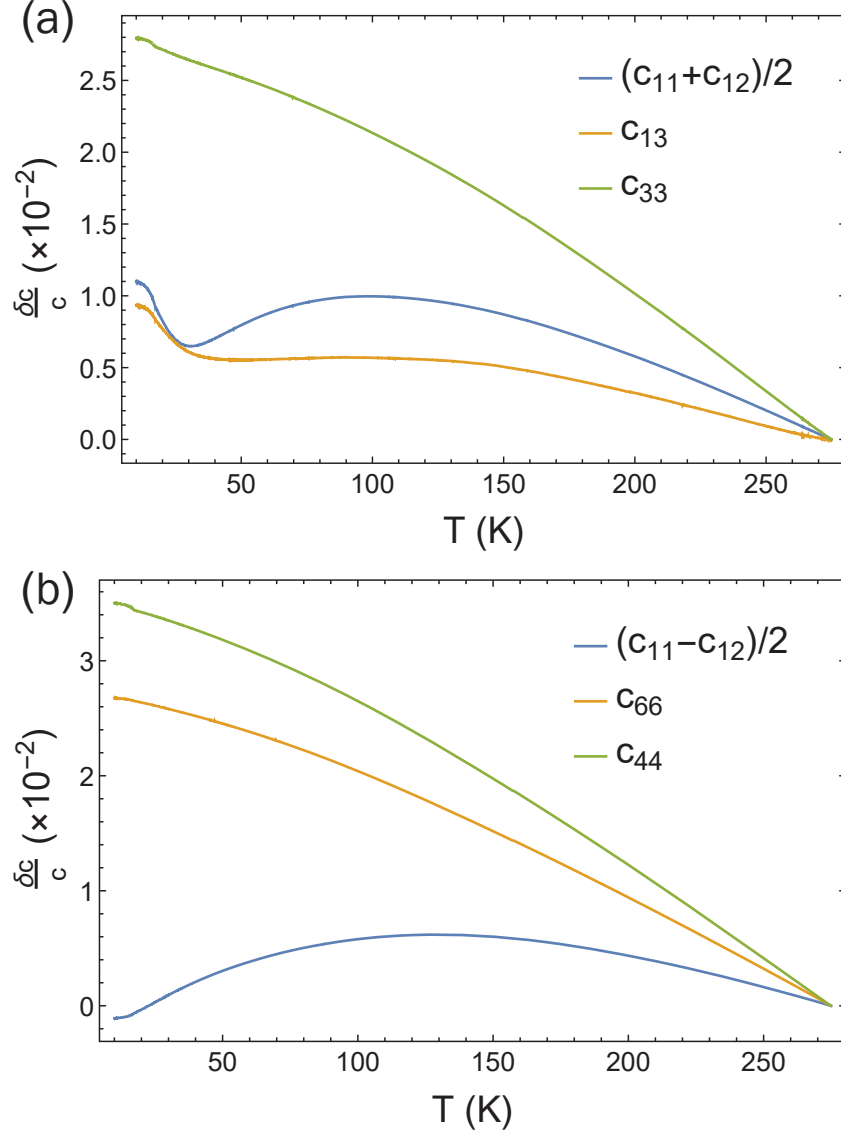


Figure 4.6: **Temperature evolution of elastic moduli in URu_2Si_2 .** (a) Compressional and (b) shear moduli of URu_2Si_2 measured with RUS between 275 K and 10 K. The HO transition occurs around 17.25 K, shown in more details in Figure 4.7. We plot the moduli as fractional changes $\frac{\delta c(T)}{c} = \frac{c(T)}{c(275 \text{ K})} - 1$.

jumps in the three A_{1g} moduli can be related as (see Equation 2.38)

$$\Delta c_{A_{1g},1} \times \Delta c_{A_{1g},2} = (\Delta c_{A_{1g},3})^2, \quad (4.1)$$

where $c_{A_{1g},1} = (c_{11} + c_{12})/2$, $c_{A_{1g},2} = c_{33}$ and $c_{A_{1g},3} = c_{13}$. Experimentally we measure relative jumps $(\frac{\Delta c}{c})$, which can be related by rewriting Equation 4.1 as

$$\begin{aligned} \frac{\Delta c_{A_{1g},2}}{c_{A_{1g},2}} \cdot c_{A_{1g},2} &= \frac{\left(\frac{\Delta c_{A_{1g},3}}{c_{A_{1g},3}} \cdot c_{A_{1g},3} \right)^2}{\left(\frac{\Delta c_{A_{1g},1}}{c_{A_{1g},1}} \cdot c_{A_{1g},1} \right)} \\ \Rightarrow \left(\frac{\Delta c_{A_{1g},2}}{c_{A_{1g},2}} \right) &= \frac{1}{c_{A_{1g},2}} \cdot \frac{\left(\frac{\Delta c_{A_{1g},3}}{c_{A_{1g},3}} \cdot c_{A_{1g},3} \right)^2}{\left(\frac{\Delta c_{A_{1g},1}}{c_{A_{1g},1}} \cdot c_{A_{1g},1} \right)} \end{aligned} \quad (4.2)$$

Using the known jumps in $(c_{11} + c_{12})/2$ and c_{13} (shown in Figure 4.8), we estimate $\frac{\Delta c_{33}}{c_{33}} \approx 4 \times 10^{-7}$, which is an order of magnitude below our experimental resolution. This explains the lack of c_{33} jump in our experimental data.

4.4.2 Machine Learning-based Analysis

Artificial neural networks (ANNs) are popular machine learning tools due to their ability to classify objects in highly non-linear ways. In particular, ANNs can approximate smooth functions arbitrarily well [104]. Here we train an ANN to learn a function that maps the jumps in ultrasonic resonances at a phase transition to one of two classes, corresponding to either a one-component or two-component OP. One-component OPs induce jumps only in compressional elastic moduli, whereas two-component OPs also induce jumps in two of the shear moduli. Phase transitions with two-component OPs should therefore show jumps in more ultrasonic resonances at a phase transition than phase transitions with one-component OPs. Our intent is that this difference in the distribution of jumps can be learned by an ANN to differentiate between one-component and two-component OPs.

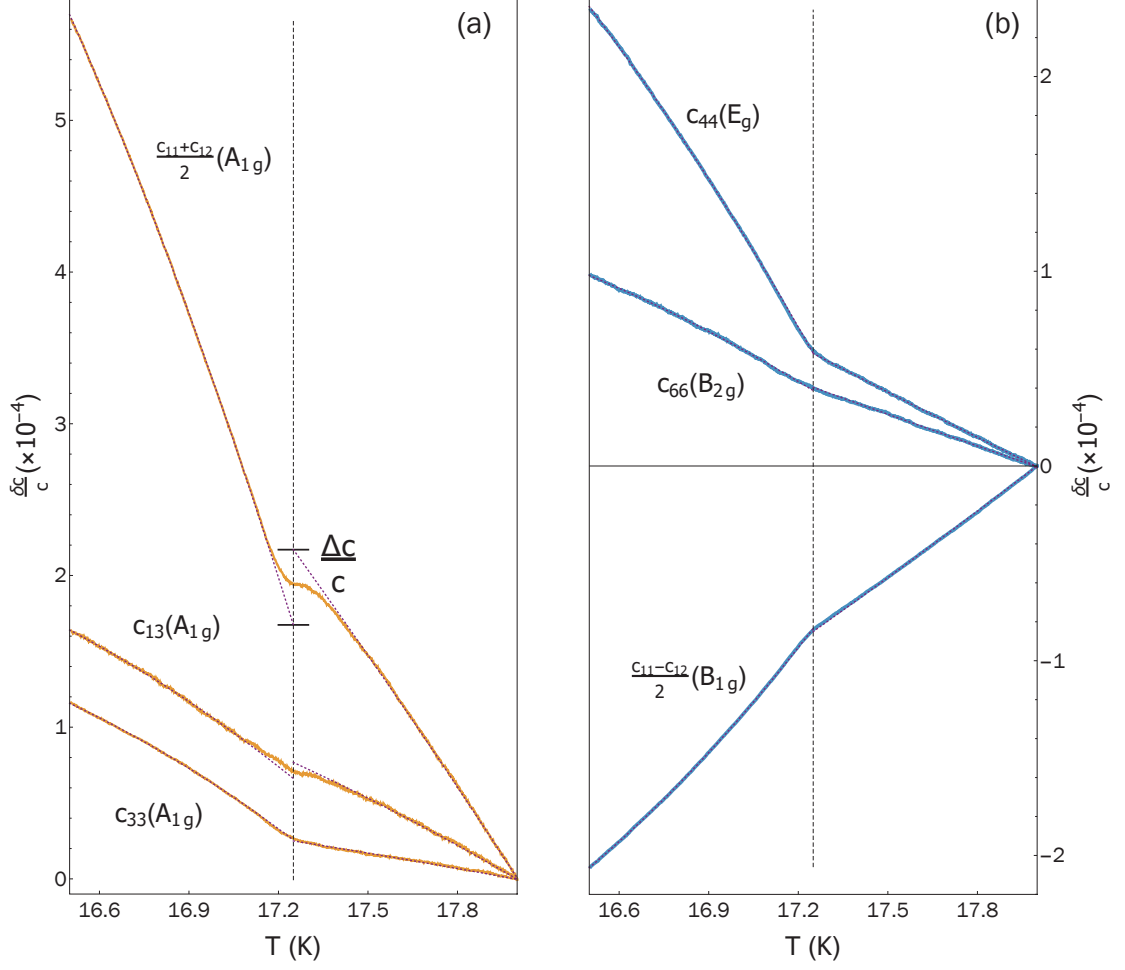


Figure 4.7: **Elastic moduli of URu_2Si_2 through T_{HO} .** (a) Compressional (shown in orange) and (b) shear (shown in blue) moduli of URu_2Si_2 measured through the hidden order transition. Dashed guides to the eye show the temperature dependence extrapolated from below and above T_{HO} , and $\frac{\Delta c}{c}$ shows how we define the jump at T_{HO} .

An ANN must be trained with simulated data that encompasses a broad range of possible experimental scenarios. In our case we simulate RUS spectra with certain assumptions about the sample and the OP dimensionality. We first solve the 3-D elastic wave equation using input parameters—density of sample, elastic constants and dimensions—which are chosen from a range that bounds our experimental uncertainties, to obtain the first N lowest frequency resonances and their compositions ($\alpha_{ij} = \partial(\ln f_i^2)/\partial(\ln c_j)$) in terms of the six independent elastic constants.

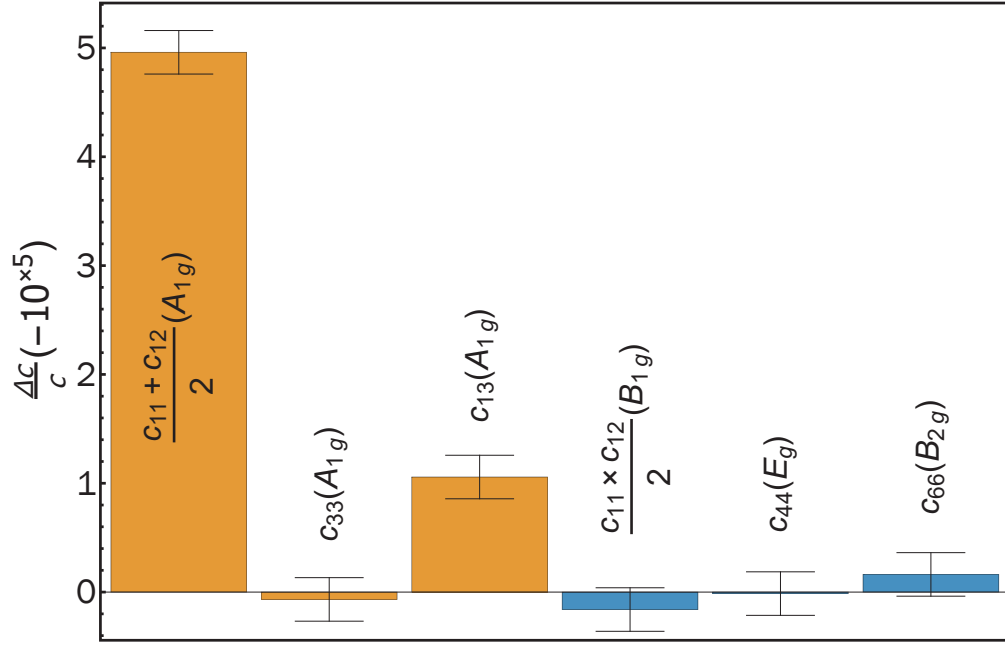


Figure 4.8: **Discontinuities in elastic moduli of URu₂Si₂.** Magnitudes of the jumps ($\frac{\Delta c}{c}$) at T_{HO} , along with their experimental uncertainties. Non-zero jumps are seen only in two of the compressional (A_{1g}) moduli, and in none of the shear moduli.

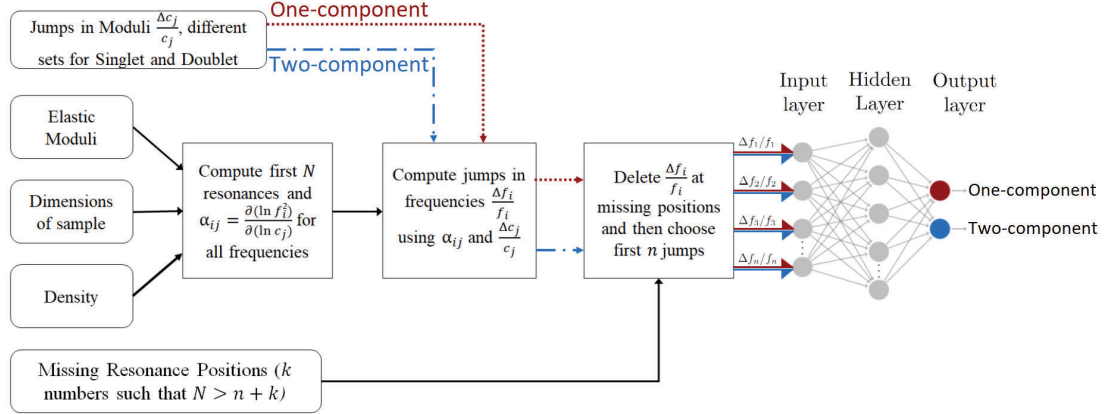


Figure 4.9: **Schematic of the algorithm used to generate training data.** Values for elastic moduli and dimensions are chosen randomly from a range that bounds our experimental uncertainties. One-component OPs give jumps only in A_{1g} moduli, whereas two-component OPs also give jumps in B_{1g} and B_{2g} moduli. Separate output files are generated corresponding to one-component and two-component OPs, each containing n jumps, where n is the number of frequencies whose temperature evolution could be experimentally measured. The output value is the network's judgment on the likelihood of whether the jumps come from one-component or two-component OP.

We expect different sets of jumps in moduli ($\Delta c_j/c_j$) for one- and two-component OPs, which translate into different sets of jumps in resonance frequencies ($\Delta f_i/f_i$) for the two OP types. Experimentally, some resonances are too noisy to be measured through the transition, and to account for that, we delete a random number (k) of jumps from the the list of N consecutive $\Delta f_i/f_i$. We then choose the first n jumps to constitute a training data set, where n is the number of jumps measured in experiment. To prepare the simulated data for interpretation by our ANN we take the first n jumps, sort the jumps by size, normalize the jumps to lie between zero and one, and label the data sets by the dimensionality of the OP that was used to create them—either one-component or two (see [Figure 4.9](#)). By varying the input assumptions we produce a large number of training data sets that are intended to encompass the (unknown) experimental parameters.

This normalized and sorted list of numbers $\{\Delta f_i/f_i\}$ is used as input to an ANN. Our ANN architecture is a fully connected, feed forward neural network with a single hidden layer containing 20 neurons (see [Figure 4.9](#)). Each neuron j processes the inputs $\{\Delta f_i/f_i\}$ according to the weight matrix w_{ji} and the bias vector b_j specific to that neuron as $\sigma(w_{ji}x_i + b_j)$ where the rectified linear activation function is given by $\sigma(y) \equiv \max(y, 0)$. The sum of the neural outputs is normalized via a softmax layer.

We train the ANN using 10000 sets of simulated RUS data for the case of a one-component OP, with varied elastic constants, sample geometries, jump magnitudes, and missing resonances, and another 10000 sets for the case of a two-component OP. We use cross-entropy as the cost function for stochastic gradient descent. We train 10 different neural networks in this way to an accuracy of $\sim 90\%$, and then fix each individual network's weights and biases. Once the networks are trained

we ask each ANN for its judgment on the OP dimensionality associated with an experimentally determined set of 29 jumps, and average the responses from each neural network. The sizes of the jumps depend on how T_{HO} is assigned—assigning T_{HO} artificially far from the actual phase transition will produce large jumps in all resonances. We therefore repeat our ANN determination using a range of T_{HO} around the phase transition, and plot the outcome as a function of T_{HO} .

While the sample geometry, density, and moduli are well determined for S1 and only varied by a few tens of percent, the dimensionality of the OP, the number of missing resonances, and the sizes of the jumps in each symmetry channel are taken to be completely unknown. We vary these latter parameters across a broad range of physically possible values. [Figure 4.10\(a\)](#) shows the results of our ANN analysis for sample S1—the same sample discussed above using the traditional analysis. To visually compare the training and experimental data in a transparent fashion, we plot the list of sorted and normalized jumps against their indices in the list. The average of the one-component training data is shown in red; the average of the two-component training data is shown in blue; the experimental jumps are shown in grey. It is clear that the experimental data resembles the one-component training data much more closely. This resemblance is quantified in the inset, showing the ANN confidence that the experimental data belongs to the one-component class for varying assignments of T_{HO} . We find that the confidence of a one-component OP is maximized in the region of assigned T_{HO} that corresponds to the experimental value of T_{HO} .

Thus far we have shown that both methods—the traditional method of extracting the elastic moduli using the elastic wave equation, and our new method of examining the resonance spectrum directly using a trained ANN—agree that the

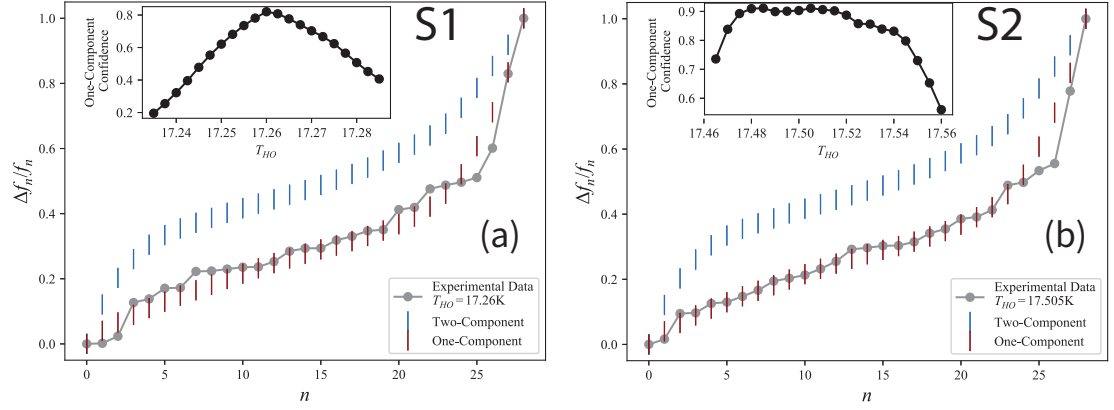


Figure 4.10: **Results of the ANN analysis for two samples of URu_2Si_2 .** Upper blue curves show the averaged, sorted, simulated frequency shift (“jump”) data plotted against its index in the sorted list for a two-component OP for (a) sample S1 and (b) sample S2. The data are normalized to range from 0 to 1. Lower, red curves shows the same for a one-component OP. Grey dots show experimental data for critical temperature assignment (a) $T_{\text{HO}} = 17.26$ K and (b) $T_{\text{HO}} = 17.505$ K, which visually aligns more closely with the average one-component simulated data than the two-component simulations. Insets: percent confidence of the one-component output neuron for various assignments of T_{HO} averaged over 10 trained networks. A maximum confidence of (a) 83.2% occurs for $T_{\text{HO}} = 17.26$ K and (b) 89.7% for $T_{\text{HO}} = 17.505$ K.

HO parameter of URu_2Si_2 is one-component. We can now use the neural network to analyze a smaller, irregular-shaped but higher quality (higher T_{HO} [94]) sample that cannot be analyzed using the traditional method due to its complicated geometry. Figure 4.10(b) shows the result of ANN analysis performed on a resonance spectrum of sample S2. The sorted and normalized spectrum looks very similar to that of S1, and the averaged ANN outcome gives 90% confidence that the OP is one-component. Despite the fact that S2 has a geometry such that the elastic moduli cannot be extracted, its resonance spectrum still contains information about the OP dimensionality and our ANN identifies this successfully.

4.5 Additional Experimental Considerations

4.5.1 Resolving the Origin of Jumps

The elastic moduli discontinuities predicted by $\eta^2 \cdot \epsilon_\mu$ coupling in Landau theory only show up in experiments under the assumption that the applied strain varies at a timescale much longer than the relaxation times of the order parameter [31]. Our experiments are in the low MHz frequency range, corresponding to timescales of order 10^{-7} s. The HO transition is a mean-field-like second order transition, and the OP relaxation timescales for similar (superconducting) transitions in other uranium-based heavy fermion compounds are of the order $10^{-10} - 10^{-12}$ s [34]. Thus our experimental frequencies are low enough to observe the moduli jumps.

To rule out anomalous OP dynamics near the phase transition interfering with our measured jumps, we look at the ultrasonic attenuation in the resonances through T_{HO} . In particular, anomalous OP dynamics would lead to large, temperature-dependent features in the attenuation near T_{HO} . In Figure 4.11, we plot the temperature evolution of three resonances, each showing a clear discontinuity at T_{HO} . The inverse quality factor of these frequencies (proportional to ultrasonic attenuation), plotted in Figure 4.11(d), show tiny features at T_{HO} , but overall unremarkable behavior. The tiny features are required by Kramers-Kronig relations, but the overall behavior is dominated by phonon anharmonicity and not OP dynamics. We also plot the background-subtracted elastic moduli through T_{HO} , to highlight the discontinuity in the A_{1g} moduli in Figure 4.12. This confirms that the moduli jumps we see originate from strain-order parameter coupling terms of the form $\eta^2 \cdot \epsilon_\mu$.

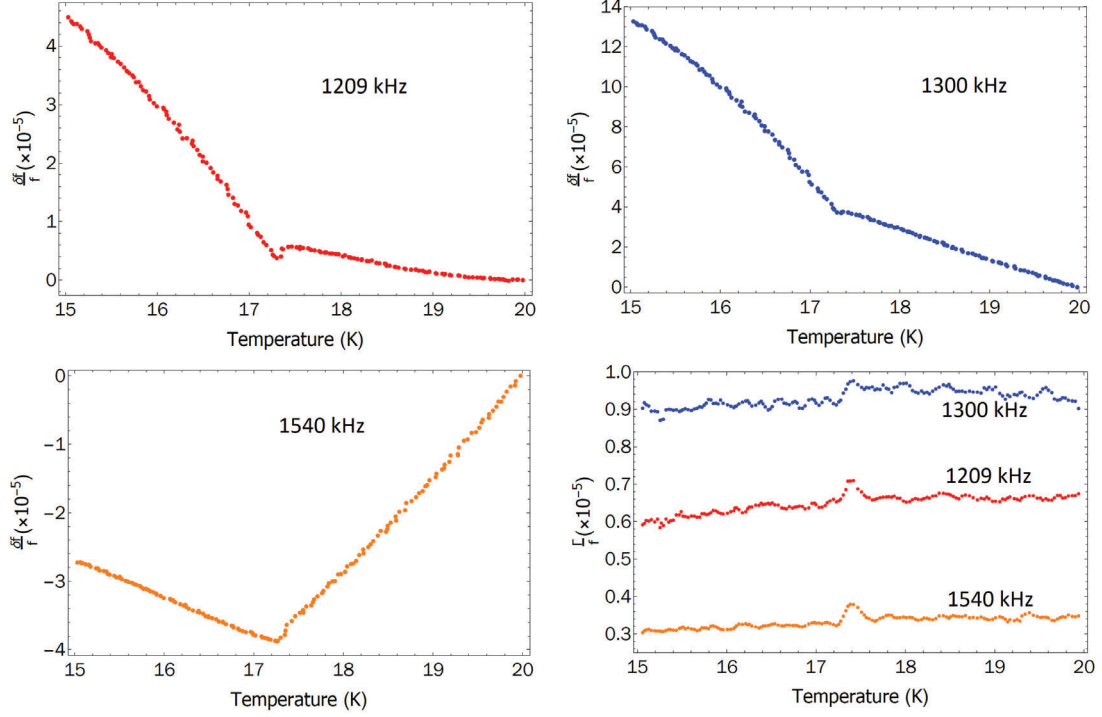


Figure 4.11: **Three frequencies and their attenuation through T_{HO} .** A clear discontinuity can be seen in all three resonances and a small peak-like feature can be seen in the attenuation at T_{HO} . The lack of any large temperature-dependent feature in the attenuation rules out anomalous order parameter dynamics interfering with our results.

4.5.2 Compositions of Resonances

The irregular shape of the higher quality sample S2 prevents directly inverting the frequency spectra to calculate the elastic moduli and the compositions of the frequencies in terms of the moduli (α_{ij} s). To estimate the compositions, we use the known temperature evolution of the 6 elastic constants between 145 K to 25 K to fit the change in frequencies as the sample is cooled in this temperature range (see Figure 4.13). This helps us ensure that the sample S2 has in-plane shear (B_{1g} and B_{2g}) modes in our experimentally accessible frequency range, and hence the data we obtain should allow us to distinguish between one- and two-component order parameters.

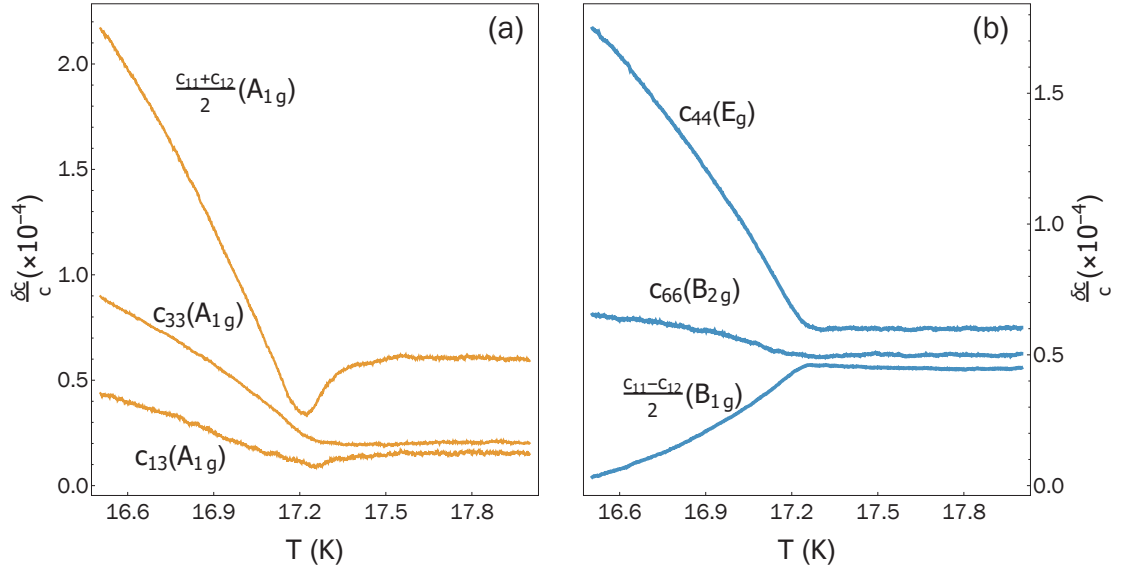


Figure 4.12: **Elastic moduli with contribution above T_{HO} subtracted.** Background subtraction above T_{HO} isolates the effect of the order parameter on the elastic moduli. Plots are vertically shifted for visual clarity. It can be clearly seen that $(c_{11} + c_{12})/2$ and c_{13} show a drop at T_{HO} before starting to stiffen in the HO phase, while all other moduli only show increased stiffening/softening through T_{HO} .

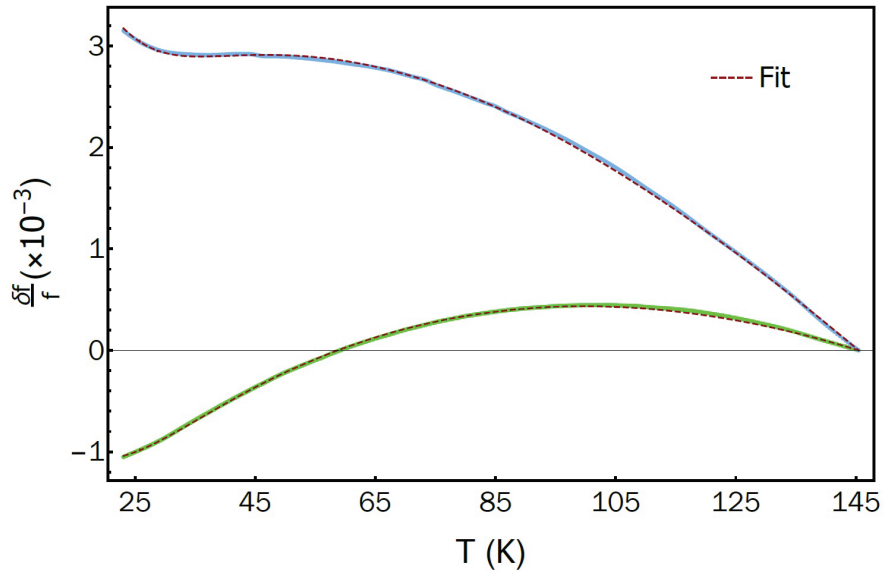


Figure 4.13: **Estimating compositions of resonances.** Temperature dependence of two representative resonances (blue and green) between ~ 25 K to 145 K. The fit estimates that the blue curve is composed of mostly E_g and some A_{1g} symmetry vibrations, whereas the green curve is dominated by vibrations in B_{1g} channel.

4.5.3 Possible Effects from Parasitic AFM

Under hydrostatic pressure, URu₂Si₂ undergoes a transition into a large moment antiferromagnet (LMAF) phase. Even at ambient pressure, URu₂Si₂ samples are known to host some amount of this parasitic AFM phase, arising from inhomogeneous strain in the sample [105]. The AFM phase shows a large discontinuity in the modulus c_{11} [106]. One could imagine that the jumps we see at T_{HO} are arising from the presence of this parasitic AFM phase, in particular for sample S1, since it has a suppressed $T_{\text{HO}} = 17.25$ K, compared to the standard $T_{\text{HO}} = 17.5$ K.

To confirm that we are seeing discontinuities from the HO phase, we obtained the high-purity sample S2, which underwent solid-state electrorefinement, and has $T_{\text{HO}} = 17.5$ K. It can be seen that sample S2 shows the same distribution of jumps as S1 (Figure 4.10). This rules against any parasitic effects leading to the jumps, since these samples must have very different concentrations of AFM puddles in them. Additionally, we note that the elastic anomalies due to strain-induced AFM should appear at T_{N} (≥ 19 K, see Figure 4.1), which is a different temperature than T_{HO} . We see only a single transition, as evidenced by a single jump in A_{1g} moduli and a change in slope in the shear moduli, all happening at the HO transition temperature (as defined by resistance measurements shown in Figure 4.4). If the elastic anomalies were to arise from strain-induced AFM, we would expect these signatures of the phase transition to show up at a different temperature than exactly T_{HO} (or more likely, a distribution of temperatures, since the strain relaxes over a finite length scale away from the parasitic regions). We resolve a sharp (~ 100 mK) transition, and hence if there were two transitions, we should be able to see them.

The fact that our results are consistent between sample S1 and S2, and we see

only a single sharp transition at precisely T_{HO} , confirms that the elastic discontinuities are from the HO transition, and not due to strain-induced AFM.

4.6 Discussion and Outlook

Our two analyses of ultrasonic resonances across T_{HO} in URu_2Si_2 strongly support one-component-type OPs, such as electric-hexadecapolar order [68], the chiral density wave observed by Raman spectroscopy [71, 72, 107], and are consistent with the lack of C_4 symmetry breaking observed in recent X-ray scattering experiments [83]. Our analysis rules against two-component OPs, such as rank-5 superspin [73, 76] and spin-nematic order [74]. The power of our result lies in its independence from the microscopic origin of the OP: group-theoretical arguments alone are sufficient to rule out large numbers of possible OPs. It could be argued that the coupling constants governing the jumps in the shear moduli are sufficiently small such that the jumps are below our experimental resolution. Previous experiments, however, have shown the shear and compression coupling constants to be of the same order of magnitude in other materials with multi-component OPs [108–110]. It has also been demonstrated that the size of the jump in heat capacity at T_{HO} is largely insensitive to RRR [93, 94, 111]. It is therefore hard to imagine that higher RRR samples would yield jumps in the shear moduli.

The use of ANNs to analyze RUS data represents an exciting opportunity to re-examine ultrasound experiments that were previously unable to identify order parameter symmetry. For example, irregular sample geometry prevented identification of the order parameter symmetry in the high- T_c superconductor $YBa_2Cu_3O_{6.98}$ [11]. Re-analysis of this spectrum using our ANN could reveal

whether the OP of the pseudogap is associated with E_u -symmetry orbital loop currents. The proposed two-component $p_x + ip_y$ superconducting state of Sr_2RuO_4 and other potential spin-triplet superconductors could also be identified in this fashion, where traditional pulse-echo ultrasound measurements have been confounded by systematic uncertainty [112].

Beyond RUS, there are many other data analysis problems in experimental physics that stand to be improved using an approach similar to the one presented here [113]. In particular, any technique where simulation of a data set is straightforward but where fitting is difficult should be amenable to a framework of the type used here. The most immediately obvious technique where our algorithm could be applied is NMR spectroscopy. NMR produces spectra in a similar frequency range to RUS, but which originate in the spin-resonances of nuclear magnetic moments. Modern broad-band NMR can produce complex temperature-dependent spectra, containing resonances from multiple elements situated at different sites within the unit cell. Given a particular magnetic order it is relatively straightforward to calculate the NMR spectrum—i.e. to produce training data. The inverse problem, however, is more challenging: recovering a temperature-dependent magnetic structure from an NMR data set. In a way similar to RUS, missing resonances, and resonances mistakenly attributed to different elements, can render an analysis entirely invalid. It should be relatively straightforward to adapt our framework for generating training data and our ANN to extract temperature (or magnetic field) dependent magnetic structures from NMR spectra.

CHAPTER 5

SUPERCONDUCTIVITY OF Sr_2RuO_4

Superconductivity in Sr_2RuO_4 was discovered almost 30 years ago and immediately generated a lot of interest as it was the first oxide superconductor (SC) without copper [114]. It has the same tetragonal layered structure as one of the parent compound of cuprate SCs, La_2CuO_4 , with RuO_2 planes instead of CuO_2 planes, which are the main contributor to superconductivity in the cuprates. Soon after its discovery, multiple authors noted that Sr_2RuO_4 had similar normal-state properties as superfluid ^3He [115, 116], motivating the idea that Sr_2RuO_4 maybe a solid state spin-triplet SC. This was an exciting prediction which attracted the experimental community and ensured decades of intense research (see Ref. [4] for a review on Sr_2RuO_4). An upshot of this effort is that extremely clean single crystals of this material are available, leading to an unprecedented level of understanding of the electronic structure in the normal state of Sr_2RuO_4 from both quantum oscillations and angle-resolved photoemission spectroscopy (ARPES) studies [117, 118]. In spite of this, the superconducting order parameter (OP) has remained a mystery [119], and we describe in this chapter how RUS can place strong constraints on the order parameter. Significant portions of this chapter have been adapted from two papers: a *Nature Physics* paper [2] with Arkady Shekhter, F. Jerzembeck, N. Kikugawa, Dmitry A. Sokolov, Manuel Brando, A. P. Mackenzie, Clifford W. Hicks, and B. J. Ramshaw and an *arXiv* preprint [3] with Thomas G. Kiely, Arkady Shekhter, F. Jerzembeck, N. Kikugawa, Dmitry A. Sokolov, A. P. Mackenzie, and B. J. Ramshaw.

Most superconductors, including the BCS superconductors and the cuprates, are known to be spin-singlet SCs, where electrons with opposite spins form Cooper

pairs in the SC state. Antisymmetry of the Cooper pair wavefunction then requires that the orbital wavefunction of the pair is symmetric, that is, it belongs to an even angular momentum state. For example, the cuprates are known to have a $l = 2$, d -wave order parameter [32]. The pair wavefunction is $d_{x^2-y^2}$ and spin-singlet, which is antisymmetric in the spin sector and symmetric in the orbital sector—leading to an overall antisymmetric product. A spin-triplet SC, on the other hand, would be symmetric in the spin sector, and hence requires an odd angular momentum orbital state. For Sr_2RuO_4 , a $l = 1$, $p_x + ip_y$ order parameter was thus proposed, and most of the early experiments were interpreted in the context of this OP [120]. Such a chiral p -wave OP was also of interest because it is an example of topological superconductivity [121], and is expected to host gapless Majorana modes which could provide a platform for quantum computing [122].

5.1 Experimental evidences in Sr_2RuO_4

It is natural to ask why the order parameter in Sr_2RuO_4 has remained a mystery, given the availability of high-quality crystals with minimal amounts of disorder and the extensive experimental efforts to pin down the OP. One of the primary reasons is the discrepancies that exist between several large bodies of experimental evidences. A somewhat comprehensive list of experimental “facts” in Sr_2RuO_4 can be found in Ref. [45], we highlight the most important ones here which are useful to understand the inconsistencies.

One of the earliest evidences for spin-triplet pairing in Sr_2RuO_4 was an NMR Knight shift that was unchanged upon entering the superconducting state [123]. Knight shift measures the difference between spin susceptibility of an atom in free space and in a crystal, which provides a way to measure the local spin susceptibility.

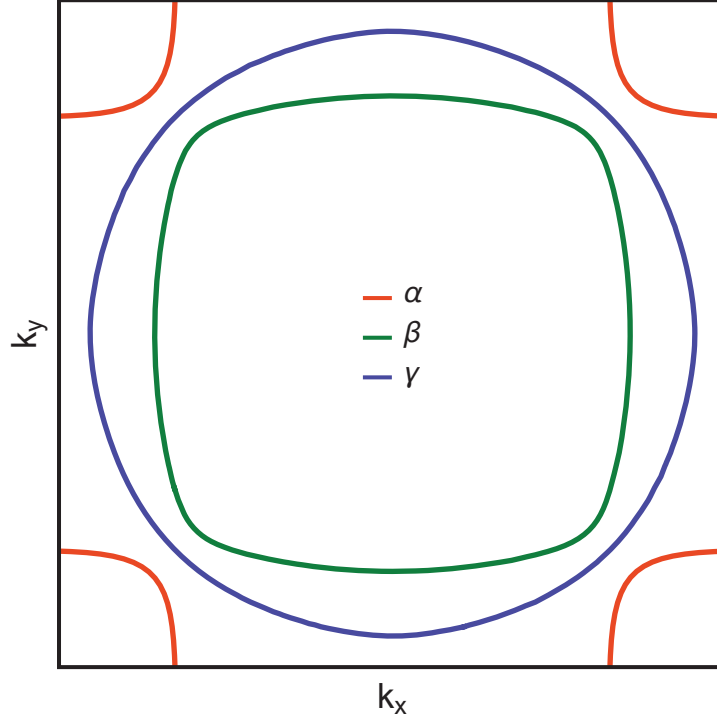


Figure 5.1: **Fermi surface of Sr_2RuO_4 .** The Fermi surface of Sr_2RuO_4 at $k_z = 0$, showing the α , β and γ bands.

For a spin-singlet SC, Knight shift decreases on entering the SC state since a singlet Cooper pair has net spin 0 in its wavefunction. In contrast, in a triplet SC, the net spin is 1 and thus the spin susceptibility may not decrease. An unchanged Knight shift was therefore compelling evidence for a triplet OP. Muon spin resonance (μSR), which probes the local magnetic environment in a SC [124], and polar Kerr effect [125] found evidence for time-reversal symmetry (TRS) breaking in the superconducting state. TRS breaking is naturally expected for a $p_x + ip_y$ OP since this is a chiral OP which can align as $p_x + ip_y$ or $p_x - ip_y$ depending on the external magnetic field direction. A field-trainable Kerr rotation, as seen by Xia et al. [125], was thus interpreted as supporting the $p_x \pm ip_y$ scenario. Evidence for triplet pairing also came from the observation of half-quantized vortices in magnetometry measurements [126].

Some of the primary objections to a triplet p-wave order parameter comes from the Pauli-limited upper critical field and the presence of nodes in the gap. The upper critical field (H_{c2}) in a spin-singlet SC occurs when the field is enough to break the Cooper pair. In units of teslas, this field is usually roughly equal to the transition temperature in kelvins. Superconductors where the critical field follows this are known as Pauli-limited in their upper critical field. The out-of-plane H_{c2} in Sr_2RuO_4 is ~ 1.5 T [127] while the T_c of best Sr_2RuO_4 crystals is ~ 1.5 K [128], providing strong evidence for a Pauli-limited H_{c2} . Given the electronic structure of Sr_2RuO_4 is essentially 2D, it should have much higher in-plane critical fields if it were a triplet SC [129]. Next, we explain why the presence of nodes does not fit into a $p_x + ip_y$ scenario. Nodes are regions in k -space where the superconducting gap, and hence the pairing strength, goes to zero. For example, in a $d_{x^2-y^2}$ gap, the nodes lie along the $[110]$ and $[\bar{1}10]$ directions. A $p_x + ip_y$ OP has a non-zero gap everywhere, and therefore should not have nodes. However, thermal conductivity [55] and ultrasound attenuation [7] measurements strongly indicate the presence of nodes in the gap. Both these experiments measure, in some way, the amount of normal quasiparticles present in the SC state. In a fully gapped SC, therefore, thermal conductivity or sound attenuation are expected to decrease exponentially. In Sr_2RuO_4 , they are seen to decrease slowly and follows a power law, which requires the presence of nodal regions in the gap giving rise to normal quasiparticles. Further support for gap nodes also come from scanning tunneling microscopy (STM) studies which conclude a $d_{x^2-y^2}$ OP for Sr_2RuO_4 [130].

The development of uniaxial strain-based experiments in the last decade has led to multiple striking observations in Sr_2RuO_4 [18, 131]. For a $p_x + ip_y$ OP, the superconducting T_c is expected to change linearly with uniaxial strain. Strain is also expected to split the transition temperatures for p_x and p_y components, and

therefore a Sr_2RuO_4 crystal under uniaxial strain should show two transitions. Though a split transition was not observed, these experiments instead showed a two-fold increase of T_c under strain along $[100]$ direction (at $\epsilon_{xx} \sim -0.44\%$). This has been understood in terms of strain tuning the γ band (see [Figure 5.1](#)) to the van Hove point that exists at the edge of the Brillouin zone, leading to an increased density of states [\[132\]](#). This motivated a revised version of the original NMR Knight shift experiment, which showed that the Knight shift is indeed suppressed below T_c [\[133, 134\]](#). Refs. [\[133, 134\]](#) found that the NMR pulses used in the original NMR experiment were actually heating the sample, thereby preventing it from becoming superconducting. This, followed by NMR experiments under in-plane magnetic fields, has now ruled out most triplet OPs [\[135\]](#). It thus becomes important to reconcile this with other existing pieces of evidence for a spin-triplet order parameter, and motivated our RUS experiments. Specifically, as we explain next, it should be possible to conclude whether Sr_2RuO_4 has one-component or two-component OP from RUS.

5.2 Strain-Order Parameter Coupling

Sr_2RuO_4 crystallizes in the tetragonal space group $I4/mmm$, along with its associated point group D_{4h} . In this crystal field environment, there are five unique strains: two compressive strains transforming as the A_{1g} irreducible representation (irrep), and three shear strains transforming as the B_{1g} , B_{2g} and E_g irreps (shown in [Figure 5.2](#)). Direct (linear) coupling between strain and the superconducting order parameter (η) is forbidden because superconductivity breaks gauge symmetry. The next relevant coupling is linear in strain and quadratic in order parameter. For one-component superconducting order parameters, including all s -wave states

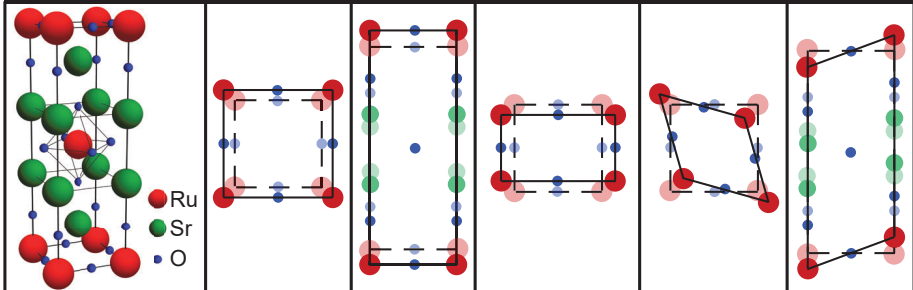
		Compression		Shear		
						
Coupling to order parameter	Representation	A_{1g}		B_{1g}	B_{2g}	E_g
	Elastic modulus	$(c_{11}+c_{12})/2$		c_{33}	$(c_{11}-c_{12})/2$	c_{66}
	One-component e.g. “d-wave” $\eta \sim d_{x^2-y^2}$	✓ $\epsilon_{A_{1g}} \cdot \eta^2$		✗	✗	✗
	Two-component e.g. “p-wave” $\eta \sim (p_x, p_y)\hat{z}$	✓ $\epsilon_{A_{1g}} \cdot (\eta_x^2 + \eta_y^2)$		✓ $\epsilon_{B_{1g}} \cdot (\eta_x^2 - \eta_y^2)$	✓ $\epsilon_{B_{2g}} \cdot (\eta_x \eta_y)$	✗

Figure 5.2: **Strain-order parameter coupling in Sr_2RuO_4 .** The tetragonal crystal structure of Sr_2RuO_4 and unit cell deformations that illustrate the irreducible representations of strain. There is an elastic modulus that corresponds to each of these strains, and a sixth modulus, c_{13} , arises from coupling between the two A_{1g} strains. Green check marks denote the allowed linear-order couplings to strain for superconducting order parameter bilinears, and red crosses denote that such coupling is forbidden. These couplings lead to discontinuities in the elastic moduli at T_c . A list of relevant possible order parameters in Sr_2RuO_4 is given in Table 5.3.

and the $d_{x^2-y^2}$ state, the only quadratic form is η^2 , transforming as A_{1g} , and thus the only allowed coupling is $\epsilon_{A_{1g}} \cdot \eta^2$. This coupling produces discontinuities in all the A_{1g} (compressional) elastic moduli across T_c . Two-component order parameters ($\vec{\eta} = \{\eta_x, \eta_y\}$), on the other hand, have three independent quadratic forms: $\eta_x^2 + \eta_y^2$, $\eta_x^2 - \eta_y^2$, and $\eta_x \eta_y$, transforming as A_{1g} , B_{1g} , and B_{2g} , respectively. Thus in addition to coupling to the A_{1g} elastic moduli, two-component order parameters couple to two of the shear moduli through $\epsilon_{B_{1g}} \cdot (\eta_x^2 - \eta_y^2)$ and $\epsilon_{B_{2g}} \cdot \eta_x \eta_y$. This produces discontinuities in the associated shear elastic moduli ($(c_{11} - c_{12})/2$ and c_{66} , respectively), based purely on symmetry considerations, and independent of

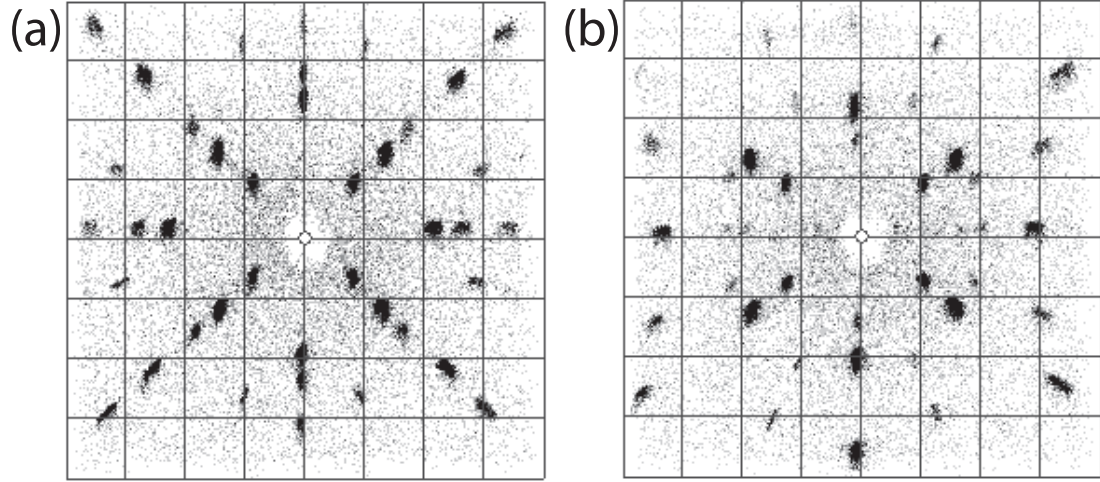


Figure 5.3: **Laue images of Sr_2RuO_4 sample.** Laue X-ray diffraction on the Sr_2RuO_4 RUS sample after aligning and polishing. Images obtained with X-rays incident on the (a) $[001]$ plane and (b) $[110]$ plane, with 110 mm distance between the X-ray source and the sample. The patterns show that the sample is extremely well-aligned with the crystal axes.

the microscopic mechanism of superconductivity.

5.3 Sample Details

The Sr_2RuO_4 sample used for all measurements reported here was grown by the floating-zone method, details of which can be found in [128]. A single crystal was oriented along the $[110]$, $[\bar{1}\bar{1}0]$ and $[001]$ directions, and polished to dimensions $1.50\text{mm} \times 1.60\text{mm} \times 1.44\text{mm}$, with 1.44mm along the tetragonal c -axis. Laue diffraction images obtained on the final sample are shown in Figure 5.3. The $[110]$ orientation of the crystal was accounted for when solving for the elastic moduli.

The quality of the Sr_2RuO_4 rod from which the RUS sample was cut was characterized by heat capacity and AC susceptibility measurements, shown in Figure 5.4. Heat capacity measurements of a large piece of the rod exhibit a T_c around 1.45

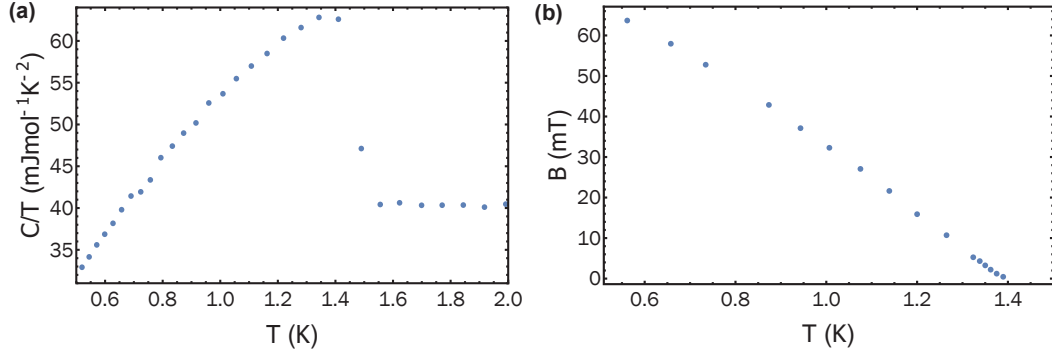


Figure 5.4: **Characterization of the Sr_2RuO_4 rod.** (a) Specific heat and (b) susceptibility measurements of the upper critical field, measured on different parts of the same rod from which the sample for RUS was obtained. T_c varies by ~ 200 mK between different parts of the rod.

K, which is close to the optimal T_c [136]. In addition to a relatively high T_c , a low concentration of ruthenium inclusions was an important criterion for the selection of the RUS sample. Ruthenium inclusions locally strain the crystal lattice and can enhance T_c up to 3 K. In order to check for ruthenium inclusions, AC susceptibility was measured by a mutual inductance method, which shows a sharp onset- T_c of 1.43 K, with no sign of a transition at 3 K, indicating a very low concentration of ruthenium inclusions. The variation in T_c between the heat capacity and the susceptibility/critical field experiments arises because the samples were taken from different parts of the same Sr_2RuO_4 rod. The Sr_2RuO_4 sample for the RUS experiments was also taken from the same rod, and the onset T_c of 1.425 K is in good agreement with the above-mentioned measurements.

5.4 High Temperature Elastic Moduli

We first measured the room temperature resonance frequencies of our Sr_2RuO_4 sample, from which we calculate the elastic constants at room temperature. Good

Temperature (K)	$\frac{c_{11}+c_{12}}{2}$ (GPa)	c_{33} (GPa)	c_{13} (GPa)	$\frac{c_{11}-c_{12}}{2}$ (GPa)	c_{44} (GPa)	c_{66} (GPa)
300 (Ref. [137])	169	208	71	63	65.7	61.2
300	176.1	243.2	84.8	62.4	67.6	64.8
60	190.4	256.2	85.3	53.0	69.4	65.3
4	190.8	257.2	85.0	53.1	69.5	65.5

Table 5.1: **Elastic moduli of Sr_2RuO_4 measured with RUS.**

agreement is found with the moduli values reported by Paglione et al. [137], listed in Table 5.1. We note that the c_{33} value we measure is more dependable than that in Ref. [137], since their resonance spectrum did not have a mode dominated by c_{33} . Once we have a reliable room temperature fit, we can measure a subset of frequencies as the sample is cooled down to get the temperature evolution of the moduli. All the frequency versus temperature data taken on this Sr_2RuO_4 sample was acquired through the standard lock-in technique. A large softening in the B_{1g} shear modulus $(c_{11} - c_{12})/2$ is observed on cooling down from room temperature. We present a simple calculation that may account for this anomalous behavior in the following section.

5.4.1 Anomalous $(c_{11} - c_{12})/2$ Softening

The behavior of the compressional modulus $(c_{11} + c_{12})/2$ and two in-plane shear moduli, $(c_{11} - c_{12})/2$ and c_{66} , associated with B_{1g} and B_{2g} shear strains respectively, is shown in Figure 5.5 (a). The increase in c_{66} on cooling is standard, and is expected from an anharmonic lattice [101, 102]. In contrast, $(c_{11} - c_{12})/2$ shows a large ($\sim 20\%$) softening from room temperature on cooling down. The softening in $(c_{11} - c_{12})/2$ can be fit well with a Curie-Weiss temperature dependence (see Figure 5.5 (b)) till it changes its behavior near $T_{FL} \approx 35$ K, which is the

temperature around which Sr_2RuO_4 becomes a coherent three-dimensional Fermi liquid [138, 139].

Generally, a strong softening in a shear modulus precedes a nematic or a structural transition in the material [15, 140, 141]. In Sr_2RuO_4 , however, this behavior is possibly attributed to the nearness of the γ -band to the edge of the Brillouin zone. In particular, uniaxial strain along [100] direction (ϵ_{xx}) is known to effectively tune the γ -band closer to the van Hove singularity (vHs) [131], leading to a so-called Lifshitz transition in the band structure at $\epsilon_{xx} \sim 0.44\%$ [132]. This amount of ϵ_{xx} , at 4 K, induces a compressional strain $(\epsilon_{xx} + \epsilon_{yy})/2 = 0.11\%$ and B_{1g} shear strain $(\epsilon_{xx} - \epsilon_{yy})/2 = 0.33\%$, so roughly 3 times more shear than compressional. On straining Sr_2RuO_4 through the Lifshitz transition, non-Fermi liquid features in resistivity [142] and NMR Knight shift [143] have also been experimentally observed.

We performed a simple calculation to check whether proximity to a van Hove singularity can lead to a softening elastic modulus. We start with the tight-binding parameters for the γ -band of Sr_2RuO_4 outlined in Burganov et al. [144], with the dispersion

$$\varepsilon_\gamma(k_x, k_y) = -\mu_1 - 2[t_x \cos(k_x a) + t_y \cos(k_y b)] - 2t_4 [\cos(k_x a + k_y b) + \cos(k_x a - k_y b)], \quad (5.1)$$

where $\mu_1 = 176$ meV, $t_x = t_y = 119$ meV, $t_4 = 49$ meV and $a = b = 3.869$ Å. Given the dispersion, we define the grand canonical free energy

$$\Xi(T, \mu, \varepsilon_\gamma(k_x, k_y)) = -k_B T \ln \left[1 + \exp \left(-\frac{\varepsilon_\gamma(k_x, k_y) - \mu}{k_B T} \right) \right], \quad (5.2)$$

where T is the temperature, μ is the chemical potential (Fermi energy in our case) and k_B is Boltzmann's constant. Under applied strain ϵ , the dispersion of the γ -band is modified, which introduces a strain dependence in Equation 5.2. We use

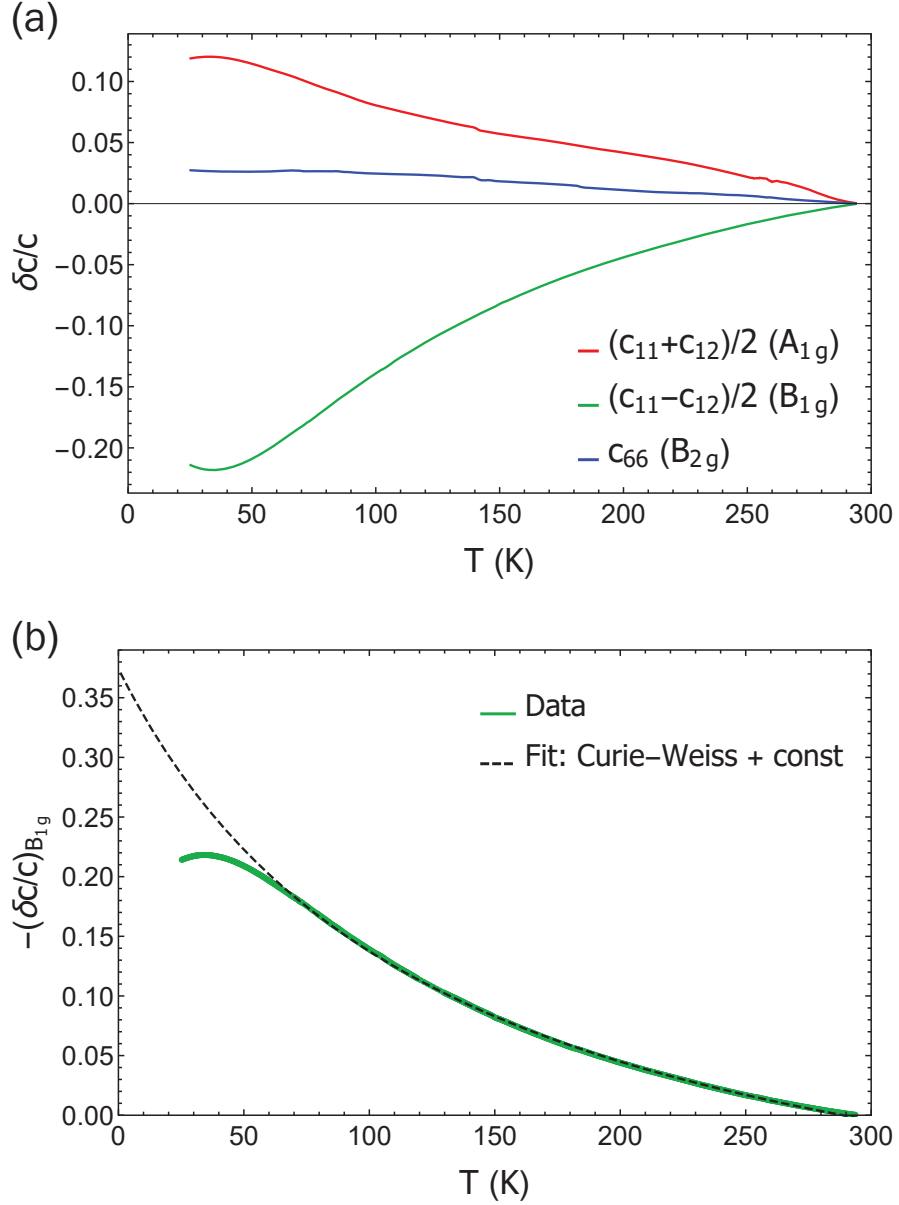


Figure 5.5: **High-temperature elastic moduli in Sr_2RuO_4 .** (a) The three in-plane elastic moduli of Sr_2RuO_4 , between room temperature and 25 K. (b) The B_{1g} modulus is fit to a Curie-Weiss form ($\sim (T - T_0)^{-1}$), yielding $T_0 \approx -128$ K. Good agreement is found over most of the temperature range, before the data is seen to deviate from the fit around 50 K. We plot the moduli as fractional changes $\frac{\delta c(T)}{c} = \frac{c(T)}{c(293 \text{ K})} - 1$.

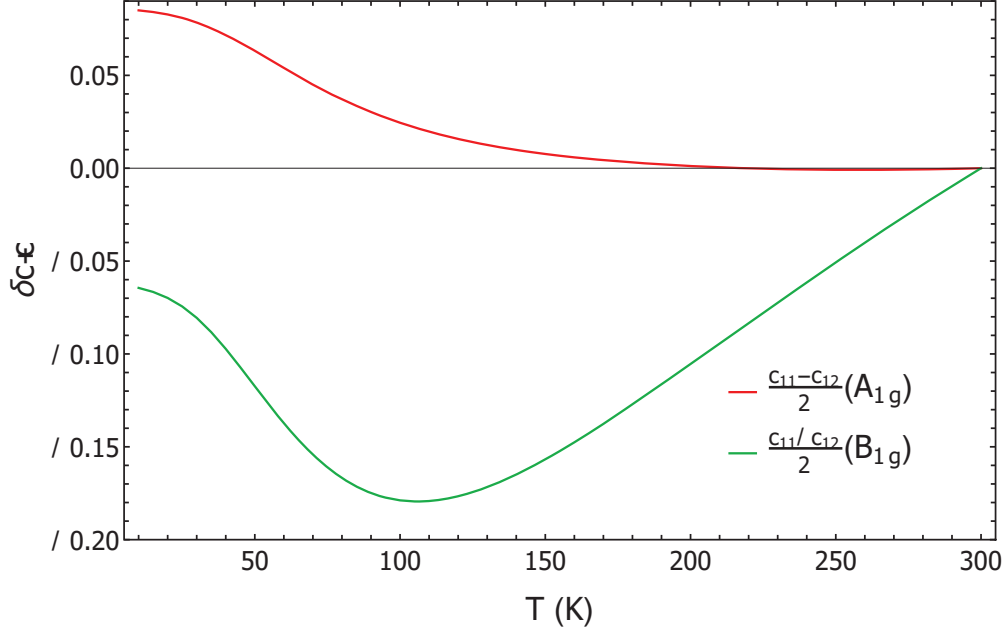


Figure 5.6: **Calculated elastic moduli in Sr_2RuO_4 .** The in-plane A_{1g} and B_{1g} elastic moduli of Sr_2RuO_4 calculated within a simple non-interacting picture of a single band close to a van Hove singularity. A large softening is seen in the B_{1g} modulus.

the strain-dependence of tight-binding parameters reported in Ref. [142]. For A_{1g} strain $\epsilon_{A_{1g}} = (\epsilon_{xx} + \epsilon_{yy})/2$, they are modified as

$$a' = b' = a(1 + \epsilon_{A_{1g}}), t'_x = t'_y = t_x(1 - \alpha\epsilon_{A_{1g}}), t'_4 = t_4(1 - 1.2\alpha\epsilon_{A_{1g}}). \quad (5.3)$$

For B_{1g} strain $\epsilon_{B_{1g}} = (\epsilon_{xx} - \epsilon_{yy})/2$, they become

$$a' = a(1 + \epsilon_{B_{1g}}), b' = b(1 - \epsilon_{B_{1g}}), t'_x = t_x(1 - \alpha\epsilon_{B_{1g}}), t'_y = t_y(1 + \alpha\epsilon_{B_{1g}}). \quad (5.4)$$

Here, α is a tunable parameter that characterizes the change in hopping strength with strain. We use $\alpha = 5$ for the calculations shown. Note that B_{1g} strain modifies the diagonal length $\sqrt{a'^2 + b'^2}$ on the order ϵ^2 , hence we assume t_4 stays the same under B_{1g} strain.

Within this formalism, the elastic moduli as a function of temperature are

calculated as,

$$\frac{c_{11} + c_{12}}{2}(T) = \int \int dk_x dk_y \frac{\partial^2}{\partial \epsilon_{A_{1g}}^2} \Xi(T, \mu, \varepsilon_\gamma(k_x, k_y, \epsilon_{A_{1g}})) , \quad (5.5)$$

$$\frac{c_{11} - c_{12}}{2}(T) = \int \int dk_x dk_y \frac{\partial^2}{\partial \epsilon_{B_{1g}}^2} \Xi(T, \mu, \varepsilon_\gamma(k_x, k_y, \epsilon_{B_{1g}})) . \quad (5.6)$$

We numerically integrate over the 1st Brillouin zone to get the results shown in [Figure 5.6](#). A large softening is found in the B_{1g} modulus as T is decreased from room temperature before it recovers to usual behavior at low enough temperatures, even though the minima appears at a different temperature in the calculations compared to data ([Figure 5.7 \(a\)](#)). The calculated behavior of $(c_{11} + c_{12})/2$ also appears to qualitatively match the measured $(c_{11} + c_{12})/2$. We note that this calculation only includes electrons in the γ -band, there are also the α and β bands in Sr_2RuO_4 whose strain-dependence is probably much weaker. Additionally, it is misleading to compare absolute values of elastic moduli obtained from this calculation to those actually measured in Sr_2RuO_4 . The presence of the lattice definitely provides most of the stiffness to a material, and our calculation does not include the lattice. We also assumed the strain-dependence of the hopping terms to be temperature independent over the 300 K range, which may not be true. Even with these caveats, our overly simplistic calculation still appears to capture the qualitative changes in these two moduli well—implying that the anomalous softening behavior of $(c_{11} - c_{12})/2$ can arise from the proximity of the γ -band to the van Hove point.

We now comment on how a physical picture maybe formed from these calculations. A B_{1g} strain brings the γ -band closer to the vHs, and thus the B_{1g} elastic modulus measures how strongly the system resists this deformation. The temperature dependence ([Figure 5.6](#)) shows it becomes easier to impose this deformation as temperature is lowered from 300 K, $\frac{\partial c_{B_{1g}}}{\partial T} > 0$. Recent elastocaloric experi-

ments [23] show that the entropy (S) is maximum at the van Hove strain $\epsilon = \epsilon_{\text{vHs}}$, that is, $\left. \frac{\partial S}{\partial \epsilon} \right|_{\epsilon_{\text{vHs}}} = 0$. Intuitively, this makes sense since there is a diverging density of states (DOS) at the van Hove point. Using the Maxwell relation

$$\frac{\partial c_{B_{1g}}}{\partial T} = -\frac{\partial^2 S}{\partial \epsilon_{B_{1g}}^2}, \quad (5.7)$$

we can relate the temperature derivative of $(c_{11} - c_{12})/2$ to an entropy derivative. At high temperatures, thermal fluctuations can access the diverging density of states (DOS) at the van Hove point, and therefore the response $\frac{\partial c_{B_{1g}}}{\partial T}$ at zero strain is qualitatively similar to what would be at the van Hove strain. It is easy to check from the above equation that

$$\frac{\partial c_{B_{1g}}}{\partial T} > 0 \implies \frac{\partial^2 S}{\partial \epsilon_{B_{1g}}^2} < 0. \quad (5.8)$$

This is indeed the expected behavior if the entropy is maximum at ϵ_{vHs} . At low enough temperatures, the access to the diverging DOS, and hence the entropy maximum, is eventually cut off. Now, zero strain point becomes a entropy minimum as any finite B_{1g} strain brings the system closer to the vHs. In this regime, the derivative

$$\frac{\partial^2 S}{\partial \epsilon_{B_{1g}}^2} > 0 \implies \frac{\partial c_{B_{1g}}}{\partial T} < 0, \quad (5.9)$$

leading to an increasing elastic modulus on cooling. The exact crossover temperature possibly depends on the DOS near the van Hove point, as well as the B_{1g} strain dependence of the hopping parameters for the γ -band.

The significance of the van Hove singularity in affecting the Fermi liquid properties in Sr_2RuO_4 has been investigated in recent times [132, 142, 143], primarily using large uniaxial strains to traverse through the vHs. Our measurements, coupled with the simple calculation for $(c_{11} - c_{12})/2$, show that certain elastic moduli (defined at zero-strain limit) can also show effects from the vHs. As a future step,

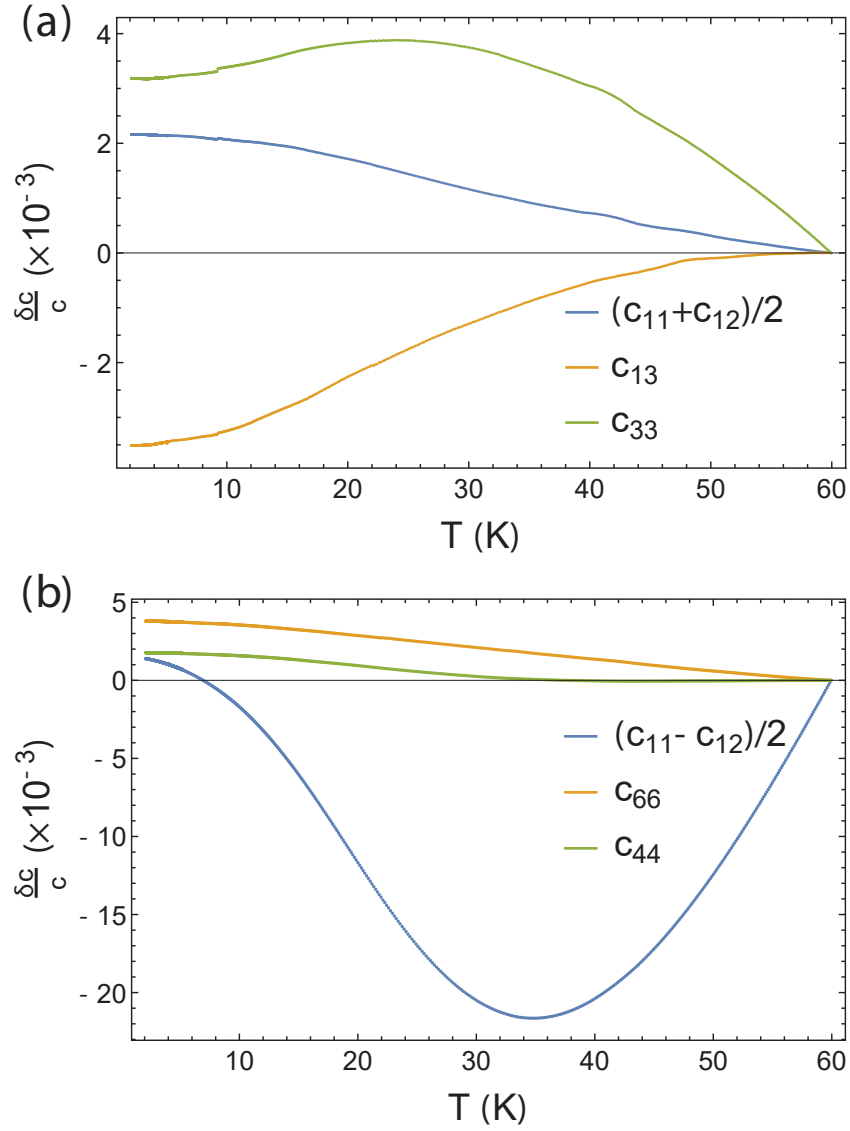


Figure 5.7: **Temperature evolution of elastic moduli in Sr_2RuO_4 .** (a) Compressional and (b) shear moduli of Sr_2RuO_4 measured with RUS between 60 K and 2 K. We plot the moduli as fractional changes $\frac{\delta c(T)}{c} = \frac{c(T)}{c(60 \text{ K})} - 1$.

it would be exciting to calculate the temperature evolution of elastic moduli of Sr_2RuO_4 with standard DFT-based tools [145–147] that can incorporate the entire band structure and effects of the lattice.

5.5 Elastic Moduli Across T_c

We measured multiple resonances across the superconducting transition of Sr_2RuO_4 to get the elastic moduli through T_c . The frequency data shown in [Figure 5.8](#), consisting of 18 resonances, was acquired over several sweeps through T_c , measuring a few resonances each time. We observe a sharp (40 mK wide) superconducting transition, signifying uniform sample cooling. To ensure consistency between different sweeps, we measured one frequency (2495 kHz) in all the sweeps and checked that its temperature evolution looks the same for different temperature sweeps.

5.5.1 Jump in c_{66}

To symmetry-resolve the frequency data into the six irreducible moduli, we interpolate the frequency versus temperature data, and then plot the elastic moduli at what we consider to be a representative set of temperatures—those from the sweep where we measured the resonances at 2495 kHz, 2549 kHz, and 2551 kHz. The final data set includes 18 resonances (see [Figure 5.8](#)). The three compressional moduli ($(c_{11} + c_{12})/2$, c_{33} , and c_{13}) and the three shear moduli ($(c_{11} - c_{12})/2$, c_{44} , and c_{66}) as a function of temperature are shown in [Figure 5.9](#). Discontinuities across T_c are clearly observed in all three compressional moduli, as required by thermodynamics for all superconductors, as well as in the shear modulus c_{66} . The discontinuity in c_{66} is forbidden by symmetry for one-component order parameters, but is allowed for two-component order parameters—this discontinuity is our central finding.

Having measured all six elastic moduli across T_c , we can perform several consistency checks. First, since there is no bilinear coupling of the order parameter to

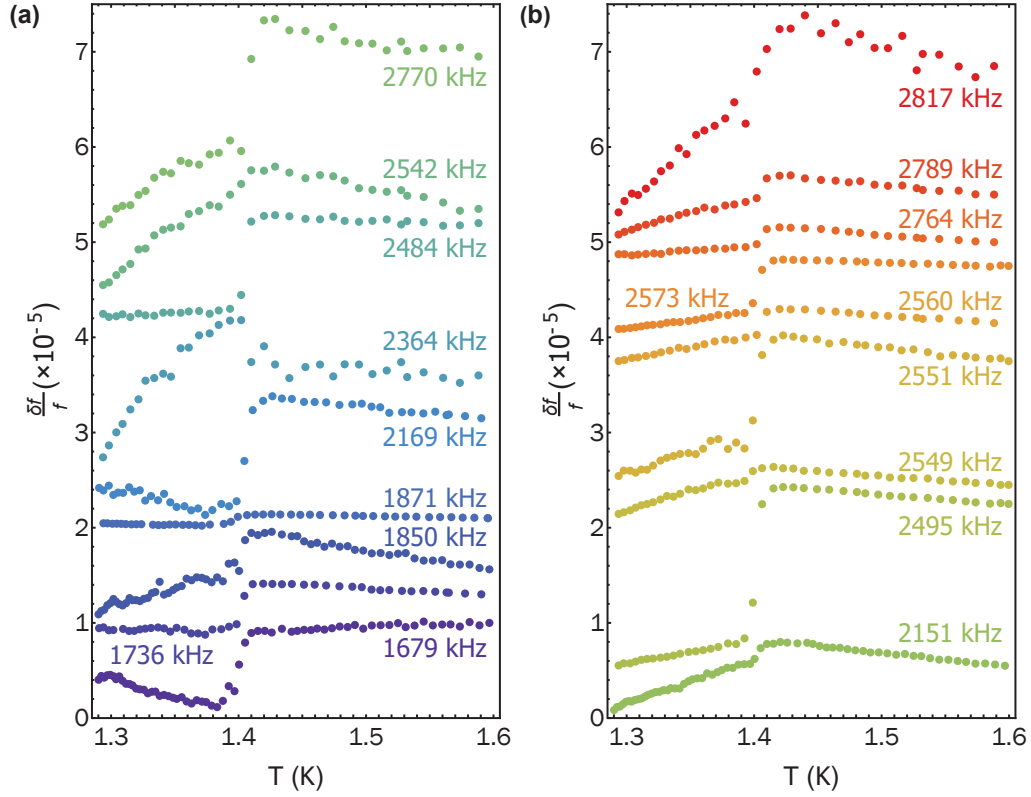


Figure 5.8: **Resonance frequencies of Sr_2RuO_4 through T_c .** Temperature evolution of 18 resonance frequencies of Sr_2RuO_4 through T_c , with panels (a) and (b) each showing 9 frequencies. These were used to calculate the six independent moduli in Sr_2RuO_4 . Plots are vertically shifted for visual clarity.

E_g strain, c_{44} should not have a discontinuity at T_c for any superconducting order parameter. Within our experimental uncertainty, we observe only a change in the slope of c_{44} at T_c , which is expected on general grounds and is not constrained by symmetry [31]. Second, thermodynamics dictates that the discontinuities in the three compressional moduli at a second order phase transition should follow a self-consistency relation (see Equation 2.38),

$$\left(\Delta \frac{c_{11} + c_{12}}{2} \right) \times (\Delta c_{33}) = (\Delta c_{13})^2. \quad (5.10)$$

From our measurement, we find $(\Delta \frac{c_{11} + c_{12}}{2}) \times (\Delta c_{33}) = (9.9 \pm 1.5) \times 10^{-5} \text{ GPa}^2$ and $(\Delta c_{13})^2 = (8.3 \pm 1.1) \times 10^{-5} \text{ GPa}^2$. These consistency checks validate our measurement of the magnitude of the jumps, and our ability to correctly decompose

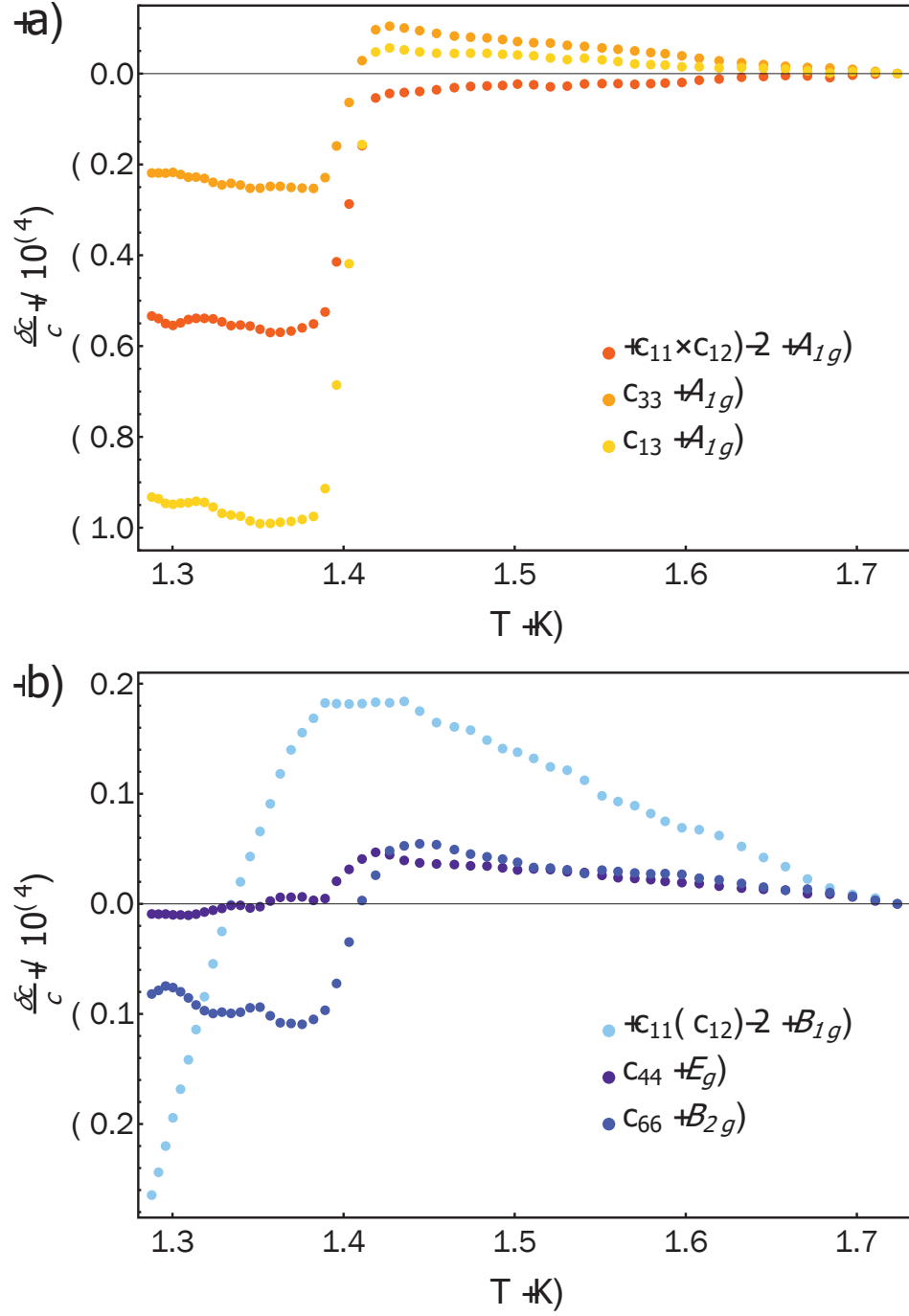


Figure 5.9: **Elastic moduli of Sr_2RuO_4 through T_c .** (a) Compressional and (b) shear moduli of Sr_2RuO_4 measured through the superconducting transition ($T_c \approx 1.42$ K).

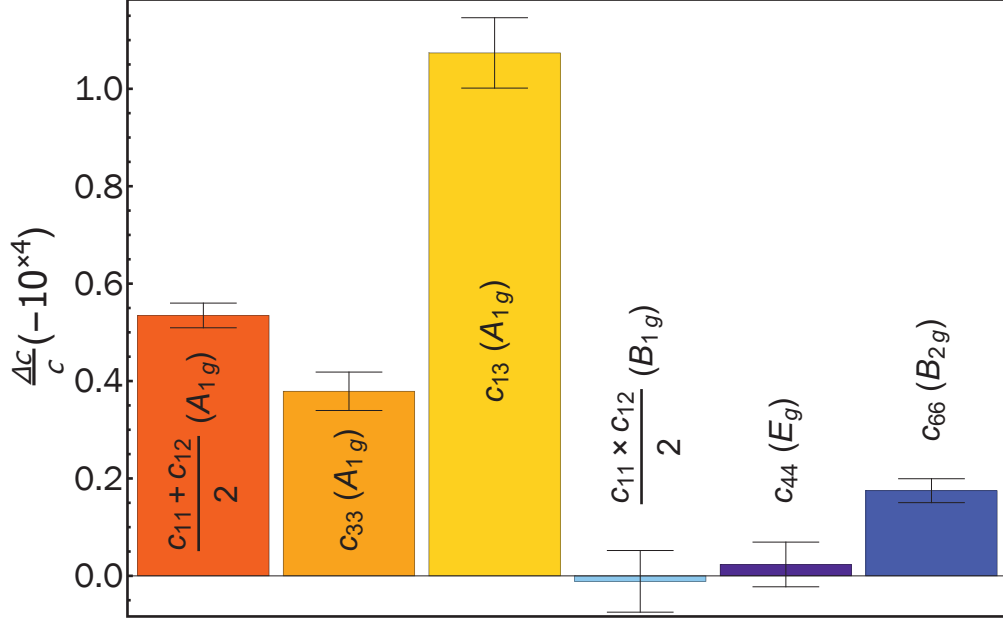


Figure 5.10: **Discontinuities in elastic moduli of Sr_2RuO_4 .** Magnitudes of the jumps ($\frac{\Delta c}{c}$) at T_c , along with their experimental uncertainties. Non-zero jumps are seen only in all the compressional (A_{1g}) moduli, and in the shear modulus c_{66} .

the jumps in frequency into jumps in the irreducible elastic moduli.

5.5.2 Uncertainty Analysis

While visual inspection is usually sufficient to determine whether or not a particular modulus shows a discontinuity at T_c , numerical values are needed to perform consistency checks on the data, and to make quantitative predictions for future experiments.

One source of uncertainty comes from the width of the superconducting transition. To extract the jump magnitudes and their associated uncertainties in a consistent fashion for all the moduli, we use fits above and below T_c to extrapolate the data across the transition (see Figure 5.11). We take the jump as the difference between the two extrapolated fits at the experimentally-obtained temperature

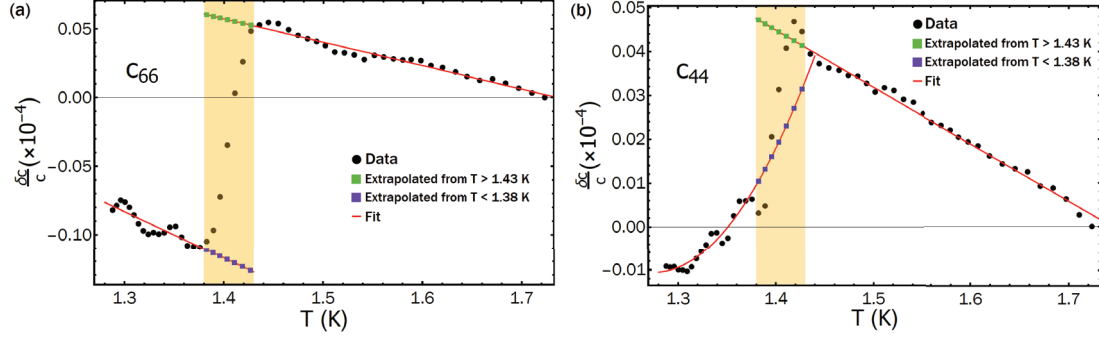


Figure 5.11: **Extracting the jumps in moduli and their uncertainties.** We extrapolate fits to data (red lines) from above and below T_c at temperature points within the transition (highlighted in yellow). The average between the minimum and maximum jump is taken to be the jump magnitude; the difference is the uncertainty. This procedure is illustrated for c_{66} in panel (a), and c_{44} in panel (b). Note the significantly reduced vertical scale in (b) as compared to (a).

points between 1.38 K and 1.43 K, which is the width of the superconducting transition. This gives a (non-Gaussian) distribution of modulus jumps that correspond to different T_c assignments. We take the uncertainty to be half the difference of the minimum and maximum jumps, and assign the jump itself to the mean.

A second source of uncertainty comes from the sample dimensions, which are used to extract the elastic moduli from the resonance frequencies. Slight deviations from parallelism, rounding of the sample corners, and other small imperfections give an upper-bound on the dimensional uncertainty of ± 20 microns in each direction. This dimensional uncertainty is then incorporated into the elastic moduli calculations (described in Ref. [12]), yielding an uncertainty in the moduli.

Assuming that the two sources of uncertainty (dimensional uncertainty, and the uncertainty in assigning T_c) are independent, we add them in quadrature to obtain the total uncertainty in each jump (see Figure 5.10), tabulated in Table 5.2.

We have neglected uncertainty due to misalignment of the crystal axes with respect to the sample faces because our crystal was aligned to better than 2° for

Elastic Modulus	$\frac{(c_{11}+c_{12})}{2}$ (A_{1g})	c_{33} (A_{1g})	c_{13} (A_{1g})	$\frac{(c_{11}-c_{12})}{2}$ (B_{1g})	c_{44} (E_g)	c_{66} (B_{2g})
Fractional Jump Size ($\times 10^{-5}$)	5.35	3.79	10.74	-0.07	0.22	1.75
Uncertainty from T_c width ($\times 10^{-5}$)	0.09	0.02	0.10	0.49	0.13	0.04
Uncertainty from Dimensions ($\times 10^{-5}$)	0.24	0.39	0.72	0.41	0.44	0.24
Total Uncertainty ($\times 10^{-5}$)	0.25	0.39	0.72	0.64	0.46	0.25

Table 5.2: **Experimental uncertainties in moduli jumps in Sr_2RuO_4 .** The two sources of uncertainty—from width of superconducting transition and from sample dimensions—are added in quadrature to get the total uncertainty in the jump in the six moduli. This leads to the error bars plotted in [Figure 5.10](#).

all 3 axes. The effect of misalignment can be calculated by finding the rotated elastic tensor \mathbf{C}' (see [Appendix C](#) for details). For example, a rotation by an angle γ about the a -axis transforms the shear elastic modulus c_{44} as

$$c'_{44} = \frac{1}{8} [4c_{44} (1 + \cos 4\gamma) + (c_{11} + c_{33} - 2c_{13}) (1 - \cos 4\gamma)]. \quad (5.11)$$

For $\gamma = 2^\circ$, c'_{44} differs from c_{44} by one part in 10^3 . This introduces a jump into c'_{44} that is 1 part in 10^7 —an order of magnitude smaller than the other sources of uncertainty. Similar expressions can be derived for the other moduli and are similarly small.

5.5.3 Ehrenfest Relations

Ehrenfest relations provide a way to relate the elastic moduli jumps to the specific heat jump at the superconducting transition. Since we know the specific heat discontinuity on our Sr_2RuO_4 sample, these relations allow us to perform further consistency checks on our measured moduli discontinuities.

For compressional, or A_{1g} , strains, there is an Ehrenfest relation (see [Subsection 2.5.1](#)) that relates the derivative of T_c with hydrostatic pressure, P , to the discontinuities at T_c in the specific heat, ΔC , and the bulk modulus, ΔB , via

$$\left(\frac{dT_c}{dP}\right)^2 = -\frac{\Delta B}{B^2} \left(\frac{\Delta C}{T}\right)^{-1}. \quad (5.12)$$

Our measurements give $\Delta B/B \sim 6.3 \times 10^{-5}$, about 9 times larger than estimated from specific heat jump for this sample (see [Figure 5.4](#)) $\Delta C/T = 25 \text{ mJmol}^{-1}\text{K}^{-2} = 435 \text{ Jm}^{-3}\text{K}^{-2}$ and $dT_c/dP_{hyd} = 0.3 \text{ K/GPa}$ [[148](#)] or, alternatively, the measured jump in the bulk modulus predicts $dT_c/dP_{hyd} = 0.9 \text{ K/GPa}$, a factor of 3 higher than the measured value. This discrepancy may be evidence for a pair of transitions occurring at or near the superconducting T_c , as discovered by μSR experiments [[19](#)]. The two transition temperatures split when stress is applied along the x direction—Meissner screening onsets at the higher transition temperature, T_c , while time reversal symmetry is broken at the lower transition, T_{TRSB} . It is necessary to map out T_{TRSB} with pressure to correctly calculate the Ehrenfest relations, which are modified under the presence of two accidentally degenerate order parameters [[45](#)].

Another possibility is the formation of order parameter domains [[41](#)], which lead to an additional slowing down of ultrasound and therefore a larger drop in the elastic moduli through T_c . We explore how domains may couple to ultrasound further in [Subsection 5.6.3](#). The value of dT_c/dP_{hyd} estimated from the data in [[148](#)] may not reflect the true pressure dependence of T_c . Since the T_c of Sr_2RuO_4 shows a strong increase with B_{1g} strain [[18](#)], the measured decrease in T_c under P_{hyd} will be less if the pressure applying medium is not completely hydrostatic. This is particularly relevant because the B_{1g} modulus is almost 4 times smaller than $(c_{11} + c_{12})/2$, which makes it easy to induce B_{1g} strain if the pressure medium is not hydrostatic.

We now consider a similar Ehrenfest relation—derived for the jump in c_{66} rather than the jump in bulk modulus. We show in [Subsection 2.5.2](#) that the shear modulus jump Δc_s can be related to $\Delta C/T$ (at zero strain) through the strain derivatives of these two transition temperatures, T_c and T_{TRSB} ,

$$\Delta c_s = -\frac{\Delta C}{T} \left| \frac{dT_1}{d\epsilon_s} \right| \left| \frac{dT_2}{d\epsilon_s} \right|, \quad (5.13)$$

where s is either B_{1g} or B_{2g} , $T_1 = T_c$, and $T_2 = T_{TRSB}$. Within weak coupling, T_c should shift linearly with B_{2g} strain, specifically as $T_c \propto |\epsilon_{xy}|$. Prior measurements of T_c as a function of ϵ_{xy} , however, have not found this linear dependence on strain [\[18\]](#). In addition, a crystal under shear strain should show two specific heat jumps [\[50\]](#), and, for a chiral OP, time-reversal symmetry breaking (TRSB) should set in at a different temperature than Meissner effect. Recent μ SR experiments [\[19\]](#) have indeed reported the latter effect.

5.5.4 Possible Two-component OPs

As explained above, a discontinuity in c_{66} at T_c can only result from a two-component superconducting order parameter (see [Table 5.3](#)). This is a critical piece of information because evidence for vertical line nodes in the superconducting gap—from ultrasonic attenuation [\[7\]](#), heat capacity [\[149\]](#), thermal conductivity [\[55\]](#), and quasiparticle interference [\[130\]](#)—are most straightforwardly interpreted in terms of a one-component, $d_{x^2-y^2}$, order parameter. With the discovery of a suppression of the Knight shift strongly suggesting that the order parameter cannot be spin-triplet [\[133, 135\]](#), $d_{x^2-y^2}$ would seem a likely contender. The discontinuity in c_{66} , however, rules against *any* one-component order parameter, including $d_{x^2-y^2}$.

Dimensionality	Order Parameter	Irrep.	Moduli Jumps	Ultrasound	NMR
One-component	s	A_{1g}	A_{1g}	\times	\checkmark
	$d_{x^2-y^2}$	B_{1g}	A_{1g}	\times	\checkmark
	d_{xy}	B_{2g}	A_{1g}	\times	\checkmark
Two-component	$\{p_x, p_y\} \hat{\mathbf{z}}$	E_u	A_{1g} B_{1g} B_{2g}	\checkmark	\times
	$p_z \{\hat{\mathbf{x}}, \hat{\mathbf{y}}\}$	E_u	A_{1g} B_{1g} B_{2g}	\checkmark	\times
	$\{d_{xz}, d_{yz}\}$	E_g	A_{1g} B_{1g} B_{2g}	\checkmark	\checkmark
	$\{d_{x^2-y^2}, g_{xy}(x^2-y^2)\}$	$B_{1g} \oplus A_{2g}$	A_{1g} B_{2g}	\checkmark	\checkmark

Table 5.3: **Some superconducting order parameters in D_{4h} .** For the odd-parity spin-triplet order parameters, $\hat{\mathbf{x}}$, $\hat{\mathbf{y}}$ and $\hat{\mathbf{z}}$ represent the pair wavefunction in spin space in the \mathbf{d} -vector notation [4]. Two-component order parameters $\{\eta_x, \eta_y\}$ can order as η_x , η_y , $\eta_x \pm \eta_y$, or $\eta_x \pm i\eta_y$, depending on microscopic details. It is this latter combination that forms the time-reversal symmetry breaking state (e.g. $(p_x + ip_y)\hat{\mathbf{z}}$, or $d_{xz} + id_{yz}$). The “Ultrasound” column indicates whether an order parameter is consistent with a jump in c_{66} at T_c , the “NMR” column indicates whether it is consistent with the suppression of the Knight shift at T_c . Note that the $B_{1g} \oplus A_{2g}$ state does not belong to a single irrep of D_{4h} , and thus transition temperatures of the d and g components must be “fine-tuned” if they are to coincide.

Our measurement is consistent with several two-component p -wave scenarios, including $(p_x \pm ip_y)\hat{\mathbf{z}}$ and $p_z(\hat{\mathbf{x}} \pm i\hat{\mathbf{y}})$. Taken at face value, however, the suppression of the Knight shift [133, 135] rules out all p -wave order parameters and is consistent only with spin-singlet order parameters. The only “conventional” spin-singlet order parameter that produces a jump in c_{66} at T_c is $\{d_{xz}, d_{yz}\}$. This state can order into the non-magnetic d_{xz} , d_{yz} , or $d_{xz} \pm d_{yz}$ states, all of which break the C_4 rotational symmetry of the lattice. It can also order into the chiral, magnetic $d_{xz} \pm id_{yz}$ state. If one considers the possibility of an accidental degeneracy between two order parameters of different representations, producing accidental

two-component order parameters, then $\{d_{xy}, s\}$ and $\{d_{x^2-y^2}, g_{xy(x^2-y^2)}\}$ are also consistent with our experiment ($\{d_{x^2-y^2}, s\}$ [150] produces a jump in $(c_{11} - c_{12})/2$ but not in c_{66}). We set aside $\{d_{xy}, s\}$ because it thought to be incompatible with the electronic structure of Sr_2RuO_4 . If one accepts time-reversal symmetry breaking at T_c as a property of Sr_2RuO_4 , there are then two remaining order parameters that are compatible with our experiment: $d_{xz} \pm id_{yz}$, and $d_{x^2-y^2} \pm ig_{xy(x^2-y^2)}$. The absence of a discontinuity in $(c_{11} - c_{12})/2$ implies that there is no order-parameter-bilinear that transforms as B_{1g} , which would rule out $d_{xz} \pm id_{yz}$. It is possible, however, that while a jump in $(c_{11} - c_{12})/2$ is required thermodynamically, it is either unobservably small because the coupling coefficient is small (for microscopic reasons), or the jump is smeared-out due to high ultrasonic attenuation in the B_{1g} channel [7]. Thus we consider the implications of both the $d_{xz} \pm id_{yz}$ and the $d_{x^2-y^2} \pm ig_{xy(x^2-y^2)}$ superconducting states in Sr_2RuO_4 .

The first of these, $d_{xz} \pm id_{yz}$, is the chiral-ordered state of $\{d_{xz}, d_{yz}\}$ —a two-component E_g representation [151]. There are two main arguments against such a state. First, $\{d_{xz}, d_{yz}\}$ has a horizontal line node at $k_z = 0$, whereas most experiments suggest that the nodes lie along the $[110]$ and $[\bar{1}10]$ directions [7, 55, 130, 149]. There is some evidence, however, for a horizontal line node from angle-dependent heat capacity measurements [152]. Second, Sr_2RuO_4 has very weak interlayer coupling [117], and in the limit of weak interlayer coupling, the pairing strength for this state goes to zero. A recent weak-coupling analysis shows that an E_g state can be stabilized by including momentum-dependent spin orbit coupling [153, 154], and such spin-orbit coupling has been quantified by ARPES in Sr_2RuO_4 [118, 155, 156]. This variant of the E_g state has Bogoliubov Fermi surfaces (rather than line nodes) that extend along the k_z direction in a manner that may mimic line-nodes as far as experiment is concerned.

The second possibility, $d_{x^2-y^2} \pm ig_{xy(x^2-y^2)}$, is less natural in that $d_{x^2-y^2}$ is a B_{1g} irrep and $g_{xy(x^2-y^2)}$ is an A_{2g} irrep [45]. Order parameters of different representations have, in general, distinct transition temperatures, and therefore the composite $B_{1g} \oplus A_{2g}$ order parameter requires fine-tuning to produce a single superconducting transition. Fine-tuning aside, this state has two attractive features. First, it produces bilinears only in the A_{1g} and B_{2g} channels ($B_{1g} \otimes A_{2g} = B_{2g}$). This would naturally explain why a jump is seen in c_{66} but not in $(c_{11} - c_{12})/2$. Second, this state has line nodes along the $[110]$ and $[\bar{1}10]$ directions [7, 55, 130]. While the $l = 4$, $g_{xy(x^2-y^2)}$ state may seem exotic, it has been shown (in the weak-coupling regime) to be competitive with $d_{x^2-y^2}$ when nearest-neighbor repulsion is accounted for [5].

Both of these two-component order parameters produce a discontinuity in c_{66} , break time reversal symmetry, are Pauli limited in their upper critical field, exhibit a drop in the Knight shift below T_c , and have ungapped quasiparticles. The accidental degeneracy of $d_{x^2-y^2} \pm ig_{xy(x^2-y^2)}$ means that its T_c should split into two transitions under any applied strain, and indeed, the aforementioned μ SR measurements have found evidence for such a splitting [19]. This suggests that Sr_2RuO_4 may indeed have two nearly degenerate transitions at ambient pressure.

5.6 Sound Attenuation in Sr_2RuO_4

The rest of this chapter is devoted to sound attenuation measurements in Sr_2RuO_4 . We first focus on how sound attenuation changes through T_c , and its implications for the superconducting order parameter. We also discuss a striking feature in the low temperature normal state shear attenuation, and how that may be understood

within a simple model of strain-tuning of the γ band.

5.6.1 Sound Attenuation in Superconductors

An important prediction of Bardeen, Cooper, and Schrieffer (BCS) theory is the contrasting behavior of the nuclear spin relaxation rate, $1/T_1$, and the ultrasonic attenuation, α [157]. Upon cooling from the normal state to the superconducting (SC) state, one might expect both $1/T_1$ and α to decrease as both processes involve the scattering of normal quasiparticles. In the SC state, however, Cooper pairing produces correlations between quasiparticles of opposite spin and momentum. These correlations produce “coherence factors” that add constructively for nuclear relaxation and produce a peak—the Hebel-Slichter peak—in $1/T_1$ immediately below T_c [158]. In contrast, the coherence factors add destructively for sound attenuation and there is an immediate drop in α below T_c [159]. These experiments provided some of the strongest early evidence for the validity of BCS theory [157], and the drop in sound attenuation below T_c was subsequently confirmed in many elemental superconductors [13, 160–162].

Against this backdrop, it came as a surprise when sound attenuation peaks were discovered below T_c in two heavy-fermion superconductors: UPt_3 and UPe_{13} [163–165]. Specifically, peaks were observed in the longitudinal sound attenuation—when the sound propagation vector \mathbf{q} is parallel to the sound polarization \mathbf{u} : $\mathbf{q} \parallel \mathbf{u}$. Transverse sound attenuation ($\mathbf{q} \perp \mathbf{u}$), on the other hand, showed no peak below T_c but instead decreased with power law dependencies on T that were ultimately understood in terms of the presence of nodes in the SC gap [166]. Various theoretical proposals were put forward to understand the peaks in the longitudinal sound attenuation, including collective modes, domain-wall fric-

tion, and coherence-factors [34, 167–169], but the particular mechanisms for UPt_3 and UBe_{13} were never pinned down (see Sigrist et al. [30] for a review).

Given that the superconductivity of Sr_2RuO_4 has many unconventional aspects, the coherence factors for Sr_2RuO_4 are expected to differ from the s -wave BCS case, and there is also the possibility of low-energy collective modes [170] and domain-wall motion [47], all of which could be observable in the ultrasonic attenuation when measured at appropriate frequencies. Prior ultrasonic attenuation measurements, using the pulse-echo technique, on Sr_2RuO_4 reported a power-law temperature dependence of the transverse sound attenuation, interpreted as evidence for nodes in the gap [7, 171], but found no other unconventional behavior. Pulse-echo operates at frequencies of order 100 MHz and higher, which may be too high to observe certain dynamical processes. Attenuation measurements using RUS operate at much lower frequencies, and can separate the compression and the shear responses. This allows us to observe features of the superconducting state in Sr_2RuO_4 not observed in previous measurements.

5.6.2 Attenuation Measurement in RUS

When the sound wavelength, $\lambda = \frac{2\pi}{q}$, is much longer than the electronic mean free path l , i.e. when $ql \ll 1$, the electron-phonon system is said to be in the ‘hydrodynamic’ limit [172] (this is different than the hydrodynamic limit of electron transport). Given that the best Sr_2RuO_4 has a mean free path that is at most of order a couple of microns, and that our experimental wavelengths are of the order of 1 mm, we are well within the hydrodynamic limit. In this limit, in a metal, sound attenuation is known to increase as ω^2 [173], where ω is the sound frequency. Usually pulse-echo ultrasound is employed to measure the sound atten-

uation coefficient α , which is extracted by fitting the exponential decay envelope of consecutive reflected pulses to

$$u = u_0 e^{-\frac{\alpha}{2}x}, \quad (5.14)$$

see Ref. [171] for details of the technique.

In our RUS experiments, sound attenuation introduces a finite linewidth Γ for each resonance, giving them a characteristic Lorentzian shape (details in [Subsection 3.4.1](#)). Each resonance ω_0 is a superposition of the various irreducible strains, and is therefore a function, \mathfrak{F} , of the independent elastic moduli c_j , the density ρ , and the dimensions l_k of the sample:

$$\omega_0^2 = \mathfrak{F}(c_j, \rho, l_k). \quad (5.15)$$

Within linear response, sound attenuation is related to the rate of strain through the viscosity tensor [166], which has the same symmetries as the elastic tensor. This can be accounted for by introducing an imaginary part to the elastic constants, which leads to energy dissipation. To relate the experimentally measured linewidths to the irreducible viscosities, we replace $\omega_0 \rightarrow \omega_0 + i\Gamma/2$ and $c_j \rightarrow c_j + i\omega_0\eta_j$ in [Equation 5.15](#) and expand to leading order in Γ and η_j :

$$\begin{aligned} (\omega_0 + i\Gamma/2)^2 &= \mathfrak{F}(c_j + i\omega_0\eta_j, \rho, l_k) \\ \implies \omega_0^2 + i\omega_0\Gamma &\approx \mathfrak{F}(c_j, \rho, l_k) + \sum_j \frac{\partial \mathfrak{F}}{\partial c_j} \cdot i\omega_0\eta_j \\ \implies \Gamma &= \sum_j \frac{\partial \mathfrak{F}}{\partial c_j} \cdot \eta_j = \omega_0^2 \sum_j \alpha_j \frac{\eta_j}{c_j}, \end{aligned} \quad (5.16)$$

where $\alpha_j = \partial(\ln \omega_0^2)/\partial(\ln c_j)$ and $\sum_j \alpha_j = 1$. Knowing the coefficients α_j , which are determined by our fitting algorithm, we can therefore use [Equation 5.16](#) to calculate the independent viscosities (six in Sr_2RuO_4) as a function of temperature by measuring the temperature evolution of sufficiently many resonance linewidths

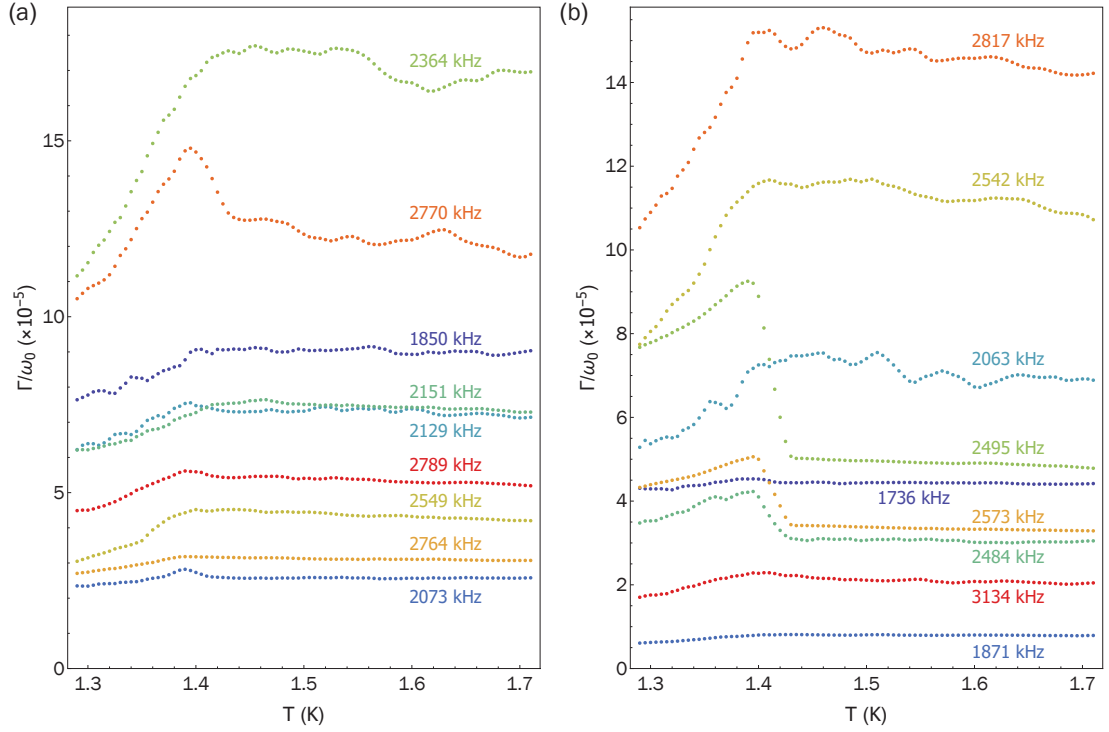


Figure 5.12: **Resonance linewidths of Sr_2RuO_4 through T_c .** Temperature evolution of normalized resonance linewidth of 18 resonances of Sr_2RuO_4 through T_c , with panels (a) and (b) each showing 9 resonances. These 18 resonances were used to calculate the six independent components of the viscosity tensor through T_c .

(typically 2-3 times the number of independent viscosities). We note that [Equation 5.16](#) is true in the weak attenuation limit ($\Gamma \ll \omega_0$), which is easily satisfied in our experiments— $\Gamma/\omega_0 \sim 10^{-4}$ for all our measured resonances.

5.6.3 Increase in Compressional Viscosities

We measured the linewidths of 18 resonances through T_c (shown in [Figure 5.12](#)) and resolved them into the independent components of the viscosity tensor. Because the viscosity itself is only very weakly frequency dependent in a Fermi liquid, and because Sr_2RuO_4 is a good Fermi liquid at low temperatures above T_c [[148](#)],

we can directly compare our measured viscosities to those made at much higher frequencies by pulse-echo ultrasound. Similar to the six independent elastic moduli, there are six independent viscosity components in Sr_2RuO_4 , arising from the five irreducible representations (irreps) of strain in D_{4h} plus one component arising from coupling between the two distinct compression strains. The six symmetry-resolved components of viscosity in Sr_2RuO_4 are plotted in [Figure 5.13](#).

The shear viscosity $(\eta_{11} - \eta_{12})/2$ decreases below T_c in a manner similar to what is observed in conventional superconductors [[13](#), [159](#)]. We find that $(\eta_{11} - \eta_{12})/2$ is much larger than the other two shear viscosities, which is consistent with previous pulse-echo ultrasound experiments [[7](#), [171](#)]. On converting attenuation to viscosity, we find very good agreement between the resonant ultrasound and pulse-echo measurements of $(\eta_{11} - \eta_{12})/2$. The small values of η_{44} and η_{66} are comparable to the experimental background and any changes at T_c are too small to resolve at these low frequencies. We briefly discuss how background attenuation affects our measurement in [Subsection 5.6.6](#).

In contrast with the rather conventional shear viscosities, the three compressional viscosities each exhibit a strong increase below T_c . For in-plane compression—the strain that should couple strongest to the largely two-dimensional superconductivity of Sr_2RuO_4 —this increase is more than a factor of seven. After peaking just below T_c , the attenuation slowly decreases as the temperature is lowered. The large increase in compression viscosity below T_c was not observed in previous longitudinal sound attenuation measurements made by pulse-echo ultrasound [[7](#), [171](#)]. There are two likely explanations for this. First, the L100 mode measured in pulse echo experiments measures η_{11} , which should be thought of as a mixture of the shear viscosity $(\eta_{11} - \eta_{12})/2$ and the compression

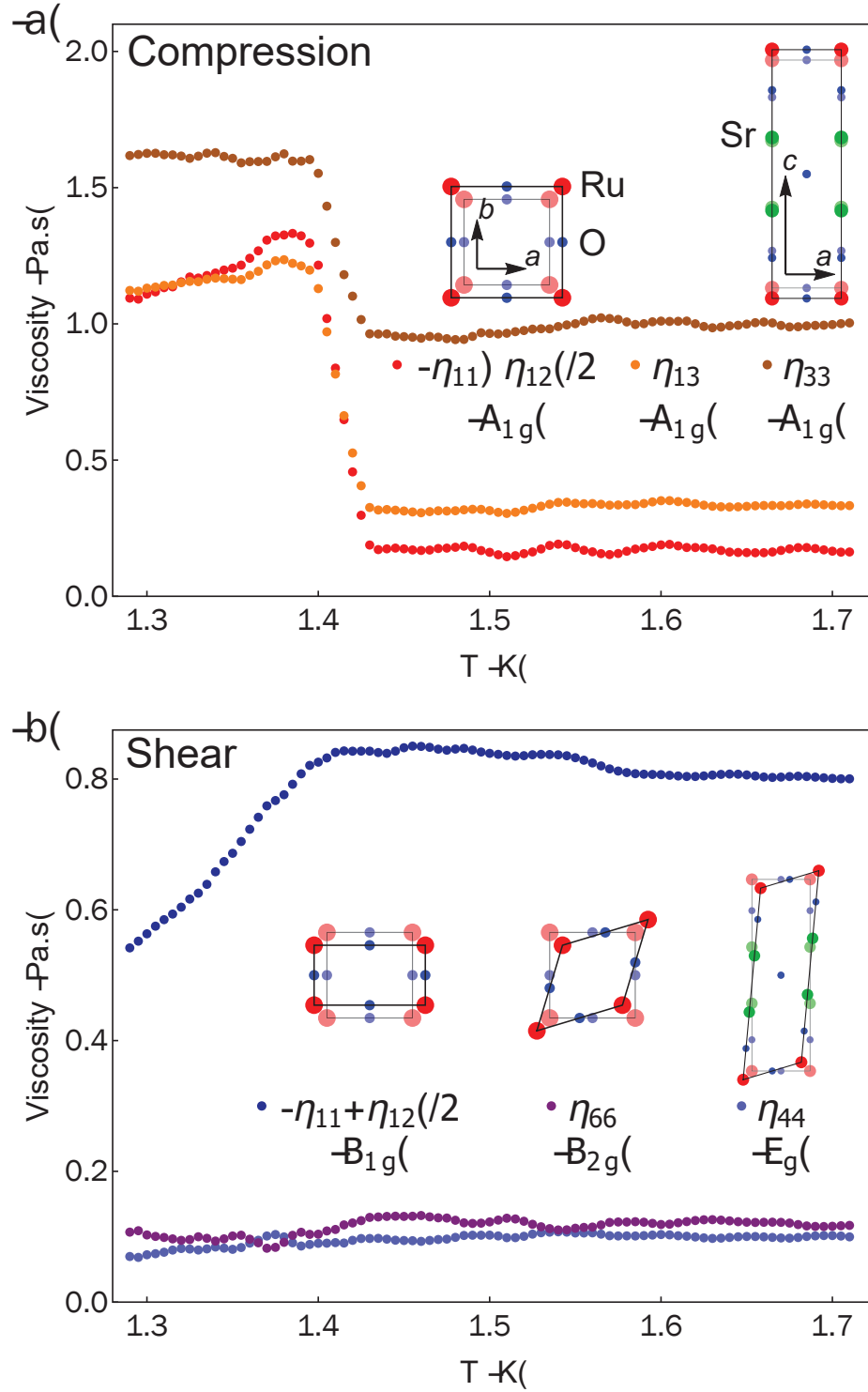


Figure 5.13: **Symmetry-resolved viscosities in Sr_2RuO_4 through T_c .** (a) Compressional and (b) shear viscosity of Sr_2RuO_4 measured through the superconducting transition ($T_c \approx 1.42$ K).

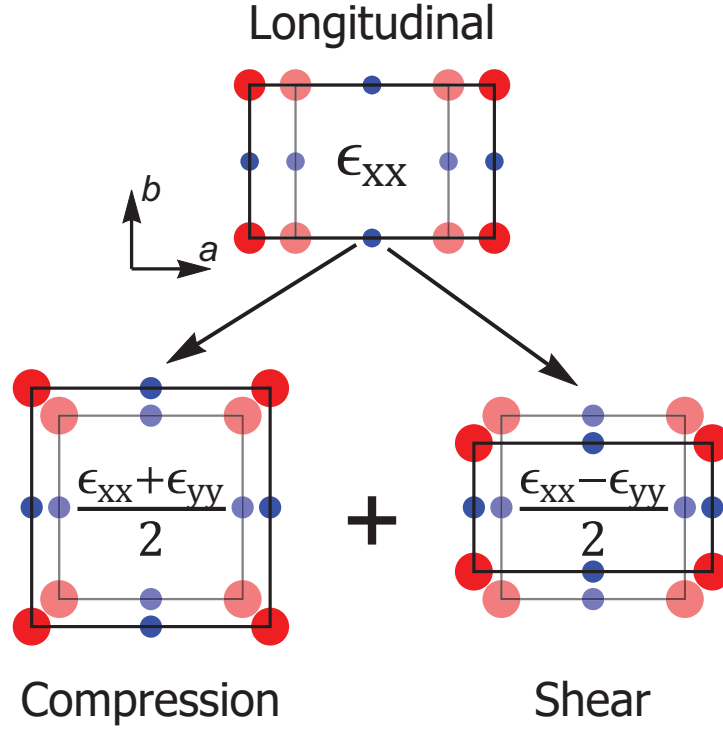


Figure 5.14: **Relation between L100 and irreducible strains.** The Sr_2RuO_4 unit cell under a deformation corresponding to the longitudinal strain ϵ_{xx} , which is excited in L100 mode in pulse-echo. This mode is a superposition of pure compression $\epsilon_{xx} + \epsilon_{yy}$ and pure shear $\epsilon_{xx} - \epsilon_{yy}$.

viscosity $(\eta_{11} + \eta_{12})/2$ (see Figure 5.14). Because $(\eta_{11} - \eta_{12})/2$ is an order of magnitude larger than the $(\eta_{11} + \eta_{12})/2$, the shear viscosity completely dominates the signal. Second, the pulse echo experiments are conducted at frequencies that are two orders of magnitude higher than those of the RUS experiments and the difference in time scales between the ultrasound and the dynamics of the attenuation mechanism plays an important role—we discuss this in details next.

5.6.4 Understanding the Increase in Viscosity

The factor of seven increase seen in the in-plane compressional viscosity is without precedent in a superconductor. For comparison, longitudinal attenuation increases by 50% below T_c in UPt₃ [165], and by a bit more than a factor of two in UBe₁₃ [164]. There is also a qualitative difference between the increase in Sr₂RuO₄ and the increase seen in the heavy fermion superconductors: the attenuation peaks sharply below T_c in both UPt₃ and UBe₁₃, with a peak width of approximately 10% of T_c . The compressional attenuation in Sr₂RuO₄, by contrast, decreases by only about 10% over the same relative temperature range. This suggests that something highly unconventional occurs in the SC state of Sr₂RuO₄, leading to a large increase in sound attenuation that is not confined to temperatures near T_c .

We consider a few possible mechanisms that could give rise to such an increase in sound attenuation below T_c . First, we calculate sound attenuation within a BCS-like framework that accounts for the differences in coherence factors that occur for various unconventional SC order parameters. We find that a peak can indeed arise under certain circumstances but not under our experimental conditions. Second, we consider phonon-induced Cooper pair breaking in the SC state that does lead to a sound attenuation peak just below T_c , but which is inaccessibly narrow in our experiment. We then show that a simple model of sound attenuation due to the formation of SC domains best matches the experimental data. We also consider relaxational order parameter dynamics near T_c , and find that domains fit the data better than absorption by OP relaxation.

First we examine the possibility of increased sound attenuation due to coherent scattering in the SC state. Sound attenuation and nuclear spin relaxation in an s-wave superconductor are proportional to the coherence factors

$F_{\pm} = (1 \pm \Delta_0^2/E_k E_{k'})$, where Δ_0 is the uniform s-wave gap and E_k is the Bogoliubov quasiparticle dispersion [157, 174]. Scattering off of a nucleus flips the spin of the quasiparticle and the resultant coherence factor is F_+ , where the + sign produces the Hebel-Slichter peak below T_c . Scattering off of a phonon, on the other hand, does not flip quasiparticle spin and the resultant coherence factor is F_- , producing a sharp drop in sound attenuation below T_c . In general, the coherence factors depend on the structure of the superconducting gap, motivating the idea that an unconventional superconducting OP might produce a peak in the sound attenuation. Calculating within the BCS framework, we find that attenuation for a $d_{x^2-y^2}$ gap decays slowly compared to the isotropic s-wave gap, but does not exhibit a peak (Figure 5.15(a)). This slow decrease can be attributed to the presence of nodes in the $d_{x^2-y^2}$ gap [175, 176]. For a TRS breaking gap such as $p_x + ip_y$ or $d_{xz} + id_{yz}$, a Hebel-Slichter-like peak appears below T_c if sufficiently large-angle scattering is allowed (Figure 5.15(b)). Scattering at these large wavevectors—essentially scattering across the Fermi surface—would require ultrasound with nanometer wavelengths. This regime is only accessible at THz frequencies, whereas our experiment operates in the MHz range. Hence we rule out coherent scattering as the mechanism of increased compressional sound attenuation below T_c .

Next we consider how phonon-induced Cooper pair breaking may give rise to a sound attenuation peak, similar to what has been observed in superfluid $^3\text{He-B}$ below T_c [177]. Pair-breaking in BCS superconductors requires a minimum energy of $2\Delta_0$, where Δ_0 is the gap magnitude. This energy scale is generally much higher than typical ultrasound energies. For example, the maximum gap magnitude in Sr_2RuO_4 is $2\Delta_0 \sim 0.65$ meV [178], which would require a frequency of approximately 1 THz to break the Cooper pairs. However, the pair-breaking

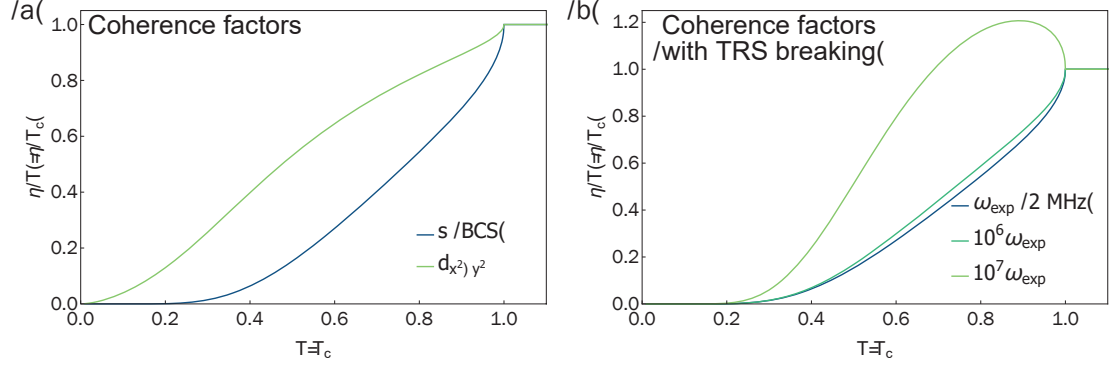


Figure 5.15: **Sound attenuation due to coherence factors.** (a) Normalized viscosity ($\eta(T)/\eta(T_c)$) for an isotropic s -wave gap and a $d_{x^2-y^2}$ gap, calculated within the BCS framework. (b) $\eta(T)/\eta(T_c)$ for a time reversal symmetry breaking gap below T_c . A peak is seen at high enough frequencies ($\sim \text{THz}$) but not at our experimental frequencies ($\sim \text{MHz}$). These calculations were done by Thomas G. Kiely.

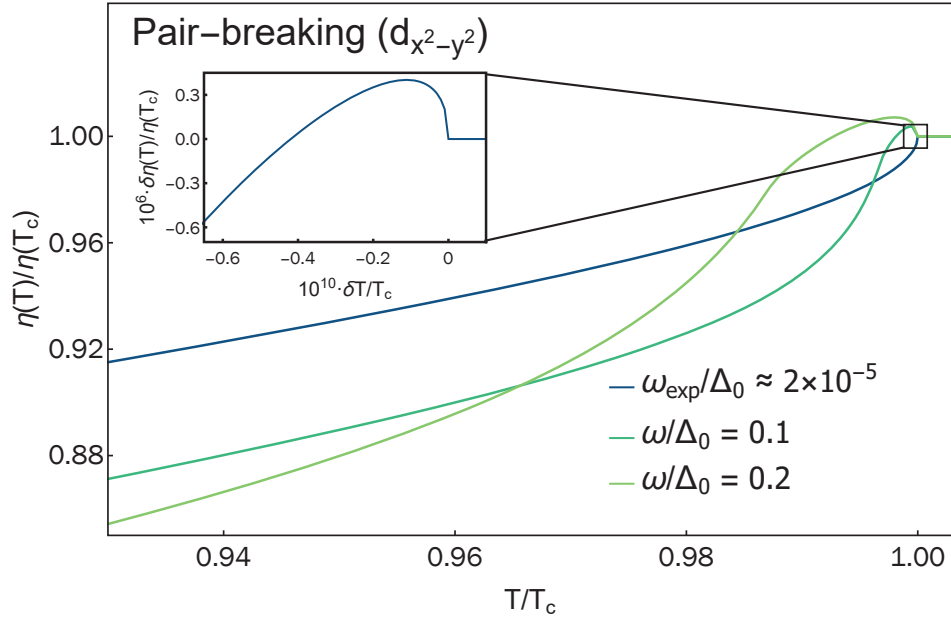


Figure 5.16: **Sound attenuation due to Cooper pair breaking.** Attenuation peak at different frequencies due to pair-breaking effects in a $d_{x^2-y^2}$ gap. The inset shows the plot at our experimental frequency in detail—a tiny peak is seen about 0.01 nK below T_c ($\delta\eta(T) = \eta(T) - \eta(T_c)$ and $\delta T = T - T_c$). These calculations were done by Thomas G. Kiely.

energy is lowered for a gap with nodes, such as $d_{x^2-y^2}$. In particular, since the gap goes to zero at T_c , it may be small enough near T_c such that pair-breaking is possible at a few MHz. Our calculations for a $d_{x^2-y^2}$ gap, however, show that ~ 10 GHz frequencies are required to produce an experimentally discernible peak (Figure 5.16). At our experimental frequencies, the peak is only visible within 0.01 nK of T_c . For a fully gapped superconductor, like the TRS breaking state $p_x + ip_y$, the peak will be even smaller. This clearly rules out pair-breaking as the origin of the increased sound attenuation.

Finally, we consider the formation of superconducting domains in a multi-component superconductor (SC), which provides an additional mechanism of sound attenuation below T_c [168]. We briefly outline the idea here followed by Sigrist et al. [30] to derive the sound attenuation due to domains. In a multi-component SC, such as $p_x + ip_y$, different order parameters are degenerate in energy and can exist simultaneously in different parts of the sample, forming domains. These domains are separated by regions where the OP changes from one of its stable configurations to another—these are the domain walls. In RUS, when a mechanical resonance of the sample is excited, a unique strain pattern is created in the sample. This deforms the domain walls and changes the relative areas of the domains it separates. This process takes energy, which comes from the ultrasonic excitation. The amount of energy it absorbs depends on the strain-OP coupling in the different domains.

In Ref. [30], an expression is derived for how domain wall motion leads to enhanced sound attenuation, which we write in the form

$$\alpha = \left(\frac{4\lambda^2\omega^2}{\pi^2 a \gamma \rho v^3} \right) \frac{\rho_s^2}{\omega^2 + \omega_{DW}^2} \implies \eta \propto \frac{\alpha}{\omega^2} \propto \frac{\rho_s^2}{\omega^2 + \omega_{DW}^2}. \quad (5.17)$$

The sound velocity v , density of sample ρ and the experimental frequency ω are known. The factors λ —the energy difference arising from the deformation of do-

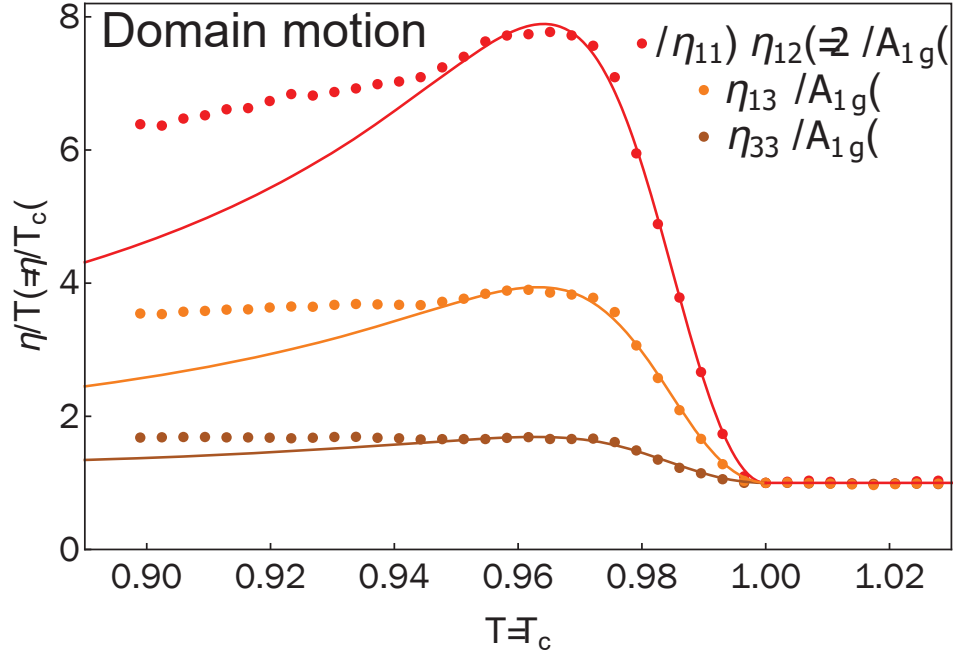


Figure 5.17: **Sound attenuation due to domain wall motion.** Normalized viscosity in the A_{1g} channels of Sr_2RuO_4 through T_c , fit to the viscosity expected from domain wall motion below T_c .

main walls by strain, a —the average size of domains and γ , which characterizes the relaxation of domain walls back to their equilibrium position, are not known quantitatively. These parameters are assumed to not depend on frequency or temperature. The temperature-dependence of this expression comes from the superfluid density ρ_s and domain wall frequency ω_{DW} , which, within a simple Ginzburg-Landau (G-L) OP expansion around T_c , vary as $\rho_s \sim |1 - T/T_c|$ and $\omega_{DW} \sim |1 - T/T_c|^{3/2}$. This gives us the expression we fit to the data,

$$\eta(\omega, T) = A \frac{|1 - T/T_c|^2}{\omega^2 + \omega_1^2 |1 - T/T_c|^3}, \quad (5.18)$$

where all the microscopic coefficients have been subsumed into the coefficient A ,

$$A = \frac{4\lambda^2\omega^2}{\pi^2 a \gamma \rho v^3}. \quad (5.19)$$

Near T_c , ρ_s and ω_{DW} can be expanded within a Ginzburg-Landau (GL) formalism as $\rho_s \propto |T - T_c|$ and $\omega_{DW} \propto |T - T_c|^{3/2}$. This gives an explicit temperature

dependence to Equation 5.18:

$$\eta(\omega, T) = A \frac{|T/T_c - 1|^2}{\omega^2 + \omega_1^2 |T/T_c - 1|^3}, \quad (5.20)$$

where ω_1 is ω_{DW} in the limit $T \rightarrow 0$.

We fit all three measured viscosities to Equation 5.20 and extract $\omega_1 = 500 \pm 25$ MHz (Figure 5.17). As the temperature approaches T_c from below, the domain wall frequency decreases to zero, producing a peak in the attenuation when the ultrasound frequency is approximately equal to the domain wall frequency. Note that η becomes frequency dependent in the presence of domain walls, in contrast to the frequency-independent viscosity of the Fermi liquid state above T_c . We use the average experimental frequency $\omega = 2.5$ MHz to extract ω_1 . Although our analysis uses resonance frequencies spanning 1.7 to 3.2 MHz, the position of the peak in η changes by only about 14 mK over this frequency range, justifying our use of a single frequency for the fit (see Figure 5.18).

The fit of Equation 5.20 deviates from the data for $T/T_c \lesssim 0.95$. This may be because of additional temperature dependencies, such as the temperature dependence of the domain wall frequency, that are not captured by the GL expansion, which is only valid near T_c [30]. Nevertheless, Equation 5.20 captures the correct shape of the rapid increase in attenuation below T_c in all three compression channels, using the same value of ω_1 for all three fits. The extracted frequency scale of $\omega_1 \approx 500$ MHz is also reasonable: studies of sound attenuation in nickel at MHz frequencies show similar magnitudes of increase in the magnetically ordered state when domains are present [179]. We note that the results of Josephson interferometry measurements have previously been interpreted as evidence for SC domains in Sr_2RuO_4 [180].

The formation of the SC order parameter below T_c can lead to relax-

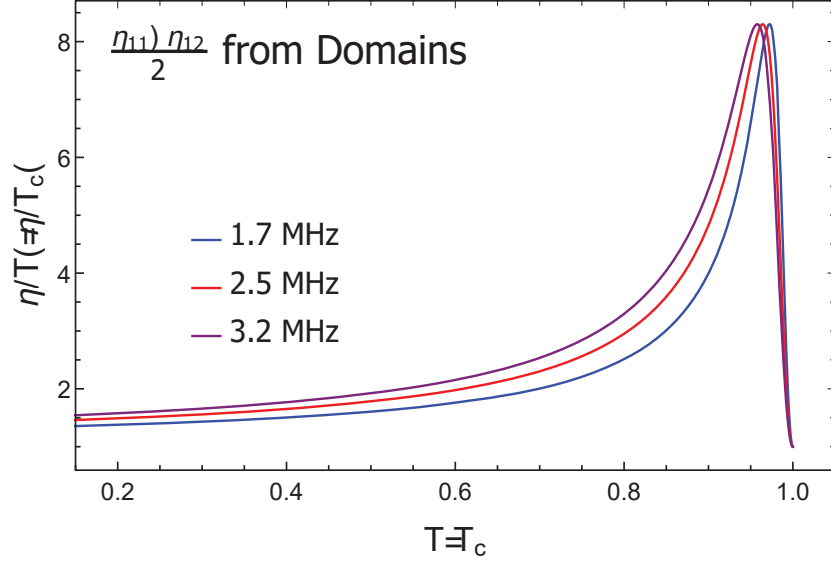


Figure 5.18: **Viscosity from domains in the RUS frequency range.** Viscosity from domains plotted at the lowest and highest frequencies used in the RUS experiment. We take 2.5 MHz as the experimental frequency to extract the domain wall frequency. The shift in the position of the peak is only $\sim 0.01T_c$ from 1.7 MHz to 3.2 MHz.

ational dynamics as the OP interacts with the strain (see discussion leading to Equation 2.49). Within a Landau theory, the relaxation timescale diverges as $|T/T_c - 1|^{-1}$ close to T_c . Unlike the resonant sound absorption arising from domains, OP relaxation can cause non-resonant absorption of ultrasound and lead to a broad peak in sound attenuation below T_c [43]. We fit our measured $(\eta_{11} + \eta_{12})/2$ to the attenuation expression

$$\eta(\omega, T) \propto \frac{\tau}{1 + \omega^2 \tau^2} \sim \frac{\tau_0 / |T/T_c - 1|}{1 + \omega^2 \tau_0^2 / |T/T_c - 1|^2}, \quad (5.21)$$

as shown in Figure 5.19. However, we find that this expression does not capture the sharp increase in attenuation below T_c , which the expression for attenuation from domain wall motion (Equation 5.18) does. In fact, the sharp peak-like behavior of attenuation right below T_c , which is already present in the raw data (for example, 2495 kHz and 2573 kHz in Figure 5.12), points strongly to a resonant absorption mechanism compared to a non-resonant one.

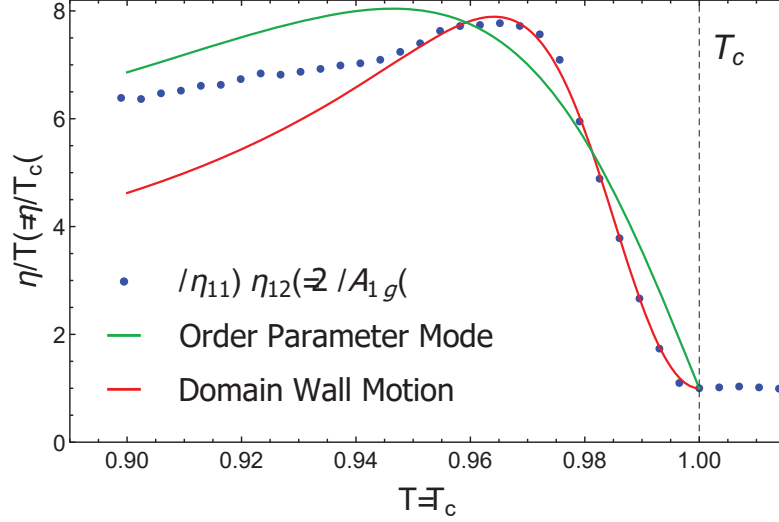


Figure 5.19: **Sound attenuation from order parameter modes.** Normalized $(\eta_{11} + \eta_{12})/2$ in Sr_2RuO_4 fit to two different models of increased sound attenuation below T_c . The green curve is a fit to Equation 5.21, which models sound attenuation due to OP collective modes. The red curve is a fit to Equation 5.18, which models the sound attenuation arising from domain wall motion. Near T_c , the red curve clearly fits the experimental data better than the green one.

5.6.5 Comparison to Pulse-echo Measurements

Our RUS measurements operate at frequencies roughly two orders of magnitude lower than the pulse-echo ultrasound measurements reported in Lupien et al. [7]. As viscosity is expected to be only weakly frequency dependent in the Fermi liquid, our measured viscosities should still be comparable to those reported in Ref. [7]. As we mention above, our measure of the B_{1g} viscosity, $(\eta_{11} - \eta_{12})/2$, agrees well in absolute terms with the pulse-echo measurement. Scaling by the value of η above T_c , Figure 5.20 shows that the relative changes in $(\eta_{11} - \eta_{12})/2$ as a function of temperature, both above and below T_c , agree between the two techniques. For η_{11} , the measurements agree well above T_c but show a striking difference immediately below T_c . This demonstrates that the peak-like feature is present only in the pure compressional viscosity $(\eta_{11} + \eta_{12})/2$. The fact that $(\eta_{11} + \eta_{12})/2$ is different at different frequencies requires an additional attenuation mechanism that does not

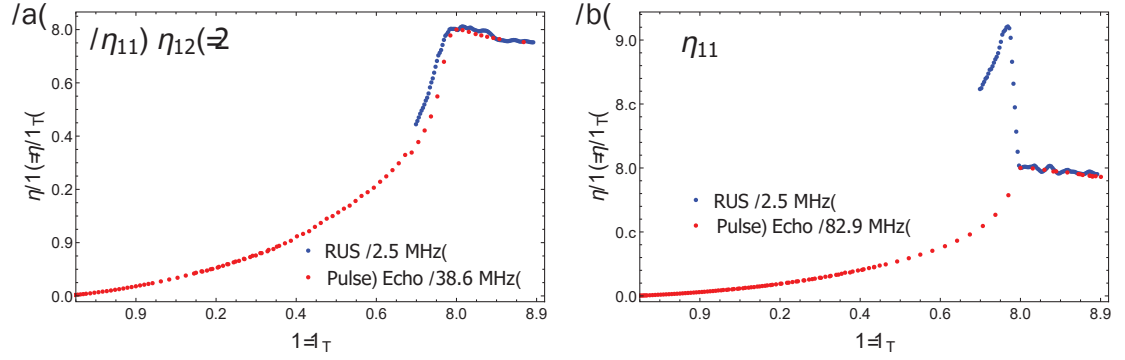


Figure 5.20: **Comparison to pulse-echo measurements of viscosity.** Normalized (a) $(\eta_{11} - \eta_{12})/2$ and (b) η_{11} measured by RUS and pulse-echo techniques. The agreement is good except right below T_c in η_{11} . Pulse-echo data reproduced from Ref. [7].

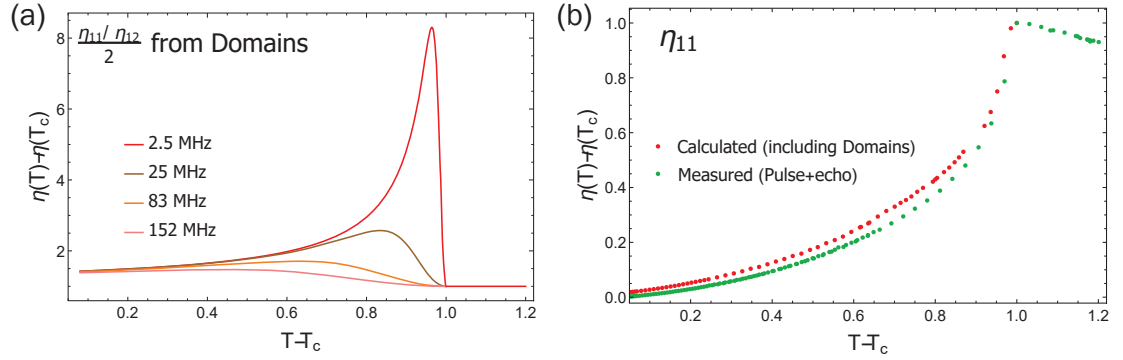


Figure 5.21: **Viscosity from domains at high frequencies.** (a) Normalized $(\eta_{11} + \eta_{12})/2$ from domains plotted at various frequencies. (b) The normalized η_{11} from Ref. [7] (green points), plus calculated including the contribution of domains and compared to pulse-echo measurements. The contribution from domains has a strong frequency dependence, so we choose the pulse-echo frequency (83 MHz) for calculating its contribution to η_{11} . Pulse-echo data reproduced from Ref. [7].

scale simply as ω^2 . This leads us to consider the formation of superconducting domains as the reason for the peak.

We now consider why there is no peak in η_{11} in pulse-echo ultrasound measurements taken at 83 MHz [7]. Figure 5.21(a) shows the increase in $(\eta_{11} + \eta_{12})/2$ from domain walls at various frequencies using the parameters from the fit to the RUS data. The sharp peak at $0.96T_c$ at 2.5 MHz becomes a broad hump around

$0.65T_c$ at 83 MHz and is barely visible at 152.2 MHz. Note that, while the absolute sound attenuation increases as frequency increases, the relative change in viscosity—compared to its value at T_c —decreases with increased frequency.

To see the effect that this contribution from domains at 83 MHz should have on η_{11} , we use the measured $(\eta_{11} + \eta_{12} + 2\eta_{66})/2$ from the L110 mode [7]. Since η_{66} (from the T100 mode) is roughly two orders of magnitude smaller than $(\eta_{11} + \eta_{12} + 2\eta_{66})/2$, $(\eta_{11} + \eta_{12} + 2\eta_{66})/2$ is dominated by $(\eta_{11} + \eta_{12})/2$. As $(\eta_{11} + \eta_{12} + 2\eta_{66})/2$ is measured at 152.2 MHz, any contribution from domains will be small compared to what is measured at 83 MHz (Figure 5.21(a)). We add the predicted increase in viscosity at 83 MHz (Figure 5.21(a)) to the measured $(\eta_{11} + \eta_{12} + 2\eta_{66})/2$, and then add the measured $(\eta_{11} - \eta_{12})/2$ (from the T110 mode in Ref. [7]). Because η_{66} is small, this gives η_{11} with the predicted contribution from domains at 83 MHz. As can be seen in Figure 5.21(b), the domain contribution is almost invisible because of the strong temperature dependence from $(\eta_{11} - \eta_{12})/2$. Note that $(\eta_{11} + \eta_{12} + 2\eta_{66})/2$, which is largely $(\eta_{11} + \eta_{12})/2$, also shows no peak below T_c . Again, this is because there is a strong background contribution from the gapping of normal quasiparticles at T_c —the broad contribution from domains at these high frequencies is washed out by the strongly temperature-dependent background.

5.6.6 Background Attenuation in RUS and Pulse-echo

Sound attenuation measured in experiments has two sources: intrinsic and extrinsic. Intrinsic attenuation is due to the sample. In the case of Sr_2RuO_4 at low temperatures, sound is predominantly attenuated due to the motion of conduction electrons. Extrinsic attenuation comes from the particulars of the experiment itself. For RUS, there is loss associated with the measurement circuit (“coupling”

loss), loss associated with the sample surfaces moving in the presence of helium exchange gas, and loss associated with frictional motion of the sample against the transducer faces. For pulse-echo, there is loss associated with the adhesive that bonds the transducer to the sample, coupling loss associated with the generation of the electrical signal at the transducer, and loss due to imperfect reflections at the sample surfaces and diffraction effects due to finite transducer size.

The total linewidth of a resonance measured in an RUS experiment— Γ_{meas} —is the sum of the intrinsic (Γ_{int}) and extrinsic (Γ_{ext}) contributions as long as each are small compared to the resonance frequency ω_0 (which is always the case in our experiment). In this limit, linewidths add together [181] to produce a total linewidth

$$\Gamma_{meas} = \Gamma_{ext} + \Gamma_{int} = \Gamma_{ext} + \omega_0^2 \sum_j \alpha_j \frac{\eta_j}{c_j}, \quad (5.22)$$

where Γ_{int} is as defined in Equation 5.16.

Similarly, the total attenuation, α_{meas} in a pulse-echo experiment is the sum of intrinsic, α_{int} , and extrinsic, α_{ext} , contributions:

$$\alpha_{meas} = \alpha_{ext} + \alpha_{int} = \alpha_{ext} + \frac{\omega_0^2}{v} \frac{\eta}{c}, \quad (5.23)$$

where c and v are the elastic modulus and velocity associated with a particular sound polarization and propagation direction.

In both experiments, the total measured signal is a background plus a term proportional to the intrinsic viscosity times a factor of frequency squared. Because the pulse-echo experiments are carried out at ~ 100 MHz, the intrinsic contribution can easily dominate α_{meas} , whereas in the RUS experiments carried out at ~ 1 MHz, the intrinsic contribution can be swamped by the extrinsic one, despite both experiments measuring the same intrinsic viscosity. It is worth noting here

that α_{ext} is subtracted out of the pulse-echo experiments in Ref. [171] by setting the attenuation to zero at the lowest measured temperature (i.e. the absolute attenuation is not reported).

Our measurements of η_{66} and η_{44} are both approximately 0.1 Pa·s—orders of magnitude larger than the pulse echo result. This suggests that η_{66} and η_{44} are entirely dominated by Γ_{ext} —the coupling loss—in our experiment. Also note that, while the pulse-echo measurements find η_{66} to be an order of magnitude larger than η_{44} , our extrinsic-dominated measurement finds them to be roughly equal. This partially justifies our assumption that Γ_{ext} is mode independent, and the lack of an observed temperature dependence in our measurements of η_{66} and η_{44} also suggests that Γ_{ext} is itself temperature independent.

5.6.7 Constraints on the Order Parameter

Assuming that we have established the likely origin of the increase in sound attenuation, we consider its implications for the superconductivity of Sr_2RuO_4 . The formation of domains requires a two-component order parameter (OP), either symmetry-enforced or accidental, reaffirming the conclusions of ultrasound studies of the elastic moduli and the sound velocity [2, 182]. We can learn more about which particular OPs are consistent with our experiment by considering which symmetry channels show an increase in attenuation. Domains attenuate ultrasound when the application of strain raises or lowers the condensation energy of one domain in comparison to a neighboring domain. A simple example is the “nematic” superconducting state proposed by Benhabib et al. [182], which is a d –wave OP of the E_g representation, transforming as $\{d_{xz}, d_{yz}\}$. Under $(\epsilon_{xx} - \epsilon_{yy})$ strain, domains of the d_{xz} configuration will be favored over the d_{yz} configuration

(depending on the sign of the strain). This will cause some domains to grow and others to shrink, attenuating sound through the mechanism proposed by Sigrist et al. [30]. We find no increase in $(\eta_{11} - \eta_{12})/2$ below T_c , suggesting that a $\{d_{xz}, d_{yz}\}$ OP cannot explain the increase in compressional sound attenuation.

More generally, the lack of increase in attenuation in any of the shear channels implies that the SC state of Sr_2RuO_4 does not break rotational symmetry. Domains that are related to each other by time reversal symmetry can also be ruled out: there is no strain that can lift the degeneracy between, for example, a $p_x + ip_y$ domain and a $p_x - ip_y$ domain. The observed increase in sound attenuation under compressional strain is therefore quite unusual: as Sigrist et al. [30] point out, compressional strains can never lift the degeneracy between domains that are related by *any* symmetry, since compressional strains do not break the point group symmetry of the lattice. Instead, attenuation in the compressional channel requires domains that couple differently to compressional strain, which in turn requires domains that are accidentally degenerate. Examples that are consistent with both NMR [133] and ultrasound [2, 182] include $\{d_{x^2-y^2}, g_{xy(x^2-y^2)}\}$ [45, 46, 183] and $\{s, d_{xy}\}$ [184]. Then, for example, domains of $d_{x^2-y^2}$ will couple differently to compressional strain than domains of $g_{xy(x^2-y^2)}$, leading to the growth of one domain type and an increase in compressional sound attenuation below T_c . Shear strain, meanwhile, does not change the condensation energy of any single-component order parameter (e.g. s , d_{xy} , $d_{x^2-y^2}$, or $g_{xy(x^2-y^2)}$) to first order in strain, which means that the lack of increase in shear attenuation below T_c is also consistent with an accidentally-degenerate OP. This is also consistent with the lack of a cusp in T_c under applied shear strain [18, 185].

Recent theoretical work [47] has shown that domain walls between $d_{x^2-y^2}$ and

$g_{xy}(x^2-y^2)$ OPs may provide an explanation of the observation of half-quantum vortices in Sr_2RuO_4 *without* a spin-triplet order parameter [126]—a result that is otherwise inconsistent with the singlet pairing suggested by NMR [133]. Willa et al. [46], followed by Yuan et al. [47], have shown that domains between such states stabilize a TRS-breaking $d_{x^2-y^2} \pm ig_{xy}(x^2-y^2)$ state near the domain wall. This would naturally explain why probes of TRS breaking, such as the Kerr effect and μSR [19, 125], see such a small effect at T_c in Sr_2RuO_4 .

One significant challenge for the two-component order parameter scenario is that, whether accidentally degenerate or not, a two component order parameter should generically produce two superconducting T_c s. The lack of a heat capacity signature from an expected second transition under uniaxial strain [50] can only be explained if the second, TRS-breaking transition is particularly weak—a result that might be consistent with the TRS-breaking state appearing only along domain walls. Finally, it is worth noting that there are other mechanisms of ultrasonic attenuation that we have not explored here, including collective modes and gapless excitations such as edge currents that might appear along domain walls even if the domains are related by symmetry. Future ultrasound experiments under applied static strain and magnetic fields are warranted as certain types of domain walls can couple to these fields, thereby affecting the sound attenuation through T_c .

5.7 Large B_{1g} Viscosity in Normal State

We now talk about an interesting feature seen in the normal state viscosities of Sr_2RuO_4 . The shear viscosity $(\eta_{11} - \eta_{12})/2$, corresponding to the B_{1g} strain $(\epsilon_{xx} - \epsilon_{yy})$ is seen to be much larger than the other viscosities at low tempera-

tures. At ~ 2 K, our measured $(\eta_{11} - \eta_{12})/2 \approx 0.78$ Pa.s (see [Figure 5.22\(a\)](#)), which compares extremely well to the $(\eta_{11} - \eta_{12})/2 \approx 0.71$ Pa.s measured by pulse-echo experiments [\[171\]](#). This is particularly impressive since the frequencies employed in pulse-echo are about 20 times higher than our experimental frequencies, and the attenuation grows as ω^2 in a metal. However, viscosity is expected to be frequency independent in a metal at low frequencies ($\hbar\omega \ll E_F$, where E_F is the Fermi energy), and hence it is important to ensure that the viscosities from these two techniques are quantitatively close. Previous works [\[132, 186\]](#) have suggested that the much larger magnitude of $(\eta_{11} - \eta_{12})/2$, in comparison to other shear viscosities, may be due to the fact that the $\epsilon_{xx} - \epsilon_{yy}$ strain is associated with pushing the γ Fermi surface pocket toward the van Hove singularity. We detail two theoretical models which we employed to understand this large B_{1g} viscosity.

5.7.1 Fermi Liquid Model

The striking increase in the B_{1g} viscosity at low temperatures can be well fit to the viscosity expected in a Fermi liquid (FL). In a FL with a single parabolic band, shear viscosity η is expected to be related to the band parameters as

$$\eta = \frac{1}{5}nm^*v_F^2\tau, \quad (5.24)$$

where n is the electron density, m^* is the effective mass of the carriers, v_F is the Fermi velocity and τ is the relaxation time [\[173\]](#). Expressing $\tau^{-1} = \tau_0^{-1} + \tau_{ee}^{-1}$, [Equation 5.24](#) becomes,

$$\eta^{-1} = \frac{5}{nm^*v_F^2} (\tau_0^{-1} + \tau_{ee}^{-1}) = A + BT^2. \quad (5.25)$$

Here, τ_0 is temperature independent (related to processes like scattering off impurities) and τ_{ee} is the time between electron-electron collisions, which is expected

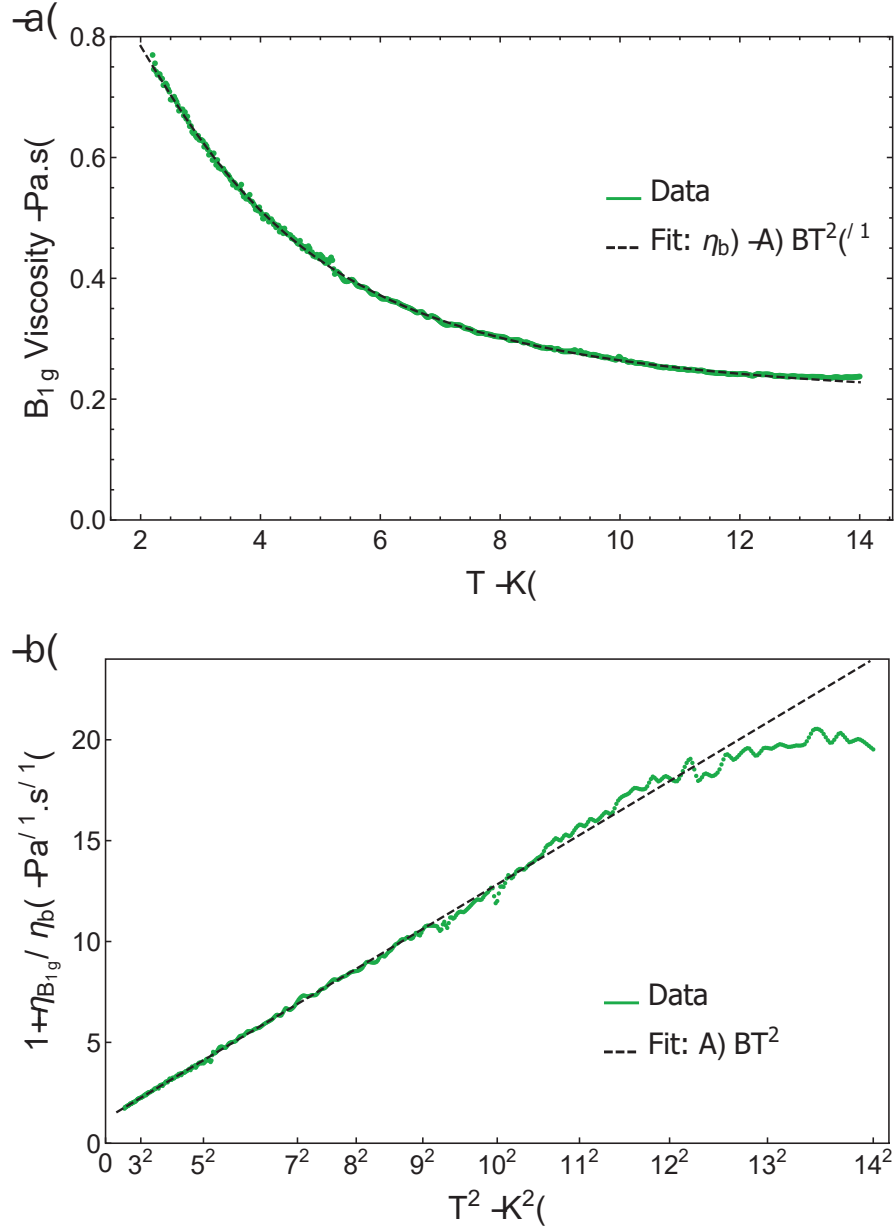


Figure 5.22: **Shear (B_{1g}) viscosity above T_c in Sr_2RuO_4 .** (a) The in-plane shear viscosity $(\eta_{11} - \eta_{12})/2$ of Sr_2RuO_4 between 2 K and 14 K. It is fit to a combination of background (η_b) and Fermi liquid contribution ($A+BT^2$). The fit gives $\eta_b = 0.19 \text{ Pa.s}$, $A = 1.21 \text{ Pa}^{-1}.\text{s}^{-1}$ and $B = 0.12 \text{ Pa}^{-1}.\text{s}^{-1}.\text{K}^{-2}$. (b) Inverse of background subtracted $(\eta_{11} - \eta_{12})/2$ along with the fit is shown. The fit is seen to deviate from the data above $\sim 12 \text{ K}$.

to go as T^2 in a FL. As shown in [Figure 5.22\(b\)](#), the fit to FL viscosity works well over a ~ 10 K range. The effects of dislocations in the sample becomes important as temperature is raised [\[187\]](#), which possibly explains the deviation of data from the fit above ~ 12 K.

Our extracted A and B coefficients also compare well to those obtained in pulse-echo experiments [\[171\]](#),

$$\begin{aligned}\frac{A_{PE}}{A_{RUS}} &= 1.06 \\ \frac{B_{PE}}{B_{RUS}} &= 1.30,\end{aligned}\tag{5.26}$$

where the subscripts denote values from pulse-echo and RUS. This is non-trivial because they were measured on different samples of Sr_2RuO_4 with presumably different concentrations of impurities, defects, etc. The fact that these coefficients still match gives us confidence that we are measuring the intrinsic B_{1g} attenuation in the sample.

We can further compare the timescales we extract to those seen in resistivity measurements in Sr_2RuO_4 . In a metal, resistivity ρ is given by the Drude formula,

$$\rho = \frac{m^*}{ne^2} \tau^{-1} = \frac{m^*}{ne^2} (\tau_0^{-1} + \tau_{ee}^{-1}) = \rho_0 + \rho_1 T^2,\tag{5.27}$$

which gives the well-known T^2 resistivity in a metal [\[188\]](#). Comparing [Equation 5.25](#) and [Equation 5.27](#) allows us to relate the timescales seen in these two measurements as,

$$\begin{aligned}\frac{\tau_{0,\eta}}{\tau_{0,\rho}} &= \frac{5e^2}{(m^*v_F)^2} \frac{\rho_0}{A} \\ \frac{\tau_{ee,\eta}}{\tau_{ee,\rho}} &= \frac{5e^2}{(m^*v_F)^2} \frac{\rho_1}{B}.\end{aligned}\tag{5.28}$$

Using $\rho_0 = 10^{-9} \text{ } \Omega\cdot\text{m}$ and $\rho_1 = 4 \times 10^{-11} \text{ } \Omega\cdot\text{m}/\text{K}^2$ from Barber et al. [\[142\]](#), and the

parameters m^* and v_F for the three bands of Sr_2RuO_4 [4], we get

$$\begin{aligned}\frac{\tau_{0,\eta}}{\tau_{0,\rho}} &\approx 35 \\ \frac{\tau_{ee,\eta}}{\tau_{ee,\rho}} &\approx 14.\end{aligned}\tag{5.29}$$

Here, we have used an effective $(m^*v_F)_{eff} = \sum_{i=\alpha,\beta,\gamma} (m^*v_F)_i$. It is important to note that Equation 5.24 is only true for an isotropic spherical Fermi surface. The real band structure of Sr_2RuO_4 and appropriate anisotropic scattering should be considered for a better estimate of the timescales, and we attempt to incorporate that partly in the following calculation.

5.7.2 Deformation Potential

A better method to extract reasonable timescales from the measured viscosities requires the knowledge of how the band structure of Sr_2RuO_4 changes under strain. Strain deforms the crystalline lattice which modifies the lattice potential seen by the electrons. Bardeen and Shockley [189] defined a deformation potential that takes into account these modifications to describe the interactions between electrons and sound waves in a solid. In particular, they related the electron-phonon scattering matrix elements to the deformed electron bands, through what is known as the deformation-potential theorem. This idea was further advanced by Khan and Allen [172] where they show how to relate the deformation potentials to various symmetry-resolved viscosities in a crystal.

We now perform the calculation for viscosities in Sr_2RuO_4 using the appropriate deformation potentials. We will assume that electrons in the γ -band are the primary contributors to the viscosity, and extract a timescale for the collision processes within a relaxation time approximation. This is the simplest model for

describing how the electron distribution, driven out of equilibrium by strain, reverts back to the equilibrium distribution. This calculation for Sr_2RuO_4 was partly done in Ref. [171], although they had to guess how the band structure parameters changes under strain. With recent developments in Sr_2RuO_4 , these variations are now experimentally known [23, 142].

Following Ref. [172], the deformation potentials D_{ij} (with strains denoted by s_{ij}) are defined as

$$\begin{aligned}
D_{ij}(\mathbf{k}) &= \lim_{s_{ij} \rightarrow 0} \frac{\epsilon(k_i - s_{ij}k_j, s_{ij}, \mu(s_{ij})) - \epsilon(\mathbf{k}, 0, \mu(0))}{s_{ij}} \\
&= \lim_{s_{ij} \rightarrow 0} \frac{\epsilon(\mathbf{k}, 0, \mu(0)) - s_{ij}k_j (\partial\epsilon(\mathbf{k})/\partial k_i) + s_{ij} (\partial\epsilon(\mathbf{k})/\partial s_{ij}) - \epsilon(\mathbf{k}, 0, \mu(0))}{s_{ij}} \\
&= -k_j \frac{\partial\epsilon(\mathbf{k})}{\partial k_i} + \frac{\partial\epsilon(\mathbf{k})}{\partial s_{ij}} \\
&= -\hbar v_i k_j + \frac{\partial\epsilon(\mathbf{k})}{\partial s_{ij}}.
\end{aligned} \tag{5.30}$$

Here, $\epsilon(\mathbf{k})$ is the dispersion of the band, μ is the chemical potential and the subscripts i, j can be x, y or z . We assume the chemical potential μ changes very weakly with strain and ignored $\partial\mu/\partial s_{ij}$ in above, which is a good approximation for in-plane strains in Sr_2RuO_4 . Written explicitly for the various in-plane strains, the deformation potentials are

$$\begin{aligned}
D_{xx}(\mathbf{k}) &= -\hbar v_x k_x + \frac{\partial\epsilon(\mathbf{k})}{\partial s_{xx}} \\
D_{yy}(\mathbf{k}) &= -\hbar v_y k_y + \frac{\partial\epsilon(\mathbf{k})}{\partial s_{yy}} \\
D_{xy}(\mathbf{k}) &= -\hbar v_x k_y + \frac{\partial\epsilon(\mathbf{k})}{\partial s_{xy}}
\end{aligned} \tag{5.31}$$

We can now use these D_{ij} s to get the viscosities η_{ijkl} , defined as [172]

$$\eta_{ijkl} = \sum_{\mathbf{k}, \mathbf{k}'} \left(-\frac{\partial f}{\partial \epsilon_{\mathbf{k}}} \right) D_{ij}(\mathbf{k}) C_{\mathbf{k}, \mathbf{k}'}^{-1} D_{kl}(\mathbf{k}'), \tag{5.32}$$

with f the Fermi-Dirac distribution function and $C_{\mathbf{k},\mathbf{k}'}$ the collision operator. At temperatures of our interest (~ 10 K), $\left(-\frac{\partial f}{\partial \epsilon_{\mathbf{k}}}\right) \approx \delta(\epsilon_{\mathbf{k}} - \epsilon_F)$ and within the relaxation time approximation, $C_{\mathbf{k},\mathbf{k}'}^{-1} = \tau(\mathbf{k})\delta_{\mathbf{k},\mathbf{k}'}$. Replacing these in the above equation gives,

$$\begin{aligned}
\eta_{ijkl} &= \sum_{\mathbf{k},\mathbf{k}'} \delta(\epsilon_{\mathbf{k}} - \epsilon_F) D_{ij}(\mathbf{k}) \tau(\mathbf{k}) \delta_{\mathbf{k},\mathbf{k}'} D_{kl}(\mathbf{k}') \\
&= \sum_{\mathbf{k}} \delta(\epsilon_{\mathbf{k}} - \epsilon_F) D_{ij}(\mathbf{k}) \tau(\mathbf{k}) D_{kl}(\mathbf{k}) \\
&= \sum_{\mathbf{k}} \sum_{\mathbf{k}_i \in FS} \frac{\delta(\mathbf{k} - \mathbf{k}_i)}{|\hbar v(\mathbf{k}_i)|} D_{ij}(\mathbf{k}) \tau(\mathbf{k}) D_{kl}(\mathbf{k}) \\
&= \sum_{\mathbf{k}_i \in FS} \frac{1}{|\hbar v(\mathbf{k}_i)|} D_{ij}(\mathbf{k}_i) \tau(\mathbf{k}_i) D_{kl}(\mathbf{k}_i)
\end{aligned} \tag{5.33}$$

The relation to symmetry-resolved viscosities are as follows,

$$\begin{aligned}
\frac{\eta_{11} + \eta_{12}}{2} &= \frac{1}{2} (\eta_{xxxx} + \eta_{xyyy}) \\
\frac{\eta_{11} - \eta_{12}}{2} &= \frac{1}{2} (\eta_{xxxx} - \eta_{xyyy}) \\
\eta_{66} &= \eta_{xyxy}.
\end{aligned} \tag{5.34}$$

To calculate the D_{ij} s, we need the variation of $\epsilon_{\mathbf{k}}$ with strain. The dispersion of the unstrained γ -band is given by [23]

$$\epsilon(\mathbf{k}) = -2t \cos(k_x a) - 2t \cos(k_y a) - 2(t' \cos(k_x a + k_y a) + t' \cos(k_x a - k_y a)) - \mu, \tag{5.35}$$

where they chose $t' = 0.39t$ instead of $t' = 0.41t$ given in Ref. [144]. The strain dependence of the hopping parameters can also be found in Ref. [23], and gives the following strain derivatives,

$$\begin{aligned}
\frac{\partial \epsilon(\mathbf{k})}{\partial s_{xx}} &= 2t\alpha \cos(k_x a) - 2t\alpha\nu \cos(k_y a) + 2t'\alpha'(1 - \nu) \cos(k_x a) \cos(k_y a) \\
\frac{\partial \epsilon(\mathbf{k})}{\partial s_{yy}} &= -2t\alpha\nu \cos(k_x a) + 2t\alpha \cos(k_y a) + 2t'\alpha'(1 - \nu) \cos(k_x a) \cos(k_y a) \\
\frac{\partial \epsilon(\mathbf{k})}{\partial s_{xy}} &= -4t'\alpha' \sin(k_x a) \sin(k_y a)
\end{aligned} \tag{5.36}$$

It is useful to note that under strain, $k_x \rightarrow k_x(1 - s_{xx})$ and $a_x \rightarrow a_x(1 + s_{xx})$ and so on. Thus $k_x a_x \rightarrow k_x a_x(1 - s_{xx}^2)$. These modifications can be ignored for our purposes since we only require 1st derivatives with respect to strain and then set strains to zero. We choose $\alpha = \alpha' = 7$ such that the γ band reaches the van Hove point at $s_{xx} = 0.44\%$ [132] and the Poisson's ratio $\nu = 0.51$ at 4 K [2]. We note that ν is important when an external stress is applied, since a stress along x direction induces finite strains along both x and y directions. In ultrasound experiments, it maybe argued that we apply strains directly and so $\nu = 0$ should be used in the above equations. We use $\nu = 0.51$ in the following calculations, and leave the question of whether we apply stress or strain experimentally for future studies.

The final step to get the viscosities η_{ijkl} requires numerically summing over the Fermi surface of the γ band. To do this, we choose $\mathbf{k}_i = (k_x, k_y)$ on the Fermi surface separated by angle $\Delta\theta$ at $k_z = 0$ and multiply by $4\pi/c$ ($c = 12.74$ Å) and the density of states. We also assume isotropic scattering, that is, $\tau(\mathbf{k}) = \tau_0$ for all \mathbf{k} .

$$\begin{aligned}
\eta_{ijkl} &= \tau_0 \Delta\theta \frac{4\pi}{c} \sum_{(k_x, k_y, 0) \in FS} \frac{2}{(2\pi)^3} \frac{\sqrt{k_x^2 + k_y^2}}{|\hbar v(k_x, k_y)|} D_{ij}(k_x, k_y) D_{kl}(k_x, k_y) \\
&= \frac{\tau_0 \Delta\theta}{\pi^2 c} \sum_{(k_x, k_y, 0) \in FS} \frac{\sqrt{k_x^2 + k_y^2}}{|\hbar v(k_x, k_y)|} D_{ij}(k_x, k_y) D_{kl}(k_x, k_y) \\
&= \frac{1}{\pi^2} \frac{\tau_0 \Delta\theta}{\hbar c} \sum_{(k_x, k_y, 0) \in FS} \tilde{\eta}_{ijkl}(k_x, k_y) \sqrt{k_x^2 + k_y^2},
\end{aligned} \tag{5.37}$$

where we have defined

$$\tilde{\eta}_{ijkl}(k_x, k_y) \equiv \frac{D_{ij}(k_x, k_y) D_{kl}(k_x, k_y)}{v_F(k_x, k_y)} \tag{5.38}$$

Note that in Equation 5.37, if we choose a small $\Delta\theta$, there will be more terms in the sum. This finally balances out to give the same answer as long as $\Delta\theta$ is reasonably small.

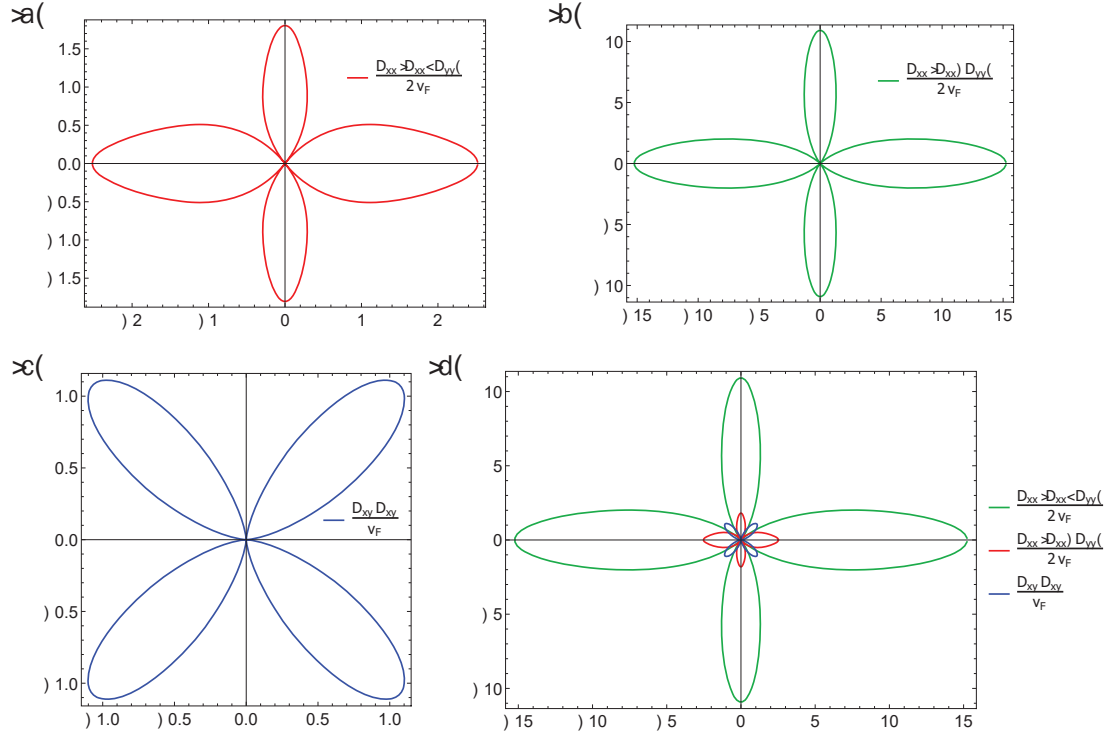


Figure 5.23: **Calculations of viscosity from deformation potentials.** Polar plot of $\tilde{\eta}_{ijkl}$ (defined in text) on the γ -band for in-plane (a) A_{1g} , (b) B_{1g} and (c) B_{2g} viscosities. They are plotted in arbitrary units. (d) The plots in (a), (b) and (c) are plotted together. It can be seen that the B_{1g} viscosity is much larger than the B_{2g} viscosity.

It is quite instructive to look at the variation of $\tilde{\eta}_{ijkl}$ around the γ band to understand the anisotropy between A_{1g} , B_{1g} and B_{2g} viscosities in Sr_2RuO_4 . As shown in Figure 5.23, the B_{1g} viscosity is a factor of 10 larger than the B_{2g} viscosity. This is primarily due to the fact that the γ band is much more sensitive to s_{xx} and s_{yy} compared to s_{xy} strain, coupled with v_F being more than twice along the axes compared to the diagonal directions. Evaluating Equation 5.37 with $\tau_0 = 17$ ps gives $(\eta_{11} - \eta_{12})/2 = 0.74$ Pa.s and $(\eta_{11} + \eta_{12})/2 = 0.05$ Pa.s, close to the experimental values at 2 K. Note that both of these depend on how the γ band changes under s_{xx} and s_{yy} strains, which is well-constrained by existing experiments. This fixes the D_{ij} s, leaving τ_0 as the only free parameter in Equation 5.37. If we take the same τ_0 for calculating η_{66} , we get $\eta_{66} = 0.1$ Pa.s, which is ~ 2000 times larger

than what is reported in Ref. [171]. An anisotropic $\tau(\mathbf{k})$ is possibly required to fix this.

On comparing this τ_0 to the scattering time from resistivity ($\tau_\rho = 81$ ps at 2 K [142]), we find that these timescales differ by less than a factor of 5. In particular, viscosity gives a shorter timescale, or a higher scattering rate, compared to resistivity. This is stark contrast to the free electron model calculation, where the timescale from viscosity was orders of magnitude higher than that from resistivity.

In a fluid, viscosity arises from collisions between the fluid particles, which are always momentum-conserving. The resistivity in a solid, in contrast, is related to momentum-relaxing scattering processes [190]. It is thus tempting to interpret the above numbers in terms of momentum-conserving and momentum-relaxing processes in Sr_2RuO_4 . The fact that the scattering rate from viscosity is $\gtrsim 5$ times the rate from resistivity would indicate that momentum-conserving processes occur more frequently than momentum-relaxing ones. This is nominally expected, since quasiparticles have to encounter defects or disorder to relax their momentum, whereas collisions among quasiparticles, which are probably much more common at low temperatures, do not relax their momentum. However, a better understanding of the scattering processes that contribute to our measured viscosity, such as momentum-conserving or momentum-relaxing, elastic or inelastic and the role of Umklapp scattering [191], is required to clarify the relation between the scattering rates extracted from viscosity and those obtained from resistivity.

CHAPTER 6

CONCLUSIONS AND OUTLOOK

This thesis investigated the order parameter of two correlated electron materials, URu₂Si₂ and Sr₂RuO₄, using RUS. Experimental advancements achieved in the process were extending RUS to relatively low (sub-4 K) temperatures, and also the use of a phase-locked loop to track resonance frequencies with high signal-to-noise. The OP in URu₂Si₂ was constrained to be one-component, which ruled out, on symmetry arguments alone, a broad class of theories based on two-component OPs. In Sr₂RuO₄, we found evidence for a two-component superconducting OP from the discontinuity at T_c seen in a shear elastic modulus. This was particularly unexpected because evidence from NMR, which had ruled out all triplet OPs, and the position of nodes seen in STM, together point toward a $d_{x^2-y^2}$ one-component OP. Our results instead narrowed down the possibilities to two OPs: $d_{xz} + id_{yz}$ and $d_{x^2-y^2} + ig_{xy(x^2-y^2)}$. Finally, sound attenuation measurements on Sr₂RuO₄ revealed an anomalous peak in compressional channels below T_c . This is best explained by the formation of superconducting domains, reaffirming the two-component nature of the OP. The fact that we only observe this peak in compression points to an accidentally degenerate $d + ig$ OP, instead of a symmetry-enforced $d_{xz} + id_{yz}$ OP in Sr₂RuO₄.

There are definite possibilities to improve the analysis techniques employed to analyze RUS data. One of the advancements in this thesis was the development of a machine learning-based analysis to analyze data from an irregularly shaped URu₂Si₂ sample. While this works for a material where the elastic constants are already known from other measurements, it is extremely desirable to have RUS directly work on irregularly shaped samples. This, in particular, is important for

samples of materials that are too brittle to polish or too small to cut and orient along specific crystal axes. Such samples still have resonances, and tomography techniques exist that can reveal the shape and size of such samples with high precision. It should, in principle, be possible to know the crystallographic orientation with X-ray diffraction. The remaining problem is to then solve the elastic wave equation over irregular shapes, which may be mathematically non-trivial. However, if this can be achieved, that would be a major advancement for the resonant ultrasound technique. Additionally, we note that all RUS measurements reported in this thesis were done at zero magnetic field, because a finite field may apply a torque on the sample and lead to the sample falling out of the transducers. There are, however, many transitions that can be promoted or suppressed by magnetic fields (such as superconductivity). Technical developments required to perform RUS in a field are therefore definitely worth thinking about.

We now mention interesting next steps for the two materials we studied: URu_2Si_2 and Sr_2RuO_4 . URu_2Si_2 has a superconducting $T_c \approx 1.5$ K, which we could not reach initially with our RUS setup. This state may have a chiral $d + id$ OP, which in the tetragonal structure of URu_2Si_2 should lead to a shear modulus jump similar to Sr_2RuO_4 . With the low temperature advancements in RUS achieved during this thesis, it should be possible to investigate the superconductivity in URu_2Si_2 and rule either for or against the chiral OP. If the data analysis can be extended to irregularly shaped samples, this experiment can even be done on the high-quality sample which should have less extrinsic contributions.

In Sr_2RuO_4 , if our interpretation of the attenuation increase in terms of domains is indeed true, the peak should not show up in higher frequency ultrasound measurements. This is what happens in the pulse-echo measurements, but it would

be interesting to measure attenuation as a function of frequency in the intermediate range, that is, between 2 to 50 MHz. The peak should gradually disappear if the domains picture is true. However, this is a challenging range of frequencies, since RUS generally does not work well above 5 MHz, which is still a very low frequency for pulse-echo measurements. Another possible way to test the domains idea is to do RUS on a second sample grown in a different batch. If domains mostly form along dislocations and defects which locally strain the sample, the size of the effect should be different in a second sample that has a different density of such defects. This is somewhat of a time-consuming exercise, to prepare a second Sr_2RuO_4 sample for RUS followed by measuring it through T_c .

Finally, we recall that RUS measurements on the normal state of Sr_2RuO_4 reveal a shear viscosity $((\eta_{11} - \eta_{12})/2)$ that is perfectly T^2 at low temperatures. From an experimental point of view, this shows the power of ultrasound to probe the intrinsic Fermi liquid viscosity in metals, where transport experiments have always been confounded by boundary effects [192]. We strongly believe theoretical efforts are required to understand the timescales that we extract from this viscosity. It is also interesting to ask what kind of scattering an ultrasound experiment is sensitive to. The fact that $(\eta_{11} - \eta_{12})/2$ from RUS matches that from pulse-echo tells us that both of these techniques see the same scattering channels. Whether the van Hove singularity plays a role in the large $(\eta_{11} - \eta_{12})/2$ (compared to η_{66}) is also unclear. Nominally, the presence of the van Hove should lead to more scattering, which would imply a smaller quasiparticle lifetime τ . However, since viscosity is proportional to τ in a Fermi liquid, the large $(\eta_{11} - \eta_{12})/2$ would require a large τ . In spite of these complications, we believe that this problem may prove to be theoretically tractable in Sr_2RuO_4 , given that most normal state properties of Sr_2RuO_4 are well-understood within a strongly correlated Fermi liquid picture.

APPENDIX A

CONVERTING BETWEEN α COEFFICIENTS

The code that fits the list of frequencies to the elastic moduli also outputs the compositions of the resonances, in terms of the α coefficients, where $\alpha_{i\mu} = 2 \frac{\partial \omega_i}{\partial c_\mu} \times \frac{c_\mu}{\omega_i}$. For tetragonal systems, the code outputs α coefficients corresponding to the moduli c_{11} , c_{33} , c_{13} , c_{12} , c_{44} and c_{66} . Among these, c_{11} and c_{12} are not associated with irreducible representations (irreps) of strain, but their linear combinations $(c_{11} + c_{12})/2 = c_{A_{1g}}$ and $(c_{11} - c_{12})/2 = c_{B_{1g}}$ are. We outline how to obtain the α coefficients for these irreps.

For small changes in the moduli c_{11} and c_{12} , a resonance frequency ω will change as

$$\frac{\Delta \omega}{\omega} = \frac{1}{2} \left(\alpha_1 \frac{\Delta c_{11}}{c_{11}} + \alpha_2 \frac{\Delta c_{12}}{c_{12}} \right) = \frac{1}{2} \left(\tilde{\alpha}_1 \frac{\Delta c_{A_{1g}}}{c_{A_{1g}}} + \tilde{\alpha}_2 \frac{\Delta c_{B_{1g}}}{c_{B_{1g}}} \right), \quad (\text{A.1})$$

where α_1 , α_2 , $\tilde{\alpha}_1$ and $\tilde{\alpha}_2$ correspond to derivatives with respect to c_{11} , c_{12} , $c_{A_{1g}}$ and $c_{B_{1g}}$ respectively. Replacing $c_{A_{1g}} = (c_{11} + c_{12})/2$ and $c_{B_{1g}} = (c_{11} - c_{12})/2$ in above equation gives,

$$\alpha_1 \frac{\Delta c_{11}}{c_{11}} + \alpha_2 \frac{\Delta c_{12}}{c_{12}} = \tilde{\alpha}_1 \frac{\Delta c_{11} + \Delta c_{12}}{c_{11} + c_{12}} + \tilde{\alpha}_2 \frac{\Delta c_{11} - \Delta c_{12}}{c_{11} - c_{12}}. \quad (\text{A.2})$$

Comparing the coefficients of Δc_{11} and Δc_{12} gives the two equations

$$\begin{aligned} \frac{\tilde{\alpha}_1}{c_{11} + c_{12}} + \frac{\tilde{\alpha}_2}{c_{11} - c_{12}} &= \frac{\alpha_1}{c_{11}} \\ \frac{\tilde{\alpha}_1}{c_{11} + c_{12}} - \frac{\tilde{\alpha}_2}{c_{11} - c_{12}} &= \frac{\alpha_2}{c_{12}} \end{aligned} \quad (\text{A.3})$$

Solving these equations give

$$\tilde{\alpha}_1 = \frac{c_{11} + c_{12}}{2} \left(\frac{\alpha_1}{c_{11}} + \frac{\alpha_2}{c_{12}} \right); \tilde{\alpha}_2 = \frac{c_{11} - c_{12}}{2} \left(\frac{\alpha_1}{c_{11}} - \frac{\alpha_2}{c_{12}} \right). \quad (\text{A.4})$$

It is easy to check that $\tilde{\alpha}_1 + \tilde{\alpha}_2 = \alpha_1 + \alpha_2$, which ensures $\sum_\mu \alpha_{i\mu} = 1$ after the conversion to irreducible moduli.

APPENDIX B

RESONANCE LINEWIDTH AND ATTENUATION COEFFICIENT

In general, stress σ and strain ϵ in a solid are related as [187]

$$\sigma_{\alpha\beta} = c_{\alpha\beta\gamma\delta}\epsilon_{\gamma\delta} - \eta_{\alpha\beta\gamma\delta}\frac{\partial\epsilon_{\gamma\delta}}{\partial t}, \quad (\text{B.1})$$

where $c_{\alpha\beta\gamma\delta}$ and $\eta_{\alpha\beta\gamma\delta}$ are the elastic and the viscosity tensors, respectively (repeated indices are summed over here). The second term accounts for how finite strain rates lead to dissipation in the solid and produce heat. Using Equation B.1 in the wave equation for classical sound gives

$$\rho\frac{\partial^2 u_\alpha}{\partial t^2} = \frac{\partial\sigma_{\alpha\beta}}{\partial x_\beta} \implies \rho\frac{\partial^2 u_\alpha}{\partial t^2} = c_{\alpha\beta\gamma\delta}\frac{\partial\epsilon_{\gamma\delta}}{\partial x_\beta} - \eta_{\alpha\beta\gamma\delta}\frac{\partial}{\partial t}\left(\frac{\partial\epsilon_{\gamma\delta}}{\partial x_\beta}\right) \quad (\text{B.2})$$

where u_α is the local displacement, and x_β is a spatial coordinate.

We will analyze a simple 1-D case of the above equation, which is sufficient to get the relation between resonance linewidth (measured in RUS) and sound attenuation coefficient (measured in pulse-echo). We also use the definition of strain ($\epsilon_{\gamma\delta} = \partial u_\gamma / \partial x_\delta$) to express everything in terms of the displacement field $u(x, t)$.

$$\frac{\partial^2 u}{\partial t^2} = \frac{c}{\rho}\frac{\partial^2 u}{\partial x^2} - \frac{\eta}{\rho}\frac{\partial}{\partial t}\left(\frac{\partial^2 u}{\partial x^2}\right), \quad (\text{B.3})$$

where c and η are combinations of elements of the elastic and viscosity tensors appropriate for the ultrasound mode excited. For ultrasound at frequency ω , Equation B.3 becomes

$$-\omega^2 \tilde{u}(x) = \left(\frac{c - i\omega\eta}{\rho}\right) \frac{\partial^2 \tilde{u}(x)}{\partial x^2}. \quad (\text{B.4})$$

The effects of viscosity can thus be simply incorporated by letting $c \rightarrow c - i\omega\eta$ in the wave equation.

In RUS, we measure the linewidth of a resonance as we sweep through it. The standing wave pattern at resonance gives a displacement field $\tilde{u}(x) \sim u_0 \cos kx$ (where $k = \omega_0 \sqrt{\frac{\rho}{E}}$). Without viscous loss, the resonance would be a δ -function while the presence of non-zero viscosity gives it a characteristic width. We can calculate the linewidth from Equation B.4 by using $\tilde{u}(x) \sim u_0 \cos kx$ and setting

$$\omega^2 - k^2 \left(\frac{c - i\omega\eta}{\rho} \right) = 0 \implies \left(\omega + \frac{i}{2} \frac{\eta k^2}{\rho} \right)^2 = \omega_0^2. \quad (\text{B.5})$$

Here, we have assumed $\eta^2 \omega^2 / c^2 \ll 1$ —which is an excellent assumption at \lesssim GHz frequencies. Thus, in the presence of dissipation, the resonance frequency ω_0 becomes

$$\begin{aligned} \omega_0 &\rightarrow \omega_0 + i \frac{\Gamma}{2} = \omega_0 + i \frac{\eta k^2}{2\rho} \\ &\implies \Gamma = \frac{\eta k^2}{\rho} = \frac{\eta \omega_0^2}{c}, \end{aligned} \quad (\text{B.6})$$

which is the linewidth Γ measured in RUS experiments.

In pulse-echo measurements, a traveling wave is sent into the sample which decays as $e^{-\alpha x/2}$ as it bounces back and forth [171]. This can be incorporated in Equation B.4 by letting $\tilde{u}(x) \sim u_0 e^{i(k + i\alpha/2)x}$ (where $k = \omega \sqrt{\frac{\rho}{E}}$). Now, Equation B.5 becomes

$$\omega^2 - \left(k + i \frac{\alpha}{2} \right)^2 \left(\frac{c - i\omega\eta}{\rho} \right) = 0 \implies \left(k + i \frac{\alpha}{2} \right)^2 = \frac{\rho \omega^2}{c - i\omega\eta}. \quad (\text{B.7})$$

Similar to above, assuming $\eta\omega/c \ll 1$, we can get the attenuation coefficient as,

$$\alpha k = \frac{\rho \omega^2}{c} \frac{\omega \eta}{c} \implies \alpha = \frac{\omega^2 \eta}{c \sqrt{c/\rho}} = \frac{\Gamma}{v}, \quad (\text{B.8})$$

where v is the sound velocity. Note that both Γ and α are related to the same viscosity η and grows as the square of frequency at low frequencies.

APPENDIX C

ROTATIONS OF MODULI

For a crystal whose physical axes are not aligned with the crystallographic axes, the elastic tensor has to be rotated accordingly (see Ref. [193] for details). This is required, for example, to get the correct elastic constants from the resonances of a sample that is not aligned to crystal axes. Being a 4th rank tensor, the elastic tensor transforms under general rotations as

$$C'_{mnop} = R_{mi}R_{nj}R_{ok}R_{pl}C_{ijkl} \quad (\text{C.1})$$

where \mathbf{C} is the un-rotated elastic tensor and \mathbf{R} is a rotation matrix. This general expression, however, can be greatly simplified using symmetry arguments for a crystal system.

A 4th rank tensor has $3^4 = 81$ elements, but for a crystal, symmetry arguments greatly reduce the number of independent elastic tensor elements. In fact, it can be shown that there can be a maximum of 21 independent moduli in a real material, which occurs for a triclinic crystal [52]. This number is even lower in higher symmetry crystals, such as cubic (3), hexagonal (5), tetragonal (6), etc., where the numbers in brackets denotes the number of independent moduli. Thus, an elastic tensor can be written as a symmetric 6×6 matrix. We can use the fact that any rotation in 3 dimensions can be decomposed into rotations about x , y and z axes, which allows us to considerably simplify the rotations. With these simplifications,

the corresponding rotation matrices are given by,

$$R_x(\theta) = \begin{pmatrix} 1 & 0 & 0 & 0 & 0 & 0 \\ 0 & \cos^2 \theta & \sin^2 \theta & \sin 2\theta & 0 & 0 \\ 0 & \sin^2 \theta & \cos^2 \theta & -\sin 2\theta & 0 & 0 \\ 0 & -\frac{1}{2} \sin 2\theta & \frac{1}{2} \sin 2\theta & \cos 2\theta & 0 & 0 \\ 0 & 0 & 0 & 0 & \cos \theta & -\sin \theta \\ 0 & 0 & 0 & 0 & -\sin \theta & \cos \theta \end{pmatrix} \quad (\text{C.2})$$

$$R_y(\theta) = \begin{pmatrix} \cos^2 \theta & 0 & \sin^2 \theta & 0 & \sin 2\theta & 0 \\ 0 & 1 & 0 & 0 & 0 & 0 \\ \sin^2 \theta & 0 & \cos^2 \theta & 0 & -\sin 2\theta & 0 \\ 0 & 0 & 0 & \cos \theta & 0 & -\sin \theta \\ -\frac{1}{2} \sin 2\theta & 0 & \frac{1}{2} \sin 2\theta & 0 & \cos 2\theta & 0 \\ 0 & 0 & 0 & \sin \theta & 0 & \cos \theta \end{pmatrix} \quad (\text{C.3})$$

$$R_z(\theta) = \begin{pmatrix} \cos^2 \theta & \sin^2 \theta & 0 & 0 & 0 & \sin 2\theta \\ \sin^2 \theta & \cos^2 \theta & 0 & 0 & 0 & -\sin 2\theta \\ 0 & 0 & 1 & 0 & 0 & 0 \\ 0 & 0 & 0 & \cos \theta & \sin \theta & 0 \\ 0 & 0 & 0 & -\sin \theta & \cos \theta & 0 \\ -\frac{1}{2} \sin 2\theta & \frac{1}{2} \sin 2\theta & 0 & 0 & 0 & \cos 2\theta \end{pmatrix} \quad (\text{C.4})$$

As an example, we consider the elastic tensor for a tetragonal system

$$\mathbf{C} = \begin{pmatrix} c_{11} & c_{12} & c_{13} & 0 & 0 & 0 \\ c_{12} & c_{11} & c_{13} & 0 & 0 & 0 \\ c_{13} & c_{13} & c_{33} & 0 & 0 & 0 \\ 0 & 0 & 0 & 4c_{44} & 0 & 0 \\ 0 & 0 & 0 & 0 & 4c_{44} & 0 \\ 0 & 0 & 0 & 0 & 0 & 4c_{66} \end{pmatrix} \quad (\text{C.5})$$

Rotation by $\pi/4$ around z is expected to swap the in-plane shear moduli $(c_{11} - c_{12})/2$ and c_{66} , leaving all the other moduli same. We can see this by calculating

$$\begin{aligned} \mathbf{C}' &= R_z^T(\pi/4) \mathbf{C} R_z(\pi/4) \\ &= \begin{pmatrix} \frac{c_{11}+c_{12}}{2} + c_{66} & \frac{c_{11}+c_{12}}{2} - c_{66} & c_{13} & 0 & 0 & 0 \\ \frac{c_{11}+c_{12}}{2} - c_{66} & \frac{c_{11}+c_{12}}{2} + c_{66} & c_{13} & 0 & 0 & 0 \\ c_{13} & c_{13} & c_{33} & 0 & 0 & 0 \\ 0 & 0 & 0 & 4c_{44} & 0 & 0 \\ 0 & 0 & 0 & 0 & 4c_{44} & 0 \\ 0 & 0 & 0 & 0 & 0 & 2(c_{11} - c_{12}) \end{pmatrix} \end{aligned} \quad (\text{C.6})$$

Generally, rotations may introduce extra terms in the elastic tensor which are some combination of the independent components. For example, a rotation by

$\pi/4$ around x transforms the tensor as

$$\begin{aligned} \mathbf{C}' &= R_x^T(\pi/4) \mathbf{C} R_x(\pi/4) \\ &= \begin{pmatrix} c_{11} & \frac{c_{12}+c_{13}}{2} & \frac{c_{12}+c_{13}}{2} & c_{12}-c_{13} & 0 & 0 \\ \frac{c_{12}+c_{13}}{2} & \frac{1}{4}c_A + c_{44} & \frac{1}{4}c_A - c_{44} & \frac{c_{11}-c_{33}}{2} & 0 & 0 \\ \frac{c_{12}+c_{13}}{2} & \frac{1}{4}c_A - c_{44} & \frac{1}{4}c_A + c_{44} & \frac{c_{11}-c_{33}}{2} & 0 & 0 \\ c_{12}-c_{13} & \frac{c_{11}-c_{33}}{2} & \frac{c_{11}-c_{33}}{2} & c_{11}+c_{33}-2c_{13} & 0 & 0 \\ 0 & 0 & 0 & 0 & 2(c_{44}+c_{66}) & -2(c_{44}+c_{66}) \\ 0 & 0 & 0 & 0 & -2(c_{44}+c_{66}) & 2(c_{44}+c_{66}) \end{pmatrix}, \end{aligned} \quad (\text{C.7})$$

where $c_A = c_{11} + c_{33} + 2c_{13}$. Note that the rotation introduces non-zero c'_{14} , c'_{24} , c'_{34} and c'_{56} , which were zero in the original elastic tensor.

APPENDIX D

BULK MODULUS AND YOUNG'S MODULI

In a tetragonal system, the relation $\sigma = C\epsilon$ becomes

$$\begin{pmatrix} \sigma_{xx} \\ \sigma_{yy} \\ \sigma_{zz} \\ \sigma_{xz} \\ \sigma_{yz} \\ \sigma_{xy} \end{pmatrix} = \begin{pmatrix} c_{11} & c_{12} & c_{13} & 0 & 0 & 0 \\ c_{12} & c_{11} & c_{13} & 0 & 0 & 0 \\ c_{13} & c_{13} & c_{33} & 0 & 0 & 0 \\ 0 & 0 & 0 & c_{44} & 0 & 0 \\ 0 & 0 & 0 & 0 & c_{44} & 0 \\ 0 & 0 & 0 & 0 & 0 & c_{66} \end{pmatrix} \begin{pmatrix} \epsilon_{xx} \\ \epsilon_{yy} \\ \epsilon_{zz} \\ 2\epsilon_{xz} \\ 2\epsilon_{yz} \\ 2\epsilon_{xy} \end{pmatrix}. \quad (\text{D.1})$$

The bulk modulus B , relevant for hydrostatic pressure experiments, is defined as

$$B = -V \frac{\Delta P}{\Delta V}, \quad (\text{D.2})$$

where ΔP is the applied pressure and $\Delta V/V$ is the fractional change in volume.

Under hydrostatic pressure, from [Equation D.1](#), we get

$$\begin{pmatrix} \epsilon_{xx} \\ \epsilon_{yy} \\ \epsilon_{zz} \\ \epsilon_{xz} \\ \epsilon_{yz} \\ \epsilon_{xy} \end{pmatrix} = C^{-1} \begin{pmatrix} -\Delta P \\ -\Delta P \\ -\Delta P \\ 0 \\ 0 \\ 0 \end{pmatrix}, \quad (\text{D.3})$$

where $C^{-1} = S$ is also called the compliance tensor. Calculating the fractional volume change $\frac{\Delta V}{V} = \epsilon_{xx} + \epsilon_{yy} + \epsilon_{zz}$ then gives the bulk modulus in terms of the elastic moduli,

$$B = \frac{\left(\frac{c_{11}+c_{12}}{2}\right) c_{33} - 2c_{13}^2}{\frac{c_{11}+c_{12}}{2} + c_{33} - 2c_{13}}. \quad (\text{D.4})$$

Note that B only has compressional, or A_{1g} , moduli in it. This is expected since hydrostatic pressure does not break any of the symmetries of the lattice, and therefore none of the elastic moduli that are associated with symmetry-breaking shear strains show up in bulk modulus.

We now consider uniaxial stress along a crystalline direction, such as $[100]$, so that only $\sigma_{xx} \neq 0$. Now, Equation D.1 becomes

$$\begin{pmatrix} \epsilon_{xx} \\ \epsilon_{yy} \\ \epsilon_{zz} \\ \epsilon_{xz} \\ \epsilon_{yz} \\ \epsilon_{xy} \end{pmatrix} = C^{-1} \begin{pmatrix} \sigma_{xx} \\ 0 \\ 0 \\ 0 \\ 0 \\ 0 \end{pmatrix}. \quad (\text{D.5})$$

The Young's modulus along $[100]$ is defined as,

$$Y_{100} = \frac{\sigma_{xx}}{\epsilon_{xx}} = \frac{4 \left(\frac{c_{11}-c_{12}}{2} \right) \left(\frac{c_{11}+c_{12}}{2} c_{33} - c_{13}^2 \right)}{c_{11}c_{33} - c_{13}^2} \quad (\text{D.6})$$

The relevant Poisson's ratios become,

$$\nu_{xy}^{100} = -\frac{\epsilon_{yy}}{\epsilon_{xx}} = -\frac{c_{33}c_{12} - c_{13}^2}{c_{33}c_{11} - c_{13}^2} \quad (\text{D.7})$$

$$\nu_{xz}^{100} = -\frac{\epsilon_{zz}}{\epsilon_{xx}} = -\frac{(c_{11} - c_{12})c_{13}}{c_{33}c_{11} - c_{13}^2} \quad (\text{D.8})$$

Note that Y_{100} has a contribution from the B_{1g} modulus $(c_{11}-c_{12})/2$, since applying stress along a $[100]$ direction introduces B_{1g} shear strain into the material.

To get the Young's modulus and Poisson's ratios along $[110]$ direction, we can simply replace $\left(\frac{c_{11}-c_{12}}{2} \right) \rightarrow c_{66}$ in the above equations. This follows from the fact that in-plane 45° rotation interchanges B_{1g} and B_{2g} shear strains. Thus,

$$Y_{110} = \frac{4c_{66} \left(\frac{c_{11}+c_{12}}{2} c_{33} - c_{13}^2 \right)}{\left(\frac{c_{11}+c_{12}}{2} + c_{66} \right) c_{33} - c_{13}^2} \quad (\text{D.9})$$

$$\nu_{xy}^{110} = -\frac{c_{33} \left(\frac{c_{11}+c_{12}}{2} - c_{66} \right) - c_{13}^2}{c_{33} \left(\frac{c_{11}+c_{12}}{2} + c_{66} \right) - c_{13}^2} \quad (\text{D.10})$$

$$\nu_{xz}^{110} = -\frac{2c_{66}c_{13}}{c_{33} \left(\frac{c_{11}+c_{12}}{2} + c_{66} \right) - c_{13}^2} \quad (\text{D.11})$$

Finally, we consider uniaxial stress along $[001]$ direction, so that only $\sigma_{zz} \neq 0$. Now, [Equation D.1](#) becomes

$$\begin{pmatrix} \epsilon_{xx} \\ \epsilon_{yy} \\ \epsilon_{zz} \\ \epsilon_{xz} \\ \epsilon_{yz} \\ \epsilon_{xy} \end{pmatrix} = C^{-1} \begin{pmatrix} 0 \\ 0 \\ \sigma_{zz} \\ 0 \\ 0 \\ 0 \end{pmatrix}. \quad (\text{D.12})$$

The Young's modulus along $[001]$ is defined as,

$$Y_{001} = \frac{\sigma_{zz}}{\epsilon_{zz}} = c_{33} - \frac{c_{13}^2}{\frac{c_{11}+c_{12}}{2}} \quad (\text{D.13})$$

Due to tetragonal symmetry, σ_{zz} induces the same strains ϵ_{xx} and ϵ_{yy} , leading to these Poisson's ratios being equal. The Poisson's ratio is,

$$\nu^{001} = -\frac{\epsilon_{xx}}{\epsilon_{zz}} = -\frac{\epsilon_{yy}}{\epsilon_{zz}} = -\frac{c_{13}}{c_{11} + c_{12}} \quad (\text{D.14})$$

APPENDIX E

TABLE OF FREQUENCIES

Table E.1: Fit for RUS frequencies of URu₂Si₂ at ~300 K.

Index	f_{exp} (kHz)	f_{calc} (kHz)	Error (%)	α_i					
				$\frac{c_{11}+c_{12}}{2}$	c_{33}	c_{13}	c_{66}	c_{44}	$\frac{c_{11}-c_{12}}{2}$
1	0	502	0.	0.01	0.01	-0.01	0.41	0.56	0.01
2	532	532	0.04	0.06	0.01	-0.01	0.	0.12	0.83
3	559	559	0.08	0.01	0.01	-0.01	0.15	0.81	0.03
4	597	597	0.06	0.35	0.15	-0.2	0.09	0.01	0.6
5	614	614	0.01	0.01	0.01	-0.01	0.	0.	0.99
6	669	669	0.06	0.36	0.23	-0.25	0.07	0.02	0.57
7	681	680	0.05	0.02	0.02	-0.02	0.	0.8	0.17
8	699	699	0.04	0.06	0.04	-0.04	0.01	0.64	0.29
9	709	709	0.05	0.39	0.36	-0.33	0.	0.	0.57
10	739	739	0.08	0.66	0.14	-0.25	0.01	0.32	0.13
11	755	755	0.04	0.13	0.01	-0.03	0.01	0.67	0.21
12	768	768	0.	0.18	0.02	-0.05	0.01	0.43	0.41
13	773	772	0.13	0.09	0.06	-0.06	0.88	0.	0.03
14	803	803	0.06	0.78	0.88	-0.74	0.	0.	0.07
15	815	814	0.08	0.09	0.78	-0.22	0.02	0.24	0.09
16	830	831	0.11	0.07	0.68	-0.18	0.02	0.23	0.18
17	835	834	0.08	0.06	0.44	-0.07	0.	0.05	0.52
18	905	904	0.06	0.21	0.06	-0.1	0.	0.34	0.48
19	918	918	0.02	0.16	0.84	-0.32	0.28	0.04	0.01
20	949	948	0.11	0.24	0.48	-0.28	0.12	0.1	0.35
21	950	949	0.12	0.57	0.78	-0.44	0.02	0.	0.07
22	959	958	0.02	0.08	0.09	-0.07	0.32	0.5	0.08
23	970	970	0.05	0.21	0.52	-0.28	0.14	0.14	0.26
24	1004	1004	0.03	0.09	0.22	-0.12	0.04	0.55	0.22

Table continued on next page.

Table 1 continued.

Index	f_{exp} (kHz)	f_{calc} (kHz)	Error (%)	α_i					
				$\frac{c_{11}+c_{12}}{2}$	c_{33}	c_{13}	c_{66}	c_{44}	$\frac{c_{11}-c_{12}}{2}$
25	1013	1014	0.13	0.14	0.12	-0.11	0.26	0.42	0.17
26	1021	1021	0.01	0.08	0.01	-0.01	0.34	0.54	0.04
27	1031	1031	0.02	0.07	0.13	-0.02	0.23	0.05	0.54
28	1057	1058	0.12	0.06	0.17	-0.07	0.	0.7	0.14
29	1080	1080	0.01	0.06	0.05	0.	0.41	0.04	0.43
30	0	1096	0.	0.43	0.53	-0.37	0.03	0.28	0.09
31	1139	1139	0.01	0.36	0.51	-0.34	0.03	0.33	0.11
32	1152	1153	0.1	0.29	0.42	0.06	0.04	0.03	0.16
33	1164	1164	0.	0.44	0.37	-0.33	0.	0.46	0.05
34	1187	1187	0.04	0.18	0.12	-0.09	0.04	0.53	0.22
35	1203	1204	0.08	0.21	0.04	-0.06	0.22	0.09	0.52
36	1210	1209	0.09	0.02	0.07	-0.03	0.05	0.3	0.59
37	1234	1233	0.06	0.02	0.	0.	0.02	0.01	0.96
38	1244	1245	0.11	0.09	0.08	-0.06	0.28	0.52	0.09
39	1246	1246	0.	0.14	0.07	-0.06	0.12	0.45	0.28
40	1253	1253	0.03	0.11	0.15	-0.05	0.04	0.46	0.29
41	1274	1273	0.03	0.11	0.13	-0.08	0.05	0.52	0.27
42	1289	1287	0.14	0.1	0.2	-0.1	0.17	0.47	0.15
43	1291	1293	0.18	0.26	0.14	-0.17	0.15	0.17	0.44
44	1294	1294	0.02	0.37	0.34	-0.27	0.08	0.37	0.11
45	1304	1301	0.24	0.14	0.25	-0.11	0.07	0.43	0.21
46	1343	1347	0.31	0.1	0.17	-0.09	0.16	0.47	0.19
47	1349	1350	0.1	0.17	0.36	-0.18	0.29	0.25	0.11
48	1415	1413	0.12	0.19	0.22	-0.12	0.1	0.53	0.09

Table E.2: **Fit for RUS frequencies of URu₂Si₂ at 20 K.**

Index	f_{exp} (kHz)	f_{calc} (kHz)	Error (%)	α_i					
				$\frac{c_{11}+c_{12}}{2}$	c_{33}	c_{13}	c_{66}	c_{44}	$\frac{c_{11}-c_{12}}{2}$
1	511	510	0.08	0.01	0.01	-0.01	0.42	0.56	0.01
2	533	533	0.04	0.06	0.01	-0.01	0.	0.12	0.83
3	569	568	0.1	0.01	0.01	-0.01	0.14	0.81	0.03
4	599	599	0.03	0.34	0.14	-0.18	0.09	0.01	0.61
5	614	614	0.	0.01	0.	-0.01	0.	0.	0.99
6	673	672	0.08	0.35	0.2	-0.22	0.07	0.01	0.59
7	691	690	0.08	0.02	0.02	-0.02	0.01	0.77	0.19
8	707	708	0.03	0.07	0.04	-0.04	0.01	0.6	0.32
9	714	714	0.01	0.38	0.33	-0.31	0.	0.	0.59
10	747	746	0.12	0.66	0.13	-0.25	0.01	0.31	0.13
11	765	765	0.07	0.12	0.01	-0.03	0.01	0.71	0.18
12	776	775	0.06	0.17	0.02	-0.05	0.01	0.46	0.39
13	783	782	0.15	0.09	0.06	-0.06	0.88	0.	0.03
14	815	815	0.03	0.78	0.86	-0.71	0.	0.	0.07
15	828	827	0.09	0.09	0.78	-0.22	0.01	0.24	0.09
16	840	840	0.01	0.06	0.46	-0.08	0.	0.06	0.5
17	842	842	0.05	0.07	0.7	-0.18	0.01	0.23	0.17
18	912	911	0.03	0.2	0.06	-0.09	0.	0.35	0.48
19	932	932	0.02	0.15	0.83	-0.31	0.28	0.04	0.01
20	959	958	0.15	0.23	0.47	-0.27	0.12	0.09	0.36
21	962	961	0.13	0.56	0.77	-0.43	0.02	0.	0.07
22	973	973	0.05	0.08	0.09	-0.07	0.32	0.5	0.09
23	982	982	0.03	0.21	0.51	-0.27	0.15	0.14	0.26
24	1018	1018	0.02	0.09	0.22	-0.12	0.04	0.54	0.23
25	1026	1028	0.11	0.14	0.12	-0.11	0.26	0.42	0.18
26	1036	1036	0.01	0.08	0.01	-0.01	0.33	0.54	0.05
27	1038	1037	0.08	0.07	0.14	-0.02	0.22	0.06	0.53

Table continued on next page.

Table 1 continued.

Index	f_{exp} (kHz)	f_{calc} (kHz)	Error (%)	α_i					
				$\frac{c_{11}+c_{12}}{2}$	c_{33}	c_{13}	c_{66}	c_{44}	$\frac{c_{11}-c_{12}}{2}$
28	1074	1074	0.07	0.06	0.17	-0.07	0.	0.7	0.13
29	1088	1088	0.	0.06	0.06	0.	0.4	0.04	0.43
30	1111	1111	0.	0.43	0.53	-0.37	0.03	0.27	0.09
31	1156	1155	0.05	0.37	0.51	-0.33	0.03	0.32	0.11
32	1161	1162	0.07	0.27	0.43	0.06	0.04	0.03	0.15
33	1182	1181	0.05	0.43	0.36	-0.31	0.	0.47	0.05
34	1202	1202	0.03	0.18	0.11	-0.08	0.04	0.53	0.22
35	1210	1211	0.11	0.19	0.03	-0.05	0.2	0.08	0.55
36	1218	1217	0.1	0.02	0.05	-0.02	0.04	0.29	0.62
37	1234	1233	0.04	0.02	0.	-0.01	0.03	0.01	0.94
38	1261	1260	0.02	0.14	0.06	-0.05	0.12	0.45	0.28
39	1262	1263	0.06	0.09	0.08	-0.06	0.29	0.51	0.1
40	1267	1267	0.04	0.11	0.16	-0.05	0.04	0.46	0.28
41	1289	1289	0.04	0.11	0.13	-0.08	0.05	0.52	0.27
42	1301	1303	0.16	0.25	0.14	-0.16	0.15	0.18	0.44
43	1307	1305	0.15	0.1	0.2	-0.1	0.17	0.47	0.16
44	1312	1311	0.04	0.37	0.34	-0.27	0.08	0.36	0.11
45	1320	1317	0.24	0.15	0.26	-0.11	0.06	0.43	0.22
46	1361	1365	0.28	0.1	0.17	-0.08	0.16	0.46	0.2
47	1368	1369	0.07	0.16	0.36	-0.17	0.29	0.25	0.12
48	1433	1433	0.01	0.17	0.2	-0.11	0.09	0.51	0.13
49	1434	1433	0.03	0.04	0.15	-0.05	0.05	0.48	0.32
50	1442	1440	0.14	0.06	0.23	-0.06	0.05	0.35	0.37
51	1444	1444	0.	0.13	0.35	-0.15	0.01	0.45	0.21
52	0	1450	0.	0.16	0.06	-0.07	0.44	0.08	0.33
53	1448	1452	0.23	0.23	0.32	-0.2	0.05	0.45	0.15
54	1457	1457	0.01	0.16	0.24	-0.14	0.15	0.49	0.11
55	1471	1471	0.	0.46	0.45	-0.38	0.06	0.12	0.29

Table continued on next page.

Table 1 continued.

Index	f_{exp} (kHz)	f_{calc} (kHz)	Error (%)	α_i					
				$\frac{c_{11}+c_{12}}{2}$	c_{33}	c_{13}	c_{66}	c_{44}	$\frac{c_{11}-c_{12}}{2}$
56	1481	1481	0.04	0.21	0.1	-0.08	0.36	0.13	0.27
57	1492	1492	0.01	0.11	0.05	-0.03	0.43	0.07	0.38
58	1505	1508	0.22	0.26	0.24	-0.2	0.18	0.22	0.3
59	1518	1517	0.05	0.14	0.15	-0.1	0.07	0.3	0.43
60	1536	1538	0.09	0.23	0.29	-0.2	0.22	0.32	0.15
61	1541	1540	0.03	0.1	0.1	-0.05	0.05	0.21	0.59
62	1544	1543	0.09	0.26	0.28	-0.21	0.07	0.23	0.37
63	1564	1564	0.02	0.19	0.09	-0.06	0.15	0.14	0.49
64	1587	1588	0.02	0.26	0.31	-0.19	0.13	0.37	0.11
65	1592	1591	0.02	0.15	0.13	-0.08	0.22	0.33	0.25
66	1595	1595	0.02	0.21	0.24	-0.14	0.05	0.44	0.19
67	1602	1603	0.03	0.17	0.18	-0.1	0.07	0.46	0.21
68	1611	1610	0.08	0.14	0.23	-0.13	0.14	0.47	0.15
69	1615	1616	0.07	0.54	0.61	-0.5	0.14	0.09	0.12
70	1620	1618	0.11	0.22	0.16	-0.09	0.15	0.36	0.2
71	1623	1623	0.01	0.13	0.1	-0.07	0.13	0.44	0.28
72	1624	1625	0.09	0.32	0.27	-0.1	0.04	0.36	0.12
73	1631	1631	0.04	0.35	0.5	-0.35	0.1	0.21	0.19
74	1645	1644	0.03	0.1	0.14	-0.09	0.36	0.26	0.22
75	1670	1673	0.15	0.12	0.22	-0.12	0.16	0.52	0.09
76	1673	1673	0.04	0.23	0.12	-0.12	0.24	0.1	0.43
77	1685	1684	0.04	0.1	0.31	-0.11	0.01	0.67	0.03
78	0	1702	0.	0.28	0.07	-0.06	0.46	0.01	0.24
79	1702	1702	0.01	0.08	0.32	-0.11	0.05	0.61	0.05
80	1704	1704	0.02	0.11	0.23	-0.09	0.3	0.32	0.13
81	0	1720	0.	0.13	0.18	-0.1	0.08	0.47	0.25
82	0	1727	0.	0.12	0.21	-0.1	0.14	0.37	0.27
83	1733	1733	0.02	0.09	0.11	-0.07	0.04	0.73	0.11

Table continued on next page.

Table 1 continued.

Index	f_{exp} (kHz)	f_{calc} (kHz)	Error (%)	α_i					
				$\frac{c_{11}+c_{12}}{2}$	c_{33}	c_{13}	c_{66}	c_{44}	$\frac{c_{11}-c_{12}}{2}$
84	1738	1737	0.07	0.1	0.13	-0.05	0.09	0.45	0.28
85	1777	1779	0.16	0.13	0.12	-0.08	0.19	0.38	0.25
86	1786	1787	0.07	0.15	0.07	-0.05	0.19	0.23	0.41
87	1787	1788	0.08	0.07	0.2	-0.05	0.1	0.59	0.09
88	1788	1789	0.04	0.14	0.29	-0.1	0.07	0.36	0.23
89	1791	1791	0.02	0.11	0.14	-0.06	0.15	0.29	0.38
90	1792	1792	0.03	0.49	0.22	-0.24	0.1	0.1	0.32
91	0	1821	0.	0.14	0.17	-0.11	0.15	0.37	0.28
92	1825	1826	0.08	0.39	0.73	-0.44	0.01	0.18	0.14
93	0	1827	0.	0.07	0.26	-0.1	0.04	0.46	0.27
94	1837	1837	0.01	0.53	0.26	-0.25	0.08	0.11	0.26
95	1839	1838	0.06	0.18	0.21	-0.12	0.07	0.43	0.23
96	0	1852	0.	0.01	0.	0.	0.02	0.01	0.97
97	1865	1866	0.02	0.08	0.15	-0.08	0.05	0.27	0.53
98	1866	1867	0.04	0.3	0.54	-0.34	0.1	0.27	0.13
99	1881	1886	0.23	0.13	0.24	-0.13	0.1	0.47	0.19
100	1887	1886	0.03	0.15	0.18	-0.11	0.47	0.22	0.09

Table E.3: Fit for RUS frequencies of Sr_2RuO_4 at ~ 300 K.

Index	f_{exp} (kHz)	f_{calc} (kHz)	Error (%)	α_i					
				$\frac{c_{11}+c_{12}}{2}$	c_{33}	c_{13}	c_{66}	c_{44}	$\frac{c_{11}-c_{12}}{2}$
1	0	944	0.	0.01	0.01	-0.01	0.	0.38	0.61
2	1071	1073	0.14	0.	0.	0.	0.02	0.9	0.07
3	1262	1263	0.05	0.05	0.01	-0.01	0.77	0.18	0.
4	1330	1334	0.32	0.03	0.01	-0.01	0.02	0.	0.95
5	1343	1346	0.2	0.33	0.16	-0.18	0.45	0.01	0.23
6	1377	1382	0.39	0.01	0.02	-0.01	0.05	0.93	0.

Table continued on next page.

Table 1 continued.

Index	f_{exp} (kHz)	f_{calc} (kHz)	Error (%)	α_i					
				$\frac{c_{11}+c_{12}}{2}$	c_{33}	c_{13}	c_{66}	c_{44}	$\frac{c_{11}-c_{12}}{2}$
7	1423	1427	0.32	0.01	0.03	-0.01	0.06	0.91	0.
8	1472	1472	0.03	0.35	0.27	-0.24	0.4	0.04	0.19
9	1474	1475	0.1	0.01	0.01	-0.01	0.99	0.	0.
10	1617	1623	0.38	0.51	0.1	-0.17	0.12	0.42	0.02
11	1631	1636	0.28	0.37	0.46	-0.34	0.5	0.	0.
12	1642	1637	0.26	0.21	0.03	-0.06	0.43	0.38	0.01
13	1681	1675	0.36	0.06	0.65	-0.15	0.07	0.31	0.06
14	1699	1699	0.01	0.21	0.03	-0.06	0.49	0.32	0.01
15	1715	1716	0.06	0.04	0.53	-0.09	0.13	0.29	0.09
16	1774	1780	0.37	0.67	0.9	-0.64	0.06	0.	0.
17	1832	1833	0.03	0.14	0.81	-0.27	0.	0.07	0.24
18	1864	1858	0.34	0.05	0.05	-0.04	0.06	0.43	0.45
19	1885	1879	0.33	0.09	0.25	0.	0.62	0.04	0.
20	1941	1948	0.34	0.03	0.02	0.	0.02	0.66	0.28
21	1982	1977	0.27	0.08	0.06	-0.06	0.1	0.39	0.42
22	2013	2007	0.34	0.25	0.06	-0.1	0.52	0.27	0.
23	2039	2041	0.09	0.05	0.14	-0.07	0.12	0.73	0.03
24	2057	2056	0.08	0.2	0.41	-0.21	0.4	0.06	0.15
25	2068	2058	0.5	0.19	0.44	-0.21	0.33	0.07	0.18
26	2084	2075	0.4	0.52	0.72	-0.36	0.09	0.	0.02
27	2144	2150	0.28	0.06	0.13	-0.03	0.34	0.05	0.45
28	2161	2164	0.14	0.07	0.15	-0.04	0.42	0.05	0.35
29	2200	2208	0.37	0.05	0.15	-0.06	0.21	0.65	0.
30	2344	2353	0.35	0.28	0.55	-0.29	0.13	0.32	0.01
31	2408	2417	0.34	0.22	0.52	-0.25	0.13	0.36	0.02
32	2455	2459	0.16	0.3	0.2	-0.17	0.13	0.45	0.1
33	2472	2481	0.36	0.27	0.33	0.08	0.22	0.02	0.07
34	2487	2485	0.1	0.16	0.03	-0.05	0.28	0.04	0.54

Table continued on next page.

Table 1 continued.

Index	f_{exp} (kHz)	f_{calc} (kHz)	Error (%)	α_i					
				$\frac{c_{11}+c_{12}}{2}$	c_{33}	c_{13}	c_{66}	c_{44}	$\frac{c_{11}-c_{12}}{2}$
35	2508	2501	0.29	0.35	0.2	-0.2	0.06	0.4	0.18
36	2533	2528	0.22	0.1	0.09	-0.05	0.25	0.53	0.07
37	2559	2560	0.06	0.08	0.12	-0.06	0.09	0.56	0.21
38	2561	2564	0.12	0.04	0.06	-0.02	0.24	0.46	0.2
39	2599	2600	0.01	0.1	0.14	-0.1	0.25	0.34	0.26
40	2625	2626	0.04	0.1	0.2	-0.07	0.18	0.48	0.11
41	2657	2651	0.24	0.17	0.3	-0.14	0.19	0.28	0.21
42	2667	2664	0.12	0.07	0.12	-0.05	0.11	0.52	0.24
43	2693	2695	0.05	0.14	0.27	-0.12	0.14	0.52	0.06
44	2699	2696	0.11	0.28	0.35	-0.23	0.06	0.44	0.09
45	2731	2718	0.49	0.13	0.18	-0.09	0.22	0.41	0.15
46	2782	2766	0.57	0.1	0.02	-0.01	0.39	0.29	0.21
47	2854	2850	0.14	0.17	0.07	-0.08	0.31	0.07	0.45
48	2903	2894	0.29	0.18	0.05	-0.07	0.36	0.05	0.44
49	2935	2906	0.98	0.14	0.19	-0.09	0.06	0.58	0.11
50	2937	2946	0.29	0.33	0.1	-0.12	0.22	0.1	0.37
51	2944	2951	0.25	0.01	0.01	0.	0.94	0.01	0.03
52	2974	2989	0.51	0.05	0.23	-0.08	0.33	0.32	0.14
53	2999	2998	0.03	0.17	0.11	-0.1	0.24	0.23	0.34
54	3000	2998	0.05	0.09	0.31	-0.12	0.22	0.49	0.01
55	3034	3049	0.47	0.12	0.34	-0.13	0.17	0.48	0.02
56	3051	3049	0.05	0.13	0.28	-0.1	0.2	0.42	0.07
57	3062	3058	0.13	0.18	0.11	-0.09	0.26	0.25	0.29
58	3074	3078	0.12	0.03	0.15	-0.05	0.51	0.31	0.05
59	3107	3115	0.27	0.06	0.03	-0.01	0.1	0.04	0.78
60	3136	3138	0.06	0.15	0.27	-0.12	0.19	0.46	0.05
61	3161	3171	0.32	0.15	0.22	-0.12	0.17	0.27	0.3
62	3188	3195	0.22	0.12	0.15	-0.08	0.16	0.6	0.05

Table continued on next page.

Table 1 continued.

Index	f_{exp} (kHz)	f_{calc} (kHz)	Error (%)	α_i					
				$\frac{c_{11}+c_{12}}{2}$	c_{33}	c_{13}	c_{66}	c_{44}	$\frac{c_{11}-c_{12}}{2}$
63	3194	3206	0.35	0.18	0.19	-0.14	0.06	0.17	0.53
64	3259	3234	0.77	0.12	0.16	-0.07	0.18	0.54	0.09
65	3279	3272	0.2	0.11	0.13	-0.07	0.18	0.41	0.24
66	3290	3291	0.05	0.09	0.12	-0.05	0.21	0.48	0.16
67	3297	3296	0.05	0.08	0.12	-0.05	0.23	0.52	0.1
68	3302	3299	0.11	0.18	0.28	-0.13	0.14	0.44	0.09
69	3305	3309	0.12	0.16	0.25	-0.12	0.18	0.48	0.06
70	3329	3322	0.2	0.33	0.31	-0.17	0.07	0.42	0.04
71	3338	3328	0.33	0.19	0.26	-0.14	0.08	0.56	0.04
72	3349	3331	0.55	0.13	0.21	-0.1	0.12	0.44	0.2
73	3361	3353	0.23	0.1	0.19	-0.07	0.04	0.67	0.07
74	3362	3357	0.14	0.14	0.21	-0.1	0.13	0.34	0.28
75	3369	3377	0.25	0.44	0.62	-0.42	0.18	0.18	0.01
76	3371	3381	0.29	0.3	0.26	-0.05	0.07	0.38	0.04
77	3463	3467	0.13	0.14	0.2	-0.1	0.14	0.35	0.26
78	3471	3473	0.06	0.02	0.06	-0.01	0.15	0.66	0.11
79	3473	3475	0.05	0.17	0.08	-0.09	0.38	0.08	0.37
80	3483	3482	0.03	0.5	0.69	-0.48	0.24	0.05	0.01
81	3494	3502	0.24	0.11	0.12	-0.06	0.22	0.56	0.07
82	3501	3512	0.33	0.03	0.11	-0.02	0.09	0.69	0.1
83	3526	3531	0.15	0.14	0.03	-0.02	0.73	0.02	0.11
84	3549	3555	0.17	0.07	0.02	-0.01	0.76	0.04	0.13
85	3662	3654	0.22	0.13	0.05	-0.05	0.33	0.21	0.33
86	3673	3661	0.35	0.12	0.11	-0.08	0.37	0.33	0.16
87	3676	3674	0.06	0.1	0.11	-0.06	0.38	0.34	0.12
88	3696	3689	0.19	0.48	0.59	-0.43	0.12	0.1	0.13
89	3700	3705	0.16	0.1	0.13	-0.07	0.28	0.38	0.19
90	3708	3709	0.04	0.11	0.27	-0.09	0.23	0.38	0.1

Table continued on next page.

Table 1 continued.

Index	f_{exp} (kHz)	f_{calc} (kHz)	Error (%)	α_i					
				$\frac{c_{11}+c_{12}}{2}$	c_{33}	c_{13}	c_{66}	c_{44}	$\frac{c_{11}-c_{12}}{2}$
91	3712	3715	0.09	0.06	0.11	-0.04	0.26	0.46	0.15
92	3722	3730	0.22	0.16	0.12	-0.08	0.04	0.35	0.42
93	3743	3752	0.25	0.1	0.17	-0.08	0.09	0.46	0.27
94	3771	3773	0.06	0.12	0.32	-0.13	0.13	0.38	0.18
95	3779	3786	0.19	0.14	0.21	-0.1	0.2	0.43	0.12
96	3799	3795	0.09	0.16	0.21	-0.12	0.19	0.28	0.29
97	3810	3806	0.12	0.13	0.17	-0.1	0.28	0.3	0.22
98	3819	3816	0.07	0.07	0.19	-0.08	0.38	0.36	0.09
99	3846	3836	0.26	0.24	0.24	-0.17	0.24	0.23	0.21
100	3888	3890	0.05	0.1	0.12	-0.04	0.18	0.15	0.5

Table E.4: Fit for RUS frequencies of Sr_2RuO_4 at 4 K.

Index	f_{exp} (kHz)	f_{calc} (kHz)	Error (%)	α_i					
				$\frac{c_{11}+c_{12}}{2}$	c_{33}	c_{13}	c_{66}	c_{44}	$\frac{c_{11}-c_{12}}{2}$
1	889	886	0.3	0.01	0.01	0.	0.	0.28	0.71
2	1084	1084	0.01	0.	0.	0.	0.02	0.94	0.03
3	1207	1213	0.47	0.02	0.	-0.01	0.02	0.	0.97
4	1291	1290	0.05	0.04	0.01	-0.01	0.77	0.18	0.
5	1338	1342	0.29	0.26	0.1	-0.12	0.41	0.01	0.35
6	1399	1404	0.33	0.01	0.02	-0.01	0.05	0.93	0.
7	1447	1450	0.19	0.01	0.02	-0.01	0.06	0.92	0.
8	1476	1475	0.08	0.27	0.15	-0.15	0.38	0.02	0.33
9	1507	1511	0.27	0.01	0.	0.	0.99	0.	0.
10	1660	1667	0.43	0.45	0.08	-0.13	0.13	0.45	0.02
11	1680	1675	0.3	0.19	0.02	-0.04	0.45	0.37	0.01
12	1694	1701	0.37	0.34	0.42	-0.29	0.52	0.01	0.
13	1721	1714	0.42	0.07	0.66	-0.16	0.03	0.33	0.07

Table continued on next page.

Table 1 continued.

Index	f_{exp} (kHz)	f_{calc} (kHz)	Error (%)	α_i					
				$\frac{c_{11}+c_{12}}{2}$	c_{33}	c_{13}	c_{66}	c_{44}	$\frac{c_{11}-c_{12}}{2}$
14	1737	1737	0.01	0.18	0.02	-0.04	0.5	0.33	0.02
15	1742	1746	0.25	0.05	0.6	-0.12	0.06	0.32	0.09
16	1794	1788	0.36	0.04	0.03	-0.02	0.06	0.39	0.51
17	1851	1847	0.22	0.12	0.78	-0.22	0.	0.11	0.22
18	1871	1878	0.36	0.62	0.87	-0.56	0.06	0.	0.
19	1915	1908	0.36	0.06	0.04	-0.03	0.08	0.37	0.49
20	1919	1921	0.14	0.02	0.02	0.	0.01	0.72	0.23
21	1933	1929	0.23	0.08	0.26	0.	0.61	0.04	0.
22	2044	2049	0.26	0.09	0.08	-0.05	0.48	0.03	0.36
23	2064	2062	0.08	0.23	0.05	-0.08	0.54	0.26	0.
24	2073	2067	0.29	0.11	0.14	-0.09	0.55	0.03	0.26
25	2076	2077	0.04	0.05	0.14	-0.06	0.12	0.72	0.03
26	2129	2124	0.23	0.14	0.5	-0.16	0.25	0.06	0.21
27	2151	2150	0.06	0.12	0.43	-0.13	0.32	0.06	0.2
28	2170	2160	0.48	0.48	0.69	-0.31	0.1	0.	0.04
29	2245	2253	0.36	0.05	0.13	-0.05	0.22	0.66	0.
30	2364	2364	0.01	0.1	0.01	-0.02	0.2	0.03	0.68
31	2423	2431	0.34	0.24	0.56	-0.25	0.12	0.31	0.02
32	2452	2442	0.4	0.08	0.04	-0.02	0.18	0.45	0.27
33	2484	2485	0.04	0.16	0.48	-0.19	0.14	0.36	0.05
34	2496	2516	0.8	0.17	0.3	0.09	0.29	0.01	0.14
35	2542	2544	0.06	0.09	0.07	-0.06	0.18	0.25	0.48
36	2549	2554	0.17	0.06	0.07	-0.03	0.28	0.52	0.09
37	2552	2556	0.18	0.04	0.08	-0.02	0.23	0.51	0.17
38	2561	2559	0.07	0.11	0.14	-0.07	0.07	0.61	0.15
39	2573	2577	0.16	0.59	0.31	-0.3	0.05	0.34	0.01
40	2644	2641	0.1	0.19	0.41	-0.16	0.13	0.13	0.3
41	2648	2645	0.1	0.07	0.09	-0.04	0.09	0.57	0.23

Table continued on next page.

Table 1 continued.

Index	f_{exp} (kHz)	f_{calc} (kHz)	Error (%)	α_i					
				$\frac{c_{11}+c_{12}}{2}$	c_{33}	c_{13}	c_{66}	c_{44}	$\frac{c_{11}-c_{12}}{2}$
42	2659	2655	0.14	0.12	0.22	-0.09	0.14	0.52	0.1
43	2743	2739	0.11	0.13	0.23	-0.11	0.15	0.5	0.09
44	2747	2743	0.13	0.24	0.32	-0.19	0.06	0.38	0.19
45	2765	2757	0.29	0.12	0.06	-0.04	0.3	0.53	0.03
46	2770	2768	0.08	0.15	0.03	-0.04	0.39	0.03	0.45
47	2789	2770	0.68	0.05	0.07	0.	0.37	0.41	0.11
48	2817	2811	0.22	0.14	0.03	-0.04	0.38	0.02	0.46
49	2852	2867	0.54	0.06	0.08	-0.02	0.07	0.08	0.74
50	2892	2902	0.36	0.08	0.11	-0.05	0.06	0.46	0.34
51	2936	2915	0.72	0.45	0.09	-0.08	0.18	0.06	0.3
52	2945	2950	0.18	0.14	0.05	-0.05	0.27	0.26	0.32
53	3003	3006	0.09	0.04	0.23	-0.07	0.25	0.35	0.2
54	3021	3016	0.16	0.13	0.05	-0.03	0.27	0.27	0.32
55	3028	3030	0.07	0.	0.	0.	0.98	0.	0.02
56	3057	3067	0.34	0.13	0.14	-0.07	0.07	0.29	0.44
57	3071	3070	0.02	0.08	0.3	-0.1	0.23	0.48	0.02
58	3110	3105	0.14	0.1	0.29	-0.09	0.2	0.43	0.07
59	3115	3125	0.32	0.11	0.35	-0.12	0.16	0.49	0.
60	3127	3138	0.37	0.15	0.2	-0.1	0.18	0.29	0.29
61	3135	3146	0.35	0.04	0.15	-0.06	0.51	0.31	0.05
62	3204	3199	0.14	0.11	0.27	-0.1	0.2	0.45	0.06
63	3244	3250	0.19	0.08	0.12	-0.05	0.19	0.41	0.25
64	3256	3251	0.15	0.09	0.15	-0.06	0.17	0.61	0.04
65	3309	3286	0.71	0.12	0.18	-0.08	0.16	0.57	0.05
66	3312	3303	0.27	0.09	0.13	-0.05	0.17	0.53	0.13
67	3323	3315	0.24	0.09	0.17	-0.07	0.11	0.42	0.27
68	3330	3321	0.26	0.17	0.26	-0.12	0.11	0.32	0.26
69	3341	3323	0.53	0.09	0.16	-0.06	0.19	0.5	0.11

Table continued on next page.

Table 1 continued.

Index	f_{exp} (kHz)	f_{calc} (kHz)	Error (%)	α_i					
				$\frac{c_{11}+c_{12}}{2}$	c_{33}	c_{13}	c_{66}	c_{44}	$\frac{c_{11}-c_{12}}{2}$
70	3353	3338	0.46	0.15	0.28	-0.12	0.14	0.39	0.17
71	3372	3383	0.33	0.16	0.21	-0.09	0.17	0.5	0.05
72	3389	3385	0.1	0.13	0.03	-0.04	0.4	0.03	0.46
73	3398	3397	0.02	0.12	0.22	-0.08	0.08	0.63	0.02
74	3399	3405	0.16	0.07	0.16	-0.04	0.04	0.74	0.03
75	3423	3417	0.18	0.34	0.33	-0.17	0.05	0.43	0.02
76	3443	3449	0.17	0.18	0.19	-0.1	0.11	0.37	0.25
77	3452	3464	0.36	0.3	0.27	-0.06	0.06	0.41	0.02
78	3476	3493	0.47	0.02	0.15	-0.03	0.08	0.68	0.1
79	3509	3511	0.05	0.06	0.04	-0.01	0.29	0.09	0.54
80	3514	3518	0.12	0.11	0.07	-0.04	0.29	0.29	0.29

BIBLIOGRAPHY

- [1] Sayak Ghosh, Michael Matty, Ryan Baumbach, Eric D. Bauer, K. A. Modic, Arkady Shekhter, J. A. Mydosh, Eun-Ah Kim, and B. J. Ramshaw. One-component order parameter in URu_2Si_2 uncovered by resonant ultrasound spectroscopy and machine learning. *Science Advances*, 6(10), 2020.
- [2] Sayak Ghosh, Arkady Shekhter, F. Jerzembeck, N. Kikugawa, Dmitry A. Sokolov, Manuel Brando, A. P. Mackenzie, Clifford W. Hicks, and B. J. Ramshaw. Thermodynamic evidence for a two-component superconducting order parameter in Sr_2RuO_4 . *Nature Physics*, 17(2):199–204, Feb 2021.
- [3] Sayak Ghosh, Thomas G. Kiely, Arkady Shekhter, F. Jerzembeck, N. Kikugawa, Dmitry A. Sokolov, A. P. Mackenzie, and B. J. Ramshaw. Strong increase in ultrasound attenuation below T_c in Sr_2RuO_4 : Possible evidence for domains. *arXiv:2109.00041*, 2021.
- [4] Andrew Peter Mackenzie and Yoshiteru Maeno. The superconductivity of Sr_2RuO_4 and the physics of spin-triplet pairing. *Rev. Mod. Phys.*, 75:657–712, May 2003.
- [5] S. Raghu, E. Berg, A. V. Chubukov, and S. A. Kivelson. Effects of longer-range interactions on unconventional superconductivity. *Phys. Rev. B*, 85:024516, Jan 2012.
- [6] Y. Kasahara, H. Shishido, T. Shibauchi, Y. Haga, T. D. Matsuda, Y. Onuki, and Y. Matsuda. Superconducting gap structure of heavy-fermion compound URu_2Si_2 determined by angle-resolved thermal conductivity. *New Journal of Physics*, 11(5):055061, May 2009.
- [7] C. Lupien, W. A. MacFarlane, Cyril Proust, Louis Taillefer, Z. Q. Mao, and Y. Maeno. Ultrasound attenuation in Sr_2RuO_4 : An angle-resolved study of the superconducting gap function. *Phys. Rev. Lett.*, 86:5986–5989, Jun 2001.
- [8] Xiao-Gang Wen. Colloquium: Zoo of quantum-topological phases of matter. *Rev. Mod. Phys.*, 89:041004, Dec 2017.
- [9] B. Keimer, S. A. Kivelson, M. R. Norman, S. Uchida, and J. Zaanen. From quantum matter to high-temperature superconductivity in copper oxides. *Nature*, 518(7538):179–186, Feb 2015.
- [10] J. A. Mydosh and P. M. Oppeneer. Colloquium: Hidden order, superconductivity, and magnetism: The unsolved case of URu_2Si_2 . *Rev. Mod. Phys.*, 83:1301–1322, Nov 2011.

- [11] Arkady Shekhter, B. J. Ramshaw, Ruixing Liang, W. N. Hardy, D. A. Bonn, Fedor F. Balakirev, Ross D. McDonald, Jon B. Betts, Scott C. Riggs, and Albert Migliori. Bounding the pseudogap with a line of phase transitions in $\text{YBa}_2\text{Cu}_3\text{O}_{6+\delta}$. *Nature*, 498:75 EP –, Jun 2013.
- [12] B. J. Ramshaw, Arkady Shekhter, Ross D. McDonald, Jon B. Betts, J. N. Mitchell, P. H. Tobash, C. H. Mielke, E. D. Bauer, and Albert Migliori. Avoided valence transition in a plutonium superconductor. *Proceedings of the National Academy of Sciences*, 112(11):3285–3289, 2015.
- [13] Moises Levy. Ultrasonic attenuation in superconductors for $q\ell < 1$. *Phys. Rev.*, 131:1497–1500, Aug 1963.
- [14] Robert Joynt and Louis Taillefer. The superconducting phases of UPt_3 . *Rev. Mod. Phys.*, 74:235–294, Mar 2002.
- [15] R. M. Fernandes, L. H. VanBebber, S. Bhattacharya, P. Chandra, V. Keppens, D. Mandrus, M. A. McGuire, B. C. Sales, A. S. Sefat, and J. Schmalian. Effects of nematic fluctuations on the elastic properties of iron arsenide superconductors. *Phys. Rev. Lett.*, 105:157003, Oct 2010.
- [16] Clifford W. Hicks, Mark E. Barber, Stephen D. Edkins, Daniel O. Brodsky, and Andrew P. Mackenzie. Piezoelectric-based apparatus for strain tuning. *Review of Scientific Instruments*, 85(6):065003, 2014.
- [17] Joonbum Park, Jack M. Bartlett, Hilary M. L. Noad, Alexander L. Stern, Mark E. Barber, Markus König, Suguru Hosoi, Takasada Shibauchi, Andrew P. Mackenzie, Alexander Steppke, and Clifford W. Hicks. Rigid platform for applying large tunable strains to mechanically delicate samples. *Review of Scientific Instruments*, 91(8):083902, 2020.
- [18] Clifford W. Hicks, Daniel O. Brodsky, Edward A. Yelland, Alexandra S. Gibbs, Jan A. N. Bruin, Mark E. Barber, Stephen D. Edkins, Keigo Nishimura, Shingo Yonezawa, Yoshiteru Maeno, and Andrew P. Mackenzie. Strong increase of T_c of Sr_2RuO_4 under both tensile and compressive strain. *Science*, 344(6181):283–285, 2014.
- [19] Vadim Grinenko, Shreenanda Ghosh, Rajib Sarkar, Jean-Christophe Orain, Artem Nikitin, Matthias Elender, Debarchan Das, Zurab Guguchia, Felix Brückner, Mark E. Barber, Joonbum Park, Naoki Kikugawa, Dmitry A. Sokolov, Jake S. Bobowski, Takuto Miyoshi, Yoshiteru Maeno, Andrew P. Mackenzie, Hubertus Luetkens, Clifford W. Hicks, and Hans-Henning Klauss. Split superconducting and time-reversal symmetry-breaking transitions in Sr_2RuO_4 under stress. *Nature Physics*, 17(6):748–754, Jun 2021.
- [20] Jiun-Haw Chu, Hsueh-Hui Kuo, James G. Analytis, and Ian R. Fisher. Divergent

- nematic susceptibility in an iron arsenide superconductor. *Science*, 337(6095):710–712, 2012.
- [21] Hsueh-Hui Kuo, Jiun-Haw Chu, Johanna C. Palmstrom, Steven A. Kivelson, and Ian R. Fisher. Ubiquitous signatures of nematic quantum criticality in optimally doped Fe-based superconductors. *Science*, 352(6288):958–962, 2016.
 - [22] Matthias S. Ikeda, Thanapat Worasaran, Elliott W. Rosenberg, Johanna C. Palmstrom, Steven A. Kivelson, and Ian R. Fisher. Elastocaloric signature of nematic fluctuations. *Proceedings of the National Academy of Sciences*, 118(37):e2105911118, 2021.
 - [23] You-Sheng Li, Markus Garst, Jörg Schmalian, Sayak Ghosh, Naoki Kikugawa, Dmitry A. Sokolov, Clifford W. Hicks, Fabian Jerzembeck, Matthias S. Ikeda, Zhenhai Hu, B. J. Ramshaw, Andreas W. Rost, Michael Nicklas, and Andrew P. Mackenzie. Elastocaloric determination of the phase diagram of Sr_2RuO_4 . *Nature*, 607(7918):276–280, Jul 2022.
 - [24] P. Ehrenfest and T. Ehrenfest. *The conceptual foundations of the statistical approach in mechanics*. Cornell University Press, Ithaca, N.Y., 1959.
 - [25] J. A. Lipa, J. A. Nissen, D. A. Stricker, D. R. Swanson, and T. C. P. Chui. Specific heat of liquid helium in zero gravity very near the lambda point. *Phys. Rev. B*, 68:174518, Nov 2003.
 - [26] L. D. (Lev Davidovich) Landau. *Statistical physics / by L.D. Landau and E.M. Lifshitz ; translated from the Russian by J.R. Sykes and M.J. Kearsley*. The Course of theoretical physics ; v. 9, pt. 2. Pergamon Press, Oxford, 3d ed. / by e.m. lifshitz and l.p. pitaeviskiĭ. edition, 1980.
 - [27] James P. Sethna. *Statistical Mechanics: Entropy, Order Parameters and Complexity*. Oxford University Press, Oxford, 2006.
 - [28] Mehran Kardar. *Statistical Physics of Fields*. Cambridge University Press, Cambridge, 2007.
 - [29] R.K. Pathria and P.D. Beale. *Statistical Mechanics*. Elsevier Science, Amsterdam, 2011.
 - [30] Manfred Sigrist and Kazuo Ueda. Phenomenological theory of unconventional superconductivity. *Rev. Mod. Phys.*, 63:239–311, Apr 1991.
 - [31] Walther Rehwald. The study of structural phase transitions by means of ultrasonic experiments. *Advances in Physics*, 22(6):721–755, 1973.

- [32] C. C. Tsuei and J. R. Kirtley. Pairing symmetry in cuprate superconductors. *Rev. Mod. Phys.*, 72:969–1016, Oct 2000.
- [33] J. D. Strand, D. J. Bahr, D. J. Van Harlingen, J. P. Davis, W. J. Gannon, and W. P. Halperin. The transition between real and complex superconducting order parameter phases in UPt_3 . *Science*, 328(5984):1368–1369, 2010.
- [34] K. Miyake and C. M. Varma. Landau-Khalatnikov damping of ultrasound in heavy-fermion superconductors. *Phys. Rev. Lett.*, 57:1627–1630, Sep 1986.
- [35] H. Jaballah, K. Nouri, N. Mliki, L. Bessais, and M. Jemmali. Universality class change from mean-field to 3D-Heisenberg in magnetocaloric compounds $\text{SmNi}_{3-x}\text{Fe}_x$. *Chemical Physics Letters*, 787:139260, 2022.
- [36] Rafael M. Fernandes, Amalia I. Coldea, Hong Ding, Ian R. Fisher, P. J. Hirschfeld, and Gabriel Kotliar. Iron pnictides and chalcogenides: a new paradigm for superconductivity. *Nature*, 601(7891):35–44, Jan 2022.
- [37] Anna E. Böhmer and Christoph Meingast. Electronic nematic susceptibility of iron-based superconductors. *Comptes Rendus Physique*, 17(1):90–112, 2016.
- [38] J. Nyhus, U. Thisted, N. Kikugawa, T. Suzuki, and K. Fossheim. Elastic and specific heat critical properties of $\text{La}_{1.85}\text{Sr}_{0.15}\text{CuO}_4$. *Physica C: Superconductivity*, 369(1):273 – 277, 2002.
- [39] S. Raghu, Suk Bum Chung, Xiao-Liang Qi, and Shou-Cheng Zhang. Collective modes of a helical liquid. *Phys. Rev. Lett.*, 104:116401, Mar 2010.
- [40] Liang Fu and Erez Berg. Odd-parity topological superconductors: Theory and application to $\text{Cu}_x\text{Bi}_2\text{Se}_3$. *Phys. Rev. Lett.*, 105:097001, Aug 2010.
- [41] K. Fossheim and B. Berre. Ultrasonic propagation, stress effects, and interaction parameters at the displacive transition in SrTiO_3 . *Phys. Rev. B*, 5:3292–3308, Apr 1972.
- [42] J O Fossum and K Fossheim. Measurements of ultrasonic attenuation and velocity in verneuil-grown and flux-grown SrTiO_3 . *Journal of Physics C: Solid State Physics*, 18(29):5549–5578, oct 1985.
- [43] Manfred Sigrist. Ehrenfest Relations for Ultrasound Absorption in Sr_2RuO_4 . *Progress of Theoretical Physics*, 107(5):917–925, 05 2002.
- [44] Wen Huang, Yi Zhou, and Hong Yao. Possible 3D nematic odd-parity pairing in Sr_2RuO_4 : experimental evidences and predictions. *arXiv e-prints*, page arXiv:1901.07041, Jan 2019.

- [45] Steven Allan Kivelson, Andrew Chang Yuan, Brad Ramshaw, and Ronny Thomale. A proposal for reconciling diverse experiments on the superconducting state in Sr_2RuO_4 . *npj Quantum Materials*, 5(1):43, Jun 2020.
- [46] Roland Willa, Matthias Hecker, Rafael M. Fernandes, and Jörg Schmalian. Inhomogeneous time-reversal symmetry breaking in Sr_2RuO_4 . *Phys. Rev. B*, 104:024511, Jul 2021.
- [47] Andrew C. Yuan, Erez Berg, and Steven A. Kivelson. Strain-induced time reversal breaking and half quantum vortices near a putative superconducting tetracritical point in Sr_2RuO_4 . *Phys. Rev. B*, 104:054518, Aug 2021.
- [48] T. H. K. Barron and G. K. White. *Heat capacity and thermal expansion at low temperatures*. Springer Science and Business Media, 2012.
- [49] Sheng Ran, Christian T. Wolowiec, Inho Jeon, Naveen Pouse, Noravee Kanchanavatee, Benjamin D. White, Kevin Huang, Dinesh Martien, Tyler DaPron, David Snow, Mark Williamsen, Stefano Spagna, Peter S. Riseborough, and M. Brian Maple. Phase diagram and thermal expansion measurements on the system $\text{URu}_{2-x}\text{Fe}_x\text{Si}_2$. *Proceedings of the National Academy of Sciences*, 113(47):13348–13353, 2016.
- [50] You-Sheng Li, Naoki Kikugawa, Dmitry A. Sokolov, Fabian Jerzembeck, Alexandra S. Gibbs, Yoshiteru Maeno, Clifford W. Hicks, Jörg Schmalian, Michael Nicklas, and Andrew P. Mackenzie. High-sensitivity heat-capacity measurements on Sr_2RuO_4 under uniaxial pressure. *Proceedings of the National Academy of Sciences*, 118(10), 2021.
- [51] N. D. Mermin and H. Wagner. Absence of ferromagnetism or antiferromagnetism in one- or two-dimensional isotropic Heisenberg models. *Phys. Rev. Lett.*, 17:1133–1136, Nov 1966.
- [52] G. E. Dieter and D. J. Bacon. *Mechanical metallurgy*. McGraw-Hill, London, 1988.
- [53] Fedor F. Balakirev, Susan M. Ennaceur, Robert J. Migliori, Boris Maiorov, and Albert Migliori. Resonant ultrasound spectroscopy: The essential toolbox. *Review of Scientific Instruments*, 90(12):121401, 2019.
- [54] William M. Visscher, Albert Migliori, Thomas M. Bell, and Robert A. Reinert. On the normal modes of free vibration of inhomogeneous and anisotropic elastic objects. *The Journal of the Acoustical Society of America*, 90(4):2154–2162, 1991.
- [55] E. Hassinger, P. Bourgeois-Hope, H. Taniguchi, S. René de Cotret, G. Grisson-nanche, M. S. Anwar, Y. Maeno, N. Doiron-Leyraud, and Louis Taillefer. Vertical line nodes in the superconducting gap structure of Sr_2RuO_4 . *Phys. Rev. X*, 7:011032, Mar 2017.

- [56] C. Sidney Burrus. Vector space and matrix methods in signal and system theory. 2019.
- [57] J. A. Mydosh and P. M. Oppeneer. Hidden order behaviour in URu₂Si₂ (a critical review of the status of hidden order in 2014). *Philosophical Magazine*, 94(32-33):3642–3662, 2014.
- [58] J. A. Mydosh, P. M. Oppeneer, and P. S. Riseborough. Hidden order and beyond: an experimental—theoretical overview of the multifaceted behavior of URu₂Si₂. *Journal of Physics: Condensed Matter*, 32(14):143002, Jan 2020.
- [59] T. T. M. Palstra, A. A. Menovsky, J. van den Berg, A. J. Dirkmaat, P. H. Kes, G. J. Nieuwenhuys, and J. A. Mydosh. Superconducting and magnetic transitions in the heavy-fermion system URu₂Si₂. *Phys. Rev. Lett.*, 55:2727–2730, Dec 1985.
- [60] M. B. Maple, J. W. Chen, Y. Dalichaouch, T. Kohara, C. Rossel, M. S. Torikachvili, M. W. McElfresh, and J. D. Thompson. Partially gapped fermi surface in the heavy-electron superconductor URu₂Si₂. *Phys. Rev. Lett.*, 56:185–188, Jan 1986.
- [61] W. Schlabitz, J. Baumann, B. Pollit, U. Rauchschwalbe, H. M. Mayer, U. Ahlheim, and C. D. Bredl. Superconductivity and magnetic order in a strongly interacting fermi-system: URu₂Si₂. *Zeitschrift für Physik B Condensed Matter*, 62(2):171–177, Jun 1986.
- [62] C. Broholm, J. K. Kjems, W. J. L. Buyers, P. Matthews, T. T. M. Palstra, A. A. Menovsky, and J. A. Mydosh. Magnetic excitations and ordering in the heavy-electron superconductor URu₂Si₂. *Phys. Rev. Lett.*, 58:1467–1470, Apr 1987.
- [63] C. Broholm, H. Lin, P. T. Matthews, T. E. Mason, W. J. L. Buyers, M. F. Collins, A. A. Menovsky, J. A. Mydosh, and J. K. Kjems. Magnetic excitations in the heavy-fermion superconductor URu₂Si₂. *Phys. Rev. B*, 43:12809–12822, Jun 1991.
- [64] P. Santini and G. Amoretti. Crystal field model of the magnetic properties of URu₂Si₂. *Phys. Rev. Lett.*, 73:1027–1030, Aug 1994.
- [65] Fusayoshi J. Ohkawa and Hirofumi Shimizu. Quadrupole and dipole orders in URu₂Si₂. *Journal of Physics: Condensed Matter*, 11(46):L519–L524, Nov 1999.
- [66] Annamária Kiss and Patrik Fazekas. Group theory and octupolar order in URu₂Si₂. *Phys. Rev. B*, 71:054415, Feb 2005.
- [67] Francesco Cricchio, Fredrik Bultmark, Oscar Grånäs, and Lars Nordström. Itinerant magnetic multipole moments of rank five as the hidden order in URu₂Si₂. *Phys. Rev. Lett.*, 103:107202, Sep 2009.

- [68] Kristjan Haule and Gabriel Kotliar. Arrested Kondo effect and hidden order in URu_2Si_2 . *Nature Physics*, 5(11):796–799, Nov 2009.
- [69] Hisatomo Harima, Kazumasa Miyake, and Jacques Flouquet. Why the hidden order in URu_2Si_2 is still hidden—one simple answer. *Journal of the Physical Society of Japan*, 79(3):033705, 2010.
- [70] Hiroaki Kusunose and Hisatomo Harima. On the hidden order in URu_2Si_2 – anti-ferro hexadecapole order and its consequences. *Journal of the Physical Society of Japan*, 80(8):084702, 2011.
- [71] H.-H. Kung, R. E. Baumbach, E. D. Bauer, V. K. Thorsmølle, W.-L. Zhang, K. Haule, J. A. Mydosh, and G. Blumberg. Chirality density wave of the “hidden order” phase in URu_2Si_2 . *Science*, 347(6228):1339–1342, 2015.
- [72] H.-H. Kung, S. Ran, N. Kanchanavatee, V. Krapivin, A. Lee, J. A. Mydosh, K. Haule, M. B. Maple, and G. Blumberg. Analogy between the “hidden order” and the orbital antiferromagnetism in URu_2Si_2 . *Phys. Rev. Lett.*, 117:227601, Nov 2016.
- [73] S. Kambe, Y. Tokunaga, H. Sakai, T. Hattori, N. Higa, T. D. Matsuda, Y. Haga, R. E. Walstedt, and H. Harima. Odd-parity electronic multipolar ordering in URu_2Si_2 : Conclusions from Si and Ru NMR measurements. *Phys. Rev. B*, 97:235142, Jun 2018.
- [74] Satoshi Fujimoto. Spin nematic state as a candidate of the hidden order phase of URu_2Si_2 . *Phys. Rev. Lett.*, 106:196407, May 2011.
- [75] Peter Thalmeier and Tetsuya Takimoto. Signatures of hidden-order symmetry in torque oscillations, elastic constant anomalies, and field-induced moments in URu_2Si_2 . *Phys. Rev. B*, 83:165110, Apr 2011.
- [76] Jeffrey G. Rau and Hae-Young Kee. Hidden and antiferromagnetic order as a rank-5 superspin in URu_2Si_2 . *Phys. Rev. B*, 85:245112, Jun 2012.
- [77] S. Tonegawa, K. Hashimoto, K. Ikada, Y.-H. Lin, H. Shishido, Y. Haga, T. D. Matsuda, E. Yamamoto, Y. Onuki, H. Ikeda, Y. Matsuda, and T. Shibauchi. Cyclotron resonance in the hidden-order phase of URu_2Si_2 . *Phys. Rev. Lett.*, 109:036401, Jul 2012.
- [78] Hiroaki Ikeda, Michi-To Suzuki, Ryotaro Arita, Tetsuya Takimoto, Takasada Shibauchi, and Yuji Matsuda. Emergent rank-5 nematic order in URu_2Si_2 . *Nature Physics*, 8:528 EP –, Jun 2012.
- [79] Shintaro Hoshino, Junya Otsuki, and Yoshio Kuramoto. Resolution of entropy

- in $\sqrt{2}$ by ordering in two-channel Kondo lattice. *Journal of the Physical Society of Japan*, 82(4):044707, 2013.
- [80] Scott C. Riggs, M. C. Shapiro, Akash V. Maharaj, S. Raghu, E. D. Bauer, R. E. Baumbach, P. Giraldo-Gallo, Mark Wartenbe, and I. R. Fisher. Evidence for a nematic component to the hidden-order parameter in URu₂Si₂ from differential elastoresistance measurements. *Nature Communications*, 6(1):6425, Mar 2015.
 - [81] R. Okazaki, T. Shibauchi, H. J. Shi, Y. Haga, T. D. Matsuda, E. Yamamoto, Y. Onuki, H. Ikeda, and Y. Matsuda. Rotational symmetry breaking in the hidden-order phase of URu₂Si₂. *Science*, 331(6016):439–442, 2011.
 - [82] S. Tonegawa, S. Kasahara, T. Fukuda, K. Sugimoto, N. Yasuda, Y. Tsuruhara, D. Watanabe, Y. Mizukami, Y. Haga, T. D. Matsuda, E. Yamamoto, Y. Onuki, H. Ikeda, Y. Matsuda, and T. Shibauchi. Direct observation of lattice symmetry breaking at the hidden-order transition in URu₂Si₂. *Nature Communications*, 5(1):4188, Jun 2014.
 - [83] J. Choi, O. Ivashko, N. Dennler, D. Aoki, K. von Arx, S. Gerber, O. Gutowski, M. H. Fischer, J. Strempfer, M. v. Zimmermann, and J. Chang. Pressure-induced rotational symmetry breaking in URu₂Si₂. *Phys. Rev. B*, 98:241113, Dec 2018.
 - [84] Tetsuo Fukase, Yoji Koike, Takashi Nakanomyo, Yoshinobu Shiokawa, Alois A. Makanomyo, John A. Mydosh, and Peter H. Kes. Ultrasonic attenuation in URu₂Si₂. *Japanese Journal of Applied Physics*, 26(S3-2):1249, 1987.
 - [85] G. L. Bullock, B. S. Shivaram, and David G. Hinks. Longitudinal ultrasound in the heavy electron superconductor URu₂Si₂. *Physica C: Superconductivity*, 169(5-6):497–500, 1990.
 - [86] B Wolf, P. Thalmeier, G. Bruls, W. Sixl, D. Finsterbusch, and B. Lüthi. Ultrasound propagation in the heavy-fermion superconductors URu₂Si₂ and CeCu₂Si₂. *Physica B: Condensed Matter*, 199:167–169, 1994.
 - [87] T Yanagisawa, H Saito, Y Watanabe, Y Shimizu, H Hidaka, and H Amitsuka. A study of elastic properties of URu₂Si₂ in comparison with the non-5f contribution of ThRu₂Si₂. *Journal of Physics: Conference Series*, 391:012079, Dec 2012.
 - [88] T. Yanagisawa, S. Mombetsu, H. Hidaka, H. Amitsuka, P. T. Cong, S. Yasin, S. Zherlitsyn, J. Wosnitzer, K. Huang, N. Kanchanavatee, M. Janoschek, M. B. Maple, and D. Aoki. Search for multipolar instability in URu₂Si₂ studied by ultrasonic measurements under pulsed magnetic field. *Phys. Rev. B*, 97:155137, Apr 2018.
 - [89] Neil Harrison and Marcelo Jaime. Hidden valence transition in URu₂Si₂? *arXiv:1902.06588*, 2019.

- [90] Premala Chandra, Piers Coleman, and Rebecca Flint. Hysteric order in the heavy-fermion compound URu₂Si₂. *Nature*, 493:621 EP –, Jan 2013.
- [91] K. A. Modic, Maja D. Bachmann, B. J. Ramshaw, F. Arnold, K. R. Shirer, Amelia Estry, J. B. Betts, Nirmal J. Ghimire, E. D. Bauer, Marcus Schmidt, Michael Baenitz, E. Svanidze, Ross D. McDonald, Arkady Shekhter, and Philip J. W. Moll. Resonant torsion magnetometry in anisotropic quantum materials. *Nature Communications*, 9(1):3975, Sep 2018.
- [92] S. L. Altmann and P. Herzig. *Point-group theory tables*. Oxford, 1994.
- [93] Andrew Gallagher, William Nelson, Kuan Chen, Tiglet Besara, Theo Siegrist, and Ryan Baumbach. Single crystal growth of URu₂Si₂ by the modified Bridgman technique. *Crystals*, 6(10):128, 2016.
- [94] R.E. Baumbach, Z. Fisk, F. Ronning, R. Movshovich, J.D. Thompson, and E.D. Bauer. High purity specimens of URu₂Si₂ produced by a molten metal flux technique. *Philosophical Magazine*, 94(32-33):3663–3671, 2014.
- [95] Juan Carrasquilla and Roger G. Melko. Machine learning phases of matter. *Nature Physics*, 13(5):431–434, May 2017.
- [96] Runhai Ouyang, Stefano Curtarolo, Emre Ahmetcik, Matthias Scheffler, and Luca M. Ghiringhelli. Sisso: A compressed-sensing method for identifying the best low-dimensional descriptor in an immensity of offered candidates. *Phys. Rev. Materials*, 2:083802, Aug 2018.
- [97] Annabelle Bohrdt, Christie S. Chiu, Geoffrey Ji, Muqing Xu, Daniel Greif, Markus Greiner, Eugene Demler, Fabian Grusdt, and Michael Knap. Classifying snapshots of the doped hubbard model with machine learning. *Nature Physics*, 15(9):921–924, Sep 2019.
- [98] Benno S. Rem, Niklas Käming, Matthias Tarnowski, Luca Asteria, Nick Fläschner, Christoph Becker, Klaus Sengstock, and Christof Weitenberg. Identifying quantum phase transitions using artificial neural networks on experimental data. *Nature Physics*, 15(9):917–920, Sep 2019.
- [99] Yi Zhang, A. Mesaros, K. Fujita, S. D. Edkins, M. H. Hamidian, K. Ch’ng, H. Eisaki, S. Uchida, J. C. Séamus Davis, Ehsan Khatami, and Eun-Ah Kim. Machine learning in electronic-quantum-matter imaging experiments. *Nature*, 570(7762):484–490, Jun 2019.
- [100] Youhei Yamaji, Teppei Yoshida, Atsushi Fujimori, and Masatoshi Imada. Hidden self-energies as origin of cuprate superconductivity revealed by machine learning. *Phys. Rev. Research*, 3:043099, Nov 2021.

- [101] Y. P. Varshni. Temperature dependence of the elastic constants. *Phys. Rev. B*, 2:3952–3958, Nov 1970.
- [102] Albert Migliori, Hassel Ledbetter, Robert G. Leisure, C. Pantea, and J. B. Betts. Diamond’s elastic stiffnesses from 322 K to 10 K. *Journal of Applied Physics*, 104(5):053512, 2008.
- [103] Jaron Kent-Dobias, Michael Matty, and B. J. Ramshaw. Elastic properties of hidden order in URu₂Si₂ are reproduced by a staggered nematic. *Phys. Rev. B*, 102:075129, Aug 2020.
- [104] Balázs Csanád Csáji. Approximation with artificial neural networks. Master’s thesis, Faculty of Sciences, Eötvös Loránd University, Hungary, 2001.
- [105] K. Matsuda, Y. Kohori, T. Kohara, K. Kuwahara, and H. Amitsuka. Spatially inhomogeneous development of antiferromagnetism in URu₂Si₂: Evidence from ²⁹Si NMR under pressure. *Phys. Rev. Lett.*, 87:087203, Aug 2001.
- [106] Tatsuya Yanagisawa. Ultrasonic study of the hidden order and heavy-fermion state in URu₂Si₂ with hydrostatic pressure, Rh-doping, and high magnetic fields. *Philosophical Magazine*, 94(32-33):3775–3788, 2014.
- [107] J. Buhot, M.-A. Méasson, Y. Gallais, M. Cazayous, A. Sacuto, G. Lapertot, and D. Aoki. Symmetry of the excitations in the hidden order state of URu₂Si₂. *Phys. Rev. Lett.*, 113:266405, Dec 2014.
- [108] B. Lüthi and T. J. Moran. Sound propagation near the structural phase transition in strontium titanate. *Phys. Rev. B*, 2:1211–1214, Aug 1970.
- [109] T. Ikeda, K. Fujibayashi, T. Nagai, and J. Kobayashi. Elastic anomaly in (NH₄)₂SO₄. *physica status solidi (a)*, 16(1):279–290, 1973.
- [110] Carl W. Garland and Joseph S. Jones. Elastic constants of ammonium chloride near the lambda point. *The Journal of Chemical Physics*, 39(11):2874–2880, 1963.
- [111] Tatsuma D. Matsuda, Elena Hassinger, Dai Aoki, Valentin Taufour, Georg Knebel, Naoyuki Tateiwa, Etsuji Yamamoto, Yoshinori Haga, Yoshichika Ōnuki, Zachary Fisk, and Jacques Flouquet. Details of sample dependence and transport properties of URu₂Si₂. *Journal of the Physical Society of Japan*, 80(11):114710, 2011.
- [112] Noriki Okuda, Takashi Suzuki, Zhiqiang Mao, Yoshiteru Maeno, and Toshizo Fujita. Unconventional strain dependence of superconductivity in spin-triplet superconductor Sr₂RuO₄. *Journal of the Physical Society of Japan*, 71(4):1134–1139, 2002.

- [113] Jonas Greitemann, Ke Liu, and Lode Pollet. Probing hidden spin order with interpretable machine learning. *Phys. Rev. B*, 99:060404, Feb 2019.
- [114] Y Maeno, H Hashimoto, K Yoshida, S Nishizaki, T Fujita, JG Bednorz, and F Lichtenberg. Superconductivity in a layered perovskite without copper. *Nature*, 372(6506):532–534, 1994.
- [115] T. M. Rice and M. Sigrist. Sr_2RuO_4 : an electronic analogue of ^3He ? *Journal of Physics: Condensed Matter*, 7(47):L643–L648, nov 1995.
- [116] G Baskaran. Why is Sr_2RuO_4 not a high T_c superconductor? Electron correlation, Hund’s coupling and p-wave instability. *Physica B: Condensed Matter*, 223:490–495, 1996.
- [117] C. Bergemann, S. R. Julian, A. P. Mackenzie, S. Nishizaki, and Y. Maeno. Detailed topography of the Fermi surface of Sr_2RuO_4 . *Phys. Rev. Lett.*, 84:2662–2665, Mar 2000.
- [118] A. Tamai, M. Zingl, E. Rozbicki, E. Cappelli, S. Riccò, A. de la Torre, S. McKown Walker, F. Y. Bruno, P. D. C. King, W. Meevasana, M. Shi, M. Radović, N. C. Plumb, A. S. Gibbs, A. P. Mackenzie, C. Berthod, H. U. R. Strand, M. Kim, A. Georges, and F. Baumberger. High-resolution photoemission on Sr_2RuO_4 reveals correlation-enhanced effective spin-orbit coupling and dominantly local self-energies. *Phys. Rev. X*, 9:021048, Jun 2019.
- [119] Andrew P. Mackenzie, Thomas Scaffidi, Clifford W. Hicks, and Yoshiteru Maeno. Even odder after twenty-three years: the superconducting order parameter puzzle of Sr_2RuO_4 . *npj Quantum Materials*, 2(1):40, 2017.
- [120] Catherine Kallin. Chiral p-wave order in Sr_2RuO_4 . *Reports on Progress in Physics*, 75(4):042501, Mar 2012.
- [121] Xiao-Liang Qi, Taylor L. Hughes, S. Raghu, and Shou-Cheng Zhang. Time-reversal-invariant topological superconductors and superfluids in two and three dimensions. *Phys. Rev. Lett.*, 102:187001, May 2009.
- [122] Chetan Nayak, Steven H. Simon, Ady Stern, Michael Freedman, and Sankar Das Sarma. Non-abelian anyons and topological quantum computation. *Rev. Mod. Phys.*, 80:1083–1159, Sep 2008.
- [123] K. Ishida, H. Mukuda, Y. Kitaoka, K. Asayama, Z. Q. Mao, Y. Mori, and Y. Maeno. Spin-triplet superconductivity in Sr_2RuO_4 identified by ^{17}O Knight shift. *Nature*, 396(6712):658–660, 1998.
- [124] G. M. Luke, Y. Fudamoto, K. M. Kojima, M. I. Larkin, J. Merrin, B. Nachumi, Y. J. Uemura, Y. Maeno, Z. Q. Mao, Y. Mori, H. Nakamura, and

- M. Sigrist. Time-reversal symmetry-breaking superconductivity in Sr_2RuO_4 . *Nature*, 394(6693):558–561, 1998.
- [125] Jing Xia, Yoshiteru Maeno, Peter T. Beyersdorf, M. M. Fejer, and Aharon Kapitulnik. High resolution polar kerr effect measurements of Sr_2RuO_4 : Evidence for broken time-reversal symmetry in the superconducting state. *Phys. Rev. Lett.*, 97:167002, Oct 2006.
 - [126] J. Jang, D. G. Ferguson, V. Vakaryuk, R. Budakian, S. B. Chung, P. M. Goldbart, and Y. Maeno. Observation of half-height magnetization steps in Sr_2RuO_4 . *Science*, 331(6014):186–188, 2011.
 - [127] S. Kittaka, T. Nakamura, Y. Aono, S. Yonezawa, K. Ishida, and Y. Maeno. Angular dependence of the upper critical field of Sr_2RuO_4 . *Phys. Rev. B*, 80:174514, Nov 2009.
 - [128] Jake S. Bobowski, Naoki Kikugawa, Takuto Miyoshi, Haruki Suwa, Han-shu Xu, Shingo Yonezawa, Dmitry A. Sokolov, Andrew P. Mackenzie, and Yoshiteru Maeno. Improved single-crystal growth of Sr_2RuO_4 . *Condensed Matter*, 4(1), 2019.
 - [129] Sheng Ran, Chris Eckberg, Qing-Ping Ding, Yuji Furukawa, Tristin Metz, Shanta R. Saha, I-Lin Liu, Mark Zic, Hyunsoo Kim, Johnpierre Paglione, and Nicholas P. Butch. Nearly ferromagnetic spin-triplet superconductivity. *Science*, 365(6454):684–687, 2019.
 - [130] Rahul Sharma, Stephen D. Edkins, Zhenyu Wang, Andrey Kostin, Chanchal Sow, Yoshiteru Maeno, Andrew P. Mackenzie, J. C. Séamus Davis, and Vidya Madhavan. Momentum-resolved superconducting energy gaps of Sr_2RuO_4 from quasi-particle interference imaging. *Proceedings of the National Academy of Sciences*, 117(10):5222–5227, 2020.
 - [131] Alexander Steppke, Lishan Zhao, Mark E. Barber, Thomas Scaffidi, Fabian Jerzembeck, Helge Rosner, Alexandra S. Gibbs, Yoshiteru Maeno, Steven H. Simon, Andrew P. Mackenzie, and Clifford W. Hicks. Strong peak in Sr_2RuO_4 under uniaxial pressure. *Science*, 355(6321):eaaf9398, 2017.
 - [132] Mark E. Barber, Frank Lechermann, Sergey V. Streltsov, Sergey L. Skornyakov, Sayak Ghosh, B. J. Ramshaw, Naoki Kikugawa, Dmitry A. Sokolov, Andrew P. Mackenzie, Clifford W. Hicks, and I. I. Mazin. Role of correlations in determining the van hove strain in Sr_2RuO_4 . *Phys. Rev. B*, 100:245139, Dec 2019.
 - [133] A. Pustogow, Yongkang Luo, A. Chronister, Y.-S. Su, D. A. Sokolov, F. Jerzembeck, A. P. Mackenzie, C. W. Hicks, N. Kikugawa, S. Raghu, E. D. Bauer, and S. E. Brown. Constraints on the superconducting order parameter in Sr_2RuO_4 from oxygen-17 nuclear magnetic resonance. *Nature*, 574(7776):72–75, 2019.

- [134] Kenji Ishida, Masahiro Manago, Katsuki Kinjo, and Yoshiteru Maeno. Reduction of the ^{17}O Knight shift in the superconducting state and the heat-up effect by NMR pulses on Sr_2RuO_4 . *Journal of the Physical Society of Japan*, 89(3):034712, 2020.
- [135] Aaron Chronister, Andrej Pustogow, Naoki Kikugawa, Dmitry A. Sokolov, Fabian Jerzembeck, Clifford W. Hicks, Andrew P. Mackenzie, Eric D. Bauer, and Stuart E. Brown. Evidence for even parity unconventional superconductivity in Sr_2RuO_4 . *Proceedings of the National Academy of Sciences*, 118(25):e2025313118, 2021.
- [136] A. P. Mackenzie, R. K. W. Haselwimmer, A. W. Tyler, G. G. Lonzarich, Y. Mori, S. Nishizaki, and Y. Maeno. Extremely strong dependence of superconductivity on disorder in Sr_2RuO_4 . *Phys. Rev. Lett.*, 80:161–164, Jan 1998.
- [137] Johnpierre Paglione, C. Lupien, W. A. MacFarlane, J. M. Perz, Louis Taillefer, Z. Q. Mao, and Y. Maeno. Elastic tensor of Sr_2RuO_4 . *Phys. Rev. B*, 65:220506, May 2002.
- [138] N. E. Hussey, A. P. Mackenzie, J. R. Cooper, Y. Maeno, S. Nishizaki, and T. Fujita. Normal-state magnetoresistance of Sr_2RuO_4 . *Phys. Rev. B*, 57:5505–5511, Mar 1998.
- [139] D. Stricker, J. Mravlje, C. Berthod, R. Fittipaldi, A. Vecchione, A. Georges, and D. van der Marel. Optical response of Sr_2RuO_4 reveals universal fermi-liquid scaling and quasiparticles beyond Landau theory. *Phys. Rev. Lett.*, 113:087404, Aug 2014.
- [140] R. O. Bell and G. Rupprecht. Elastic constants of strontium titanate. *Phys. Rev.*, 129:90–94, Jan 1963.
- [141] J. R. Sandercock, S. B. Palmer, R. J. Elliott, W. Hayes, S. R. P. Smith, and A. P. Young. Brillouin scattering, ultrasonic and theoretical studies of acoustic anomalies in crystals showing Jahn-Teller phase transitions. *Journal of Physics C: Solid State Physics*, 5(21):3126–3146, Oct 1972.
- [142] M. E. Barber, A. S. Gibbs, Y. Maeno, A. P. Mackenzie, and C. W. Hicks. Resistivity in the vicinity of a van hove singularity: Sr_2RuO_4 under uniaxial pressure. *Phys. Rev. Lett.*, 120:076602, Feb 2018.
- [143] Aaron Chronister, Manuel Zingl, Andrej Pustogow, Yongkang Luo, Dmitry Sokolov, Naoki Kikugawa, Clifford Hicks, Fabian Jerzembeck, Jernei Mravlje, Eric Bauer, Andrew Mackenzie, Antoine Georges, and Stuart Brown. Tuning the Fermi liquid crossover in Sr_2RuO_4 with uniaxial stress. *arXiv:2111.05570*, 2021.
- [144] B. Burganov, C. Adamo, A. Mulder, M. Uchida, P. D. C. King, J. W. Harter, D. E. Shai, A. S. Gibbs, A. P. Mackenzie, R. Uecker, M. Bruetzam, M. R. Beasley, C. J.

- Fennie, D. G. Schlom, and K. M. Shen. Strain control of fermiology and many-body interactions in two-dimensional ruthenates. *Phys. Rev. Lett.*, 116:197003, May 2016.
- [145] W.F. Perger, J. Criswell, B. Civalleri, and R. Dovesi. Ab-initio calculation of elastic constants of crystalline systems with the CRYSTAL code. *Computer Physics Communications*, 180(10):1753–1759, 2009.
- [146] Rostam Golesorkhtabar, Pasquale Pavone, Jürgen Spitaler, Peter Puschnig, and Claudia Draxl. ElaStic: A tool for calculating second-order elastic constants from first principles. *Computer Physics Communications*, 184(8):1861–1873, 2013.
- [147] Zhong-Li Liu, C.E. Ekuma, Wei-Qi Li, Jian-Qun Yang, and Xing-Ji Li. Elas-Tool: An automated toolkit for elastic constants calculation. *Computer Physics Communications*, 270:108180, 2022.
- [148] D. Forsythe, S. R. Julian, C. Bergemann, E. Pugh, M. J. Steiner, P. L. Alireza, G. J. McMullan, F. Nakamura, R. K. W. Haselwimmer, I. R. Walker, S. S. Saxena, G. G. Lonzarich, A. P. Mackenzie, Z. Q. Mao, and Y. Maeno. Evolution of fermi-liquid interactions in Sr_2RuO_4 under pressure. *Phys. Rev. Lett.*, 89:166402, Sep 2002.
- [149] Kazuhiko Deguchi, Z Q. Mao, and Yoshiteru Maeno. Determination of the superconducting gap structure in all bands of the spin-triplet superconductor Sr_2RuO_4 . *Journal of the Physical Society of Japan*, 73(5):1313–1321, 2004.
- [150] A. T. Rømer, D. D. Scherer, I. M. Eremin, P. J. Hirschfeld, and B. M. Andersen. Knight shift and leading superconducting instability from spin fluctuations in Sr_2RuO_4 . *Phys. Rev. Lett.*, 123:247001, Dec 2019.
- [151] Igor Žutić and Igor Mazin. Phase-sensitive tests of the pairing state symmetry in Sr_2RuO_4 . *Phys. Rev. Lett.*, 95:217004, Nov 2005.
- [152] Shunichiro Kittaka, Shota Nakamura, Toshiro Sakakibara, Naoki Kikugawa, Taichi Terashima, Shinya Uji, Dmitry A. Sokolov, Andrew P. Mackenzie, Koki Irie, Yasumasa Tsutsumi, Katsuhiro Suzuki, and Kazushige Machida. Searching for gap zeros in Sr_2RuO_4 via field-angle-dependent specific-heat measurement. *Journal of the Physical Society of Japan*, 87(9):093703, 2018.
- [153] Aline Ramires and Manfred Sigrist. Superconducting order parameter of Sr_2RuO_4 : A microscopic perspective. *Phys. Rev. B*, 100:104501, Sep 2019.
- [154] Han Gyeol Suh, Henri Menke, P. M. R. Brydon, Carsten Timm, Aline Ramires, and Daniel F. Agterberg. Stabilizing even-parity chiral superconductivity in Sr_2RuO_4 . *Phys. Rev. Research*, 2:032023, Jul 2020.

- [155] M. W. Haverkort, I. S. Elfimov, L. H. Tjeng, G. A. Sawatzky, and A. Damascelli. Strong spin-orbit coupling effects on the fermi surface of Sr_2RuO_4 and Sr_2RhO_4 . *Phys. Rev. Lett.*, 101:026406, Jul 2008.
- [156] C. N. Veenstra, Z.-H. Zhu, M. Raichle, B. M. Ludbrook, A. Nicolaou, B. Slomski, G. Landolt, S. Kittaka, Y. Maeno, J. H. Dil, I. S. Elfimov, M. W. Haverkort, and A. Damascelli. Spin-orbital entanglement and the breakdown of singlets and triplets in Sr_2RuO_4 revealed by spin- and angle-resolved photoemission spectroscopy. *Phys. Rev. Lett.*, 112:127002, Mar 2014.
- [157] J. Bardeen, L. N. Cooper, and J. R. Schrieffer. Theory of superconductivity. *Phys. Rev.*, 108:1175–1204, Dec 1957.
- [158] L. C. Hebel and C. P. Slichter. Nuclear relaxation in superconducting aluminum. *Phys. Rev.*, 107:901–902, Aug 1957.
- [159] R. W. Morse, T. Olsen, and J. D. Gavenda. Evidence for anisotropy of the superconducting energy gap from ultrasonic attenuation. *Phys. Rev. Lett.*, 3:15–16, Jul 1959.
- [160] J. R. Leibowitz. Ultrasonic shear wave attenuation in superconducting tin. *Phys. Rev.*, 133:A84–A96, Jan 1964.
- [161] Lewis T. Claiborne and Norman G. Einspruch. Energy-gap anisotropy in In-doped Sn. *Phys. Rev. Lett.*, 15:862–864, Nov 1965.
- [162] K. Fossheim. Electromagnetic shear-wave interaction in a superconductor. *Phys. Rev. Lett.*, 19:344–344, Aug 1967.
- [163] B. Batlogg, D. Bishop, B. Golding, C. M. Varma, Z. Fisk, J. L. Smith, and H. R. Ott. λ -shaped ultrasound-attenuation peak in superconducting (U,Th)Be₁₃. *Phys. Rev. Lett.*, 55:1319–1322, Sep 1985.
- [164] Brage Golding, D. J. Bishop, B. Batlogg, W. H. Haemmerle, Z. Fisk, J. L. Smith, and H. R. Ott. Observation of a collective mode in superconducting UBe₁₃. *Phys. Rev. Lett.*, 55:2479–2482, Nov 1985.
- [165] V. Müller, D. Maurer, E.W. Scheidt, Ch. Roth, K. Lüders, E. Bucher, and H.E. Bömmel. Observation of a lambda-shaped ultrasonic attenuation peak in superconducting UPt₃. *Solid State Communications*, 57(5):319 – 321, 1986.
- [166] J. Moreno and P. Coleman. Ultrasound attenuation in gap-anisotropic systems. *Phys. Rev. B*, 53:R2995–R2998, Feb 1996.
- [167] H. Monien, L. Tewordt, and K. Scharnberg. Ultrasound attenuation due to order

- parameter collective modes in impure anisotropic p-wave superconductors. *Solid State Communications*, 63(11):1027 – 1031, 1987.
- [168] Robert Joynt, T. Maurice Rice, and Kazuo Ueda. Acoustic attenuation due to domain walls in anisotropic superconductors, with application to $\text{U}_{1-x}\text{Th}_x\text{Be}_{13}$. *Phys. Rev. Lett.*, 56:1412–1415, Mar 1986.
 - [169] L. Coffey. Theory of ultrasonic attenuation in impure anisotropic p-wave superconductors. *Phys. Rev. B*, 35:8440–8448, Jun 1987.
 - [170] Suk Bum Chung, S. Raghu, Aharon Kapitulnik, and Steven A. Kivelson. Charge and spin collective modes in a quasi-one-dimensional model of Sr_2RuO_4 . *Phys. Rev. B*, 86:064525, Aug 2012.
 - [171] C. Lupien. *Ultrasound attenuation in the unconventional superconductor Sr_2RuO_4* . PhD thesis, 2002.
 - [172] F. S. Khan and P. B. Allen. Sound attenuation by electrons in metals. *Phys. Rev. B*, 35:1002–1019, Jan 1987.
 - [173] AB Pippard. Cxxii. ultrasonic attenuation in metals. *The London, Edinburgh, and Dublin Philosophical Magazine and Journal of Science*, 46(381):1104–1114, 1955.
 - [174] Michael Tinkham. *Introduction to Superconductivity*. McGraw-Hill, New York, 1996.
 - [175] Hyekyung Won and Kazumi Maki. d-wave superconductor as a model of high- T_c superconductors. *Phys. Rev. B*, 49:1397–1402, Jan 1994.
 - [176] I. Vekhter, E. J. Nicol, and J. P. Carbotte. Ultrasonic attenuation in clean d-wave superconductors. *Phys. Rev. B*, 59:7123–7126, Mar 1999.
 - [177] S. Adenwalla, Z. Zhao, J. B. Ketterson, and Bimal K. Sarma. Measurements of the pair-breaking edge in superfluid $^3\text{He}-B$. *Phys. Rev. Lett.*, 63:1811–1814, Oct 1989.
 - [178] I. A. Firmo, S. Lederer, C. Lupien, A. P. Mackenzie, J. C. Davis, and S. A. Kivelson. Evidence from tunneling spectroscopy for a quasi-one-dimensional origin of superconductivity in Sr_2RuO_4 . *Phys. Rev. B*, 88:134521, Oct 2013.
 - [179] R.W. Leonard, A. Barone, Rohn Truell, Charles Elbaum, and B. E. Noltingk. *Acoustics II*. Springer-Verlag, Berlin Heidelberg, 1962.
 - [180] Francoise Kidwingira, J. D. Strand, D. J. Van Harlingen, and Yoshiteru Maeno.

- Dynamical superconducting order parameter domains in Sr_2RuO_4 . *Science*, 314(5803):1267–1271, 2006.
- [181] Thomas Christopoulos, Odysseas Tsilipakos, Georgios Sinatkas, and Emmanouil E. Kriezis. On the calculation of the quality factor in contemporary photonic resonant structures. *Opt. Express*, 27(10):14505–14522, May 2019.
 - [182] S. Benhabib, C. Lupien, I. Paul, L. Berges, M. Dion, M. Nardone, A. Zitouni, Z. Q. Mao, Y. Maeno, A. Georges, L. Taillefer, and C. Proust. Ultrasound evidence for a two-component superconducting order parameter in Sr_2RuO_4 . *Nature Physics*, 17(2):194–198, Feb 2021.
 - [183] Jonathan Clepkens, Austin W. Lindquist, Xiaoyu Liu, and Hae-Young Kee. Higher angular momentum pairings in interorbital shadowed-triplet superconductors: Application to Sr_2RuO_4 . *Phys. Rev. B*, 104:104512, Sep 2021.
 - [184] Astrid T. Rømer, P. J. Hirschfeld, and Brian M. Andersen. Superconducting state of Sr_2RuO_4 in the presence of longer-range coulomb interactions. *Phys. Rev. B*, 104:064507, Aug 2021.
 - [185] Christopher A. Watson, Alexandra S. Gibbs, Andrew P. Mackenzie, Clifford W. Hicks, and Kathryn A. Moler. Micron-scale measurements of low anisotropic strain response of local T_c in Sr_2RuO_4 . *Phys. Rev. B*, 98:094521, Sep 2018.
 - [186] M. B. Walker, M. F. Smith, and K. V. Samokhin. Electron-phonon interaction and ultrasonic attenuation in the ruthenate and cuprate superconductors. *Phys. Rev. B*, 65:014517, Dec 2001.
 - [187] A. B. Bhatia. *Ultrasonic absorption: an introduction to the theory of sound absorption and dispersion in gases, liquids and solids*. Clarendon P., Oxford, 1967.
 - [188] W. G. Baber and Nevill Francis Mott. The contribution to the electrical resistance of metals from collisions between electrons. *Proceedings of the Royal Society of London. Series A - Mathematical and Physical Sciences*, 158(894):383–396, 1937.
 - [189] J. Bardeen and W. Shockley. Deformation potentials and mobilities in non-polar crystals. *Phys. Rev.*, 80:72–80, Oct 1950.
 - [190] Philip J. W. Moll, Pallavi Kushwaha, Nabhanila Nandi, Burkhard Schmidt, and Andrew P. Mackenzie. Evidence for hydrodynamic electron flow in PdCoO_2 . *Science*, 351(6277):1061–1064, 2016.
 - [191] N. W. Ashcroft and N. D. Mermin. *Solid State Physics*. Holt-Saunders, 1976.

- [192] Egor I. Kiselev and Jörg Schmalian. Boundary conditions of viscous electron flow. *Phys. Rev. B*, 99:035430, Jan 2019.
- [193] William S. Slaughter. *The Linearized Theory of Elasticity*. Birkhäuser, Boston, 2002.